Preoperative Surgical Planning

Fauser, Johannes Ludwig

(2020)

Preoperative Surgical Planning

Toward an Automatic Pipeline for Segmentation and Nonlinear Trajectory Planning in Robot-Assisted Interventions

Zur Erlangung des akademischen Grades Doktor-Ingenieur (Dr.-Ing.)
genehmigte Dissertation im Fachbereich Informatik von Johannes Ludwig Fauser aus Tübingen
Tag der Einreichung: 20.02.2020, Tag der Prüfung: 29.04.2020

1. Gutachten: Prof. Dr.-techn. Dieter W. Fellner
2. Gutachten: Prof. Dr. Arjan Kuijper
3. Gutachten: Prof. Dr. Caroline Essert
Darmstadt – D 17
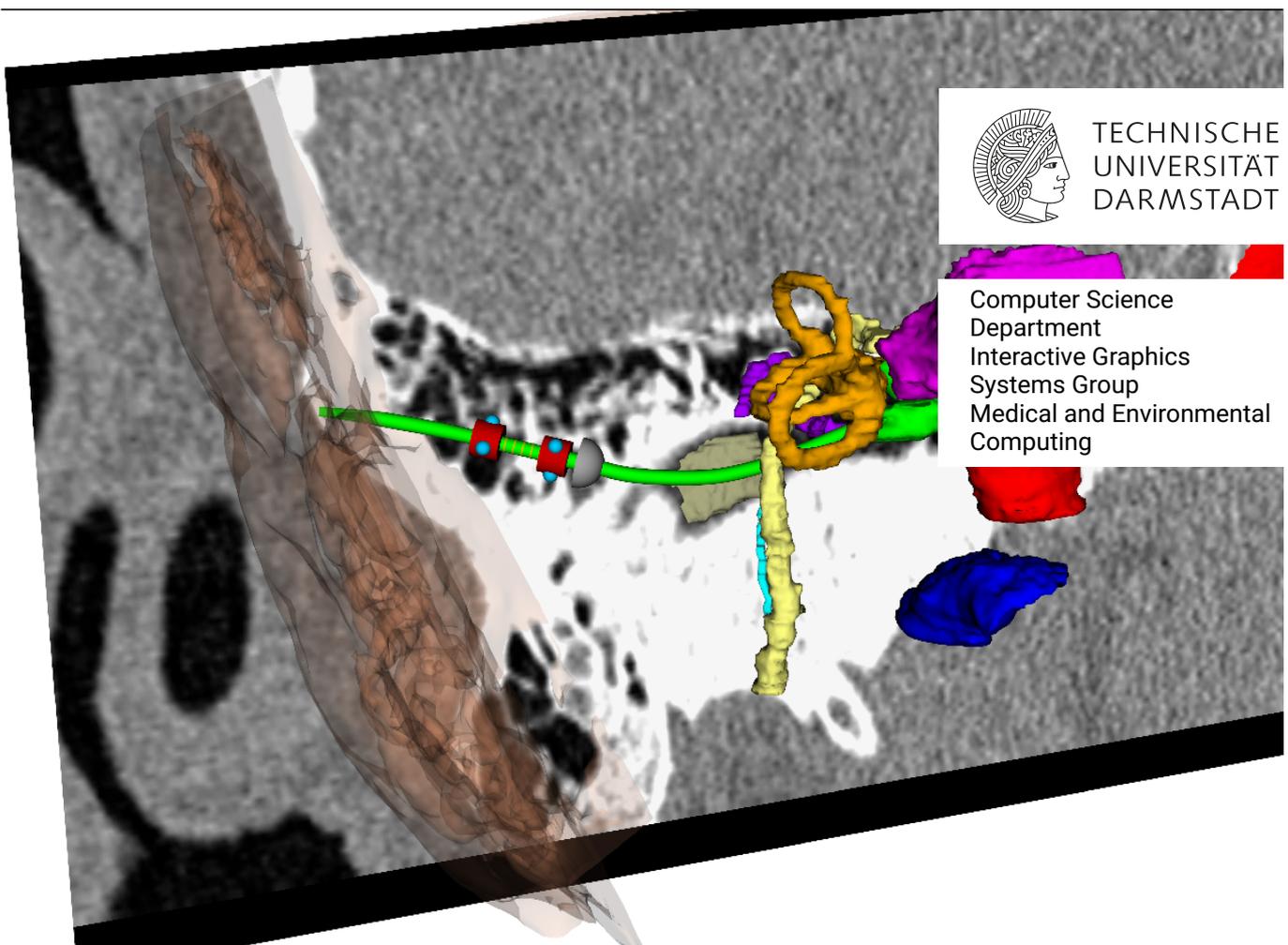
TECHNISCHE UNIVERSITÄT DARMSTADT

Computer Science Department
Interactive Graphics Systems Group
Medical and Environmental Computing

Preoperative Surgical Planning
Toward an Automatic Pipeline for Segmentation and Nonlinear Trajectory Planning in Robot-Assisted Interventions

Doctoral thesis in Computer Science by Johannes Ludwig Fauser

1. Review: Prof. Dr.-techn. Dieter W. Fellner
2. Review: Prof. Dr. Arjan Kuijper
3. Review: Prof. Dr. Caroline Essert

Date of submission: 20.02.2020
Date of thesis defense: 29.04.2020

Darmstadt – D 17

To Janine,
for following my rather short-termed decision to do a PhD,
for her constant and enduring support and encouragement,
for her most generous tolerance to my self-deceiving forecasts
about the duration of our stay.

Erklärungen laut Promotionsordnung

§8 Abs. 1 lit. c PromO

Ich versichere hiermit, dass die elektronische Version meiner Dissertation mit der schriftlichen Version übereinstimmt.

§8 Abs. 1 lit. d PromO

Ich versichere hiermit, dass zu einem vorherigen Zeitpunkt noch keine Promotion versucht wurde. In diesem Fall sind nähere Angaben über Zeitpunkt, Hochschule, Dissertationsthema und Ergebnis dieses Versuchs mitzuteilen.

§9 Abs. 1 PromO

Ich versichere hiermit, dass die vorliegende Dissertation selbstständig und nur unter Verwendung der angegebenen Quellen verfasst wurde.

§9 Abs. 2 PromO

Die Arbeit hat bisher noch nicht zu Prüfungszwecken gedient.

Darmstadt, den 20.02.2020 _____

J. Fauser

Abstract

Since several decades, minimally-invasive surgery has continuously improved both clinical workflow and outcome. Such procedures minimize patient trauma, decrease hospital stay or reduce risk of infection. Next generation robot-assisted interventions promise to further improve on these advantages while at the same time opening the way to new surgical applications.

Temporal Bone Surgery and Endovascular Aortic Repair are two examples for such currently researched approaches, where manual insertion of instruments, subject to a clinician's experience and daily performance, could be replaced by a robotic procedure. In the first, a flexible robot would drill a nonlinear canal through the mastoid, allowing a surgeon access to the temporal bone's apex, a target often unreachable without damaging critical risk structures. For the second example, robotically driven guidewires could significantly reduce the radiation exposure from fluoroscopy, that is exposed to patients and surgeons during navigation through the aorta.

These robot-assisted surgeries require preoperative planning consisting of segmentation of risk structures and computation of nonlinear trajectories for the instruments. While surgeons could so far rely on preoperative images and a mental 3D model of the anatomy, these new procedures will make computational assistance inevitable due to the added complexity from image processing and motion planning. The automation of tiresome and manually laborious tasks is therefore crucial for successful clinical implementation.

This thesis addresses these issues and presents a preoperative pipeline based on CT images that automates segmentation and trajectory planning. Major contributions include an automatic shape regularized segmentation approach for coherent anatomy extraction as well as an exhaustive trajectory planning step on locally optimized Bézier Splines. It also introduces thorough in silico experiments that perform functional evaluation on real and synthetically enlarged datasets. The benefits of the approach are shown on an in house dataset of otobasis CT scans as well as on two publicly available datasets containing aorta and heart.

Zusammenfassung

Seit mehreren Jahrzehnten verbessern minimal-invasive Eingriffe sowohl klinische Arbeitsabläufe als auch chirurgische Ergebnisse. Diese Verfahren minimieren beispielsweise das Trauma für Patienten, verkürzen deren Klinikaufenthalt oder reduzieren das Risiko von Infektionen. Momentan sich in der Forschung befindliche roboter-assistierte Interventionen versprechen, diese Vorteile weiter zu verbesssern sowie neue chirurgische Eingriffe zu ermöglichen.

Felsenbeinchirurgie und Endovaskuläre Aortenreparatur sind zwei Beispiele für derartige Ansätze, bei denen das manuelle Einführen von Instrumenten, das von der Erfahrung eines Arztes und seiner täglichen Leistungsfähigkeit abhängt, durch eine robotergeführte Lösung ersetzt wird. Der erste Fall sieht einen flexiblen Bohrroboter vor, der einen nichtlinearen Kanal durch das Mastoid bohrt und dem Chirurgen so einen Zugang zur Felsenbeinspitze ermöglicht. Diese ist mit derzeitigen Verfahren oft nur unter Beeinträchtigung kritischer Risikostrukturen zu erreichen. Im zweiten Beispiel wird ein Führungsdraht für Katheter automatisch in die Aorta eingeführt. Bei diesem unter Fluoroskopie durchgeführten Verfahren verspricht eine robotische Lösung sowohl Ärzten als auch Patienten eine deutliche Verminderung der ihnen ausgesetzten Strahlung.

Derartige roboter-assistierte Operationen benötigen präoperative Planung, die aus der Segmentierung von Risikostrukturen und der Berechnung nichtlinearer Trajektorien für die flexiblen Instrumente besteht. Während sich Chirurgan bisher auf präoperative Bilddaten und ein daraus erstelltes mentales Modell der Anatomie verlassen konnten, werden diese neuartige Ansätze eine rechnergestützte Lösung jedoch aufgrund der zusätzlichen Komplexität aus Bildverarbeitung und Pfadplanung zwingend benötigen. Um eine erfolgreiche Umsetzung dieser Eingriffe zu erreichen, ist daher eine Automatisierung von ermüdenden oder arbeitsaufwändigen Aufgaben entscheidend.

Diese Thesis adressiert diese Aspekte und präsentiert eine präoperative Pipeline auf Grundlage von CT-Daten, die automatisch sowohl eine Segmentierung von Risikostrukturen als auch eine Trajektorienplanung durchführt. Der Hauptteil der Arbeit beinhaltet

einen automatische Form-erhaltenden Segmentierungsansatz für kohärente Extraktion von Anatomien sowie einen mehrstufigen Pfadplanungsschritt, der zu lokal optimierten Bézier Splines führt. Die Arbeit stellt außerdem gründliche In Silico Experimente vor, die eine funktionale Auswertung von Algorithmen auf echten und synthetisch erweiterten Datensätzen durchführt. Die Vorteile des vorgeschlagenen Ansatzes werden anhand Experimenten auf CT-Bilder der Otobasis sowie zweier öffentlich zugänglicher Datensätze evaluiert.

Contents

1. Introduction

Minimally-invasive procedures are an ongoing trend in surgery [12, 85]. Applications such as laparoscopic keyhole surgery or endovascular treatment of aneurysms tremendously increase patient benefit and clinical outcome. These solutions reduce trauma as well as scarring and result in both shorter recovery time and hospital stay [52, 274]. Major benefits also lie in reduced risk of infections [219] or other complications during surgery [93], thus decreasing morbidity associated to the particular disease. Consequently, a variety of continuum robots for medical applications are currently researched to further improve these procedures. The survey of Burgner-Kahrs et al. [26] gives a great outlook on upcoming solutions promising advantages such as access to yet unreachable surgical sites or applicability to new clinical applications. The presented flexible instruments (Figure 1.1) replace manual insertion and instrument handling by a robotically-driven procedure along nonlinear trajectories.

However, a robotic procedure heavily increases the complexity of the minimally-invasive approach and requires **preoperative surgical planning**. The envisioned applications, e.g. needle insertion into soft tissue [187], drilling access canals through bone [126], ribbon design for intracavitary brachytherapy [188] or steerable guidewires [88], all share the same setup: Based on an image volume that is acquired before surgery, e.g. a Computed Tomography (CT) image, a segmentation algorithm extracts organs at risk which are then used to create a 3D representation of the patient's anatomy. In a subsequent trajectory planning step, a designated motion planning algorithm computes feasible trajectories for the underlying instrument which circumvent the previously detected risk structures. Successful clinical implementation would require automation of major parts of this workflow while still keeping the surgeon in the loop for control of critical sub-steps. Consequently, automatic segmentation algorithms [15, 225], fast and robust motion planning algorithms [38, 194] as well as tools for intuitive and suitable workflows [90] are an active research field and crucial for successful clinical implementation.
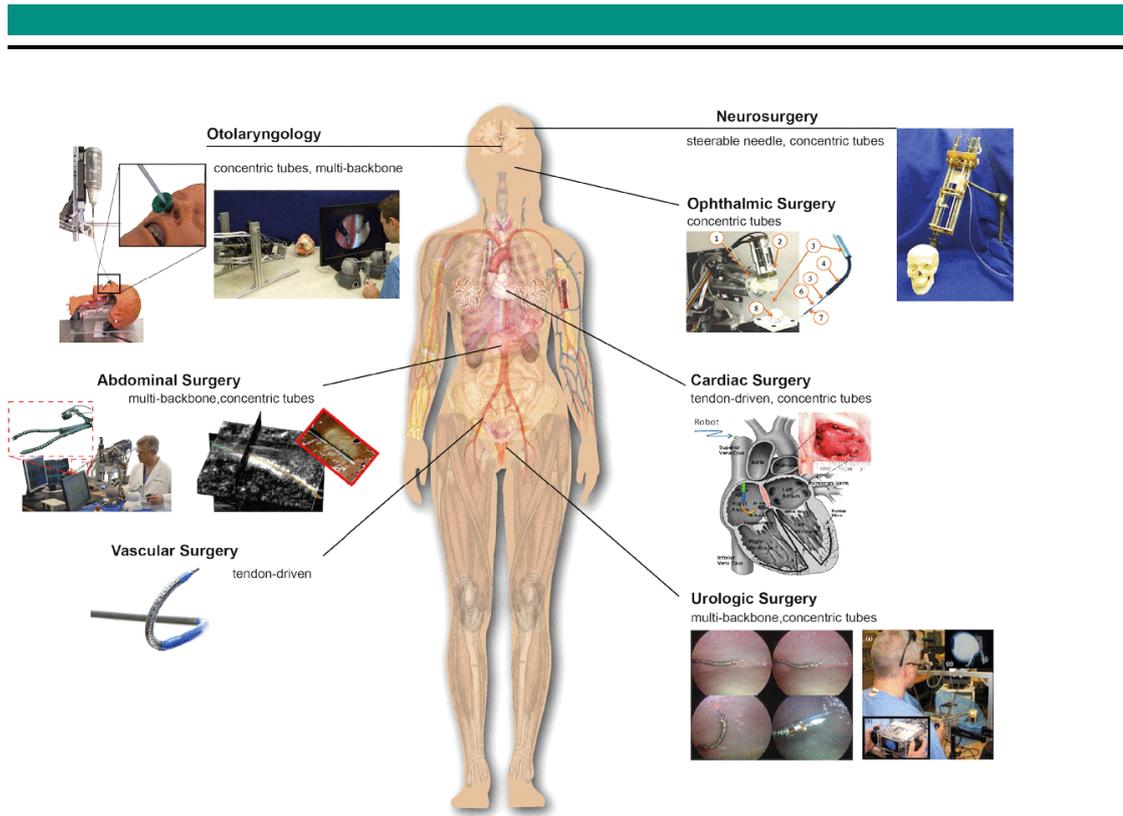
Figure 1.1.: Example applications that could benefit from robotically-driven flexible instruments. This thesis presents a preoperative planning pipeline for custom applications in otolaryngology and endovascular surgery. Figure adapted from [26] © [2015] IEEE.

Current research focuses on individual tasks of these new approaches, such as segmentation, path planning or robot development. While these works achieve important results on specific sub-steps, their experiments often give an isolated view on the presented task. This results, for example, in method evaluation with metrics such as Dice that looks at image processing performance only. However, the clinical implementation and workflow rely on all these parts working together. Evaluation of an algorithm for preoperative surgical planning should thus consider the complete procedure. **This thesis introduces** a full preoperative surgical planning pipeline for minimally-invasive interventions using flexible instruments. It proposes two strategies for retrospective in silico experiments: Functional evaluation on downstream tasks, e.g. rating segmentation performance on path planning outcome, and experiments on synthetic anatomies for extensive tests where

■ Jugular vein ■ Carotid artery ■ Facial nerve ■ Chorda tympani ■ External auditory canal ■ Internal auditory canal ■ Cochlea ■ Semicircular canals ■ Ossicles
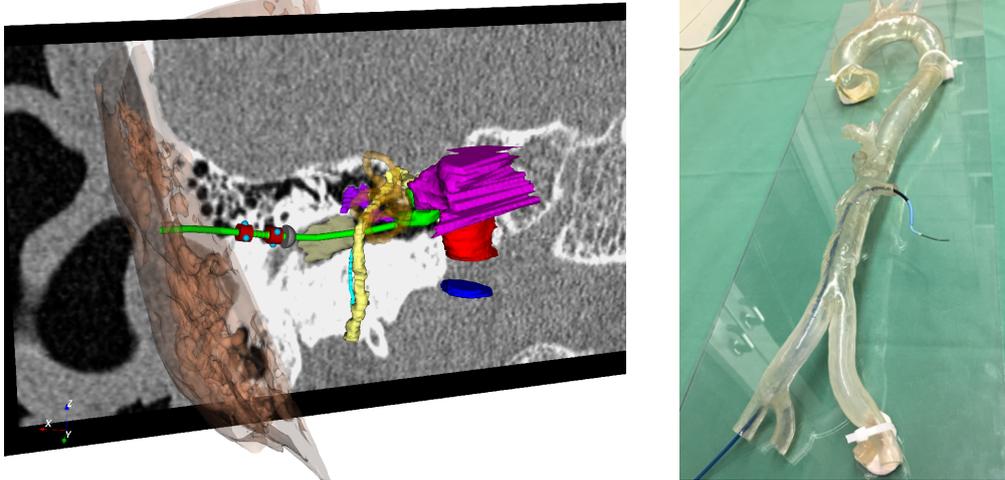
Figure 1.2.: Example applications in this thesis are Temporal Bone Surgery (Left: using a bendable drilling unit, colored object on green trajectory) and Endovascular Aortic Repair (Right: catheter insertion into a side branch of a 3D printed aortic model).

only limited expert annotated data is available. It contributes a segmentation method combining Deep Learning with Active Shape Models for extraction of coherent anatomies. It proposes an extensive trajectory planning step for a novel motion planning problem, solving a two-point boundary problem in the presence of obstacles, including initial planning, optimization and generalization. Finally, it presents an open source framework with GUI for interactive preoperative planning, so the research community can benefit from this work.

Experiments are conducted for two example applications that benefit from robotically-driven procedures: Temporal Bone Surgery and Endovascular Aortic Repair.

In Temporal Bone Surgery an access canal needs to be drilled through the mastoid to reach the surgical site while avoiding vessels, nerves and organs of the hearing and equilibrium senses (Figure 1.2 left). For procedures such as a cochlear implantation or vestibular schwannoma removal, curved access canals would allow larger clearance to

risk structures and access to regions deeper within the temporal bone, thus increasing accessibility of the surgery for more patients. Despite the rigid environment, tiny structures such as the nerves and high anatomical variability between patients remain a serious challenge for segmentation. During cochlear implantation, robust and precise trajectory planning could benefit the proper insertion of the electrode. For this purpose, path planning algorithms should consider an optimal angle at the entry point of the electrode to the cochlea, such that it aligns with the centerline of its basal turn. Preoperative surgical planning could therefore greatly benefit the necessary navigation accuracy [211] during surgery.

Endovascular Aortic Repair requires the insertion of a catheter into the aorta or its side branches (Figure 1.2 right) and the subsequent deployment of tools, e.g. stent grafts, at the aneurysm's position. Beforehand, the extraction of a 3D surface model from 3D angiography images is necessary [54], which is currently done via manual segmentation. This allows to create a 3D print of the patient's aortic model that can be used for both patient education and treatment planning. During surgery, the surgeon navigates under fluoroscopy, i.e. x-ray guidance, which offers limited support for 3D orientation. In cases with complex aortic anatomy, insertion of the catheter into side branches of the aorta is very difficult. Repeated attempts to navigate into these branches extends the length of the procedure and results in accumulated high doses of radiation for the surgeon. Here, preoperative planning could again greatly reduce the time needed for segmentation and enable a robotically-driven procedure with less radiation by computing feasible nonlinear trajectories for the instrument.

1.1. Preoperative Surgical Planning

The following section describes the four major parts of preoperative surgical planning (Figure 1.3), each having a significant impact on clinical workflow:

1. 3D-image acquisition using, for example, CT or Magnetic Resonance Imaging (MRI),

2. segmentation of Organs at Risk (also called risk structures, obstacles in the remaining thesis),

3. trajectory planning for the underlying instrument,

4. retrospective in silico evaluation.

| Image Acquisition | Segmentation | Trajectory Planning | In Silico Evaluation |
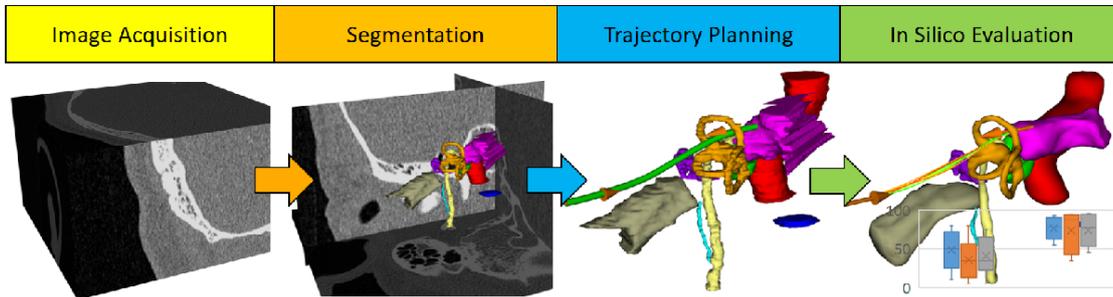
Figure 1.3.: Schematic view of a preoperative surgical planning pipeline for robot-assisted surgery. Based on a CT image (1), risk structures of the surgery are segmented (2). The extracted 3D environment enables motion planning for nonlinear trajectories (3), where segmented objects are used for collision detection. In silico evaluation (4) assesses the suitability of individual segmentation and planning algorithms even on small datasets.

Image Acquisition follows dedicated hardware acquisition protocols for the application. For temporal bone surgery, this could include CT and MRI scans to measure clinical characteristics such as the cochlear duct length [86] influencing implant design or to detect malformations [218] such as aplasia or incomplete partitions of the cochlea. While this step is not considered in this thesis, knowledge about this part is important. Especially computer scientists can benefit from dedicated articles [109, 128] around clinical practices in this field.

Segmentation is the process of partitioning an image into several regions. In medical image processing for preoperative planning this results in either a 3D label image distinguishing between foreground and background voxels or a triangle mesh representing the organs' boundaries. It has been a core unsolved problem in the medical field. While model-based algorithms like Active Shape Model (ASM) have shown promising results, the rise of Deep Learning in recent years has since shown that outstanding general architectures such as U-Net often outperform the former. Independent of the method, *automation* of segmentation can benefit the clinical workflow. First, it can significantly reduce time and thus free the surgeon from a laborious and tiresome task. For endovascular surgery, a combination of Deep Learning prediction and ASM regularization would reduce manual aortic segmentation for 3D printing [54, 104], currently done in roughly 2 hours per patient at our collaborators institute, to an automatic procedure of 10 minutes. These
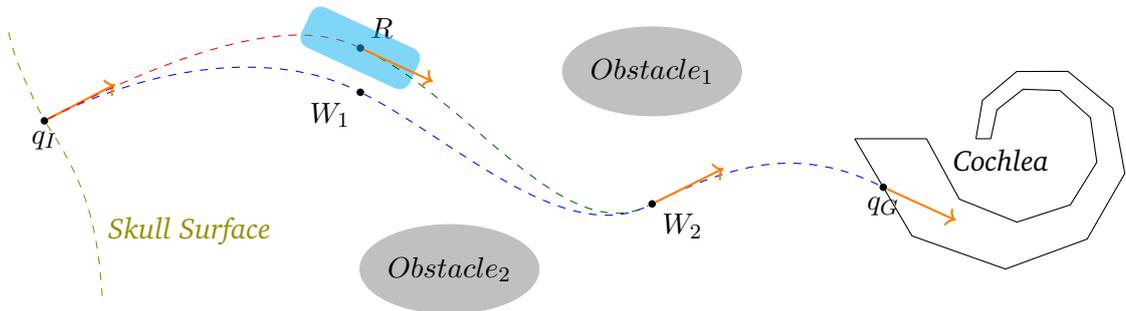
Figure 1.4.: Sketch of the novel motion planning problem in surgical planning for Temporal Bone Surgery, which includes hard constraints on position and direction at q_I and q_G of a potential trajectory. The goal q_G marks the entry point of the electrode at the cochlea and should be reached along the centerline of the lower ductus. The initial state q_I should align with the robot's orientation either preoperatively at the skull's surface or during navigation, when replanning is required from the current pose of robot R to a waypoint W_2.

models could be used for planning, patient education or surgeon training [92]. Second, it reduces intra- and inter-clinician bias [252], leading to a more robust and reproducible procedure.

Trajectory Planning   is responsible for finding feasible trajectories for the underlying instrument. This thesis covers interventions with instruments that follow curvature constrained trajectories, e.g., needles, drilling units or catheters. Figure 1.4 sketches the problem. From an initial state c_I with given position and direction a trajectory has to be found to a goal state c_G with given position and direction. In temporal bone surgery, this initial state could be given by a positioning unit for the instrument. The goal state could be given by the optimal insertion angle at the round window at the cochlea [240]. The problem occurs in two phases: First, a preoperative confirmation of the feasibility of the minimally-invasive approach is needed by providing at least one collision-free trajectory for the instrument from c_I to c_G. Second, during navigation of the instrument along the path, misalignment might require a replanning for feasible trajectories from R to W_2. Suitable motion planning algorithms thus have to quickly solve a two point boundary value problem in the presence of obstacles. Beside this technical challenge, clinical constraints for a safe procedure require for example optimized distances to obstacles along a path, further increasing problem complexity.

■ Aorta ■ Heart ■ Esophagus ■ Trachea
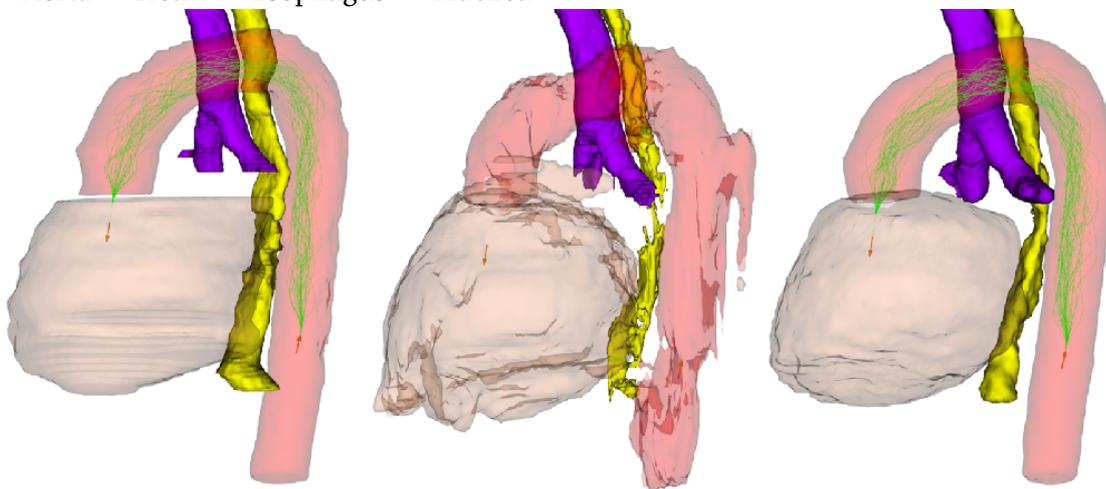
Figure 1.5.: Surfaces models from (left to right) expert annotations, U-Net segmentation and shape regularization. Because Deep Learning architectures perform only pixel-wise classification, results may contain fragmented structures. The computation of nonlinear trajectories (green lines) thus requires the extraction of plausible anatomies, possible by our shape regularized approaches.

Retrospective In Silico Evaluation Preoperative surgical planning thus combines two orthogonal research fields, segmentation and motion planning, where the latter heavily relies on the quality of the former. However, segmentation quality is usually measured by objective measurement functions such as Dice or Hausdorff Distance (HD). These metrics are useful for general assessment of segmentation algorithms or applications such as volume estimation of the left ventricle [171]. In contrast, segmentation for surgical planning provides representations of organs at risk, which are used for collision detection in downstream tasks such as trajectory planning (see Figure 1.5). The topology and shape of a segmented object matter and fragmented surface meshes or isolated labels, unrecognized by metrics such as Dice, are problematic. Finally, motion planning algorithms for our clinical applications should be robust, converging to solutions in the highly varying anatomies of patients. In motion planning, this is usually done using random worlds, randomly created setups with obstacles and start and goal states, in which algorithms have to find solutions. However, for these clinical settings only scarce datasets are usually available and experiments on a statistically meaningful sample size could greatly benefit evaluations. Such in silico experiments, performed before the use of

phantoms, could thus add significant scientific value because it thoroughly evaluates the interplay of these two parts.

1.2. Problems & Contributions

Combining all aspects, the problem of preoperative surgical planning can be described as follows: Automatically segment a patient's anatomy that enables the computation of collision-free nonlinear trajectories, such that these paths optimize clinical outcome by guaranteeing optimal alignment and clearance to risk structures. In particular, such planning faces the following challenges:

- a thorough evaluation of the preoperative pipeline regarding both scarcity of data and influence of segmentation on trajectory planning.

- automatic segmentation for Temporal Bone Surgery with results suitable for collision detection.

- motion planning capable of quickly solving and optimizing the two point boundary value problem under clinical constraints.

This thesis contributes to each of these problems, resulting in automated segmentation and trajectory planning steps. The methods are evaluated on both in house and publicly available datasets and published as open source code in a framework with GUI that allows both technical and clinical researchers to improve and evaluate the suggested preoperative surgical workflow. Future work can thereby address individual parts of this pipeline while improving the complete preoperative surgical planning task through evaluation of the whole procedure. In particular, this thesis includes the following contributions:

- It introduces automatic shape regularized segmentation as a prerequisite for surgical planning, proposing a combination of Deep Learning and Probabilistic Active Shape Models as a solution.

- It describes a general motion planning problem formulation for nonlinear interventions.

- It propose a three step solution for this formulation by presenting

    - Trajectory planning with Bidirectional RRTs on cubic Bézier Splines,

    - Sequential convex optimization on these paths for local optimality,

– Translation of these paths to Circular Arcs, making this 3 step approach suitable to instruments such as bevel-tip needles

- It shows the applicability of this solution on different applications using instruments such as drilling units, flexible needles and guidewires.

- It makes the complete open source framework with GUI available to the research community, enabling interactive segmentation and trajectory planning employing Deep Learning based segmentation, trajectory planning and optimization.

1.3. Thesis structure

The remaining of the thesis is structured as follows: **Chapter 2** first gives an introduction to preoperative surgical planning (Section 2.1). It then gives a short introduction to model and learning based semantic segmentation (Section 2.2) with methods such as ASM, Conditional Random Field (CRF)s and influential state of the art Deep Learning architectures. This section on segmentation finishes with a review on specialized solutions for Temporal Bone Surgery, endovascular procedures and shape regularization. Finally, the chapter summarizes the state of the art for motion planning (Section 2.3) with a focus on random sampling and solutions for surgical instruments.

The next three chapters contain contributions to preoperative surgical planning, segmentation and motion planning. In **Chapter 3**, a thorough retrospective in silico evaluation strategy for a preoperative surgical planning pipeline is proposed, using synthetic anatomies and functional evaluation [73, 75]. It finishes with the presentation of an interactive planning pipeline, which is suitable to setup the experiments. The shape regularized segmentation using a slice-by-slice U-Net approach followed by Probabilistic Active Shape Models [75] is presented in **Chapter 4**. **Chapter 5** proposes an extensive trajectory planning step. It starts with motivating the technical and clinical constraints and then follows the common motion planning step of deriving a custom *Problem Formulation* for the two point boundary value problem. This formulation can be solved by to Bi-RRTs proposed by me [74]. It follows optimization of the Bézier Spline variant [77] and a generalization adapted to the clinical workflow [76]. Finally, it presents an extension to movement along circular arcs, extending the methodology to more instruments and thus more applications [72].

In **Chapter 6**, extensive evaluation of the complete pipeline is presented for Temporal Bone Surgery and Endovascular Aortic Repair. The thesis finishes with a summary and

look into the future in **Chapter 7**. The appendix lists my publications, awards as well as supervision activities, includes my resumé and contains a glossary.

2. State of the Art

This chapter reviews in three sections the concepts of preoperative surgical planning and its two major parts: segmentation and trajectory planning. Section 2.1 gives an overview on approaches combining both segmentation and trajectory planning to a complete workflow. Specifically, it takes a deeper look on experimental validation. Section 2.2 introduces state of the art segmentation approaches such as Active Shape Model (ASM)s, Conditional Random Field (CRF)s and Convolutional Neural Network (CNN)s. It then reviews segmentation techniques for the two major applications targeted in the experiment section: Temporal Bone Anatomy and Endovascular Aortic Repair. It concludes with a survey on spatially-consistent segmentation and shape regularization. Finally, Section 2.3 gives an introduction to motion planning focusing on sampling based approaches such as Rapidly-exploring Random Tree (RRT)s. The survey starts with a general review on motion planning algorithms for nonlinear curvature constrained trajectories. It then specifically targets publications for minimally-invasive interventions with flexible instruments such as bevel-tip needles or guidewires.

2.1. Preoperative Surgical Planning

Minimally-invasive surgery has been extensively studied in the last decades and new solutions for various applications are an active research field [12, 26]. These include, among others, drilling linear canals for multi-port Temporal Bone surgery [230], steerable needles for soft tissue [201, 203, 236], flexible endoscopes [35, 81] or guidewires [69, 88] to insert catheters for stenting or treatment of aneurysms. Such robotically-driven approaches promise preciser interventions, easier ways through complex anatomies or safe access to yet unreachable regions. They come, however, at a cost: They now require extensive preoperative planning, where segmentation of risk structures provides a 3D environment for trajectory planning.

■ Jugular vein ■ Carotid artery ■ Facial nerve ■ Chorda tympani ■ External auditory canal ■ Internal auditory canal ■ Cochlea ■ Semicircular canals ■ Ossicles
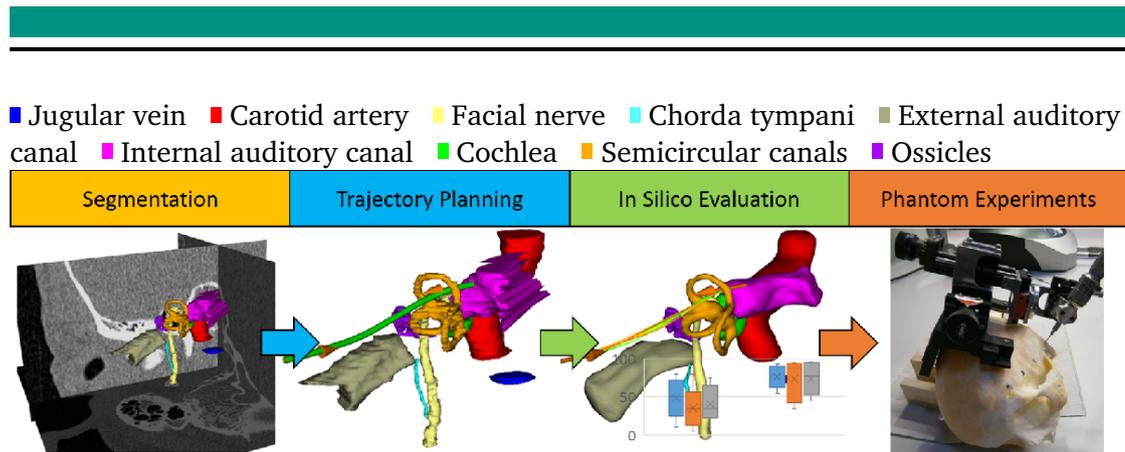
Figure 2.1.: Evaluation of pipelines for preoperative surgical planning usually performs isolated experiments on segmentation and trajectory planning before moving on to phantom evaluation. Thorough analysis in an extensive in silico simulation that considers both steps is often missing.

Research for new approaches evaluates the pipeline shown in Figure 2.1 in different ways. Most works present unique solutions for a particular step and evaluate it in isolation. That means, segmentation algorithms are evaluated on segmentation metrics such as Dice, Hausdorff distance or volume overlap. Papers proposing new planning algorithms are evaluated using ground truth risk structures as obstacles. The results report feasibility of the algorithm and show performance compared with existing solutions. The next step often consists of experiments on cadaver specimens or phantoms. However, works on new Computer Assisted Interventions are often based on only a very small dataset and thorough in silico evaluation on a large test set is not feasible.

The following presents a survey on publications addressing such a complete view on preoperative planning (see Table 2.1) and gives an overview on their evaluation strategy. These works either utilize open source tools (such as MITK [257], Slicer 3D [79], SOFA [71], ROS [198]) or present own customized solutions. For Temporal Bone Surgery in particular, the survey of Dahroug et al. [49] gives a good review on existing systems and approaches, including concepts and robotic solutions for cochlear implantation.

Noble et al. [179] combined a registration based segmentation of risk structures with a planning step for linear cochlear access. Monte Carlo simulation on 18 samples was performed to evaluate the computation of an optimal trajectory. Eilers et al. [63] evaluated the drilling of a linear canal to the cochlea planned by a custom surgical planning tool that makes use of the automatic segmentation algorithm for facial nerve and chorda by [178]. Experiments on five cadaver specimens of the human temporal bone were conducted and

Table 2.1.: Preoperative planning papers. Abbreviations: Statistical Shape Model (SSM).

Reference	Segmentation	Trajectory	Topic	Datasets
Noble et al. (2007)	automatic	monte carlo optimization	Temporal Bone Surgery	18 CT images
Eilers et al. (2009)	automatic	linear drilling	Temporal Bone Surgery	5 cadaver specimen
Seitel et al. (2011)	semi-automatic, MITK	pareto optimization	Needle Insertion	10 CT images
Spottiswoode et al. (2013)	semi-automatic		3D printing for neurosurgery	2 MRI images
Gerber et al. (2014)	semi-automatic	interactive planning	Temporal Bone Surgery	8 cadaver experiments
Liu et al. (2014)	manual segmentation, ITK-SNAP	none	Temporal Bone Surgery	2 cadaver experiments
Ren et al. (2014)	manual segmentation, ITK-SNAP	integer programming	Brain Tumor Ablation	1 phantom, 1 swine experiment
Mangado et al. (2016)	registration, SSM	none	Temporal Bone Surgery	25 CT images
Chen et al. (2017)	semi-automatic, Slicer 3D	interactive planning	Implant Placement Surgery	1 phantom, 1 cadaver experiment
Golkar et al. (2019)	interactive segmentation, MITK	none	Percutaneous Cryoablation	1 phantom & 5 MRI scans
Essert et al. (2019)	interactive segmentation, MITK	none	Percutaneous Cryoablation	5 MRI scans
Herz et al. (2019)	automatic	none	Prostate Biopsy	10 + 73 MRI images
Liu et al. (2019)	manual, Slicer 3D	interactive planning	Radiofrequency Ablation	1 phantom, 1 swine experiment

no damage of risk structures were reported. Seitel et al. [216] presented a trajectory planning framework based on MITK for needle insertion in liver biopsy. It uses MITK's software tools for manual interactive segmentation and computes linear trajectories optimizing hard and soft constraints. An evaluation on 10 datasets from interventions resulting in complications showed that the framework would propose clinically safer alternatives than the ones that were actually chosen by surgeons. Spottiswoode et al. [228] presented a software package for neurosurgery that computes a 3D printable model of the brain and computes linear trajectories for brain tumor biopsy. Experiments on 2 patients allowed evaluation of the accuracy of the printed 3D models. Gerber et al. [90] presented a custom surgical planning tool for robotic cochlear implantation that was evaluated on eight cadaver heads. The solution included a semi-automatic segmentation procedure, patient on image registration using fiducial markers and interactive definition of a safe drilling trajectory. A cadaver study showed the feasibility of cochlear implantation using a master-slave–system [147]. Using a da Vinci surgical system, these experiments on 2 specimen manually segmented obstacles using [277] and performed a mastoidectomy with a custom drill adapter for the system. A pipeline for treatment planning for radiofrequency ablation of large tumors was presented by Ren et al. [202]. Using ITK-SNAP an interactive semi-automatic segmentation was performed before computing trajectories and subsequent ablation in phantom and animal studies.

Mangado et al. [158] proposed to physically simulate the insertion of a cochlear implant electrode array. The authors presented a framework that includes registration of a SSM, build from μCT, onto a preoperative CT image, electrode placement, creation of auditory nerve fibers of the inner ear and finally the building of a mesh for finite element simulation. A surgical navigation system based on Slicer 3D that made used of its semi-automatic segmentation and linear path planning modules was presented by Chen et al. [34]. Phantom and cadaver experiments for implant placement were conducted

to show the accuracy of the system. Golkar et al. [95] and Essert et al. [67] performed planning for cryoablation by modeling the iceball of the probe and solving the Partial Differential Equation (PDE) of a heat equation that describes the propagation of heat in human tissue. The planning accounted for risk structures that were manually segmented using MITK. SliceTracker [110] is a recently published open source framework based on Slicer 3D for prostate biopsy. The system included the automatic segmentation method DeepInfer [161] for prostate segmentation and supervised manual placement of needles. A functional evaluation regarding biopsy targeting error and mean landmark registration error evaluated in 10 prospective and 73 retrospective experiments. [146] presented a planning and insertion procedure for radiofrequency ablation using only a single incision port. The planning pipeline relied on manual segmentation of risk structures using Slicer 3D. Experiments on a phantom and a swine showed the feasibility of the robot-assisted system.

2.2. Segmentation

Segmentation is the task of dividing an image into distinctive regions [96] that together cover the whole image. The result is either a label image (Figure 2.2), masking each pixel that corresponds to a certain region, or a direct extraction of each surface. An exhaustive introduction into image processing is given by Gonzalez and Woods [96], with detailed chapters about segmentation, feature extraction and an early introduction to deep learning with CNNs. A focus on medical image processing is found in [2, 57] which cover, among others, extensive description of level set methods and deformable models, including ASM. The Probabilistic Active Shape Model (PASM) used in this thesis is introduced in [124].

Classic gray level algorithms such as thresholding or region growing and early model based approaches such as level set methods or graph cuts are still being applied for cases with very limited available data or unique challenging features [19]. While more advanced model based approaches such as atlas-based registration [24, 120] or ASMs [45] achieve good results in many applications, the field has been dominated by Deep Learning solutions for several years, now. The recent surveys by Shen et al. [222] and Litjens et al. [144] give a good overview of Machine Learning advances regarding different modalities such as Computed Tomography (CT), Computed Tomographic Angiography (CTA), Magnetic Resonance Imaging (MRI) or Ultrasound, applications such as breast-, cardiac-, or abdominal image analysis, or tasks such as segmentation and classification.
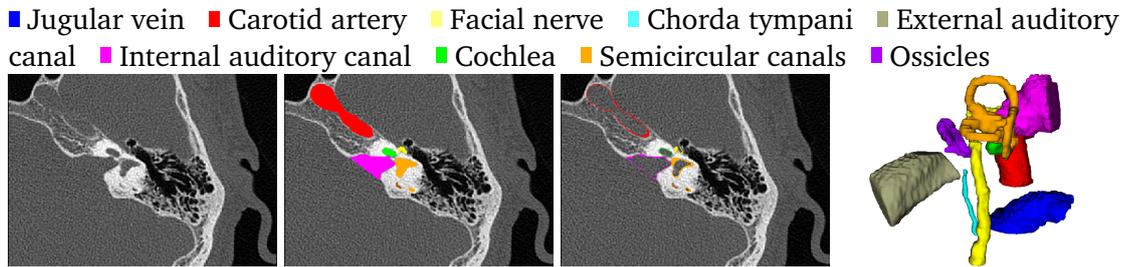
Figure 2.2.: Left to Right: A raw CT images of the temporal bone. Overlayed by segmentation masks representing an objects volume and boundary. Surface representation.

The following sections focus on the two application domains covered by experiments in Chapter 6: Temporal Bone Surgery (Section 2.2.3) and Abdominal Aortic Repair (Section 2.2.4). Section 2.2.5 then gives a broader look on shape regularization. Summaries of publications are also listed in Table 2.2, Table 2.3 and Table 2.4, each giving remarks on image modality, segmented anatomy and general methodology. For the sake of completeness, short reviews on ASM and Deep Learning are given first in Section 2.2.1 and Section 2.2.2.

2.2.1. Active Shape Models

Active Shape Models, first presented by Cootes et al. [45], are a local search algorithm that iteratively adjusts a learned representation of an object onto a new image. The setup of the whole method is complex and usually subject to lot of parameter tuning [15, 124]. Figure 2.3 shows a figurative example of creating a SSM and performing ASM segmentation. The training set consists of labeled images, from which surface representations are extracted using, e.g. Marching Cubes [150]. In order to generate a SSM, each of the surface meshes has to have the same number of landmarks N_L. These can be generated using remeshing algorithms such as approximated centroidal voronoi diagrams [244] that generate topology conserving triangle meshes with a predefined number of vertices. The vertices of these meshes then form the landmark vector of the respective shape. For the subsequent computation of a point distribution model, the landmark vectors of each training shape have to correspond to each other. For this correspondence search, several methods have been proposed in the past. Linear or kernel Principal Component Analysis (PCA) [154] can be used to transform the shapes into a
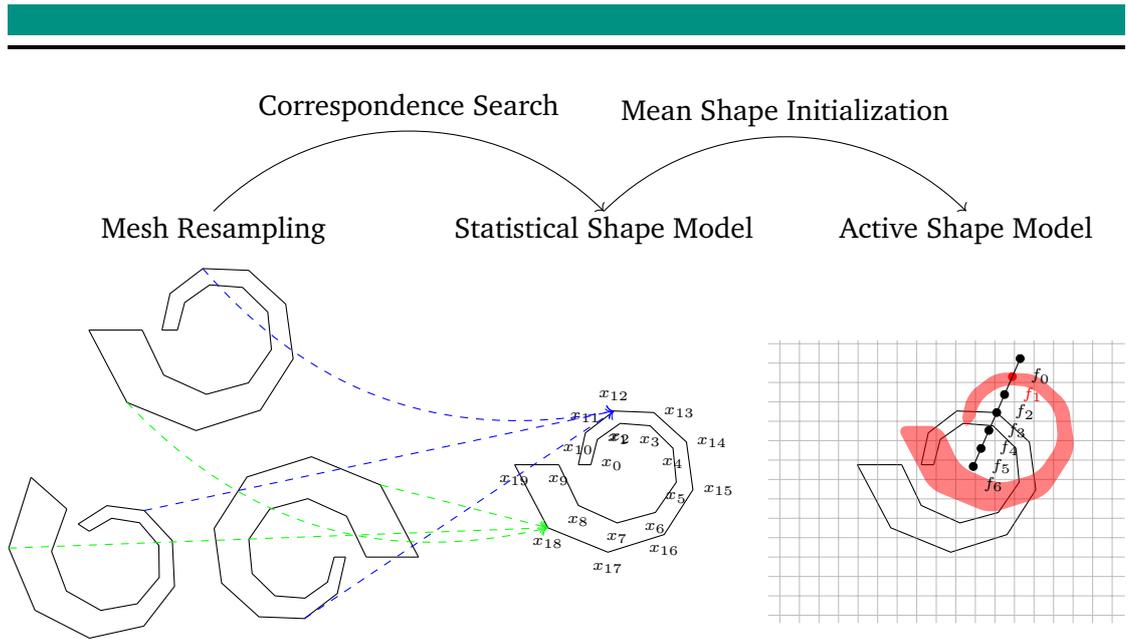
Figure 2.3.: Setup of Active Shape Models. First, surface models with an equal number of vertices are generated from a training set. Applying correspondence search brings the landmark vectors containing the vertices in a common coordinate frame and allows the computation of a statistical shape model. Using the SSM's mean shape as a first guess, it can be iteratively adapted to the image by searching along the normal of each landmark for corresponding image features.

common coordinate system whereas strategies such as nonrigid surface registration [124] for objects of arbitrary topology or consistent parameterization for shapes with specific genus [17] find corresponding vertices. Once these correspondences are defined, the original shape model [45] includes a point distribution model to describe the statistical variation between samples.

The ASM procedure is shown in Algorithm 1. A necessary prerequisite is the SSM that encodes a vector space (or *shape space*) of valid forms of the object. The algorithm is usually initialized with the mean shape of this shape space, which is manually or automatically placed within the image. It then repeatedly switches between deformation of the current shape and restriction to the shape space. For deformation, new positions for the landmark vector are computed along each landmark's normal. Then, a fitness function computes scores for each of those new positions, e.g. based on image gradients or intensity values [108, 245]. For restriction, the deformed landmark vector is then

Algorithm 1 Active Shape Model algorithm

Input: Image I, Statistical Shape Model (SSM) $\mathcal{S}$, mean shape $x = (x_1, \ldots, x_{N_L})$.
Output: Label Image, Label Surface.

1: **procedure**
2:     $x \leftarrow$ place_mean_shape()
3:     **while** $i < I_{max}$ && !converged **do**
4:         $F \leftarrow$ image_features(x)
5:         $x_{new} \leftarrow$ best_fitness(x, F)
6:         $x \leftarrow$ constrain_shape($\mathcal{S}, x_{new}$)
7:     **end while**
8: **end procedure**

projected back into the shape space. This procedure is repeated until either convergence or a maximum iteration limit. Due to restriction to only valid representations, the algorithm returns segmentations with only anatomically plausible shapes [261].

As an example, Becker [13] performed an extensive evaluation for the nine risk structures in Temporal Bone Surgery. This resulted in a unique combinations of landmark vector sizes, parameter choices for multi-scale correspondence search, fitness functions for feature classifications and different weighing parameters in a PASM.

2.2.2. Convolutional Neural Networks and Conditional Random Fields

Convolutional Neural Networks (CNNs) were shown to outperform existing model-based approaches for many applications in medical image processing [144] and are currently the method of choice for semantic segmentation. These networks are based on the idea of Multi-Layer Perceptrons (MLPs) (see e.g. [96]), where each perceptron p consists of a nonlinear activation function σ that evaluates a trainable biased weighted sum, that is

$$MLP_M(\mathbf{x}) = p_0(\ldots p_M(\mathbf{x})), M > 0, \text{where}$$
$$p_j(\mathbf{x}) = \sigma_j(\sum_{i=1}^{N} w_{j,i} x_i + b_j), x \in \mathbb{R}^N, N > 0, 0 \le j \le M, \sigma : \mathbb{R} \to \mathbb{R}.$$

A popular choice for σ is ReLU (Rectified Linear Unit) activation [168] to prevent the vanishing gradients problem in deep neural networks. A CNN now uses *convolutional kernels* as linear functions inside activation and thus takes an image instead of a vector as
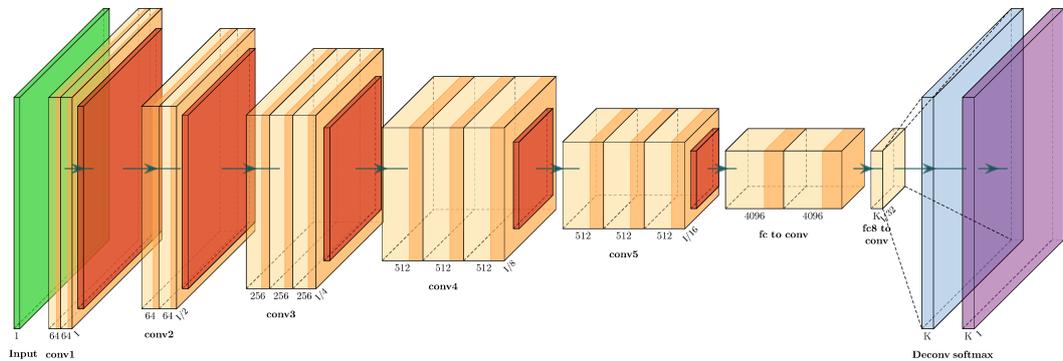
Figure 2.4.: A CNN architecture. Starting from an input image (green), a series of layers consisting of two successive feature maps (yellow boxes) and pooling functions (red) creates a latent representation (yellow box *fc8*) of $K > 0$ feature maps. These are deconvoluted to the original image size (blue). Softmax activation (purple) on this final layer then creates the K segmentation maps, one for each label.

input. Multiple pooling layers are typically added, combining several perceptrons using max or mean operations. This reduces the size of feature maps and thus the number of overall network parameters. Figure 2.4 shows this architecture in a fully convolutional neural network [148].

One of the most successful and widely adopted networks for semantic segmentation is the U-Net architecture [41, 204]. The use of skip-connections to the upsampling part (Figure 2.5) of an auto-encoder network greatly increase the performance of CNNs. This outstanding performance was backed up by the recent work of Isensee et al. [118], which outperformed competing methods in almost all of the ten segmentation challenges of the 2019 Medical Segmentation Decathlon with the use of three different vanilla U-Nets and suitable preprocessing schemes.

One major drawback of these CNNs lies in their pixelwise classification of the label image. Unlike for model-based approaches such as active contours, there is no guarantee that the segmented object keeps a smooth surface or is a completely filled region. Segmented structures thus might include holes, appear as fragmented contours, or suffer from very high curvature at the boundary. A popular way in current research that deals with this problem is the use of CRFs as a post processing method after CNN segmentation. A CRF

is a discriminative undirected probabilistic graphical model that consists of two random fields connected via unary and pairwise edge potentials [132] (Figure 2.6). The first models the intensity values of an input image I of size $N \times M$, considering each pixel $P_{i,j}$ as a random variable $X_{i,j}, 0 \leq i, j \leq N, M$ that maps into the set of possible intensities. The second tries to infer the label image, using an equal number of random variables
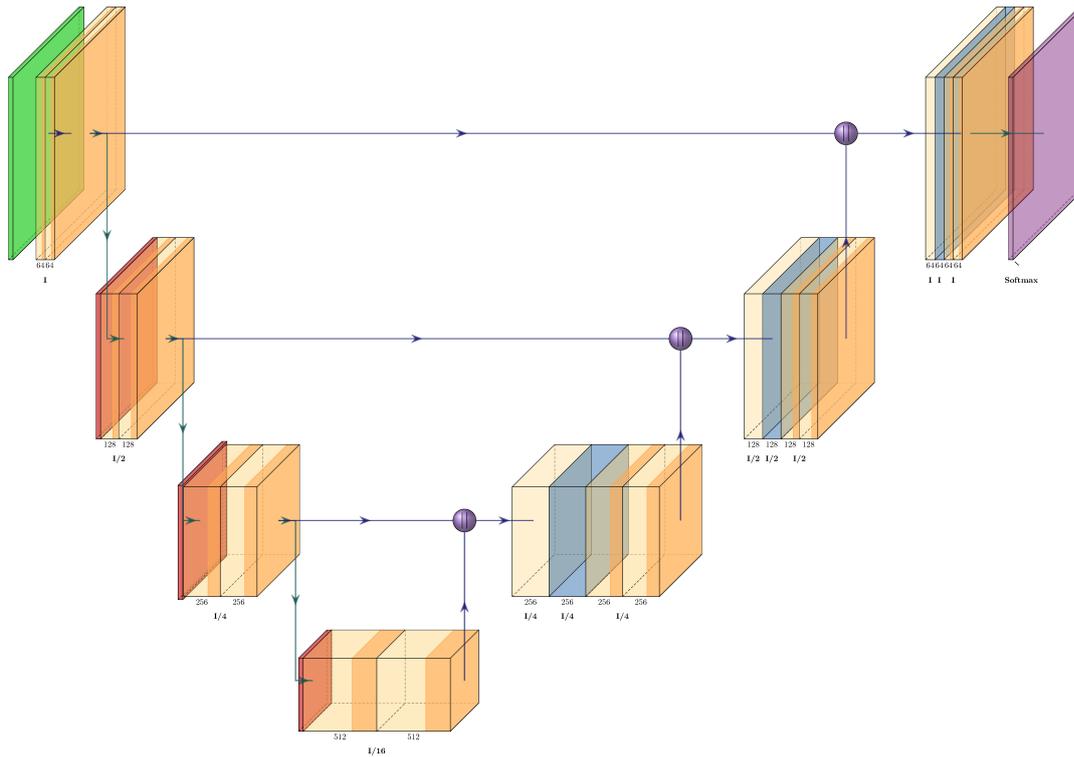
Figure 2.5.: A 2D U-Net architecture with a single input image (green). The Encoder-Decoder structure is represented by a set of convolution (orange), pooling (red) and upsampling operations (blue). In each encoder layer, 2D convolution filters are applied to generate two successive sets of feature maps (orange boxes), doubling the numbers of maps each time. In the decoder layer, the introduced skip-connections concatenate the last feature maps of the respective encoder layer (transparent yellow box) with the upsampled maps (blue box). From these two concatenated tensors, two more sets of feature maps (orange boxes) are created. The final layer performs a softmax activation to generate the desired label image (purple).
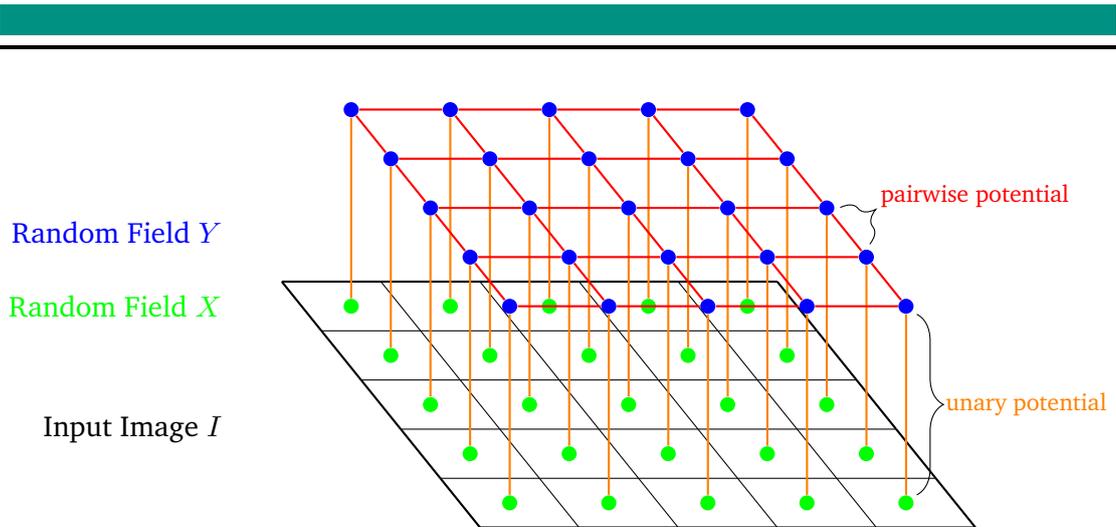
Figure 2.6.: Conditional Random Fields can be used for segmentation while boosting spatial consistency. Unary potentials between fields X and Y capture image information for individual pixels while pairwise connections in field Y enforce label similarity in local neighborhoods.

$Y_{i,j}, 0 \leq i, j \leq N, M$ that map into the set of possible labels. The unary potentials depend only on the corresponding pixel could incorporate apart from intensity values additional information such as location. The pairwise potentials connect neighboring pixels and enable the CRF to learn spatial consistency. In *fully connected CRFs*, each random variable $Y_{i,j}$ is connected with pairwise potentials to all other variables of the random field Y in order to maximize the effect. A highly efficient inference algorithm using Gaussian kernels and mean field approximation Krähenbühl and Koltun [127] reduced the computational complexity from quadratic to linear in the number of variables. This made the whole problem tractable and applicable to the medical field, where it was applied either on the segmentation output of a CNN or directly on the last activation layer [1, 82, 180]. Finally, the mean field iteration of [127] consists of a combination of differentiable functions, making it applicable in forward and backward passes of Deep Learning architectures. Fu et al. [83] exploited this property to setup a CRF as an Recurrent Neural network (RNN). This combination of a CNN and an RNN, or CRF-RNN, represents a convolutional neural networks that is both trainable end-to-end and enforces spatial consistency.

■ Jugular vein ■ Carotid artery ■ Facial nerve ■ Chorda tympani ■ air cavities (EAC, tympanic cavity, eustachian tube) ■ Internal auditory canal ■ Cochlea ■ Semicircular canals ■ Ossicles ■ paranasal sinuses
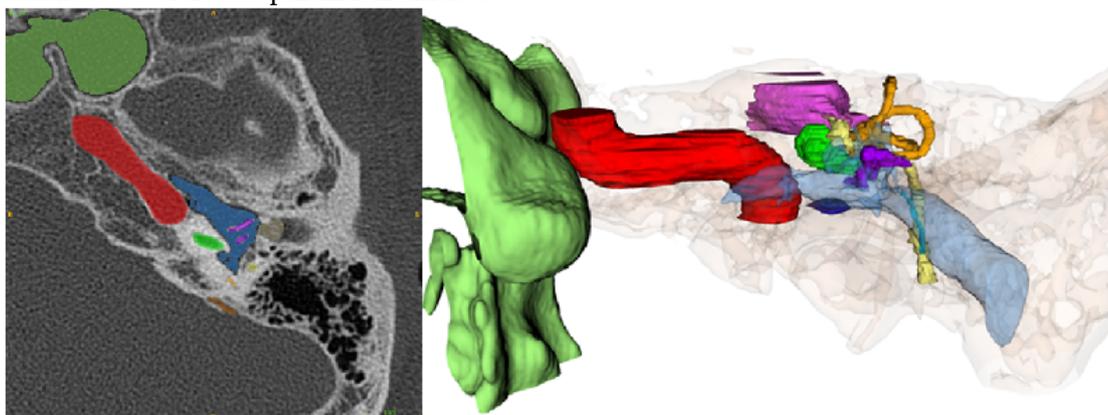
Figure 2.7.: *Left:* Typical CT scan of the temporal bone with ground truth annotations. *Right:* Respective surface models for all risk structures.

2.2.3. Temporal Bone Segmentation

The temporal bone includes the following major risk structures [230]: external and internal auditory canal (external auditory canal (EAC), internal auditory canal (IAC)), ossicles (ossicles (Oss)), cochlea (Cochlea), semicircular canals (semicircular canals (SCC)), facial nerve (facial nerve (FN)), chorda tympani (chorda tympani (Chorda)), jugular vein (jugular vein (JV)) and internal carotid artery (internal carotid artery (ICA)) (Figure 2.7). As shown in Figure 2.8, several of these structures provide a serious challenge for segmentation. They appear as fragmented structures that observe only limited image contrast and have in some directions open boundaries, leading to often diverse expert annotations. Depending on the application, some papers just segment the posterior canal wall (PCW) of the EAC or differentiate between malleus, incus and stapes rather than extracing the ossicles as a whole. Other papers segment the whole inner ear or labyrinth instead of giving individual labels to SCC, vestibule and Cochlea.

An early review on ear segmentation is given by [80]. To the best of our knowledge, Becker et al. [15] provides the only work targeting surgery at the petrous apex and therefore segments all of these risk structures. The authors use the Probabilistic Active Shape Model (PASM) [124], but manual initialization is still needed where bounding boxes and points
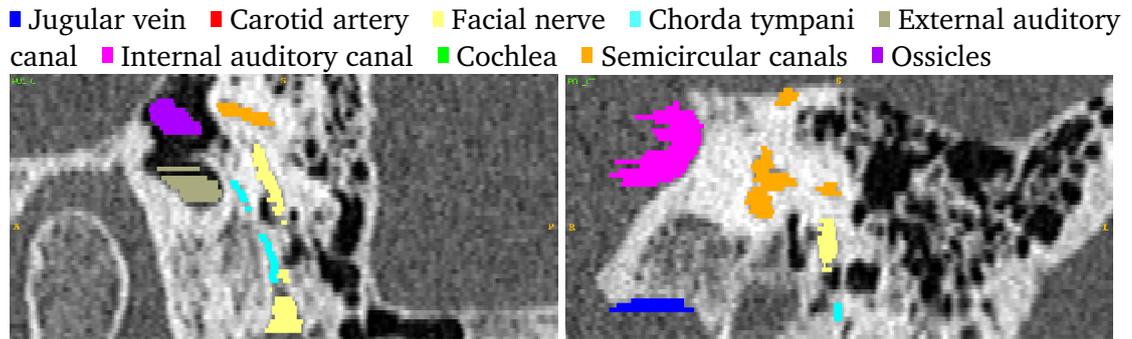
Figure 2.8.: Zoom in on a saggital (left) and coronal (right) slice with ground truth annotation for chorda tympani (cyan) and facial nerve (yellow).

on the medial axis of individual structures have to be selected. Most other approaches focus on cochlear implantation and therefore segment only structures at the middle ear.

Due to the severe constraints, several works provide *semi-automatic solutions* for a limited selection of organs. Early work in this field uses customized solutions [80] for individual structures such as a safety zone for the facial nerve [246] or level set methods with interactive pre- and post-adaptations [259]. Caversaccio et al. [30] realized a successful clinical implementation of a cochlear implantation. They present a custom planning tool [90] that allows interactive segmentation of the outer wall of the EAC, the facial nerve and chorda tympani, the ossicles and the cochlea. Lu et al. [152] add a refinement strategy for the facial nerve based on a super resolution approach on in Cone Beam Computed Tomography (CBCT) images.

For some structures *automatic solutions* exist: Noble et al. [176] use a registration procedure based on radial basis functions for facial nerve and chorda tympani. The approach was labeled NOMAD and generalized to tubular structures such as the optic tracts [173]. Together with customized solutions for intracochlear anatomy [175] and refined segmentation of these nerves [174] the majority of temporal bone anatomy can be segmented. More recent work includes a non rigid registration approach on μCT data by Kjer et al. [125] that uses skeleton similarity as a metric. Recent work of Zhu et al. [284] segments the SSC, the vestibule and the cochlea in MRI data also via SSMs but uses additional post processing with level sets. In Powell et al. [196] present an atlas based approach for Cochlea, superior semicircular canal (SSC), ossicles and facial nerve. In [195], they extend their approach on tegmen, sigmoid sulcus, EAC, ICA and the posterior canal wall. In recent years, Deep Learning solutions have been proposed. Ruiz Pujadas et al. [206]

Table 2.2.: Segmentation for temporal bone and aortic anatomy. Pre- and postprocessing includes simple filters such as thresholding, morphological or binary operations. Abbreviations: contrast-enhanced CT (ce-CT), Support Vector Machine (SVM).

Reference	Modality	Anatomy	Method
Temporal bone			
Xianfen et al. (2005)	CT	labyrinth	manual preprocessing + level sets
Salah et al. (2006)	CT	mastoid	region growing, manual refinement
Noble et al. (2008)	CT	FN, Chorda	NOMAD
Noble et al. (2009)	CT	labyrinth, Oss, EAC	atlas-based registration
Noble et al. (2011)	CT, μCT	Intracochlear Anatomy	ASM
Voormolen et al. (2012)	CT	FN	centerline + safety zone
Oliveira et al. (2014)	CT	incus and malleus	registration, postprocessing
Becker et al. (2014)	CT	Cochlea, Oss, SCC, EAC, IAC, FN, Chorda, JV, IAC	PASM
Kjer et al. (2016)	μCT	Cochlea	free-form registration based on skeleton similarity
Powell et al. (2017)	CT	Cochlea, Oss, SCC, FN	Atlas-Based Segmentation
Lu et al. (2018)	CBCT, CT, μCT	FN refinement	super resolution classification
Zhu et al. (2017)	MRI	Cochlea, SCC, vestibule	SSM registration + level set refinement
Ruiz Pujadas et al. (2018)	μCT	Cochlea, SCC	Random walks with SSM priors
Zhang et al. (2018)	CT	labyrinth Bounding Box	Deep Volume-to-Volume Regression Network
Powell et al. (2019)	CT	EAC, PCW, IAC, tegmen, sigmoid sulcus	Atlas-based segmentation, postprocessing
Wang et al. (2019)	MRI	vestibular schwannoma	2.5D CNN
Aorta			
Bruijne et al. (2004)	CTA	Abdominal Aortic Aneurysm (AAA)	2D active contours
Zhuge et al. (2006)	CTA	AAA	3D level set method, SVM
Macía et al. (2009)	CTA	AAA, lumen and thrombus	radial functions
Zohios et al. (2012)	CTA	AAA, thrombus and outer wall	2D level sets
Martínez-Mera et al. (2013)	CTA	AAA	active contour, graph matching
Czajkowska et al. (2014)	ce-CT	AAA	active contour, graph matching
Maiora et al. (2014)	CTA	aorta, thrombus	Random Forest Active Learning
Wang et al. (2017)	MRI	AAA lumen and outer wall	registration based active contours
Lalys et al. (2017)	CTA	aortic thrombus	centerline extraction, deformable models
Trullo et al. (2017)	CT	aorta, heart, esophagus, trachea	SharpMask + CRF
López-Linares et al. (2018)	CTA	aortic thrombus	DCNN
Siriapisith et al. (2018)	CTA	outer wall of AAA	active contours, graph cut
Lareyre et al. (2019)	ce-CT	AAA, lumen, thrombus, calcification	morphological snakes
Han et al. (2019)	CT	aorta, heart, esophagus, trachea	multi-res VB-nets
Tahoces et al. (2019)	CT	aortic lumen estimation	Hough-trafo, ellipse tracking
Lu et al. (2019)	CT, ce-CT	aorta segmentation + classification	3D-U-Net + ellipse fitting

utilize SSMs to segment the cochlea in micro CT images. Also following a Deep Learning approach, Zhang et al. applied a Regression Network [280] for bounding box localization of the inner ear in CT data. Most recently, segmentation of vestibular schwannoma via CNN has been investigated by Wang et al. [249].

2.2.4. Endovascular Aortic Repair

Automatic segmentation of Abdominal Aortic Aneurysm (AAA) could enabled the use of routine abdominal CT scans for AAA detection [42], which can be determined by fitting an ellipse on the aorta in axial slices of an abdominal ce-CT scan. It also speeds up

■ Aortic lumen ■ Aortic outer wall
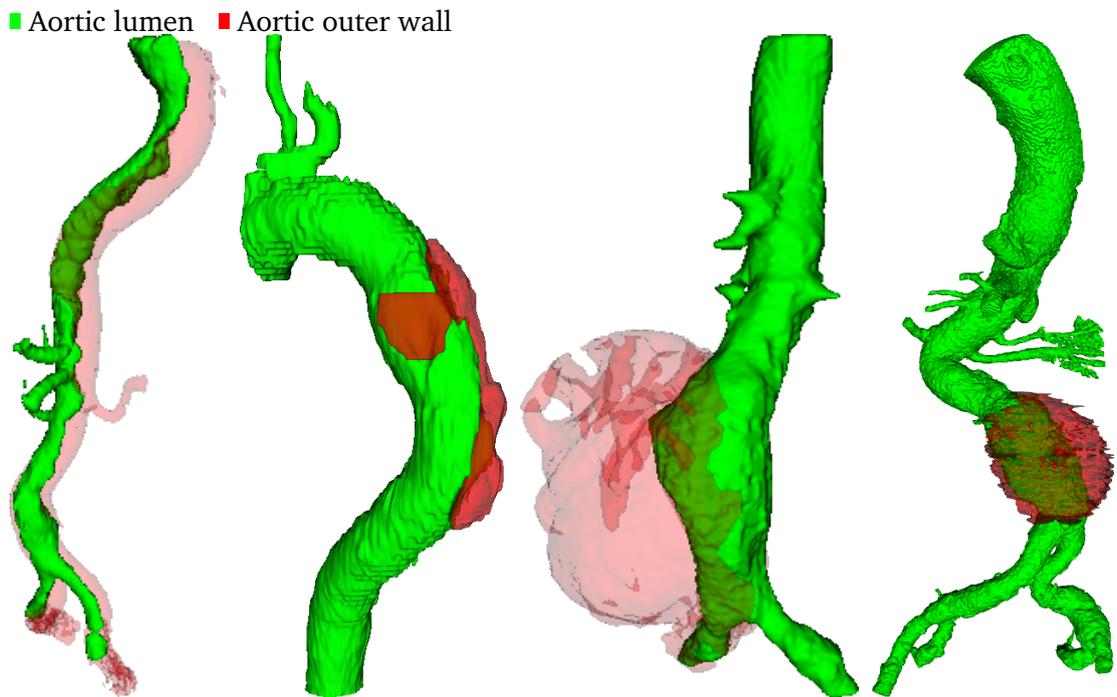
Figure 2.9.: Examples of aortic aneurysms and thrombi. High variety in size and extent of pathologies is a serious challenge for automatic segmentation. The same is true for the sometimes winding course of the aorta.

segmentation during planning for Endovascular Aortic Repair (EVAR), where surgeons use a 3D printed aortic model to determine the size of stent grafts. Proposed solutions therefore segment the aorta, aortic lumen, outer wall and thrombus (see Figure 2.9), sometimes followed by ellipse fitting for a classification of aneurysm existence.

The majority of EVAR cases are AAA and research focuses on both detection and segmentation of these pathologies. Early work relied on semiautomatic solutions that can be corrected easily. Others use a variety of methods such as level set functions, deformable models, graph matching techniques or different deep learning architectures. To the best of our knowledge, publicly available datasets showing aortic aneurysms do not exist, but evaluation on data of the SegTHOR challenge allows testing algorithms for both segmentation and planning on patient data having labeled both ascending and decending aorta on a chest CT scan.

We first look at *semi-automatic* solutions that require a manual initialization by the user. Early work in this field proposed interactive methods on AAA segmentation on CTA images using manually initialized a 2D active contour that is automatically propagated through subsequent slices [25]. Zohios et al. [286] segment AAA thrombus and outer wall for a reliable estimate of rupture risk on 10 patients. The authors used 2D active contours with a custom stopping criteria to prevent boundary leaking and a refinement scheme for thrombus and outer wall. For each slice, the active contour is interactively initialized. Maiora et al. [157] proposed an interactive active learning approach to overcome the limitations of previous work that were sensitive to noise. The authors used a random forest classifier to classify thrombus voxels in a slice-by-slice manner, requiring user input for where uncertainty of the classification was high. Wang et al. [251] investigated a registration approach to segment AAA lumen and outer wall in MR images. Their approach combines both MRI and contrast enhanced MR angiography information to segment lumen and outer wall using active contours where the first contour has to be initialized manually. Lalys et al. [133] proposed a thrombus segmentation solution based on manually initialized centerline extraction using minimal cost paths and deformable models applied to a preprocessed image. The authors performed an extensive analysis on 145 patients and showed the versatility of the approach for both preoperative planning as well as postoperative monitoring. Lareyre et al. [134] use 2D and 3D active contours and morphological operations to segment the aortic lumen, calcifications and thrombi in a complete preoperative planning tool. The system allows interactive online error-correction to improve the iterative process.

Automatic solutions have also been presented. Zhuge et al. [285] presented an automatic approach, using a connected component analysis to find an initial surface and trained a SVM to serve as a local prior in a 3D level set iteration. Martínez-Mera et al. [159] segment the thoracic aorta on 10 patients using a multi step approach that distinguishes four different parts of the aorta and uses custom region growing and level set methods for the individual parts. The Hough transform is used for automatic initialization. Czajkowska et al. [48] proposed a registration between pre- and post-operative ce-CT scans based on graph matching of aortic lumen skeletons and evaluated it on 8 patients. The required segmentation for skeletonization of the aortic lumen was performed using level sets. López-Linares et al. [149] proposed a 2 step approach for thrombus segmentation with a region of interest detection followed by fine segmentation both on customized dep CNNs. The method is designed for postoperative thrombus volume estimation and validated on 13 CTA scans. Siriapisith et al. [225] proposed an alternating scheme of active contours and graph cuts to overcome the limitations of previous solutions: converging to local minima. By switching between two search spaces the method outperforms previous

solutions on a dataset of 20 subjects. Tahoces et al. [238] propose an optimization scheme for a slice-by-slice active contour in aortic lumen segmentation. It consists of ellipse tracking and optimization of the aortic cross section's 3D orientation. The authors show the robustness of their method on a dataset of 385 CT scans, with both normal and pathological cases. Most recently, Lu et al. [151] proposed a solution on 3D U-Net and ellipse fitting for segmentation and detection of AAA. The method is evaluated on a dataset of 378 patients, exhibiting contrast and non-contrast CT images as well as different acquisition characteristics.

Although recent publications show promising results on large datasets [151, 238], most of the approaches are evaluated on only a small number of samples. Unfortunately, neither of these datasets is publicly available. This limits comparability due to high inter-patient variety in aortic anatomy and aneurysm size, different image modality and specific volume of interest. There is thus further need for segmentation methods related to preoperative surgical planning. More publicly available data from challenges could also benefit the comparison of different approaches. For example, challenges such as ISBI's SegTHOR [190] and MICCAI's MMWHS [68] currently allow evaluation on parts of the aorta. Trullo et al. [241] proposed a CNN to segment aorta, heart, esophagus, trachea in the thoracic CT scans of SegTHOR. In the follow up ISBI challenge [190], a combination of custom multi-resolution V-Nets [162] achieved best performance [103]. The MMWHS challenge [68] focuses on the individual heart chambers but includes segmentation of the ascending aorta.

2.2.5. Shape Regularization

Deep Learning solutions achieve unprecedented accuracy in terms of segmentation metrics such as Dice and predict segmentation masks in a fraction of the time than preceding model based approaches. However, by design the architectures' results are pixelwise predictions, contrary to model-based solutions that give strong topological guarantees (Figure 2.10). This drawback limits the use of Deep Learning in preoperative planning [73, 75], where segmentation masks are required in subsequent steps such as 3D printing or trajectory planning. While larger datasets might solve this issue, it is neither guaranteed nor is the acquisition of such an unknown amount of expert annotated images reasonable in clinical settings. The following section reviews the resulting increasing interest to bring strong model assumptions into Deep Learning architectures. It starts with a look into CRFs as a learning based approach that regards spatial consistency. Here, the work of Krähenbühl and Koltun [127] on CRFs with Gaussian edge potentials influenced many

■ Aorta ■ Heart ■ Esophagus ■ Trachea ■ Jugular vein ■ Carotid artery ■ Facial nerve ■ Chorda tympani ■ External auditory canal ■ Internal auditory canal ■ Cochlea ■ Semicircular canals ■ Ossicles
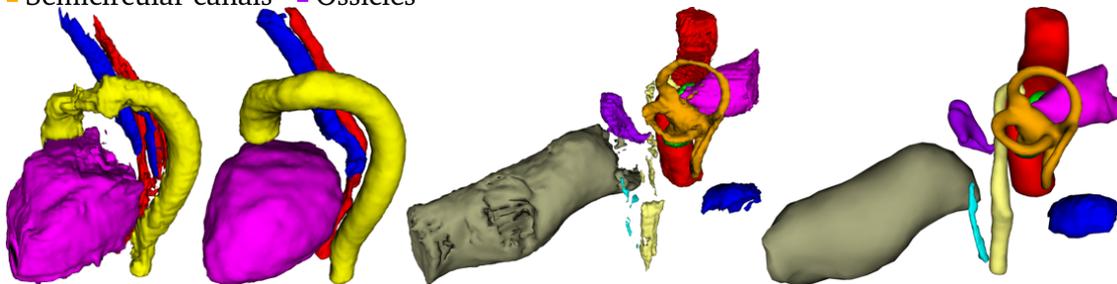
Figure 2.10.: Shape regularization enforces topological constraints on the output of a segmentation algorithm. Mesh generated from U-Net segmentation (Left) and after Active Shape Model postprocessing (Right).

papers that added CRFs as post processing steps into Deep Learning solutions. Fu et al. [83] proposed an influencial RNN architecture that resembles a CRF, allowing end-to-end training and optimization of a shape regularized CNN. Table 2.3 and Table 2.4 list the individual papers presented in this section.

Many solutions follow the approach of [122] that enforces spatial consistency by using fully-connected CRFs for *post processing*. Alansary et al. [1] utilize a 3D CNN with 3D CRF postprocessing for segmentation of the human placenta. Fu et al. [82] utilize holistically-nested edge detection [260] with CRF post processing for retinal vessel segmentation on the DRIVE [58] and STARE [229] datasets. Christ et al. [40] proposed a cascaded CNN based on two 3D U-Nets, one for liver, one for lesions segmentation, and utilize a 3D CRF [127] for further postprocessing. Shakeri et al. [220] segment subcortical regions in MRI slices using a CNN and a Markov Random Field (MRF), where the CNN output serves as potentials for a MRF. Gao et al. [89] propagate partial annotations for the lung using a CNN to predict a first label mask and a fully connected CRF to postprocess the results. For pancreas segmentation in MRI, Cai et al. [28] used two CNNs, one for pancreatic and non-pancreatic tissue classification, the other for pancreatic boundary segmentation, and forwarded these features to a CRF for fine-tuned segmentation. Nogues et al. [180] addressed lymph node segmentation, where Holistically-Nested Neural Network (HNN)s [260] predict volume and boundary masks as initial predictions. The authors then evaluated different postprocessing schemes (CRF, graph-cut and Boundary Neural Fields [21]) for refinement of the segmentation. Shen and Zhang [223] improved the

initialization of a CRF using learned priors that include anatomic features such as tumor centroids into a probabilistic model. Li et al. [141] applied a CRF as a postprocessing step on a CNN in low-grade glioma segmentation. Kamnitsas et al. [122] adapt a post-processing scheme with fully connected CRF to a 3D CNN for brain tumor, injuries and ischemic stroke evaluated on both BRATS 2015 and ISLES 2015 challenges. Dou et al. [56] apply a CRF for postprocessing to a deeply supervised 3D CNN for liver (CT) and whole heart and vessel (MRI) segmentation. Rajchl et al. [199] introduced a combination called DeepCut that uses a Fully Convolutional Neural Network (FCNN) to classify voxels in a bounding box into foreground and background. The result is refined using a fully connected CRF as post-processor. Wachinger et al. [247] applied a CRF as a postprocess-ing step on a custom CNN for brain anatomy segmentation on the MICCAI Multi-Atlas Labeling challenge dataset. Xia et al. [258] propose a two step approach, where a CNN predicts an initial mask and a MRF combines label image, a priori spatial information and smoothing information into a final segmentation. Jin et al. [119] applied a 3D CRF on the results of a slice-by-slice 2D CNN for left ventricle appendage segmentation. Hu et al. [116] combined a FCNN and a CRF such that in can be trained end-to-end and segmented brain tumors. Postprocessing using connected component analysis and threshold was still applied. Hu et al. [116] proposed the use of a cascaded CNN and a postprocessing CRF for brain tumor segmentation, evaluated on three datasets of the BraTS challenge. Zhai and Li [279] use CNNs with atention modules and apply CRFs as a postprocessing step for brain tissue segmentation on the Brats, MSSEG and MRBrainS datasets. Yaguchi et al. [265] address multi component lung nodule segmentation by a 3D CNN with CRFs as postprocessing method.

End-to-end trained CNN + CRF architectures have also been investigated. Fu et al. [83] proposed an end-to-end framework consisting of a CNN with intermediate layers and a CRF-RNN to add spatial coherency. The authors reported competitive performance on fundus image datasets of DRIVE, STARE, and CHASE DB1 [33]. An alternative was proposed in [282, 283], where a three step straining scheme was proposed for brain tumor segmentation. First, the FCNN and the CRF were trained separately while an end-to-end training scheme for the combined CRF-RNN was applied afterwards. Monteiro et al. [165] applied the idea of implementing a CRF as a RNN on 3D medical images and evaluated it on two publicly available dataset for prostate and glioma segmentation (PROMISE 2012, BraTS 2015). Their evaluation against a sole CRF indicated no performance gain by the end-to-end trained RNN. Xu et al. [264] proposed the use of a CNN with a fully connected CRF-RNN for automatic bladder segmentation. In comparison with a V-Net architecture and CNNs with CRF postprocessing, their approach showed increased Hausdorff Distance (HD), but better accuracy in Dice score, volume overlap, relative volume difference and

Table 2.3.: Shape regularization papers using CRFs as regularizers. Abbreviations: Myocardial Contrast Echocardiography (MCE), High Resolution Computed Tomography (HRCT), Magnetic Resonance Neurography (MRN), Active Contour (AC), Myocardium (MYO), Left Ventricle (LV), Right Ventricle (RV), Adversarial Variational Autoencoder (aVAE), Markov Random Field (MRF).

Reference	Modality	Anatomy	Notes
CNN + CRF			
Alansary et al. (2016)	MRI	placenta	CRF
Fu et al. (2016)	RGB	retinal vessels	CRF
Dou et al. (2016)	ce-CT	liver	CRF
Christ et al. (2016)	ce-CT	liver, lesions	CRF
Shakeri et al. (2016)	2D MRI	subcortical regions	MRF postprocessing
Gao et al. (2016)	HRCT	lung + pathologies	label propagation
Cai et al. (2016)	MRI	pancreas	CRF
Nogues et al. (2016)	CT	lymph nodes	CRF
Shen and Zhang (2017)	MRI	brain tumor	FC-CRF pipeline
Li et al. (2017)	MRI	brain tumor	CRF for postprocessing
Kamnitsas et al. (2017)	MRI	brain tumors, injuries, ischemic stroke	CNN + CRF for
Dou et al. (2017)	MRI	MYO, blood pool	CRF for postprocessing
Rajchl et al. (2017)	MRI	fetal lung & brain	CRF regularization during training
Wachinger et al. (2018)	MRI	brain anatomy	CRF for postprocessing
Xia et al. (2018)	CT	kidney	MRF postprocessing
Jin et al. (2018)	CTA	left atrial appendage	CRT
Hu et al. (2019)	MRI	brain tumor	CRF for postprocessing
Zhai and Li (2019)	MRI	brain tissue	CRF postprocessing
Yaguchi et al. (2019)	CT	lung nodules	CRF
End-to-end trained CNN & CRF			
Fu et al. (2016)	RGB	retinal vessels	CRF-RNN
Zhao et al. (2016)	MRI	brain tumor	3 step training, CNN, RNN, CRF-RNN
Monteiro et al. (2018)	MRI	brain tumor, prostate	CRF-RNN
Xu et al. (2018)	CT	bladder	CNN + CRF-RNN

average symmetric surface distance.

Model-based post processing with methods such as active contours or ASM were also proposed [31, 261]. Cha et al. [31] proposed a two step approach for urinary bladder segmentation. First, a CNN classified patches lying inside or outside the bladder and the resulting label mask is fine-tuned by thresholding and hole-filling. A level set method is initialized with this information and produced a regularized contour. For nucleus segmentation in histopathology images, Xing et al. [261] train a CNN to predict a probability map that initializes a shape model. Repulsive constraints on deformable models are then used to segment the numerous nuclei in the images. A similar approach by Zhao et al. [281] uses a CNN to initialize an active contour than refines the segmentation based on internal and external energies. Hatamizadeh et al. [106] proposed a combination of CNNs and AC for lesion segmentation and evaluated it on different modalities of the

Multiorgan Lesion Segmentation dataset. A pixelwise weighting function is added to the ACM's energy function while both are initialized from a CNN. Recently, Xu et al. [263] followed the strategy of using a CNN do initialize an ACM for breast histopathological images. As a final step, they performed ellipse fitting to deal with cluttered and overlaying nuclei. For teeth segmentation in CBCT, Ma and Yang [155] employ a CNN for initial labeling and a geodesic AC for refined segmentation. Fang et al. [70] segment breast tumor in ultrasound images by initializing a phase-based AC with V-Net. Hu et al. [117] followed the same approach but used a dilated CNN for initialization.

An *alternative way* is to use shape models and compute their features or deformation fields by Depp Learning architectures. Rupprecht et al. [207] propose an interactive AC approach by training a CNN that predicts motion vectors for evolving the underlying contour. The algorithm is evaluated on the STACOM challenge dataset for left ventricle segmentation. Cheng et al. [37] use an atlas-based Active Appearance Model for prostate segmentation employing a CNN to classify feature points along the normal of the propagating contour. Tang et al. [239] proposed the use of a level set method for both boosting training of and applying postprocessing on a CNN. In their evaluation on CT and MRI data for liver and left ventricle segmentation the combined method outperforms the individual solutions. Li et al. [140] use a level set method on the segmentation result of a VGG16 net as one of several postprocessing steps for segmentation of the left ventricle in the SunnyBrook database. Hoogi et al. [111] propose a CNN-based AC for liver lesion segmentation. The CNN predicts for each voxel a probability for the voxel lying far inside, far outside or close to the boundary. The AC then uses these values to adapt the weighting function of the two Heaviside functions within the energy function. Li et al. [138] propose random forest segmentation with priors from a statistical shape model to segment the MYO in MCE. The method uses a CNN to detect the bounding box of the MYO. Salimi et al. [209] proposed to use a multi-layer perceptron to predict a rough segmentation of he prostate. Applying an additional image processing step with connected component search to extract the largest volume initializes an active contour for final segmentation. He et al. [107] refine an active contour with a CNN, that classifies voxels into inside, outside and close to the boundary. Guo et al. [99] presented an AC that includes the label map of a CNN output in the external force. The authors report competitive results on the SLIVER07 and LiTS training dataset. For knee menisci segmentation in MRI, Tack et al. [237] regularize the results of slice-by-slice U-Nets by statistical shape models. The authors then use a 3D U-Net to predict a final segmentation based on the extracted ROI from the regularization step. Ambellan et al. [4] follow a similar approach for knee bone and cartilage segmentation in MRI.

More recently, *strong model assumptions* have found their way into deep learning archi-

tectures. Oktay et al. [181] incorporate shape priors by making utilizing learned vector representations of objects [94] in the latent space of an underlying network. The proposed anatomically-constrained neural network features an additional euclidean distance loss in the training phase based on this latent representation to achieve accurate results during inference. Ma et al. [153] presented a combination of Dense U-Net and a robust kernel

Table 2.4.: Shape regularization papers using model-based approaches or unique solutions as regularizers. Abbreviations: Myocardial Contrast Echocardiography (MCE), High Resolution Computed Tomography (HRCT), Magnetic Resonance Neurography (MRN), Active Contour (AC), Myocardium (MYO), Left Ventricle (LV), Right Ventricle (RV), Adversarial Variational Autoencoder (aVAE), Markov Random Field (MRF).

Reference	Modality	Anatomy	Notes
CNN + model-based			
Cha et al. (2016)	CT	bladder	CNN initializes 2D/3D level-set
Xing et al. (2016)	RGB	nucleus	CNN initializes ASM
Zhao et al. (2018)	RGB	nucleus	CNN initializes ACM
Hatamizadeh et al. (2019)	MRI, CT	lung nodules, liver lesion	CNN + AC
Xu et al. (2019)	RGB	nucleus	CNN initializes ACM
Ma and Yang (2019)	CBCT	teeth	CNN initializes ACM
Fang et al. (2019)	US	breast tumor	V-Net initializes ACM
Hu et al. (2019)	US	breast tumor	CNN initializes ACM
Others			
Rupprecht et al. (2016)	MRI	left ventricle	ACM with CNN features
Cheng et al. (2016)	MRI	prostate	AAM, CNN for feature classification
Tang et al. (2017)	CT, MRI	liver, left ventricle	ACM iteratively, deep Level Set
Li et al. (2017)	MRI	left ventricle	ACM
Hoogi et al. (2017)	MRI, CT	liver lesion	CNN for parameter estimation of AC
Li et al. (2018)	MCE	myocardium	Random forests + ASM
Salimi et al. (2018)	MRI	prostate	MLP initializes ACM
He et al. (2018)	MRI	prostate	ASM, CNN for feature classification
Guo et al. (2019)	CT	liver	ACM with CNN energy
Tack et al. (2018)	MRI	knee menisci	2D U-Net + SSM + 3D U-Net
Ambellan et al. (2019)	MRI	knee bone & cartilage	2D U-Net + SSM + 3D U-Net
Deep Neural Networks only			
Oktay et al. (2018)	MRI, US	left ventricle	Auto-Encoder + shape loss
Ma et al. (2018)	CT	pancreas	DenseNet + SSM
Navarro et al. (2019)	CT	whole-body, thorax	U-Net + new output layer
Qin et al. (2019)	CT	airways	U-Net + new output layer
Yao et al. (2019)	CT	liver	U-Net + Graph-based CNN
Balsiger et al. (2019)	MRN	peripheral nerve	PointCNN
Painchaud et al. (2019)	MRI	LV, RV, MYO	aVAE
Zeng et al. (2019)	MRI	liver	CNN for deformation

SSM to segment the pancreas in CT images. The authors train a Gaussian Mixture Model on the probability output of U-Net to initialize the shape model. Navarro et al. [169] propose to use multiple output images in a U-Net architecture, resulting in a segmentation map, a distance map and a contour map. Based on a sum of individual loss functions the networks is trained end-to-end. Qin et al. [197] presented a 3D U-Net like approach that, instead of a segmentation mask, predicts a 26-channel-sized connectivity encoding, on channel for each neighboring voxel in a 26-neighborhood. The resulting masks are postprocessed using graph refinement. Yao et al. [273] proposed a novel graph-based CNN [250] that is trained together with a normal U-Net like architecture for segmentation. By combining different loss function for both segmentation and mesh quality, the network is capable of predicting accurate and high quality meshes starting from an initial ellipsoid. Balsiger et al. [8] combine the PointCNN architecture [139] for point cloud inference with and the output probability map from a CNN. Experiments on nerve segmentation outperformed both CNNs and baseline PointCNN on Dice, HD and volumetric similarity. Painchaud et al. [184] proposed to use the latent space representation of a aVAE for constraining output masks of LV, RV and MYO segmentation in short-axis cardiac MR image stacks. By sampling valid a high number of valid shapes in the latent space during training, a back projection onto the nearest training sample during inference allows to predict an anatomically plausible result. Zeng et al. [278] present an approach that predicts a deformation field for an organs mean shape. The authors evaluate the use of a FCNN for liver segmentation on the LiTS dataset.

2.3. Motion Planning

Motion Planning addresses the computation of collision-free trajectories from initial to goal configurations of a robot as well as the theoretical understanding of the underlying algorithms, e.g. in terms of determinism, run-time or probabilistic behavior. An exhaustive introduction can be found in [135]. Consider, for example, the problem of moving an object through 2-dimensional space while avoiding risk structures (see Formulation 1). This is formalized by a world space $W = \mathbb{R}^2$ partially covered by a number of obstacles O. With given initial and goal configurations q_I, q_G for a robot, this forms a well defined problem for finding a set of collision free configurations C_{free} connecting start and goal. More precisely, the task is to find a trajectory $\gamma : [0,1] \rightarrow C_{free}$ from start to goal, represented by a set of configurations q_{j_j} with collision free transitions from q_j to q_{j+1}.

In the medical field, research focuses on nonholonomic systems such as flexible steerable needles, guidewires or drilling robots [3, 26], where instrument steering is limited to

---

Formulation 1 Basic Problem Formulation

1: Let $O \subset \mathbb{R}^2$ be the obstacle region.
2: Let $C_{free} = \{q \in \mathbb{R}^3 | q \notin O\}$ be the space of collision free configurations.
3: Let $q_I \in C_{free}$ be an initial configuration.
4: Let $q_G \in C_{free}$ be a goal configuration.
5: Let $T_{max} \in \mathbb{R}^+$ be the maximally allowed run-time of a motion planning algorithm.
Task
6: Find a collision free trajectory from start to goal, i.e. a path $\gamma(t) : [0,1] \rightarrow C_{free}$ satisfying

- $\gamma(0) = q_I$,
- $\gamma(1) = q_G$.

If no such solution exists, report that no path was found in T_{max}.

---

certain directions and one major common characteristic is a constraint on the instrument's curvature. In other fields such as autonomous driving [10], Underwater Glider (UWG)s [29] or Unmanned Aerial Vehicle (UAV) [268], similar characteristics occure. This section first gives a short introduction to different approaches in motion planning, specifically the Rapidly-exploring Random Tree (RRT). It then presents a survey on curvature constrained motion planning in general (Section 2.3.2), introducing different approaches for finding feasible trajectories. Finally, a more distinct review for surgical instruments is given in Section 2.3.3.

2.3.1. Approaches in Motion Planning

Two main strategies to solve Formulation 1 include **discrete planning** on a grid and **sampling based** approaches as shown in Figure 2.11. An alternative method is **optimization** [214], which starts with a, sometimes infeasible, solution connecting start and goal and then iteratively adjust it, thereby improving a cost function than penalizes constraints such as distance to obstacles.

In **discrete planning**, the road map is already collision free and a shortest path definitely exists. Here, Dijkstra's algorithm [51] can be used to find the shortest path or an heuristic approach such as A* [105] that speeds up the search. However, the extraction of a feasible road map can be computationally prohibitive or even impossible. In such cases, which is often the case in clinical settings, **sampling based motion planning** offers an efficient
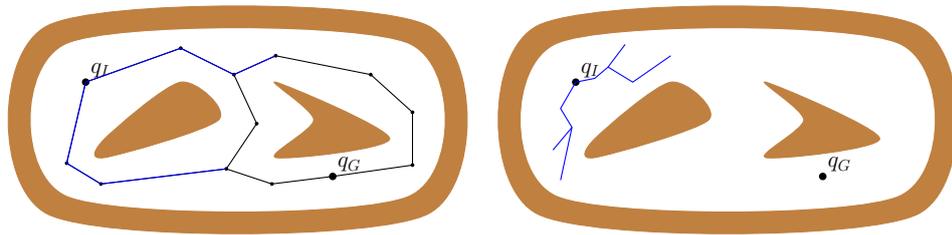
Figure 2.11.: Motion Planning can be performed on a discrete grid or road map in C_{free} (left, black lines and nodes) or in continuous space by sampling valid states with collision free transitions (right). Blue lines show explored states. In discrete planning, feasible solutions already exist as part of the road map. In sampling based planning, existence of solutions is not guaranteed and both building the road map and finding a solution is done simultaneously.

alternative. A review on existing methods is given in [64]. The RRT, introduced in 1998 by Steve M. LaValle, is still one of the most used algorithms to solve a motion planning problem with a sampling-based approach.

A randomized search with no prior knowledge of existence of solutions either returns a solution or reports failure for convergence within the given time frame T_{max}. Algorithm 2 presents the general principle and Figure 2.12 shows a visual impression: The search tree is initialized with the initial state q_I (Line 1) before the algorithm searches for a solution within the given time T_{max} (Line 2). The search first picks either the goal state q_G or create a new random state in C_{free} (Lines 3-7). This *goal biasing* draws the search towards the goal based on the bias ρ. In the remaining steps, the algorithm will try to expand the tree towards q_{rand}. To this purpose (Line 8), the nearest neighbor within the search tree $\mathcal{T}$ is computed using, for example, a kd-Tree. In Line 9, the steering function computes a motion towards the random sample, thereby creating a new state q_{next}. This steering function depends on the respective robot and application. This could be, for example, a circular arc describing the precise motion of a steerable needle [254] or a Bézier Spline with upper curvature constraint which approximates the motion of a UAV [267]. If the whole path between the nearest neighbor q_{near} and the newly created state q_{next} is collision free, the state is added to the search tree (Lines 10-12). Finally, a check for convergence ends the current iteration (Lines 13-15).

An alternative to searching for a feasible trajectory from a a given start configuration is the **optimization** of an existing one. Algorithms like Covariant Hamiltonian Optimization for Motion Planning (CHOMP) [200] and its adaptations [121, 185, 287] can start with a

Algorithm 2 Rapidly-exploring Random Tree

Input: q_I, q_G
Output: a set of states, $\{q_j\}_j, j \geq 0$
Parameters: step size Δt, goal bias ρ, search time T_{max}

1: $\mathcal{T} \leftarrow$ initial_states()
2: **while** time_spend() $< T_{max}$ **do**
3:     **if** random(0,1)$< \rho$ **then**
4:         $q_{rand} \leftarrow q_G$
5:     **else**
6:         $q_{rand} \leftarrow$ sample_state(C_{free})
7:     **end if**
8:     $q_{near} \leftarrow$ nearest_neighbor($\mathcal{T}, q_{rand}$)
9:     $q_{next} \leftarrow$ steer($q_{near}, q_{rand}, \Delta t$)
10:     **if** collision_free(q_{near}, q_{next}) **then**
11:         extend_tree($\mathcal{T}, q_{near}, q_{next}$)
12:     **end if**
13:     **if** goal_reached() **then**
14:         return extract_solution($\mathcal{T}$)
15:     **end if**
16: **end while**

trajectory in collision and optimize it until a feasible trajectory has been found. Similarly, Schulman et al. [214] proposed a sequential convex optimization approach to find feasible trajectories from a path initially in-collision.

2.3.2. Curvature Constrained Motion Planning

This section gives an overview of the papers listed in Table 2.5, which address curvature constrained motion planning in different fields. The listing differentiates between motions of **Circular Arcs**, mainly developed by [61] for bevel-tip needles [254]. These motions are suitable to reach a sphere like target such as a tumor. To solve the two point boundary value problem that interpolates between two states in $\mathbb{R}^3 \times \mathbb{S}^2$ (see Figure 1.4), approaches such as **Dubins Paths** [60, 235] have to be solved in 3D. An alternative for curvature constrained movement in 3D was developed by Yang and Sukkarieh [268] using **cubic Bezier Splines**. Finally, **further approaches** and some important **acceleration strategies** are considered.
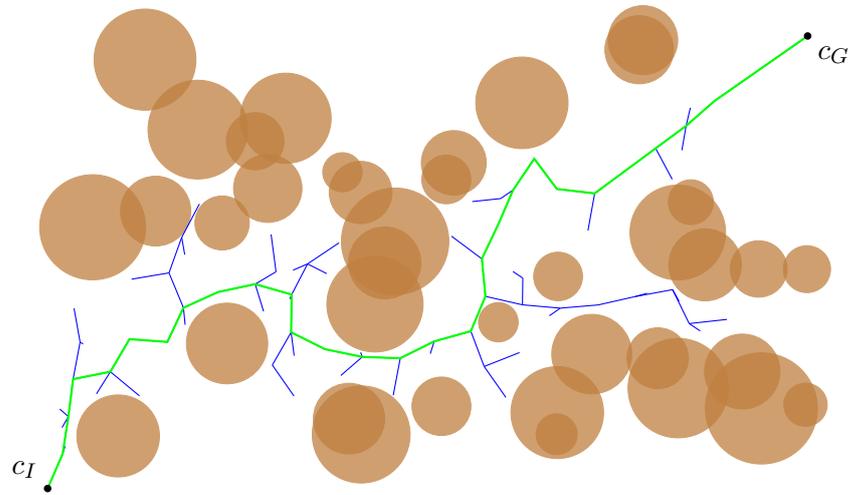
Figure 2.12.: Environments that are cluttered with obstacles (brown blobs) might not provide enough space to connect start and goal states q_I, q_G. A Rapidly-exploring Random Tree is a sampling based approach that grows a search tree (blue lines) until it connects it with the goal state. The solution (green lines) is then easily extracted by a traversing the search tree reversely from the final node.

Regarding **Circular Arcs**, the nonholonomic modeling of needle steering [254] led to several planning methods. Duindam et al. [61] presented a formulation describing screw-based motions for bevel-tip needles. This early work considered an analytic solution for a cost function based on a discrete set of motions. Xu et al. [262] integrated circular motions into an RRT and used a backchaining approach, that computed feasible solutions starting from the target and converging to the initial state. Duindam et al. [62] also presented an inverse kinematics approach for bevel-tip needles. However, obstacle avoidance was only possible by providing proper waypoints that split the original problem into several sub-tasks. Duan et al. [59] used SCO [214] to compute feasible trajectories for both bevel-tip needles and channel layouts in intracavitary brachytherapy. The authors compared initial linear trajectories in collision with obstacles with feasible solutions computed by RRTs, showing that the SCO procedure often failed to push infeasible initial solutions out of obstacles. Finally, Nikolajevic and Belanger [172] investigated the use of motion primitives to connect two states in $\mathbb{R}^3 \times \mathbb{S}^2$ obeying constraints on torsion but with no obstacles. The core idea was an approximation of the Dubins path problem in 3D by varying the curvature.

Table 2.5.: Curvature constrained planning along different motions. This table gives an overview on different approaches. Abbreviations: Sequential Convex Optimization (SCO), Rapidly-exploring Random Tree (RRT), Unmanned Aerial Vehicle (UAV), Underwater Glider (UWG), Genetic Algorithm (GA).

Reference	Method	Vehicle	Remarks
Circular Arcs			
Duindam et al. (2008)	analytic	Bevel-tip needles	discrete
Xu et al. (2008)	RRT	steerable needles	uses backchaining
Duindam et al. (2009)	inverse kinematic	Bevel-tip needles	no obstacles
Duan et al. (2014)	SCO	Bevel-tip needles, 3D printed implants	$c_I \in \mathbb{R}^3, c_G \in \mathbb{R}^3 \times \mathbb{S}^2$
Dong et al. (2016)	SCO	Bevel-tip needles	addresses uncertainty
Nikolajevic and Belanger (2016)	analytic	helicopters	circular motion primitives
Dubins Paths			
Ambrosino et al. (2006)	RTT	UAV	no obstacles
Hota and Ghose (2010)	analytic	theory	geometric solution
Hota and Ghose (2013)	waypoint following	aerial vehicle	no obstacles
Lin and Saripalli (2014)	RRT	UAV	3D Aerial Dubins Curves
Wehbe et al. (2015)	analytic	theory, UAV, UWG	2D Dubins Paths
Pharpatara et al. (2015)	analytic	aerial vehicle	adaptation of [112]
Pharpatara et al. (2015)	RRT*	aerial vehicles	optimality guarantees
Cao et al. (2016)	GA	UWG	Dubins Paths in 2D
Cubic Bézier Splines			
Yang and Sukkarieh (2008)	RRT	UAV	smoothing in 2D & 3D
Yang et al. (2014)	RRT	UAV	planning in 3D
Yang et al. (2014)	RRT*	UAV	optimality guarantees
Sudhakara et al. (2017)	Bi-RRT	cars	2D Dubins cars
Others			
Shanmugavel et al. (2007)	analytic	UAV	pythagorean hodographs, $c_G \in \mathbb{R}^3$
Acceleration			
Shkolnik et al. (2009)	RRT	cars, pendulum	sampling on reachability set
Yang et al. (2014)	RRT*	UAV	attractive & repulsive forces

Complete solutions using **Dubins Paths** got a lot of attention with varying approaches in 2D, 2.5D and 3D. Ambrosino et al. [5] proposed an interpolation scheme based on 2D Dubins paths and evaluate it on an environment for UAVs without obstacles. Similar approaches that divide the task into two seperate problems are found, for example, in [143, 255]. Lin and Saripalli [143] incorporated the solution of Dubins Airplane Paths [183] in an RRT to compute feasible trajectories for UAV in the presence of obstacles. Wehbe et al. [255] proposed the use of two 2D Dubins paths, one in the XY-plane, the other in the XZ-plane, to solve motion planning problems for UAV and UWG. Hota and Ghose [112] presented the first analytical solution to the 3D Dubins problem but without regarding helicoidal types. A geometric ansatz for paths of CSC type lead to a 4-DOF

nonlinear system of equations that could be solved numerically. The authors applied the solution to solve interpolation between position and orientation in 3D for aerial vehicles without obstacles [113] and presented a waypoint following strategy to iteratively solve a motion planning problem with a two point boundary value problem [114]. Pharpatara et al. [192] built on the geometric solution of [112] to consider circular motions of variable curvature for a hypersonic aerial vehicle. The authors used the method for the steering function in an RRT* [193] and presented an acceleration for the optimal search by using artificial potential fields [191]. The latter altered the random states using attractive forces towards the goal and repulsive forces away from obstacles. Finally, Cao et al. [29] used a GA to solve a Dubins path like problem for UWGs that is expressed in terms of an energy function. However, direction constraints were only considered in 2D on the water surface.

Cubic Bézier Splines were extensively studied by Yang and Sukkarieh [268]. The complete work presented an RRT that computes collision-free trajectories in $\mathbb{R}^3$ based on 2D cubic Bézier Splines with bounded upper curvature [248]. The work started with path smoothing algorithms using the curvature constrained cubic Bézier Splines in 2D [268, 269]. These were applied on feasible piecewise linear solutions computed by an RRT. The authors extended the smoothing part to directly planning in 3D with an RRT [267]. Finally a probabilistic complete and asymptotically optimal RRT* version [266] was proposed. Sudhakara et al. [232] applied the 2D Bézier Spline approach by [269] in a Bi-RRT* to connect two states in $\mathbb{R}^2 \times \mathbb{S}^1$ in the presence of obstacles.

Other work includes the approach of Shanmugavel et al. [221], that investigated the use of 5th order pythagorean hodographs for multiple UAVs. The application required simultaneous arrival of vehicles, which motivated the use of hodographs that describe paths of equal length.

Regarding **Acceleration** of RRTs, Shkolnik et al. [224] introduced the Reacha-bility-Guided RRT for motion planning problems in narrow regions such as tube like structures. By including an optimized sampling strategy that favored nodes with higher probability of expansion, it speeded up the search in kinodynamic environments. Yang et al. [270] proposed an altered steering function that took obstacles into consideration. The extension of an RRT* during the steering part towards the random node is altered by a vector field representing repulsive and attraction forces based on ellipsoids that cover the obstacles.

2.3.3. Surgical Motion Planning

With over 5000 different approaches in the last 30 years [212], robot-assisted interventions remain an active research field. Topics address insertion of instruments, soft tissue deformation and their physical modeling as well as optimization of clinical outcome [3]. This thesis targets minimally-invasive procedures where the underlying instrument moves along *nonlinear trajectories*. Beside the design and modeling of prototypes, the research of adequate motion planning algorithms [46] is an important issue for the realization of such approaches. The following section thus takes a closer look into curvature constrained motion planning in surgical robotics, with related work summarized in Table 2.6. The following starts with methods for **Steerable Needles**, continues with a short look at **suturing** and then covers **individual** solutions. Due to the focus on Temporal Bone Surgery in this thesis, the survey finishes with a look on **Linear** planning.

Planning for **Steerable Needles** has been done since the modeling of needle steering [163, 254] and the subsequent experimental validation using duty-cycled spinning [65]. Duindam et al. [61] presented a formulation for screw-based motions for bevel-tip needles and an analytic solution to a cost function based on a discrete set of motions. Xu et al. [262] proposed the use of an RRT with sampling in control space, i.e. in terms of velocities of forward (insertion) and rotational movement. Experiments were performed of a virtual environment with spheres as obstacles for urethra, prostate, pubic arch and penile bulb. Patil and Alterovitz [186] use the reachability-guided RRT [224] for rapid planning of bounded curvature trajectories for bevel-tip needles. Experiments in a virtual environment for percutaneous prostate access show the benefits of the approach.

Patil et al. [187] presented a needle steering system based on Electromagnetic Tracking (EMT) feedback and evaluated it both on a tissue phantom and an ex-vivo porcine tissue sample. The system consisted of an RRT that computes trajectories based on a novel distance metric and a replanning strategy within a closed-loop. Sanan et al. [210] used an A* like heuristic search on a dynamically extended graph. A path set, i.e. a number of feasible motion primitives for a bevel-tip needle, is initially created and the current node of the search is extended by each of these possible motions. Duan et al. [59] adapted the SCO approach for bevel-tip needle motions with either forward or backward integration. Experiments were performed for multiple needle trajectories in prostate access as well as channel layouts in intracavitary brachytherapy. Sun and Alterovitz [234] investigated belief space planning for liver biopsy with a flexible bevel-tip needle. Trajectory planning for an initial solution was performed using an RRT and an iterative LQG optimization [18] resulted in optimal trajectories regarding sensor and input uncertainty. Sun et

Table 2.6.: Motion planning papers for flexible curvature constrained clinical instruments. Abbreviations: Adaptive Fractal Tree (AFT), Genetic Algorithm (GA), Linear-Quadratic-Gaussian (LQG), Reinforcement learning (RL), Sequential Convex Optimization (SCO).

Reference	Method	Topic	Remarks
Steerable Needles			
Duindam et al. (2008)	inverse kinematics	spherical obstacles	first planning method
Xu et al. (2008)	RRT	prostate	control space sampling, prostate
Patil and Alterovitz (2010)	RRT	prostate	bounded-curvature trajectories
Patil et al. (2014)	RRT	liver tumor ablation	replanning on EMT feedback
Sanan et al. (2014)	A*	brain tumor	paths sets / motion primitives
Duan et al. (2014)	SCO	prostate cancer	multiple collision-free paths
Sun and Alterovitz (2014)	RRT + LQG	liver biopsy	belief space planning
Sun et al. (2016)	LQG	liver biopsy	novel linear quadratic regulator
Liu et al. (2016)	AFT	liver tumor	GPU-based
Comber et al. (2017)	simplex method	transforamenal hippocampotomy	trajectory optimization
Fu et al. [84]	RRT	lung cancer	image-based cost maps
Suturing			
Sen et al. (2016)	SCO	soft tissue phantom	da Vinci surgical system
Pedram et al. (2017)	brute force search	soft tissue phantom	Raven II surgical system
Others			
Bano et al. (2012)	inverse kinematics	neurosurgery	steerable probe STING
Caborni et al. (2012)	RRT	neurosurgery	2D, post optimization
Duan et al. (2014)	SCO	Intracavitary Brachytherapy	channel design
Patil et al. (2015)	RRT + SCO	Intracavitary Brachytherapy	torsion and curvature constraints
Kuntz et al. (2015)	medial axis + RRT	Lung Access	Three-Stage Multilumen Transoral Lung Access System
Chen et al. (2017)	neural dynamic algorithm	transoral surgery	tendon-driven serpentine manipulator
Kuntz et al. (2017)	RRT	pleural effusion	planning for the CRISP robot
Azizi et al. (2017)	centerline extraction	vascular catheterization	piecewise linear paths
Chi et al. (2018)	RL	endovascular access	addressing flow dynamics inside blood vessels
Pinzi et al. (2019)	AFT	neurosurgery, STING	GPU-based, geometric Hermite Curves
Granna et al. (2019)	particle swarm optimization	Laser-induced thermotherapy	Concentric Tube Robot
Linear			
Noble et al. (2007)	monte carlo	cochlear implantation	planning on segmented obstacles
Seitel et al. (2011)	sampling	liver tumor	hard & soft constraints
Essert et al. (2012)	simplex method	Deep Brain Stimulation	hard & soft constraints
Becker et al. (2014)	sampling	Temporal Bone Surgery	multi-port access
Hamzé et al. (2016)	multi-objective dominance	Deep Brain Stimulation	Pareto ranking scheme
Hamze et al. (2017)	evolutionary	Deep Brain Stimulation	Pareto ranking scheme
Liang et al. (2019)	sampling	liver tumor ablation	Pareto ranking scheme

al. [233] propose the Stochastic Extended Linear-Quadratic-Regulator which builds on previous work [234] to consider motion and sensor uncertainty for liver biopsy. Liu et al. [145] proposed to implement planning algorithms on the GPU to accelerate the search for feasible trajectories. Their approach, called AFT, uses a set of motion primitives to extend search tree's nodes and distributes the computation of different subbranches to GPU threads. The overall path planning algorithm then consists of three parts: tree extension, collision detection and back-tracing. Comber et al. [43] proposed a strategy to compute optimal trajectories for a robotically-driven curved needle in transforamenal hippocampotomy. The hippocampus medial axis was extracted using a skeletonization approach [137]. A manually created trajectory was then planned following the medial axis and the Nelder-Mead simplex method [170] as used to further optimize according

to length, curvature, torsion and distance to the medial axis. Fu et al. [84] proposed an extended version of an RRT [131] that considers in collision detection the use of a cost map extracted from CT images. Experiments for planning access to the lung shows that quality based on a cost function is increased compared to the original RRT.

For **Suturing**, Sen et al. [217] presented a complete setup for automated suturing with a da Vinci system using SCO [215] as a path planning approach where the kinematic model of the needle is expressed in terms of the Lie group SE(3) and its corresponding Lie algebra se (see e.g. [167]). The approach is evaluated on soft tissue phantom and showed promising results. Pedram et al. [189] presented a kinematic model for needle suturing obeying clinical suturing guidelines. Based on these formulation a multi-objective optimization formulation is derived for planning needle trajectories and numerically solved using a brute force sampling approach.

Individual solutions for **other curvatures constrained instruments** are also available. Bano et al. [9] planned curvature constrained trajectories for a neurosurgical probe. Their method consisted of a gradient-based nonlinear optimization regarding distance to risk structures as an additional cost, thus starting with initially infeasible paths that are transformed to such ones out of collision. Caborni et al. [27] used the reachability-guided RRT Shkolnik et al. [224] to plan multiple feasible trajectories for a flexible neurosurgical probe. Resulting feasible paths are then sorted according to a weighted cost function. Patil et al. [188] adapted the initial planning and subsequent SCO approach for planing curvature and torsion constrained ribbons for intracavitary brachytherapy. Kuntz et al. [131] presented a planning algorithm for a three stage lung access system, consisting of a bronchoscope, a concentric tube robot and a steerable needle. The bronchoscope is guided along sampled points on the medial axis of the bronchial tree, the tube is deployed and an RRT searches for feasible trajectories towards the target within the lung. Chen et al. [36] employ a novel neural dynamic model [271] for a tendon-driven serpentine manipulator in transoral surgery. Comparison with classic algorithms such as RRT* and previous models [272] show competitive computational performance and lower sweeping area. Kuntz et al. [130] present a planning algorithm based on an RRT for CRISP robot, which consists of multiple flexible tubes. For vascular navigation of catheters, Azizi et al. [7] proposed the extraction of a tree representation of the vascular structure's centerlines. Chi et al. [38] plan for robotically-inserted guidewires in endovascular procedures using RL. Experiments on aortic models showed that the approach leads to shorter paths and less contact to the aortic wall. Pinzi et al. [194] proposed a variant of the AFT that extends via optimized geometric Hermite curves [275] to meet position and heading constraints at both start and goal. The algorithm is applied on planning trajectories for the STING probe in neurosurgery. Granna et al. [98] worked on laser-induced thermotherapy for brain

tumor ablation using a concentric tube robot that deploys a variable number of curved laser fibers. The authors proposed the use of multi-objective particle swarm optimization to solve first the task specific problems, i.e. number and type of fibers, and then the robot specific problem, i.e. feasible robot parameters.

Finally, several works addressed **linear trajectories** for insertion of needles into soft tissue as well as for drilling access canals in Temporal Bone Surgery. The following publications have proposed both planning and optimization schemes. Noble et al. [179] presented a monte carlo approach for computing linear trajectories to the cochlea. An improved version is presented in [177]. The presented algorithm estimates for a given path the probability that it is effective and stays out of collision, resulting in a cost that is minimized. Seitel et al. [216] presented a solution for planning a linear liver access for tumor ablation considering multiple hard and soft constraints such as obstacles, occlusion, safety margins needle length and insertion angle. The authors proposed a weighted cost function as well as a pareto front approach to guide a clinician to a safe trajectory. Essert et al. [66] considered planning needle trajectories for deep brain stimulation and construct a weighted cost function on multiple hard and soft constraints. A rough pre-computation of feasible candidate trajectories followed by the Nelder-Mead simplex method [170] for optimization is used to compute optimal paths.

Becker et al. [14] presented an interactive planning scheme for multi-port temporal bone surgery, where a surgeon manually defines start and entry regions for three linear canals by clicking on voxels in CT data. Based on a weighted cost function on clinical and technical constraints the parameter space is discretized and an exhaustive search finds optimal solutions. Hamzé et al. [102] proposed a multi-objective method for path planning in Deep Brain Stimulation, resulting in a set of Pareto-optimal solutions and compared it against the mono-objective approach in [66]. Hamze et al. [101] further evaluated an evolutionary multi-objective method, NSGA-II [50], for finding a better Pareto-front of non-dominant solutions that can be presented to the surgeon. Multi-port approaches for the temporal bone were also considered by [76] in a general path planning formulation for nonlinear minimally-invasive approaches. Liang et al. [142] considered liver tumor treatment using microwave ablation with linear electrodes. Their multi-objective optimization for maximum coverage with minimal number of insertions lead to a Pareto front and considered a number of trajectories computed from sampled voxels at the target and entry.

2.4. Summary

Robot-assisted surgery requires multi-disciplinary research including robotics, image processing and motion planning. In **Section 2.1**, linear approaches for Temporal Bone Surgery have been presented that combined individual solutions in these field to a complete pipeline. For Endovascular Aortic Repair (EVAR), current work is focusing only on image processing to detect or classify the targeted diseases. Due to limited available data, an extensive retrospective in silico evaluation for robot-assisted surgery is available for neither of these two examples. **Section 2.2** then presented isolated segmentation approaches for both applications. While there are automatic solutions for EVAR, the proposed methods are designed for classifying aortic aneurysms and thrombi. The results may thus not be suitable for computer-assisted interventions that rely on downstream task such as trajectory planning. An automatic solution for the complete Temporal Bone is missing and promising Deep Learning techniques such as U-Net perform only pixelwise classification. Extracted risk structures may thus be fragmented and likewise hinder the computation of feasible trajectories. With **Section 2.2.5**, this chapter also introduced methods on shape regularization as a suitable countermeasure. Regarding trajectory planning, **Section 2.3** reported suitable methods using Circular Arcs, 3D Dubins Paths and cubic Bézier Splines for the computation of curvature constrained motions. Each of those used sampling based approaches on RRT. However, neither of these are designed for the solving of the two point boundary value problem in the presence of obstacles motivated in Chapter 1 . While 3D Dubins Paths principally solve the problem, the proposed ansatz requires the two states to be sufficiently far away [112] while solving a computational expensive nonlinear system of equations [193].

We address these issues in **Chapters 3**, **4** and **5**. For an extensive **in silico evaluation** of preoperative surgical planning pipelines, we introduce synthetic anatomies. These clinical equivalents to *random worlds* allow the sampling of an infinite amount of anatomical variations, thereby enabling a statistically robust analysis of motion planning algorithms. With an evaluation of segmentation algorithm quality on down stream task, we further expand these in silico experiments. In **Chapter 4**, we propose a **shape regularized Deep Learning** solution that first computes an initial label from a slice-by-slice U-Net architecture. It then registers the mean shape of a statistical shape model against the extracted surface mesh and refines this segmentation using Probabilistic Active Shape Models of the individual organs. For trajectory planning (**Chapter 5**), we introduce the first solution that efficiently solves the two point boundary value problem in dense, cluttered environments using **Bidirectional Rapidly-exploring Trees**. We propose two different steering methods: **cubic Bézier Splines** and **Circular Arcs**. We also present a

optimization scheme for Bézier Splines based on sequential convex optimization as well as a translation of such trajectories to motions of Circular Arcs.

3. Preoperative Surgical Planning

This chapter serves two purposes: First, it introduces the preoperative clinical workflow addressed in this thesis, so the work in Chapter 4 and Chapter 5 is put into context. It then contributes an extensive retrospective *in silico evaluation* of this step.

Preoperative Surgical Planning for image-guided robot-assisted surgery is built upon an extensive pipeline (Figure 3.1). Risk structures are extracted from a CT or MRI image, usually taken a few days before surgery, using either manual interaction or (semi-)automatic algorithms. A 3D environment of the surgical site is created from these results, which allows visualization and serves for further planning. In this extracted representation, a surgeon has to define target and entry points for the instrument. In Temporal Bone Surgery, this could include marking the surface of the lateral skull base as possible entry points of a drilling robot and marking the round window of the cochlea as the designated target [90]. During computation of feasible trajectories, the extracted geometry is used for collision detection. For planning of trajectories by sampling based approaches, no guarantee of global optimality exists and instead of a final path a pool of sub-optimal solutions is usually presented [14, 102, 187]. This workflow relies on the clinician to select the most suitable path based on technical and clinical constraints. A complete automation of these two tasks might lead to faster interventions and more reproducible results, benefiting clinical workflow and patient health. Automation of these two steps would also relieve the surgeon of tedious and complex tasks, allowing more time for preparation or patient education.

The review in Chapter 2 shows that a thorough evaluation of such a pipeline is often problematic. In silico evaluation is often performed isolated for just the two major parts before going on to ex vivo experiments on phantoms. This ignores the influence of segmentation on trajectory planning, because image metrics such as Dice or Hausdorff Distance (HD) do not cover topological irregularities which might prevent a successful subsequent step, such as fragmentation or holes in segmentation results. If both tasks are instead considered as a single entity, experiments could evaluate the whole procedure. Quantitative evaluation
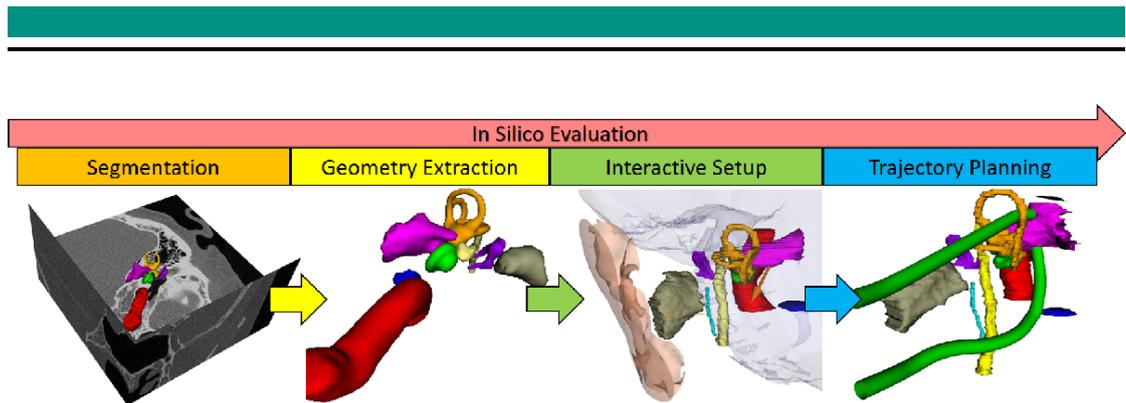
Figure 3.1.: A preoperative surgical planning pipeline first performs segmentation to extract a 3D representation of the surgical site. In this 3D environment the surgeon defines start and goal of the robots path and lets a motion planning algorithm compute feasible trajectories. Thorough in silico evaluation should analyse these steps both individually and as a single entity.

of this complete pipeline could then be based on relevant CAI parameters such as the abundance of feasible paths and their distance to risk structures. Moreover, the lack of sufficiently large datasets limit experimental validation of path planning algorithms in terms of both robustness and path quality for the specific application. While in motion planning, random worlds offer a suitable method for evaluation, a clinical equivalent does not exist.

Extensive in silico evaluation could thus benefit

1. **segmentation algorithms**, because they could be judged whether or not they provide topologically coherent shapes that do not interfere with collision detection.

2. **motion planning algorithms**, because experiments could be based on synthetically enlarged datasets that allow drawing results from a statistically sound sample size.

This chapter is based on two papers I co-authored [73, 75]. My contributions consist of

- an interactive preoperative pipeline combining shape regularized deep neural networks with a precise trajectory planning step.

- synthetic anatomies as a novel implementation of random worlds in the field of Computer-Assisted Interventions (CAI).

- a functional evaluation on down stream tasks to evaluate segmentation and trajectory planning methods as a single entity.

3.1. Interactive Preoperative Pipeline

With both medical image segmentation and motion planning for a novel problem formulation, evaluation of the complete pipeline requires the combination of state of the art algorithms of multiple fields within a single framework. While open source tools such as Slicer 3D of the medical community or ROS in the field of robotics provide adequate and extendable frameworks for complex approaches, a solution for nonlinear interventions has not yet been presented.

Along with our publications on segmentation [73, 75], trajectory planning [72, 74, 76, 77] and pipeline evaluations [73, 75], we published our algorithms within a custom open source framework with interactive GUI on MUKNO-Framework. Our framework provides an interactive setup for image processing pipelines (see Figure 3.2), covering algorithms from ITK and VTK, remeshing algorithms required for active shape models [243] using ACVD, and deep learning inference algorithms using tensorflow [160]. It features an interactive definition and setup of the motion planning formulations presented in Chapter 5 for placement of suitable start and goal configurations as well as mesh adaptation for correction of segmentation errors. It thereby allows the quick setup of trajectory planning algorithms for different clinical applications such as endovascular guidewire insertion, drilling access canals for temporal bone surgery or needle insertion into soft tissue. Finally, it includes our path planning and optimization algorithms based on OMPL and Gurobi, allowing fast execution of Bi-RRTs on Bézier Splines and Dubins Paths (see Section 5.3.3), translation to circular arcs (Section 5.3.4) as well as sequential convex optimization (Section 5.6). Overall, it gives the research community of CAI access to a framework implementing a preoperative pipeline for nonlinear interventions.

In particular, an image processing pipeline is represented by a directed acyclic graph that can be interactively generated using drag and drop. Figure 3.2 **A**) shows an example consisting of deep learning segmentation, remeshing for initialization of the mean shape of a Statistical Shape Model (SSM) and finally Active Shape Model (ASM) segmentation. In the resulting 3D environment of extracted risk structures, necessary placement of start and goal states of the motion planning formulation is possible with custom VTK widgets that allow interaction with the surface models. For Temporal Bone Surgery (Figure 3.2 **B**), one could for example mark the surface of the skull as potential entry points for an access to the cochlea and place an anchor at the facial recess to indicate proper orientation at individual states at the surface. For the goal state at the round window, vertices at the surface of the cochlea can be marked and the orientation manually aligned to the centerline of the lower ductus as motivated by Torres et al. [240]. Finally, after computing

■ Jugular vein ■ Carotid artery ■ Facial nerve ■ Chorda tympani ■ External auditory canal ■ Internal auditory canal ■ Cochlea ■ Semicircular canals ■ Ossicles
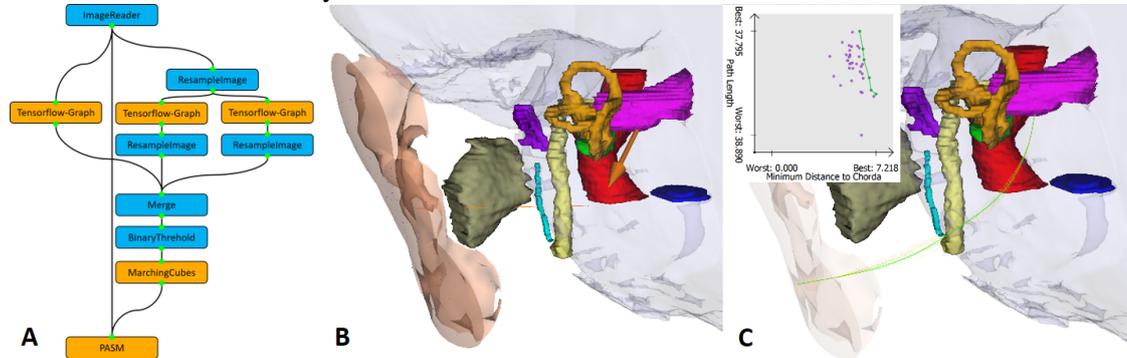
Figure 3.2.: Examples of interaction. A: Image processing pipeline performing deep learning inference with slice by slice U-Net, Marching Cubes surface extraction with remeshing and finally ASM segmentation (orange nodes). B: Interaction with custom VTK widgets to set up start and goal regions C_I, C_G based on extracted surface models of risk structures (skull's surface, orange arrow at internal auditory canal). C: Visualization and selection based on a Pareto front of feasible solutions (colored lines).

multiple solutions for feasible nonlinear access paths, a Pareto front optimization allows a surgeon easy selection of the clinically most optimal path similar to the approach in [102].

3.2. Synthetic Anatomies

Scarce datasets with only a very small number of patient images present a challenging base for evaluation of different methods. Current work presents experiments with only a very limited number of samples or even a single one [14, 194]. Statistical conclusion for robustness of trajectory planning approaches or other metrics are hardly achievable. The possibility of generating random patient data bases for more robust evaluation would greatly benefit the significance of conducted experiments.

In the field of motion planning, a widely adopted strategy for investigating planner properties is the use of *Random Worlds* (Figure 3.3 *Left*). First, a bounded environment such as $[0, B]^2, B > 0$ is defined as the working environment. Then, new motion planning

problems are randomly created. For each new world, the space is filled with obstacles, for example by randomly putting spheres inside it up to a certain percentage. Then, start and goal configurations are randomly chosen and the planner under investigation has to find a feasible trajectory. This strategy can be repeated arbitrarily often until a statistically meaningful sample size is reached. However, the approach does not translate one-to-one into our CAI scenario.

Neither the creation of random obstacles in an anatomical workspace nor placement of random start and goal configuration makes sense in a clinical setting. We propose *Synthetic Anatomies*, anatomically plausible and clinically meaningful random worlds [74] (Figure 3.3 *Right*), as a clinical adoption of random worlds. These anatomies can be built from a scarce dataset of patient label images. First, we create statistical shape models [45] of the available segmented risk structures. For each new synthetic anatomy, one of the real anatomies is then chosen randomly to serve as an atlas that creates a corresponding 3D environment. This replaces the creation of a simple bounded scenario as in the case of random worlds. The sampling of randomly created obstacles is replaced by the use of statistical variation of organs. For each SSM, its corresponding eigenmodes are changed between $\pm\delta$ times their standard deviation, $\delta > 0$, to create an anatomically plausible variation. This altered version is then registered to the atlas to replace the original structure. Finally, the random placement of start and goal configurations has to be replaced by a clinical more meaningful alternative. We propose the inclusion of these states within the atlas and the use of anatomical landmarks for further adjustment. An atlas for Synthetic Anatomies thus consists of surface models of organs as well as predefined positions for start and goal configurations. Because their original pose in the atlas might be invalid due to the deformation of shape models, a modification is necessary for each new sample. This modification is dependent on the application and we present two examples in the experiment section, one for cochlear implantation and the other for vestibular schwannoma removal at the internal auditory canal. Using these Synthetic Anatomies, a proper evaluation of the robustness of planning methods is possible.

3.3. Functional Evaluation

Image metrics such as Dice or HD allow an objective comparison between expert annotations and segmentation algorithm results and thus serve as a major quality criteria to analyze different segmentation approaches. For tasks such as volume estimation of organs, e.g. the left ventricle, these metrics are fully associated to the clinical application (mass
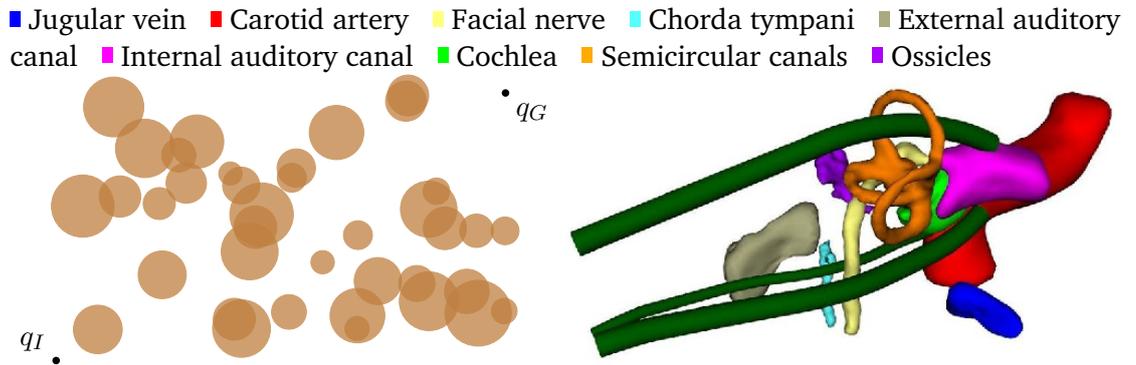
Figure 3.3.: *Left:* A *Random World* to evaluate a 2D motion planner based on a bounded environment filled to 30% with spherical obstacles. *Right:* A *Synthetic Anatomy* based on SSMs of risk structures of the temporal bone. Planned paths from modified start and goal configurations of the atlas are shown in green for a cochlear access and two different accesses to the internal auditory canal.

volume, stroke volume, wall motion [140]). However, for robot-assisted interventions and the preoperative planning of trajectories in particular, additional analysis on the results is required. Consider, for example, Figure 3.4 that shows results from two different segmentation algorithms in a CT image of the lateral skull base. While the expert annotation as well as both algorithms capture the clinically relevant characteristic of the jugular vein, i.e. the bulb of the jugular vein reaching into the temporal bone, segmentation of the complete vein varies resulting in mediocre scores for Dice and Hausdorff distance. For Temporal Bone Surgery, though, volume estimation is of less importance. Instead, segmentation output should allow proper trajectory planning and suitable metrics should thus quantify the quality of the subsequent step in the preoperative pipeline.

A functional evaluation of a preoperative pipeline considers the final goal of the procedure and analyses the quality of individual sub steps such as segmentation on the downstream task, i.e. trajectory planning. This gives, together with existing image metrics, additional feedback on the usefulness of algorithms for the complete pipeline.

We proposed three different scores for functional evaluation of a preoperative planning step for robot-assisted surgery [73, 75] (Table 3.1). Each is based on two rounds of trajectory planning, once using surface models from ground truth risk structures, M^{GT}, and once using surface models from segmentation output, $M^{\mathcal{P}}$. Scores are then computed using the resulting sets of trajectories, T^{GT} and $T^{\mathcal{P}}$, respectively. First, a *success rate* ϕ^s for

■ Jugular vein ■ Carotid artery ■ Facial nerve ■ Chorda tympani ■ External auditory canal ■ Internal auditory canal ■ Cochlea ■ Semicircular canals ■ Ossicles
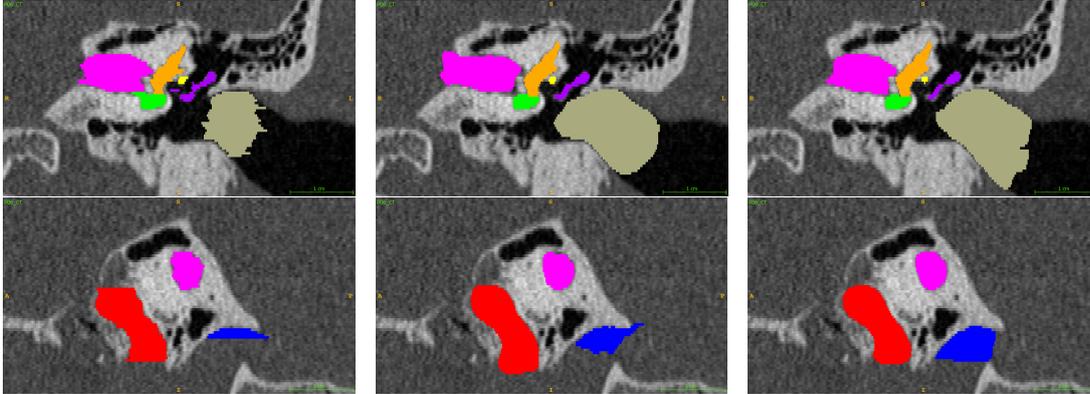
Figure 3.4.: Examples for low Dice coefficient of EAC (brown), IAC (pink) and jugular vein (blue). Left to right: ground truth, algorithm 1, algorithm 2.

motion planners is computed, defined as the percentage of datasets where at least one path was found for T^{GT} and $T^{\mathcal{P}}$. This indicates the robustness of trajectory planning algorithms for the clinical task by measuring how often planning was possible with segmentation result when it was already possible with ground truth annotations. Next, the distances to risk structures for T^{GT} and $T^{\mathcal{P}}$ using only shapes M^{GT} as obstacles is computed. This gives for each trajectory the true distance to risk structures when planning on segmentation results. We then introduced the *mean minimal distance* ϕ^d of computed trajectories. This gives an indicator to the quality of computed trajectories as it allows comparing the maximally achieved clearance to different organs between planning on ground truth and segmentation output. Finally, we define the *failure rate* ϕ^f as the number of datasets were a path computed on segmentation results was actually in collision. Pipeline evaluations resulting non-zero failure rates indicate that either trajectory planning or segmentation algorithms have to be improved before further evaluations such as phantom experiments should be considered.

3.4. Summary

While designated experiments on segmentation and trajectory planning methods with specialized metrics give a good view on isolated tasks, their significance as a metric for

Table 3.1.: Functional metrics for downstream analysis of combined segmentation and trajectory planning.

	Symbol	Range	Remarks
success rate	ϕ^s	$[0,1]$	success when planning with segmentation, robustness
failure rate	ϕ^f	$[0,1]$	violation when planning with ground truth, quality criteria
mean minimal distance	ϕ^d	$\mathbb{R}^{0+}$	distance to risk structures, quality criteria

preoperative surgical planning is limited. First, global metrics such as Dice or Hausdorff distance neither adequately capture variations in expert annotations nor to they detect topological irregularities. Second, the limited sample size in clinical research for new CAI procedures do not allow proper evaluation of sampling-based motion planner on random worlds, a standard approach in motion planning.

This chapter introduced a thorough in silico evaluation of the complete pipeline. It proposed *synthetic anatomies* as a clinical equivalent to random worlds. These setups combine statistical variations of risk structures with calibrated motion planning formulations, i.e. predefined parameters as well as templates for start and goal states. The resulting environment allows the sampling of an indefinite number of new scenarios for evaluation of motion planning algorithms. It introduced metrics for a functional analysis of segmentation algorithms on downstream tasks. By comparing the performance of path planning and the quality of resulting paths on both expert annotations and segmented surfaces, the suitability of segmentation algorithms can be efficiently evaluated. These metrics ignore diversity in inter-clinician bias on ground truth labeling and are sensitive to shape irregularities. Together with existing scores on Dice or Hausdorff distance, they add substantial information to the evaluation of a preoperative surgical pipeline.

Finally, a C++ framework with interactive GUI, implementing the entire preoperative surgical pipeline, is made publicly available. The code allows reproduction of our experiments that are based on publicly available datasets. It also presents an implementation of the individual segmentation and trajectory planning methods that are proposed in the following two chapters.

4. Shape-regularized Segmentation

Contrary to radiologists, who analyze image intensities and textures in a slice-by-slice manner for diagnosis, surgeons are more interested in organ shapes for treatment planning. A 3D representation of the risk structures can be compared with the surgeon's mental model of the patient's anatomy, used for 3D printing in endovascular surgery or utilized in collision detection when planning trajectories in Temporal Bone Surgery. These last two examples also emphasize why strong topological guarantees are an important quality measure for segmentation algorithms in preoperative surgical planning. State of the art deep learning solutions such as U-Net achieve outstanding accuracy but perform pixelwise classification. Their results may thus contain irregularities such as holes or isolated regions, preventing 3D printing or collision-free paths to the surgical site. In complex environments with many tiny or accentuated structures, CNN segmentation even provides only fragmented pieces [75]. Using model-based algorithms such as Active Contours (ACs) or Active Shape Models (ASMs) could result in smooth shapes with defined topology. However, these methods are outperformed by deep neural networks and suffer, for example, from initialization problems as well as complex and parameter-heavy setup.

A combination of Deep Learning architectures with model-based approaches could provide the best of both worlds:

1. Automatic segmentation with state of the art accuracy,

2. Modeling of plausible anatomical shapes.

Our proposed automatic pipeline is shown in Figure 4.1: For segmentation, we adapt the shape regularized U-Net approach of Tack et al. [237] from knee menisci segmentation: U-Net architectures [204] achieve a first localization of every risk structure. Then, ASMs regularize the fragmented contours to realistic structures. In our experiments we showed, that this shape regularized deep learning approach is capable of detecting both the cluttered tiny structures of temporal bone anatomy as well as the highly varying course of the aorta.
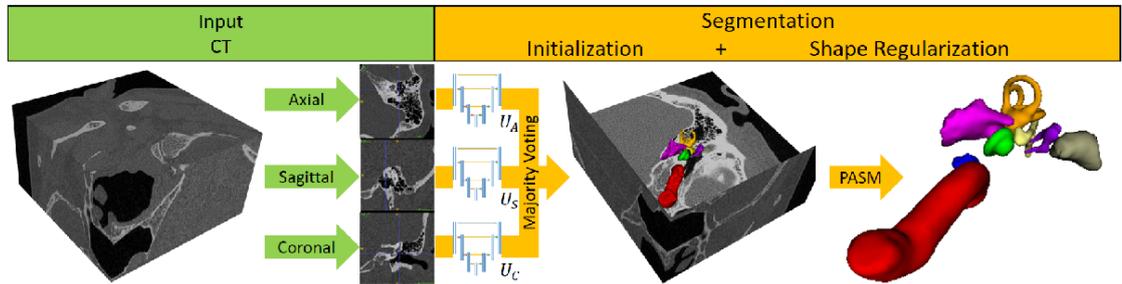
Figure 4.1.: Pipeline for automatic segmentation consisting of a slice-by-slice U-Net approach for initialization and a Probabilistic Active Shape Model (PASM) for shape regularization.

This chapter is based on two papers I co-authored [73, 75]. My contributions consist of

- an automatic segmentation approach for Temporal Bone Surgery and Endovascular Guidewire Insertion.

- a novel initialization of PASMs based on (non-)rigid registration against a deep neural network's output.

- shape-regularized segmentation for preoperative surgical planning.

4.1. Deep Learning Initialization

Due to the small number of annotated training datasets, we abandoned a potential 3D U-Net approach in favor of 2D architectures with slice-by-slice prediction. For each axial, sagittal and coronal slice (Figure 4.1) we predict 2D segmentations of all risk structures using individually trained U-Nets U_A, U_S, U_C. These three predictions are then combined to an initial 3D segmentation U_{ASC}.

Approach The ratio of available class labels in datasets is often highly unbalanced. Consider for example a CT image of the otobasis in temporal bone surgery. Here, a huge percentage (99%) of the whole image is usually just background. Even worse, within class labels, the chorda tympani appears with a much lower percentage than other structures (Figure 4.3). In such cases, we further subdivide the nets U_A, U_S, U_C into two parts, subnets U_{Am}, U_{Sm}, U_{Cm} for multi class segmentation of all labels and subnets
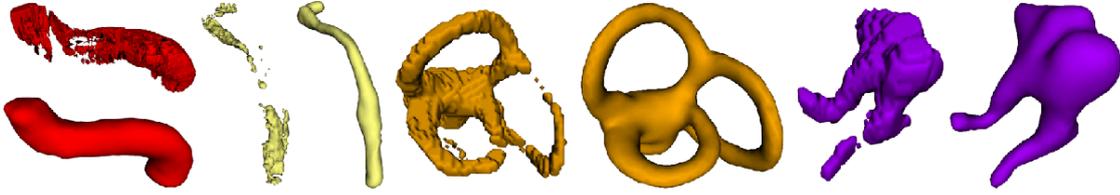
Figure 4.2.: Representative fragmented structures and regularized counterparts.
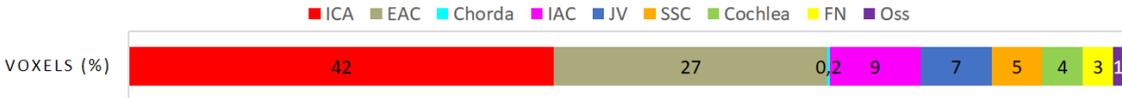
Figure 4.3.: A typical temporal bone CT observes widely different volumes for different risk structures.

U_{Ac}, U_{Sc}, U_{Cc} for binary classification between background and underrepresented label. Equation 4.1 shows this setup as a function of a Hounsfield calibrated CT slice in $\mathbb{Z}^{N \times M}$ with N rows and M columns to a predicted label image $\hat{Y}_{2D} \subset \mathbb{L}^{N \times M}, \mathbb{L} := \{0, \ldots, N_L\}$ with N_L positive labels for the list of risk structures:

$$U_{Am}, U_{Sm}, U_{Cm} : \mathbb{Z}^{N \times M} \to \mathbb{L}^{N \times M}$$
$$U_{Ac}, U_{Sc}, U_{Cc} : \mathbb{Z}^{N \times M} \to \{0, 1\}^{N \times M}$$

(4.1)

After slice-by-slice prediction of all nets for a $N \times M \times K$ dimensional CT scan, $K > 0$, a majority vote first unites the results of the three multi class nets to a prediction of the whole volume. The results of the individual binary nets are then added to this vote for the final prediction $\hat{Y}_{3D} \subset \mathbb{L}^{N \times M \times K}$.

Architecture   CT datasets usually have a fixed dimension, e.g. 512×512, in the xy-plane and varying size in the xz- and yz-planes due to inter-patient variation. Prediction on the axial plane is therefore straight forward implemented by networks with input size 512×512. For prediction on the saggital and coronal planes, a fixed network size has to be defined dependent on the available data. Each input slice then needs to be resampled. This can be done by either cropping of region of interests [75] or resampling [73]. The architectures of our used networks are shown in Figure 4.4: In each block, we have two 3×3 convolutions with ReLU-activation. Max pooling then halves the image size to the next block. After five blocks we go back with standard concatenation and upsampling.
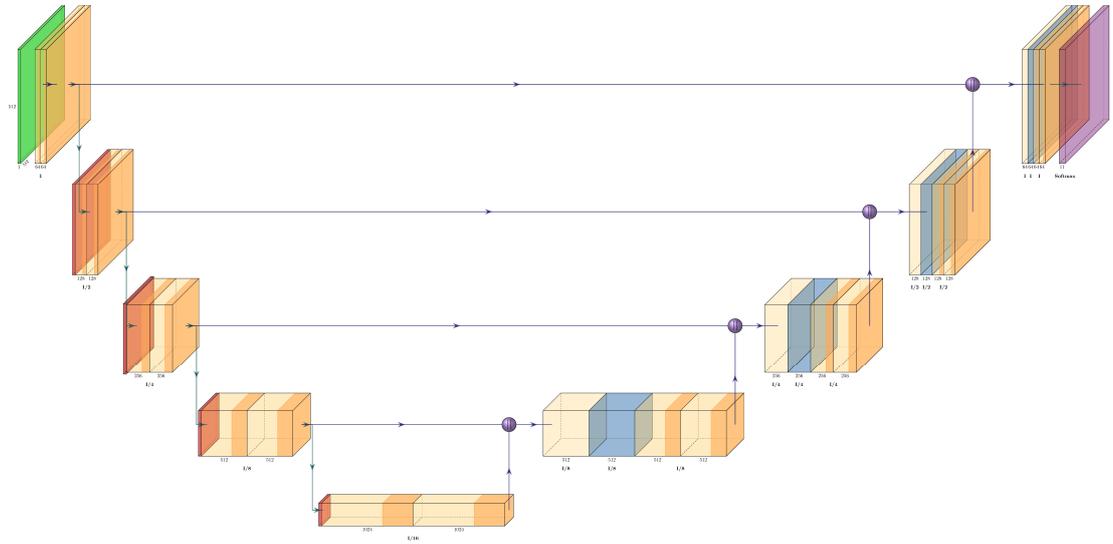
Figure 4.4.: 2D U-Net architecture for networks U_{Am}, U_{Sm}, U_{Cm} and U_{Ac}, U_{Sc}, U_{Cc}. Input and output size depends on application (512×512 for axial and 128×512 for sagittal and coronal slices.

In the end, classification is done for both multi class nets U_{Am}, U_{Sm}, U_{Cm} and binary prediction of the chorda U_{Ac}, U_{Sc}, U_{Cc} via a softmax operation.

Training Our implementation is based on tensorflow [160] with Keras [39]. During training we use as loss function a custom weighted loss for multi class nets U_{Am}, U_{Sm}, U_{Cm} (see Algorithm 3), where we weight all entries in w equally, i.e. $w = 1^{1 \times L}$. For the binary nets U_{Ac}, U_{Sc}, U_{Cc} we use tensorflow's *'binary_crossentropy'*. All nets are trained for 30 epochs. In each epoch, every slice of the dataset is given to the respective U-Net once.

Output The initial 3D segmentation often suffers from small artifacts or small missing pieces as no shape knowledge of the individual structures is built into the neural nets. Figure 4.2 shows some representative examples for temporal bone surgery: The internal carotid artery (red) is broken in several pieces and the semicircular canals (orange) observe holes in their arcs. The stapes of the ossicles (purple) are decayed and the facial nerve (yellow) often has missing parts. We propose the following procedure to regularize these fragmented structures.

Algorithm 3 Sample of our weighted loss function for multi class training on 512×512 slices.

> **procedure** class_weighted_crossentropy(w, y_{true}, y_{pred})
>   // *weights $w \in \mathbb{R}^{L \times 1}, images\ y_{true}, y_{pred} \in \mathbb{Z}^{512 \times 512}$*
>
> $y_{pred} \leftarrow y_{pred} / \Sigma_{i,j}^{M \times N} y_{pred}(i,j)$
> $loss \leftarrow y_{true} * log(y_{pred}) * w$
>   *return loss*
> **end procedure**

4.2. Active Shape Model Regularization

Unlike U-Net - trained in an end-to-end fashion with no knowledge of geometry - Active Shape Models (ASM) [45] inherently respect the shape by restricting the segmentation to the trained shape space. We proposed the use of Probabilistic Active Shape Models [124], because these allow a more flexible adaptation by leaving the shape space if image features provide enough evidence. Applying these PASMs to the result of a U-Net approach gives us the best of both worlds: Deep Learning segmentation accuracy with shape regularization.

Approach   The original ASM projects a shape vector $v \in \mathbb{R}^{T \times 3}$, with $T > 0$ landmarks in $\mathbb{R}^3$, into the learned shape space. The PASM instead minimizes an energy function E to enforce shape constraints via

$$E : \mathbb{R}^{T \times 3} \times \mathbb{R}^{T \times 3} \to \mathbb{R}$$
$$E(v, \bar{v}) = \alpha[E_I(v, \bar{v}) + E_M(v)] + E_S(v). \tag{4.2}$$

During each iteration, it balances between a weighted local energy term $\alpha[E_I + E_M], \alpha > 0$, and a global shape energy E_S. In short, $E_I(v, \hat{v})$ represents the distance from landmarks v to image features $\bar{v}$. These are defined by the appearance model and push, in each iteration, the landmark vector to learned features such as high gradients. $E_M(v)$ controls the mesh regularity by setting, for example, constraints on its smoothness. Finally, $E_S(v)$ punishes unknown shapes based on a distance *in* feature space (DIFS) and distance *from* feature space (DFFS) [164]. This way, a PASM allows the mesh to adapt to geometries outside the learned space. In particular, we use the parameter setup proposed by Becker et al., which outperforms classic ASM for Temporal Bone Anatomy, and refer the reader

to [15] for a detailed description. For each of the individual risk structures we learn PASMs $P_l, 1 \leq l \leq 9$.

$$\textit{Initialization: } \mathbb{Z}^{N \times M \times K} \xrightarrow{U_{ASC}} \mathbb{L}^{N \times M \times K}$$

$$\textit{Mesh Building: } \mathbb{L}^{N \times M \times K} \xrightarrow{MC} \mathbb{R}^{\tilde{K}_l \times 3} \xrightarrow{ICP} \mathbb{R}^{K_l \times 3} \qquad (4.3)$$

$$\textit{Regularization: } \mathbb{R}^{K_l \times 3} \xrightarrow{P_l} \mathbb{R}^{K_l \times 3} \times \mathbb{L}^{N \times M \times K}, 1 \leq l \leq L,$$

Equation 4.3 now shows the connection to the trained U-Nets: After our U-Net initialization, we create landmark vectors $\mathbb{R}^{\tilde{K}_l \times 3}, \tilde{K}_l > 0, 1 \leq l \leq L$, from the fragmented structures using marching cubes (MC) [150]. It follows a rigid registration of the mean shape of each model to these vectors using the iterative closest point algorithm (ICP) [22], resulting in initialized probabilistic active shape models. We then start the iterative segmentation of PASM to receive both regularized meshes and corresponding segmentation masks.

Architecture The use of active shape models requires a parameter-heavy setup during mesh generation, remeshing, correspondence analysis for shape model generation and finally feature extraction during segmentation. We extract meshes from label images using marching cubes [150] and course the resulting triangles meshes using approximated centroidal voronoi diagrams [244] to a fixed number of vertices. These vertices form landmark vectors in the following correspondence problem. For establishing correspondence , we first perform nonrigid registration with a symmetric similarity measure [44] and use the root mean square difference between surfaces as underlying metric [124]. We also employ a multi-scale approach, starting with a coarse mesh and subsequent refinement. As shown by Becker et al. [16], this optimization achieves robust registration even in case of highly variable shapes of the temporal bone. After registration, landmark propagation is performed using shape similarity trees [166] based on the approach discussed in [124] using shortest paths in Jordan centered graphs. Using the resulting corresponding meshes, we create a linear shape model as in [45]. During segmentation, we follow the PASM adaptation of Becker et al. [15]. The approach, thoroughly evaluated for Temporal Bone Anatomy, used image intensity values as image features. It uses a k-nearest-neighbor classifier as fitness function for differentiating voxels lying either on or off the shape model's boundary [108] or inside or outside the shape model's volume [245].

4.3. Summary

This chapter presented an automatic segmentation approach based on Deep Learning initialization with a post processing regularization scheme on Probabilistic Active Shape Models. It motivates the necessity of shape regularization for preoperative surgical planning with two examples from Temporal Bone Surgery and Endovascular Aortic Repair. Finally, it introduced a specialized solution for the tiny and unevenly distributed risk structures of the otobasis.

Preoperative surgical pipelines for robot-assisted interventions greatly benefit from an automated procedure that can relieve surgeons from tedious and tiresome tasks. Such implementations reduce inter-clinician bias and reduce the time necessary for planning, benefiting both clinical output and workflow. The proposed solution is suitable for both applications investigated in this thesis and is applicable to other scenarios where risk structures are representable by Statistical Shape Models. It thus fully meets the requirements of the preoperative surgical pipeline motivated in Chapter 1.

5. Curvature-Constrained Trajectory Planning

Minimally-invasive interventions often operate in narrow regions with highly sensitive structures such as the organs of the hearing sense or blood vessel. These obstacles provide only minimal clearance for surgical instruments. In existing solutions with rigid linear tools, such structures then either block potential paths to the surgical site completely or allow access only from a sub-optimal angle. Flexible instruments following nonlinear trajectories could provide larger distances to risk structures and optimized orientations of tool-tips, thus improving clinical outcomes when compared to existing linear approaches.

In the linear case, trajectory planning usually consists of an optimization procedure based on a predefined set of start and goal states. When planning for novel flexible instruments, algorithms have to consider differential constraints such as the maximum curvature that these tools can achieve during turning. For these problems, Rapidly-exploring Random Trees (RRTs) are currently the most successful solutions when fast computation is a requirement [145, 187, 191]. For novel robot-assisted approaches, new motion planning algorithms thus have to be developed that obey technical as well as clinical constraints. Suitable algorithms should

1. interpolate between predefined positions and directions to allow precise alignment at initial as well as goal configurations.

2. show robustness in complex anatomies.

3. converge quickly to a feasible solution if one exists, so rapid feedback to the clinician is possible.

4. generalize to different instruments such as guidewires, drilling units or flexible needles.
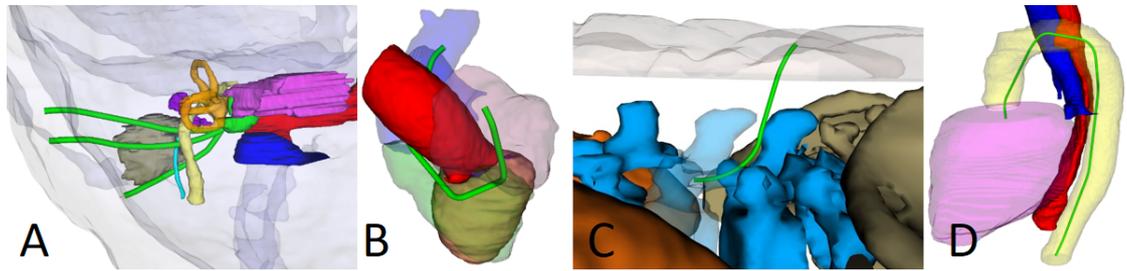
Figure 5.1.: Feasible trajectories for nonlinear access in temporal bone surgery (A), catheter insertion into pulmonary arteries (B), needles in spine biopsy (C) and guidewires approaches for Abdominal Aortic Aneurysm (AAA) (D).

This chapter is based on the following publications I co-authored [73, 74, 76, 77]. My contributions consist of

- a planning formulation suitable for a variety of approaches such as cochlear implantation, needle biopsy, or endovascular access for catheter or guidewires (Figure 5.1).

- two novel Bi-RRTs, one using Circular Arcs with 3D Dubins Paths, and another using cubic Bézier Splines, to find collision-free, curvature constrained trajectories interpolating given positions and directions at start and goal.

- a geometric translation scheme to transform Bézier Spline trajectories to movements along Circular Arcs, rendering these methods suitable for bevel-tip needles, guidewires or nonlinear drilling units.

- an adaptation of sequential convex optimization that works on Bézier Spline trajectories, providing locally optimal solutions with maximum clearance to risk structures.

In this chapter, we first briefly describe the two flexible instruments used in our projects, their technical limitations as well as resulting challenges in trajectory planning. We then define a *strict problem formulation* for precise interpolation between two states in $\mathbb{R}^3 \times \mathbb{S}^2$, i.e. position and direction, in the presence of obstacles. Section Section 5.3.3 presents two steering functions that create curvature-constrained trajectories suitable for flexible instruments. The section then introduces a Bidirectional RRT with two different steering functions that solves the problem formulation. The following two sections extend planning with Bézier Splines by an optimization scheme on convex optimization and an extension to planning in SE(3). Finally, a relaxed problem formulation that allows

deviation of the direction is presented and we show how this extension represents the clinical workflow of a preoperative surgical planning pipeline.

5.1. Problem Description

Flexible instruments are tailored to specific applications and observe unique clinical challenges (Figure 5.1). *Temporal Bone Surgery* operates in a very small and dense environment compared to other setups. Numerous obstacles - nerves, blood vessels and the organs of the hearing and equilibrium senses - limit the free space and thus complicate motion planning. This raises special needs for the extension of the search tree as well as the collision detection. In *endovascular procedures*, trajectories have to be planned through tube-like structures. Motion planning algorithms have to find feasible paths through risk structures instead of around these. Such narrow environments often need tailored algorithms for sufficiently fast planning [270]. *Needle biopsy* acts in environments with highly sensitive regions where precise planning is critical. An example would be liver tumor treatment, where branches of the hepatic artery and portal vein create cluttered obstacles.

This thesis considers two novel robot-assisted applications as examples, creating non-linear access paths in Temporal Bone Surgery (Figure 5.1) and catheter insertion using guidewires for endovascular access.

At the lateral skull base (Figure 5.1, Left), a custom drilling unit creates an access canal from the surface of the skull to a clinical target within the temporal bone. Along its path the robot avoids organs of the hearing and equilibrium senses, blood vessels, cranial nerves and the brain's dura. We consider planning for the prototype design shown in (Figure 5.2, left). Two base cylinders (red) are connected via a flexible inflatable bellow (yellow). Each cylinder has three inflatable pads (cyan) attached in angles of 120°. Finally, an independently controlled drill tip (grey) is attached to the front side. By iteratively inflating all three pads of one cylinder, deflating the others and adjusting the flexible bellow, this continuum robot performs a worm-like movement. Bending is achieved by asymmetric inflation.

For endovascular applications, we envision heart catheterizations, which are the most administered invasive examinations in western countries for diagnostic and therapeutic purposes, and Endovascular Aortic Repair (EVAR) supported by robotically-driven guidewires (Figure 5.1, Right). A clinical implication for the first application would be a
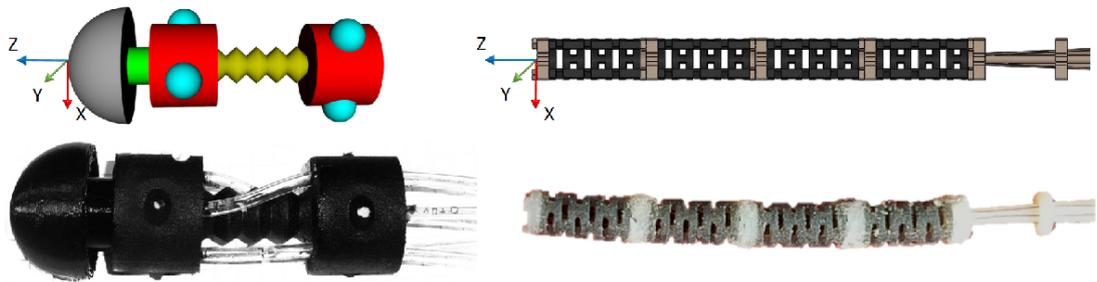
Figure 5.2.: *Left:* Drilling robot for temporal bone surgery. Model (top) and current prototype (bottom) with length = 6.8 cm and diameter 1.5 cm. *Right:* Smart Guide Wire for catheter insertion (model & current prototype with length = 40 mm and diameter = 3.6 mm).

percutaneous transluminal coronary angioplasty (PTCA) due to arteriosclerosis where guidewires are used to position catheters to dilate an occlusion in coronary vessels. Recent research focuses on steerable guidewires based on shape memory alloy (SMA) actuators to facilitate navigation through complex vessel geometries. This is achieved by integrating a spring element (Figure 5.2) where three SMA wires of 50 μm diameter, are fixed at the tip of a guidewire. Due to the shape memory effect, the SMA wires contract when heated up to their transition temperature which is done by applying current. Thus, the guide wire bends when one or two SMA wires are activated. By actuating all wires the spring element contracts and the tip of the guide wire stiffens. Actuating one wire by applying a current of 110 mA results in a bending of the guidewire up to 98°. This guidewire is inserted at the groin and follows the aorta right before the entrance to the left ventricle where it branches off into one of the coronary vessels. In conclusion, trajectories in this scenario thus run through several blood vessels and have to avoid piercing or otherwise harming their boundaries.

We search for sequences of circular arcs (guidewire) and trajectories of Bézier Splines (drilling unit), both with bounded curvature, that interpolate between the given start and goal states (Figure 5.3). Moreover, an automatic procedure requires to continuously re-evaluate the planned path, because navigation errors typically result in slight deviations. Thus, given the latest sensory inputs, a new trajectory has to be replanned from the currently measured pose of the instrument to the target of the intervention. As these are highly sensitive anatomical regions, a robust and clinically acceptable workflow requires quick feedback from a motion planning algorithm whether such a feasible trajectory still exists.

■Jugular vein ■Carotid artery ■Facial nerve ■Chorda tympani ■External auditory canal ■Internal auditory canal ■Cochlea ■Semicircular canals ■Ossicles ■Aorta ■Heart ■Esophagus ■Trachea

Figure 5.3.: **Left:** Bidirectional RRTs grow two search trees - one from the initial region (blue), the other from the goal region (green)- and attempts to connect them in between. A successful connection results in a feasible nonlinear trajectory. **Right:** Catheter insertion into the heart's coronary vessels with the help of guidewires enables easier access. Navigating through the aorta (yellow) is the first challenge during such interventions.

5.2. Strict Problem Formulation in $\mathbb{R}^3 \times \mathbb{S}^2$

In motion planning, parameters and tasks of the application dependent problem are expressed in a specific Problem Formulation [135]. The following Formulation 2 represents the challenging environment described above for a motion planning algorithm that precisely interpolates between given start and goal configurations (or states) in $\mathbb{R}^3 \times \mathbb{S}^2 \equiv \{(x,\omega)|x,\omega \in \mathbb{R}^3, \|\omega\| = 1\}$ while circumventing risk structures and obeying technical and clinical constraints.

Item 1%2 of this Problem Formulation introduce obstacles in $\mathbb{R}^3$ that have to be circumnavigated, as well as the free space, which defines potential positions the instrument can occupy. **Item 3** corresponds to potential positions, e.g. at the body's surface, that serve as entry points for instruments, whereas **Item 4** defines potential targets at the surgical site. For the robots shown in Figure 5.2, we consider the z-Axis in the local coordinate frame of each model as the its *line of view*, and have to match it with the predefined directions at

Formulation 2 Strict Problem Formulation in $\mathbb{R}^3 \times \mathbb{S}^2$

1: Let $O \subset \mathbb{R}^3 \times \mathbb{S}^2$ be the obstacle region, defined by the location of several risk structures $\{\mathcal{R}\}_i \subset \mathbb{R}^3, 0 \leq i \leq N$:
$O := \{q = (x, h) \in \mathbb{R}^3 \times \mathbb{S}^2 | \exists i, 0 \leq i \leq N : x \in \mathcal{R}_i\}$.

2: Let $C_{free} = \{q \in \mathbb{R}^3 \times \mathbb{S}^2 | q \notin O\}$ be the free space of the configuration space.

3: Let $C_I \subset C_{free}$ be the initial region.

4: Let $C_G \subset C_{free}$ be the goal region.

5: Let $d_{max} \in \mathbb{R}^+$ be the safety distance to risk structures and $\kappa_{max} \in \mathbb{R}^+$ the maximum curvature constraint of the instrument.

6: Let $T_{max} \in \mathbb{R}^+$ be the maximum time constraint available for planning.

Task

7: Find a path $\gamma(t) : [0, 1] \rightarrow \mathbb{R}^3 \times \mathbb{S}^2$ satisfying

   (i) $\gamma(0) \in C_I$

   (ii) $\gamma(1) \in C_G$

   (iii) $\forall t \in (0, 1) : \|\gamma''(t)\| < \kappa_{max}$

   (iv) $\forall t \in [0, 1], o \in O : \|\gamma(t) - o\|_{\mathbb{R}^3} > d_{max}$

or report that no path could be found in the available time T_{max}.

---

start and goal states: Initial states should be close to the body's surface normal in order to minimize deviation from the desired trajectory due to forces applied during insertion. For a cochlear implantation, for example, goal states at the round window would represent the optimal insertion angle. Here, work has been done to limit the deviation from the optimum to less than 5° [240]. In a multi-port cochlear implantation, more states could represent different optimal directions for tools such as endoscopes or light sources [230].

The instrument's limitations are then included via **Item 5**: A safety distance d_{max} accounts for navigation errors or heat generation and can be used as a distance constraint in collision detection. Additionally, the maximum turning angle of the tool results in a curvature constraint. **Item 6:** Potential misalignment during navigation requires an intra-interventional replanning step to either provide a new corrected trajectory or stop insertion. Therefore, an algorithm has to be fast enough to provide a smooth intervention which is enforced via a time constraint T_{max}. **Item 7:** A motion planning algorithm for this procedure will then try to find a feasible path in the available time which would result in a trajectory connecting both a start and a goal state (i, ii), observing a maximally

allowed curvature (iii) and last, a necessary distance to risk structures (iv).

Note 1: This formulation remains valid in the case of replanning where the initial region C_I of Item 3 will be set to the current pose of the robot.

Note 2: This formulation extends the problem of trajectory planning in soft tissue for bevel-tip needles, where alignment of instruments [214] and regular fast replanning [187] is needed, by introducing constraints on both start and goal directions. We expect our planners to be useful for this kind of applications as well.

5.3. Motion Planning in $\mathbb{R}^3 \times \mathbb{S}^2$

The major novelty in Formulation 2 lies in the introduction of the two point boundary value problem, represented by start and goal states in $\mathbb{R}^3 \times \mathbb{S}^2$. We investigate two kinds of curvature-constrained trajectories, one based on Bézier Splines and another on Circular Arcs, to solve the problem. Short introductions to these two types are given in Section 5.3.1 and Section 5.3.2. An intuitive way to solve for such trajectories is to use an RRT-Connect [129]. This method, unlike basic RRTs, grows search trees from both the goal and the initial region in an attempt to connect these two. With this strategy more possible connections are available than just those between search tree and goal regions. Thus, successfully finding an access path is more likely. In Section 5.3.3, we propose a suitable version that is both robust and fast. For Bézier Spline trajectories, also present a way to translate these paths to such ones following circular arcs. This allows algorithms that work on Bézier Splines to be useful for applications with instruments characterized by movements along circular arcs.

5.3.1. Curvature constrained Bézier Splines

Sequences of cubic Bézier Splines can be used to form a curvature constrained trajectory interpolating between two given states in $\mathbb{R}^3 \times \mathbb{S}^2$. The basis of our 3D trajectories are 2D Bézier Splines that connect a given start state $(P_b, T_b) \in \mathbb{R}^2 \times \mathbb{S}^1$ with a given end state $(P_e, T_e) \in \mathbb{R}^2 \times \mathbb{S}^1$ (Figure 5.4, left). Such a spline consists of two cubic Bézier spirals, i.e. Bézier curves where the first three control points are colinear (without loss of generality (w.l.o.g.) B_0, B_1, B_2, blue curve). Given an upper bound κ_{max} on the curvature and an arbitrary upper bound on the angle γ, Walton and Meed's theorems [248] give limits on where the control points $B_0 \ldots B_3$ and $E_0 \ldots E_3$ can be placed with respect to the
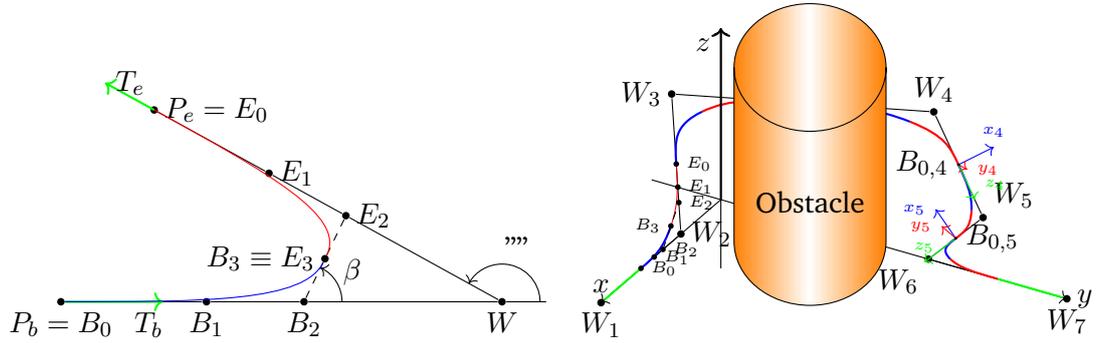
Figure 5.4.: A Bézier spline (left) connecting two points with predefined directions and obeying an upper curvature constraint can be constructed from two Bézier spirals with control points $B_0, \ldots, B_3$ and $E_0, \ldots, E_3$ (blue & red). This strategy can be used (right) to interpolate between two points with given directions by properly placing a series of waypoints in $3D$, where each triple (W_i, W_{i+1}, W_{i+2}) implicitly defines a spline interpolating between the middle of $\overline{W_i W_{i+1}}$ and $\overline{W_{i+1} W_{i+2}}$.

waypoint W to generate a curvature constrained Bézier spline. We refer the reader to [248] for a more detailed description and proof of theorems.

This implicit definition can be extended to 3D (Figure 5.4, right): Suppose we have given three waypoints $W_1, W_2, W_3 \in \mathbb{R}^3$. We then set $P_b = \frac{1}{2} \cdot (W_1 + W_2)$, $T_b = \overrightarrow{P_b W_2}$ and $P_e = \frac{1}{2} \cdot (W_2 + W_3)$, $T_e = \overrightarrow{P_e W_3}$. We can therefore use the above 2D Bézier Spline approach to interpolate between these two states within the plane defined by W_1, W_2, W_3. If a new waypoint W_4 is added, its distance to W_3 and the angle $\angle(\overrightarrow{W_2 W_3}, \overrightarrow{W_3 W_4})$ has to conform with constraints from Walton and Meed's theorems to guarantee the curvature constraint κ_{max}. We refer the reader to [268] for details on the construction and smoothness guarantees.

Using this scheme, we create a series of waypoints $W_1, \ldots, W_N \in \mathbb{R}^3, N > 0$. The resulting series of *Bézier triples* $\{\mathbb{W}_i\}_i, = (W_i, W_{i+1}, W_{i+2}) \in \mathbb{R}^3 \times \mathbb{R}^3 \times \mathbb{R}^3, 0 \leq i \leq N-2$, implicitly defines 2D Bézier Splines of the above fashion within the planes defined by $\mathbb{W}_i$ and interpolating between the centers of $\overline{W_i W_{i+1}}$ and $\overline{W_{i+1} W_{i+2}}$. By respecting the 2D construction scheme these splines conform with the upper bounded curvature κ_{max}. The common tangents at start and end points result in smooth transition from one spline to the next. Overall, this generates a sequence of Bézier Splines that interpolate between

the given start and goal states q_I and q_G.

5.3.2. Circular Arcs

Sequences of circular arcs of bounded curvature can also be used to form a trajectory interpolating between two given states in $\mathbb{R}^3 \times \mathbb{S}^2$. An application for such movement is for example given by the nonholonomic modeling of Bevel-tip needles described by Webster III et al. [254]. Following the approach of Duan et al. [59], this movement can be expressed as two incremental twists ω_1, ω_2 in the Lie-Algebra $\mathfrak{se}(3)$ of SE(3) $= \mathbb{R}^3 \times$ SO(3) (see [167] for an introduction to SE(3) $= \mathbb{R}^3 \times$ SO(3), $\mathfrak{se}(3)$). Given poses $X_i, X_{i+1} \in$ SE(3), we then reach the latter via

$$X_{i+1} = \exp(\hat{\xi}_2) \cdot \exp(\hat{\xi}_1) \cdot X_i.$$

Now we set (Figure 5.5)

$$\xi_1 = (0, 0, 0, 0, 0, \phi)^\top, \tag{5.1}$$

$$\xi_2 = (0, 0, l/r, l, 0, 0)^\top, \tag{5.2}$$

where l describes the length of the arc, r its radius and ϕ the rotation to align the x-axis of local coordinate system at X_i with the one at X_{i+1}. In short, we move from one pose to the next via a rotation ξ_1 about the local z-Axis followed by an incremental push ξ_2 along the line of view while rotating around the local x-Axis.

While the above formulation gives a nice representation for needle propagation, it does not solve the two point Boundary Value Problem (BVP). However, we can adopt the method of Hota and Ghose [113] for numerically solving the Dubins Path problem in 3D. Using an approach for a Dubins CSC Path, their mathematical ansatz results in a 5×5 nonlinear system of equations that can be efficiently solved using, for example, a forward Euler scheme. Combining both methods, a propagation along circular arcs together with the solving of a two point boundary value problem is possible in $\mathbb{R}^3 \times \mathbb{S}^2$.

5.3.3. An RRT-connect for the Strict Problem Formulation

The motion planning problem described by Formulation 2 can be efficiently solved using our custom RRT-Connect [74]. It uses either Bézier Splines or Circular Arc motions and can be described as follows (Algorithm 4): two trees $\mathcal{T}_I, \mathcal{T}_G$ are initialized with states of
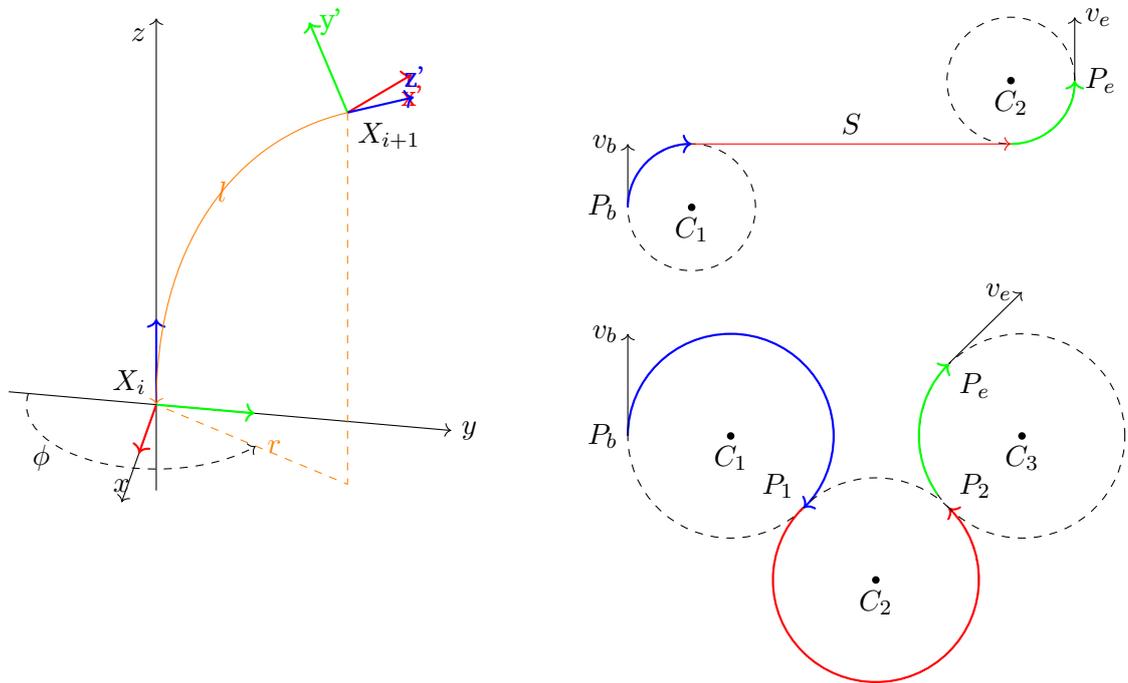
Figure 5.5.: Left: Needle movement according to Patil et al. [187] by rotating an instrument along the line of view z and a push forward along a circular arc. Right: The two types of 2D Dubins paths, CSC (curve, straight line, curve) and CCC, that interpolate between positions (P_b, P_e) and directions (v_b, v_e). For the first type, an equivalent exists in 3D to connect two states in $\mathbb{R}^3 \times \mathbb{S}^2$ following the ansatz in [113].

the initial and the goal region, respectively. Both trees are iteratively extended until either the maximally allowed time T_{max} is reached or the graphs are connected successfully. In each iteration the two search trees take turn in the following procedure: a random state is drawn from the free space C_{free}. Then, the nearest neighbors to the current tree are computed according to a previously defined distance function. For each of these configurations the local steering function computes an expansion towards the random state. If no collision with obstacles occurs along this path the state is added to the tree. Last, the algorithm tries to connect both trees according to the state space's constraints (in our case the path needs to be two times continuously differentiable). If both trees are connected within the given time threshold T_{max} the resulting path is returned. Otherwise,

Algorithm 4 κ-RRT-Connect

Input: $q_I \in C_I$, $q_G \in C_G$
Output: a set of states, $\{q_j\}_j, j >= 2$
Parameters: step size Δt, goal bias ρ, search time T_{max}, maximum number of children n_c, nearest neighbor radius r, cone radius c_r, cone height c_h

```
 1: 𝒯_I ← initial_states()
 2: 𝒯_G ← goal_states()
 3: while time_spend() < T_max and not_connected(𝒯_I, 𝒯_G) do
 4:     q_rand ← sample_state(C_free)
 5:     𝒯, 𝒯̃ ← alternate(𝒯_I, 𝒯_G)
 6:     {q}_k ← nearest_ball(r, 𝒯, q_rand)
 7:     for all q_near in {q}_k do
 8:         q_next ← steer(q_near, q_rand, Δt)
 9:         if collision_free(q_near, q_next) then
10:             extend_tree(𝒯, q_near, q_next)
11:             q_other ← inside_cone(q_next, 𝒯̃, c_r, c_h)
12:             if q_other then
13:                 attempt_connection(q_next, q_other)
14:             end if
15:         end if
16:     end for
17: end while
```

---

failure is reported.

The individual steps in Algorithm 4 (lines 4,6,8,12) are then as follows:

sample_state: Sampling in $\mathbb{R}^3 \times \mathbb{S}^2$ would require solving a two point boundary value problem, i.e. matching both location and orientation at the random state. This is not possible with either of the two strategies presented in sections Section 5.3.1 and Section 5.3.2. Instead, a state is merely sampled in $\mathbb{R}^3$ and the direction is implicitly defined according to the respective method.

nearest_ball: The nearest neighbor function and its underlying metric have significant impact on the time efficiency and the theoretical properties of the algorithm. For curvature constrained instruments the Euclidean metric does not represent a good approximation on the actual distance. On the other hand, the computation of a more complex metric like the reachable set of a particular state [224] can be very time consuming. As the main

interest in this application lies in the fast computation of a feasible path, we return the nearest neighbors within a ball of predefined radius r.

steer: For Bézier Splines we use the strategy presented in section Section 5.3.1 by Yang et al. [267]. For Circular Arc motions we adopt the strategy of Patil et al. [187].

attempt_connection: The original RRT-Connect does not address nonholonomic planning and considers the trees connected if both trees meet at the random sample. This approach would result in a discontinuous orientation at the connecting state as we sample only in $\mathbb{R}^3$ and do not enforce a specific orientation. Instead, a two point boundary value problem has to be solved in our approach to match both position and orientation:

First, we search for a state of the other tree in the vicinity of q_{next}. Specifically, we check if a state lies within a cone $C \equiv C(c_h, c_r)$ with apex located at q_{next} and direction given by the current line of view. If such a state is found, we try to connect these two:

If using Circular Arcs, we connect two corresponding states by solving the 3D Dubins problem with the geometric approach presented in [112]. A similar method is used in [191]. Both papers address the computational complexity of their approach. However, our C**++**implementation requires on average only 45 microseconds to solve the underlying nonlinear system of equations which makes it suitable for fast computation.

If the algorithm is based on Bézier Splines, we iteratively use the local steering function to steer from q_{next} to its counterpart and vice versa. For each iteration we get a triple $(W_j^I, W_{j+1}^I, W_{j+2}^I), j \geq 0$, of $\mathcal{T}_I$ and a triple $(W_k^G, W_{k+1}^G, W_{k+2}^G), k \geq 0$, of $\mathcal{T}_G$. Then, the two triples $(W_{j+1}^I, W_{j+2}^I, W_{k+2}^G)$ and $(W_{k+1}^G, W_{k+2}^G, W_{j+2}^I)$ define two new Bézier Splines that would connect the trees. For each such resulting pairs of triples we check for feasibility of the curvature constraint and their underlying trajectory for collision. If both are satisfied, the connection attempt is successful. This procedure is repeated until either the interpolation criterion of the Bézier-Spline is satisfied during an iteration or the states missed each other and thus no connection is possible.

5.3.4. Translation to Circular Arcs

While we showed that the use of circular arcs and Dubins Paths was feasible for temporal bone surgery, experiments for steering through vascular structures showed weak performance. On the other hand, steering with Bézier Splines proved to be effective in various different environments such as the temporal bone, vascular structures of aorta and heart as well as through liver tissue avoiding vessels [73].
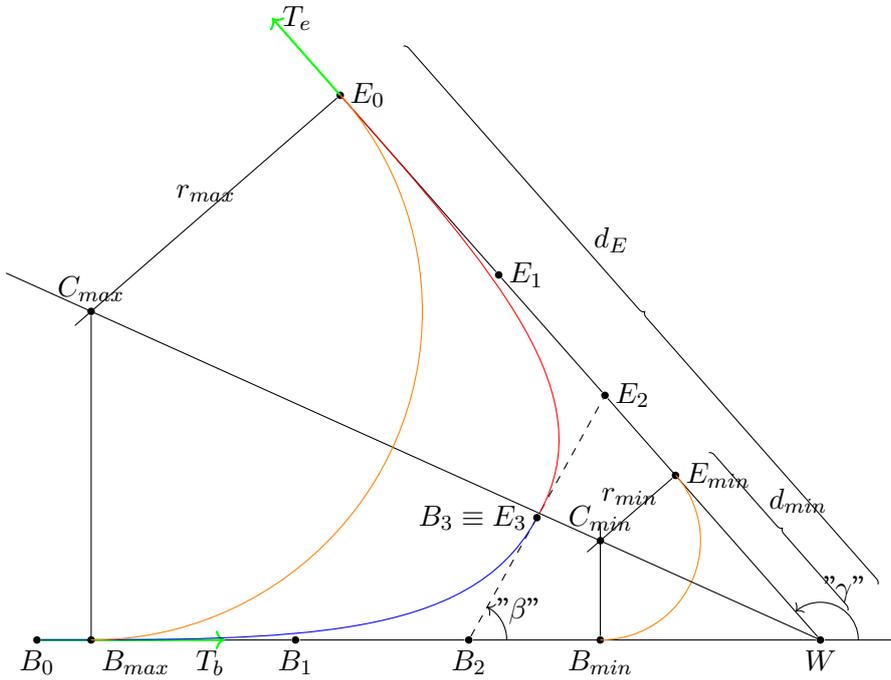
Figure 5.6.: Translation from Bézier Splines (red/blue) to circular arcs (orange).

We proposed a hybrid planning scheme as a general solution for circular arc motions that is both robust and safe [72]: An RRT-connect with cubic Bézier Splines as a steering function to quickly solve for curvature constrained trajectories, followed by a transformation of the resulting paths to such that follow circular arcs. The implicitly defined cubic Bézier Splines provide a fast and robust way to interpolate along a curvature constrained trajectory. Their use circumvents computing Dubins Paths in 3D, which directly solve the two point BVP for circular movements but are computationally expensive. They still are close enough to being of circular shape to obtain collision-free trajectories.

This transition works as follows: A successful search of the Spline-Based RRT-connect returns a series of waypoints $\{W_i\}_i, 0 \leq i \leq N$ in $\mathbb{R}^3$. Its corresponding series of Bézier triples $\{\mathbb{W}_i\}_i, 0 \leq i \leq N - 2$, defines a smooth curvature constrained trajectory using cubic Bézier Splines. Consequently, instead of using Bézier Splines, we can search for other implicitly defined trajectories. If all of these new transitions are collision free, the resulting path is feasible and interpolates between the given initial and goal states q_I, q_G.

We therefore explore geometric translations from our Bézier triples $\{\mathbb{W}_i\}_i$ to circular arcs (Figure 5.6). As shown in [248], a Bézier spline consists of two Bézier spirals with the first observing a continuously increasing (blue) and the second having a continuously decreasing (red) curvature. Due to this varying curvature, we can always find circular arcs with minimal and maximal radius ($r_{min}, r_{max} \in \mathbb{R}$) within the triangle B_0WE_0 that interpolate between the pairs (B_0, T_b) and (E_0, T_e).

W.l.o.g, we assume that $\overline{B_0W}$ is longer than $\overline{E_0W}$. Then, the intersection C_{max} of the normals at E_0 and B_{max} is the center of a circle with radius r_{max}. Due to first increasing (blue) and then decreasing (red) curvature, the underlying arc has a lower curvature than the original spline and interpolates, together with the line $\overline{B_0B_{max}}$, smoothly between B_0 and E_0. For the same reason, a circular arc of minimally allowed radius $r_{min} = 1/\kappa_{max}$ exists that smoothly translates from a trajectory at B_0 in direction T_b to E_0 in direction T_b. Here, the transition points B_{min} and E_{min} are given by the Intercept Theorem with

$$d_{min} = d_E \cdot \frac{r_{min}}{r_{max}}.$$

Using this relationship, we iterate over each set $\{\mathbb{W}_i\}_i$ created by a successful call to the Spline-Based RRT-connect. For each triple we create a maximal circle (C_{max}, r_{max}) and a minimal circle (C_{min}, r_{min}) and check for collision. If for all triples $\mathbb{W}_i$ at least one of the circles is collision free, an implicit conversion to circular arcs is possible.

5.4. Relaxed Problem Formulation in $\mathbb{R}^3 \times \mathbb{S}^2$

Having multiple start and goal regions, e.g. in the case of a start region representing positions at the bodies' surface (Figure 5.7), can significantly reduce a Bi-RRT's computational efficiency. In such cases, the use of a simple RRT is favorable to generate a first list of feasible solutions, connecting individual pairs of start and goal states $(q_I^i, q_G^i) \in C_I \times C_G, i \geq 0$. However, RRTs are not suitable to precisely interpolate between two states, i.e. solving Formulation 2, which motivates the following formulation for an approximated problem. Using these initial solutions, one can then go back to the Bi-RRT case for precise rapid planning under Formulation 2.

Planning is again done in SE(3) = $\mathbb{R}^3 \times$ SO(3), to account for the instrument's position ($\mathbb{R}^3$) and its orientation (SO(3)), the latter represented by quaternions. The configuration space $C \subset$ SE(3) = $\mathbb{R}^3 \times$ SO(3) is then divided into an obstacle region $C_{Obs} \subset C$ and the free space $C_{free} = \{q \in C | q \notin C_{Obs}\}$. Valid start and goal states of trajectories
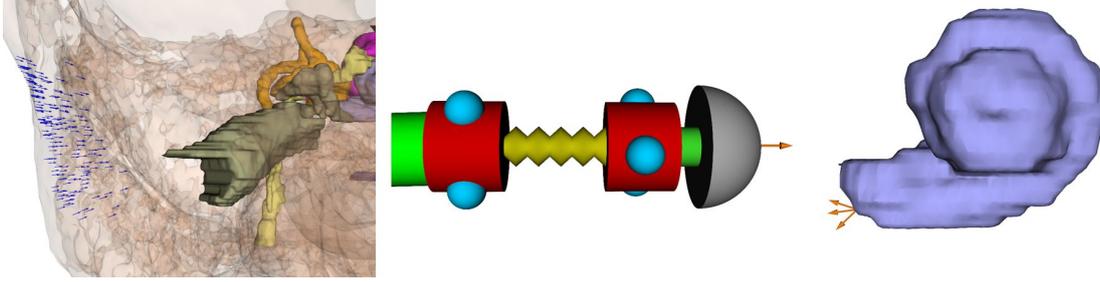
Figure 5.7.: Different initial and goal regions for cochlear implantation. *(Left)* Multiple initial states at the skull's surface (blue arrows). *(Middle)* A single initial state pointing in the robot's current direction. *(Right)* Three precise goal states for a multi-port cochlear access.

are defined via subsets of C_{free}: Given a set $M \subset C_{free}$ and the quaternion metric $\rho : \mathrm{SO}(3) \times \mathrm{SO}(3) \to \mathbb{R}$ (e.g. [135])

$$\rho(h_1, h_2) = \min\{\rho_s(h_1, h_2), \rho_s(h_1, -h_2)\}$$
$$\rho_s(h_1, h_2) = cos^{-1}(a_1 a_2 + b_1 b_2 + c_1 c_2 + d_1 d_2), \tag{5.3}$$

we define the *approximated set* $\tilde{M}(\epsilon, \phi)$ of M, $\epsilon \in \mathbb{R}^+$, $\phi \in [0, \pi]$, as

$$\tilde{M}(\epsilon, \phi) = \{q(x, h) \in C_{free} \mid \exists \, \hat{q}(y, g) \in M : \|x - y\|_{\mathbb{R}^3} < \epsilon, \rho(h, g) < \phi\}. \tag{5.4}$$

Given a number of *clinically ideal* configurations for trajectories, such sets resemble *clinically acceptable* states that lie in the vicinity of the position and observe only a small perturbation in orientation. Further constraints are given by the minimum distance d_{min} to risk structures, the instrument's curvature constraint κ_{max} and the time T_{max}, in which a feedback is required. The problem formulation for an individual intervention is then expressed as:

Figure 5.7 shows examples of initial and goal regions, M_I, M_G, for a multi-port cochlear access. For preoperative planning of potential access canals, a surgeon manually defines a set of initial states at the surface of the lateral skull base (blue arrows, left image). Three goal states are defined at the round window of the cochlea as the ideal end points of the three canals for multi-port access (orange arrows, right image). Once the intervention starts, replanning of a feasible trajectory might be necessary. Here, the current pose of the drilling unit replaces the initial region (middle image, orange arrow) and one of the three goal states is fixed as the single target state.

Formulation 3 Relaxed Problem Formulation in $\mathbb{R}^3 \times \mathbb{S}^2$

1: Let $O \subset \mathbb{R}^3 \times \mathbb{S}^2$ be the obstacle region, defined by the location of several risk structures $\{\mathcal{R}\}_i \subset \mathbb{R}^3, 0 \leq i \leq N$:
   $O := \{q = (x, h) \in \mathbb{R}^3 \times \mathbb{S}^2 | \exists i, 0 \leq i \leq N : x \in \mathcal{R}_i\}.$
2: Let $C_{free} = \{q \in \mathbb{R}^3 \times \mathbb{S}^2 | q \notin O\}$ be the free space of the configuration space.
3: Let $M_I \subset C_{free}, \epsilon_I \in \mathbb{R}^+, \phi_I \in [0, \pi]$.
4: Let $M_G \subset C_{free}, \epsilon_G \in \mathbb{R}^+, \phi_G \in [0, \pi]$.
5: Let $d_{min} \in \mathbb{R}^+, \kappa_{max} \in \mathbb{R}^{0+}, T_{max} \in \mathbb{R}^+$.

Task
6: Find a path $\gamma(t) : [0, 1] \to \mathbb{R}^3 \times \mathbb{S}^2$ satisfying

   (i) $\gamma(0) \in \tilde{M}_I(\epsilon_I, \phi_I)$

   (ii) $\gamma(1) \in \tilde{M}_G(\epsilon_G, \phi_G)$

   (iii) $\forall t \in (0, 1) : \|\gamma''(t)\| < \kappa_{max}$

   (iv) $\forall t \in [0, 1], o \in C_{Obs} : \|\gamma(t) - o\|_{\mathbb{R}^3} > d_{min}$

   or report that no path could be found in the available time T_{max}.

Note: This definition extends the strict formulation Formulation 2 to individual approximations at both start and goal. With $\kappa_{max} = 0$ it is suitable for linear approaches. With $\phi_I = \pi$ or $\phi_G = \pi$ it falls back to more general cases where the direction at only one end point of the trajectory is relevant.

5.5. Motion Planning in SE(3)

While $\mathbb{R}^3 \times \mathbb{S}^2$ well describes the clinically relevant directions that an instrument should point along, robot configurations are often given in the Lie-Group $SE(3) = \mathbb{R}^3 \times SO(3)$ to describe its pose, i.e. position and orientation. Such a representation is especially helpful, when movement of the instrument can be modeled in the Lie-Algebra $\mathfrak{se}(3)$ [167]. This section reflects the possibility of planning using Bézier Splines, translating the results to circular arcs and further to trajectories in SE (Figure 5.8).

For each triple (W_i, W_{i+1}, W_{i+2}) we therefore define a local coordinate system at $B_{0,i} = 1/2 \cdot (W_i + W_{i+1})$ with axis $z_i = \overrightarrow{W_i W_{i+1}}, y_i = z_i \times z_{i+1}, x_i = z_i \times y_i$ (Figure 5.4 right). We then use two incremental twists $\omega_1, \omega_2 \in \mathfrak{se}(3)$ in the Lie-Algebra [167] of SE(3) to
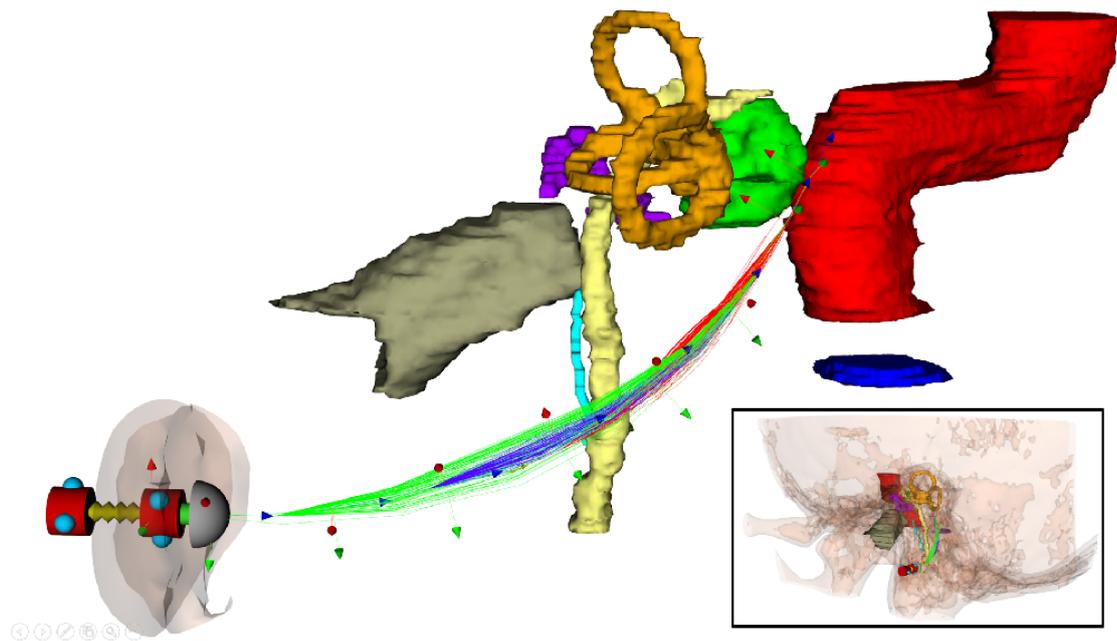
Figure 5.8.: Temporal bone scenario with surface models from real patient data. A minimally-invasive intervention requires the drilling unit to create a curvature constrained access canal through the mastoid bone (empty space) while avoiding risk structures (colored). Colored lines show replanned trajectories to the internal auditory canal (pink) along circular arcs.

model movement along a circular arc. Similar to the approach for needle movement introduced in section Section 5.3.2, we set

$$\xi_1 = (0, 0, 0, 0, 0, \phi_i)^\top, \tag{5.5}$$

$$\xi_2 = (0, 0, l_i/r_i, l_i, 0, 0)^\top, \tag{5.6}$$

where l_i describes the length of the arc, r_i its radius and ϕ_i the rotation to align the x-axis of the local coordinate system at $B_{0,i}$ with the one at $B_{0,i+1}$. Given poses $X_i, X_{i+1} \in \mathrm{SE}(3)$ at $B_{0,i}$ and $B_{0,i+1}$, we then reach the latter via

$$X_{i+1} = \exp(\hat{\xi}_2) \cdot \exp(\hat{\xi}_1) \cdot X_i.$$

Note: Using this representation, our method conforms with planning for steerable needles [187], which are used in clinical scenarios such as liver [234] or lung nodule biopsy [84].

5.6. Optimization for Bézier Splines

Trajectories computed by RRTs or Bi-RRTs naturally observe twists and closeness to risk structures due to the stochastic nature of the algorithms. We proposed a convex optimization approach featuring clearance-optimized Bézier Splines that respects the strict formulation Formulation 2 while at the same time optimizing distance to obstacles [77].

We use our RRT-connect [74] with Bézier Splines as steering function to find an initial solution that interpolates between q_S and q_G while staying away from obstacles. To extract a locally optimal solution we use the computed waypoints as optimization variables in a Sequential Convex Optimization (SCO)-formulation. The convex optimization solver then rearranges these waypoints such that the implicitly defined Bézier Splines feature larger clearance to obstacles.

Bézier Spline RRT-connect: The Bézier Spline RRT-connect of section Section 5.3.3 provides fast and accurate initial solutions for curvature constrained trajectories around obstacles. A computed path consists of a series of waypoints $\mathcal{W} \equiv \{W_i\}_i \subset \mathbb{R}^3, 0 \leq i \leq N_\mathcal{W}$ (Figure 5.10). Each triple $(W_{j-1}, W_j, W_{j+1}), 1 \leq j \leq N_\mathcal{S} \equiv N_\mathcal{W} - 1$, implicitly defines a Bézier Spline S_j, a combination of two cubic Bézier Spirals, that respects the curvature constraint κ_{max}.

■ Jugular vein ■ Carotid artery ■ Facial nerve ■ Chorda tympani ■ External auditory canal ■ Internal auditory canal ■ Cochlea ■ Semicircular canals ■ Ossicles
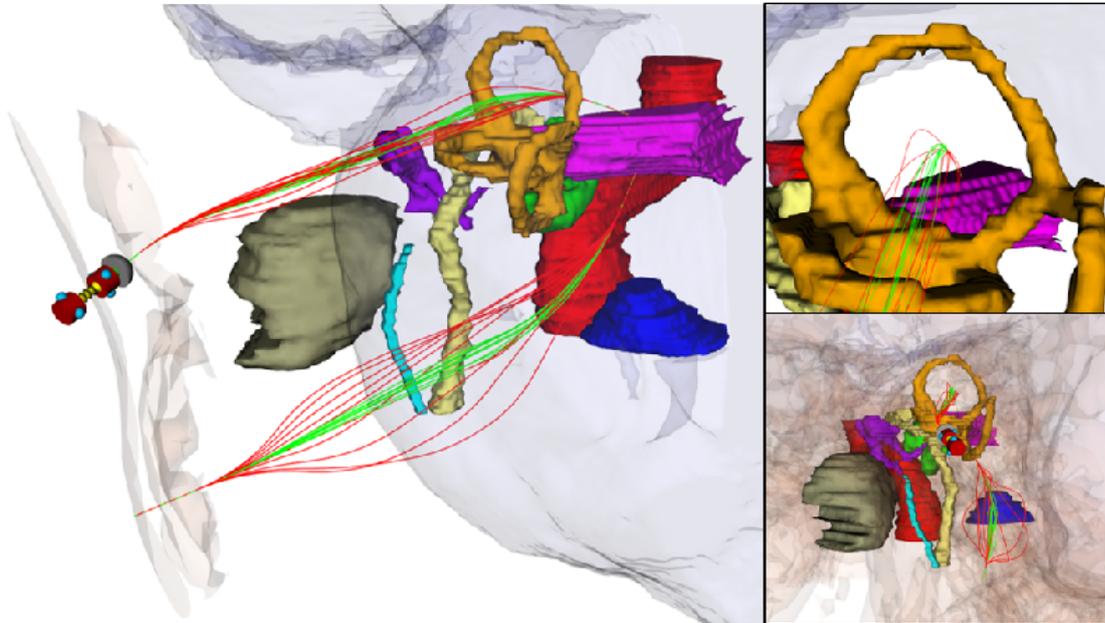
Figure 5.9.: A 3D surface representation of the temporal bone. Trajectories for a micro robot to the internal auditory canal via the superior semicircular canal (top) and retrolabyrinthine region (bottom). Paths locally optimized with SCO (green) achieve larger clearance to risk structures than those initially planned with RRTs (red).

Clearance Optimization: We then define a constrained optimization objective over these set of waypoints $\mathcal{W} \subset \mathbb{R}^3$ that minimizes a cost function f while satisfying a set of N_E equality and N_I inequality constraints h_i, g_j, i.e.

$$\begin{aligned} \underset{\mathcal{W}}{\text{minimize}} \quad & f(\mathcal{W}) \\ \text{subject to} \quad & h_i(\mathcal{W}) = 0, \quad i = 0, \dots, N_E \\ & g_j(\mathcal{W}) \leq 0, \quad j = 0, \dots, N_I. \end{aligned}$$

Efficient numerical solvers require each of these functions to be linear or quadratic convex functions [23]. In our case, these functions are, however, nonconvex and we thus consider an approximation rather than the original problem. By formulating adequate convex
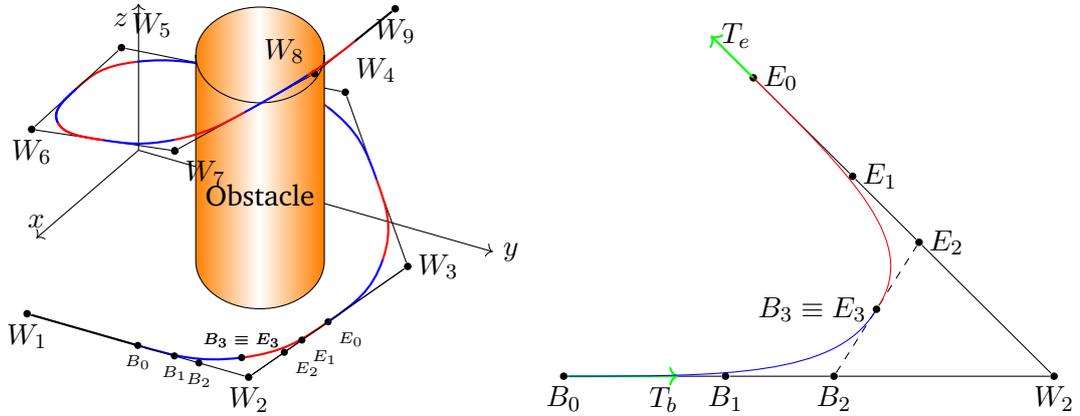
Figure 5.10.: *Left:* The RRT-connect is used to compute a series of waypoints $\mathcal{W} = \{W_1, \ldots, W_9\}$. Each triple of three subsequent waypoints defines a Bézier Spline (combination of one blue and one red path). *Right:* A Bézier Spline is a combination of two cubic Bézier Spirals, i.e., Bézier Curves with three colinear sample points (e.g. $B_0, \ldots, B_3$). Each spline then interpolates between the middle of subsequent waypoints, e.g. $B_0 = 1/2 \cdot (W_1 + W_2)$ and $E_0 = 1/2 \cdot (W_2 + W_3)$ on the left.

quadratic versions, convexifications, of the respective cost and constraint functions f, h_i and g_j, we derive an approximation of our original problem that is suitable for numerical solvers.

In particular, our cost function measures the quality of trajectories by a weighted sum of its length f_Γ and distance to obstacles $f_{i,O}, 0 \leq i \leq N_S$, i.e.

$$f = \alpha_\Gamma f_\Gamma + \sum_i \alpha_O f_{i,O},$$

with $\alpha_\Gamma, \alpha_O \in \mathbb{R}^{0+}$. We approximate the length as

$$f_\Gamma = \sum_{i=0}^{N_{\mathcal{W}}-1} \sum_{k=\{x,y,z\}} |W_{i,k} - W_{i+1,k}|^2.$$

Similar to [214], we measure distance to obstacles via linearized signed distances

$$\mathrm{sd}_{\mathcal{S}O}(\mathbf{x}) = \mathrm{sd}_{\mathcal{S}O}(\mathbf{x_0}) + \mathbf{n}(\mathbf{x_0})^\top (\mathbf{x} - \mathbf{x_0}),$$
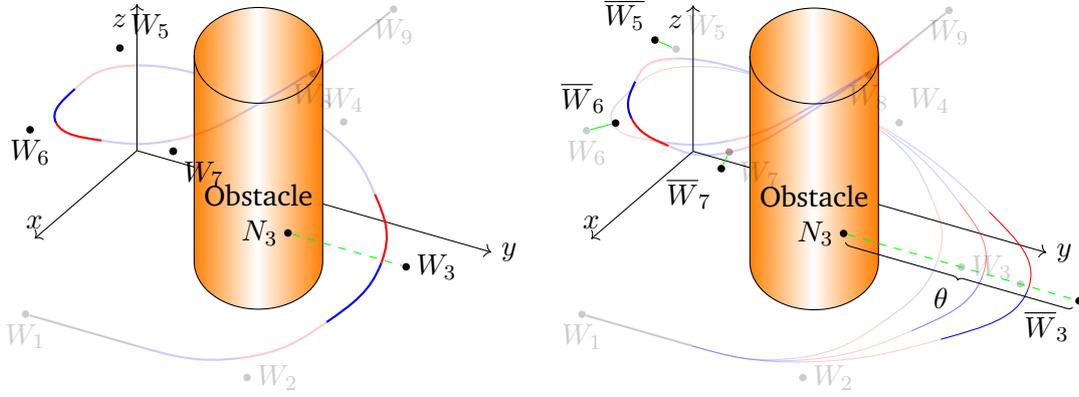
Figure 5.11.: One sample iteration of SCO. Spline $S_3 \equiv S_3(W_2, W_3, W_4)$ (opaque) is close enough to the obstacle such that the convexified cost function $f_{3,O}$ tries to enforce a distance of threshold θ from the nearest neighbor N_3 by translating W_3 several times. Spline S_6 violates the curvature constraint, resulting in constraint $g_{6,\kappa}$ translating corresponding waypoints W_5, W_6, W_7 to a smoother configuration $\overline{W}_5, \overline{W}_6, \overline{W}_7$.

where $\mathrm{sd}_{SO}(\mathbf{x_0})$ is the signed distance from a spline S to the nearest obstacle O, $\mathbf{x_0} \in O$ is a point on the surface and $\mathbf{n}$ the obstacle's normal at $\mathbf{x_0}$. The point $\mathbf{x_0}$ stays fixed within an inner convex iteration sequence and is computed by a nearest neighbor search for $\mathbf{x}$. The weighted convexified clearance cost functions $f_{i,O}$ then try to match a distance threshold $\theta \in \mathbb{R}^+$ on the central waypoint W_i of a spline S_i, i.e.

$$f_{i,O} = \theta - \mathrm{sd}_{S_i O}(W_i).$$

We add constraints to guarantee the upper curvature bound κ_{max}, the safety distance d_{min} and position and direction at q_S, q_G. To ensure that the upper bound κ_{max} on the curvature and the minimal distance d_{min} to obstacles stay valid during the optimization we introduce for each spline constraint functions $g_{i,\kappa}$ and $g_{i,O}, 0 \leq i \leq N_S$. Each curvature constraint $g_{i,\kappa}$ smooths its spline, if the upper bound κ_{max} is exceeded, by slightly translating the three corresponding waypoints. With $P_i = 1/2(W_{i-1} + W_{i+1})$ and $Q_i = 1/2(W_i + P_i)$,

new waypoints $\overline{W}_{i-1}, \overline{W}_i, \overline{W}_{i+1}$ are given as

$$\overline{W}_{i-1} = Q_i + (W_{i-1} - P_i),$$
$$\overline{W}_i = \frac{1}{2}(W_i + Q_i),$$
$$\overline{W}_{i+1} = Q_i + (W_{i+1} - P_i).$$

A constraint $g_{i,\kappa}$ then penalizes the difference between the original positions and these translations, i.e.

$$g_{i,\kappa} = \sum_{j=-1}^{1} \sum_{k=\{x,y,z\}} |W_{i+j,k} - \overline{W}_{i+j,k}|^2.$$

The $g_{i,O}$ are defined like the distance cost functions via signed distances. Note, that we have to set $\theta >> d_{min}$ to achieve significant improvement on clearance. Finally, we enforce that position and direction at start and goal stay the same by disallowing any changes in position of the first and last two waypoints.

We then use SCO [214] to solve for a locally optimal solution given the above costs and constraints. This iterative method repeatedly creates convexified functions based on the current solution and makes progress on this approximated objective. We refer the reader to [214] for a detailed description and show in Figure 5.11 one iteration of the proposed clearance optimization method as an example.

5.7. Summary

This chapter described the clinical and technical constraints of the trajectory planning step. It translated the requirements of the precise interpolation between start and goal states into a strict Formulation 2. The interactive workflow of the preoperative surgical pipeline (Figure 3.1) was represented by a relaxed Formulation 3 . The novel challenge - quickly solving the two point boundary value problem of interpolating in $\mathbb{R}^3 \times \mathbb{S}^2$ in the presence of obstacles - is then solved by a combination of several methods. First, a Bi-RRT on Bézier Splines solves for multiple collision-free trajectories. These are further optimized regarding distance to risk structures using a sequential convex optimization scheme, where constraints on position, direction, curvature and length are approximated by linear and quadratic functions. For applications, where motions along Circular Arcs are required, the Bézier Spline trajectories are translated by a geometric solution to a sequence of linear and circular motions.

The presented formulations together represent clinical workflow and technical constraints. Once the start and goal states are defined, the proposed successive trajectory planning step can be executed automatically and results in a set of feasible and locally optimal solutions. Using, for example, Pareto front optimization [102], a surgeon could then chose between different trajectories depending on competing constraints such as distance to individual risk structures or length of the paths.

6. Experimental Results

The main task of a preoperative surgical pipeline for robot-assisted surgery is the provision of feasible trajectories for the underlying instrument. A thorough evaluation should therefore quantitatively measure desirable properties of automated computation of risk structures and trajectories. Suitable segmentation algorithms should extract necessary parts of organs such that subsequent trajectory planning is feasible. Proper motion planning algorithms should be robust, fast and precise enough for the investigated surgery. Finally, a general planning approach could be applied to a diverse set of anatomies.

This chapter is based on our publications [72, 73, 74, 75, 76, 77]. First, the used datasets (Section 6.1) and metrics (Section 6.2) are introduced. Then, a broad overview of the published open source framework (Section 6.3) is given. Finally, Section 6.4 describes the setup of real as well as synthetic anatomies.

We first show the feasibility of our proposed interactive pipeline on two different applications: Temporal Bone Surgery and Endovascular Aortic Repair. In our functional evaluations (Section 6.5), we show that

- our shape regularized segmentation results in anatomically plausible shapes while achieving Dice and Hausdorff scores similar to state-of-the-art solutions.

- planning on segmented surface meshes was almost as successful as planning on expert annotations.

In Section 6.6, we apply our relaxed Formulation 3 and planning methods to several more applications to show the general applicability. Here, we consider

- a linear approach for cochlear implantation.

- a nonlinear approach for liver and spine biopsy.

- a pulmonary access via the right heart chambers using again the nonlinear approach.

Finally, we perform a thorough robustness analysis of our multi-step planning approach consisting of Bi-RRTs, convex optimization and translation from Bézier Splines to Circular Arcs (Section 6.7). In particular, we

- successively show the robust performance of our optimized planning approach by

  1. outperforming state-of-the-art Rapidly-exploring Random Trees (RRTs) with our Bi-RRT counterparts on the strict Formulation 2.

  2. providing locally optimal solutions, suitable for clinical experiments, with our sequential convex optimization scheme on Bézier Splines.

  3. planning for instruments such as needles and guidewires by successfully applying our translation method from Bézier Splines to Circular Arc.

- extend our novel in silico evaluation on synthetic anatomies to achieve statistically significant performance in scarce clinical datasets.

All experiments were carried out on a system with an Intel Core i5-6500 CPU @ 3.20 GHz and 32,0 GB RAM. Training of the U-net models was done on a Geforce GTX 1080 Ti.

6.1. Datasets

For our experiments we mainly used 3 different datasets.

Dataset 1 An in-house dataset of 42 temporal bone CT images (Siemens Somatom). The acquired volumes had an average resolution of $0.2 \times 0.2 \times 0.4\,\text{mm}^3$. For each 3D image, corresponding ground truth data of external auditory canal (EAC) and internal auditory canal (IAC), facial nerve (FN) and chorda tympani (Chorda), internal carotid artery (ICA) and jugular vein (JV), ossicles (Oss), semicircular canals (SCC) and cochlea (Cochlea) was available. Further labels for the skull's surface and brain's dura were available in 24 of these label images. A representative example is shown in Figure 6.1.

Dataset 2 The training dataset of 40 CT images from the SegTHOR challenge [190]. The acquired volumes had an average resolution of $0.43 \times 0.43 \times 0.58\,\text{mm}^3$. The segmented Organs at Risk (OAR) included the visible aorta, esophagus, trachea and heart. A representative example is shown in Figure 6.2.

■ Jugular vein ■ Carotid artery ■ Facial nerve ■ Chorda tympani ■ External auditory canal ■ Internal auditory canal ■ Cochlea ■ Semicircular canals ■ Ossicles
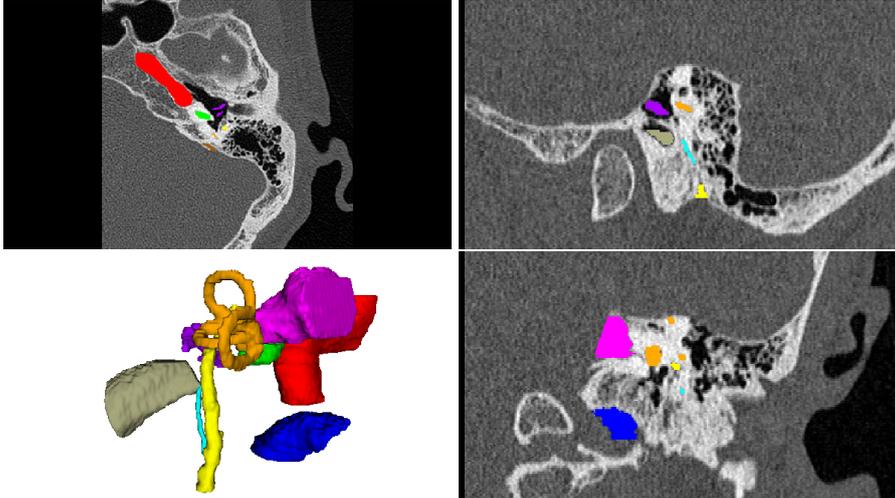
Figure 6.1.: Representative CT data of the temporal bone with 3D view of risk structures.

■ Aorta ■ Heart ■ Esophagus ■ Trachea
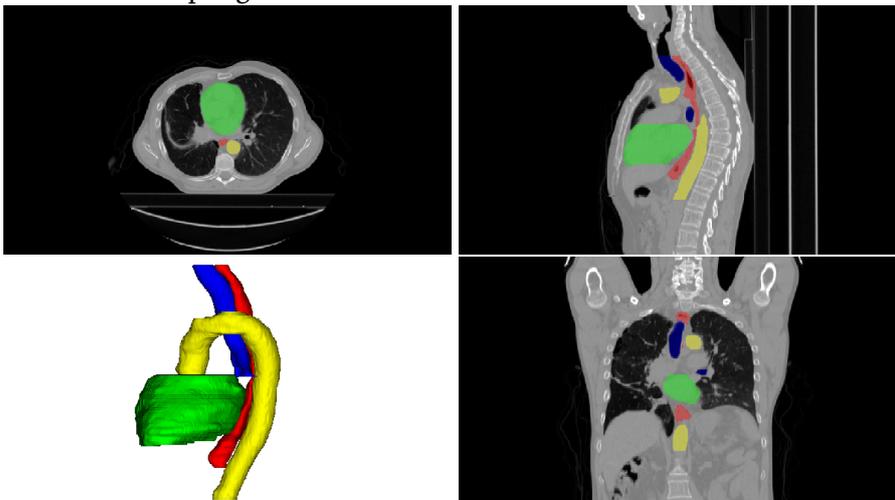
Figure 6.2.: Representative chest CT image of the SegTHOR challenge with 3D view of risk structures.
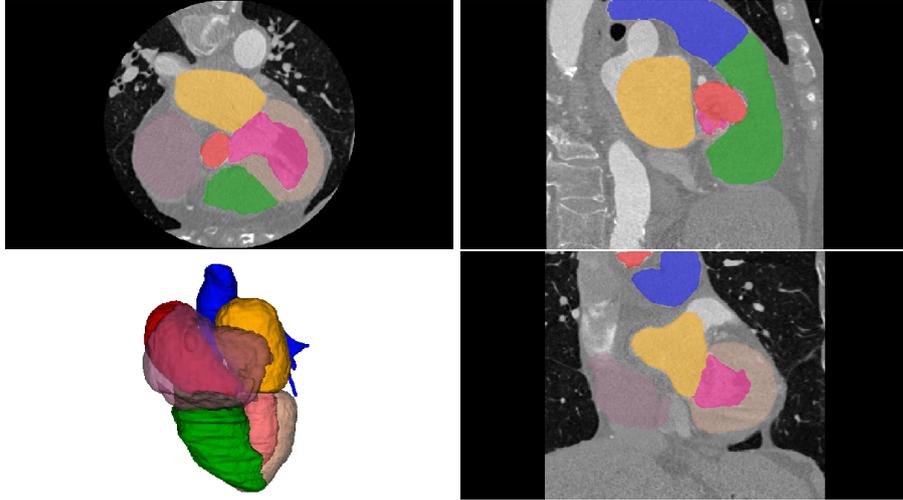
Figure 6.3.: Representative chest CT image of the MMWHS challenge with 3D view of risk structures.

Dataset 3   The two training CT datasets of totally 20 images from the MMWHS challenge [68]. The acquired volumes had an average resolution of $1.0 \times 1.0 \times 2.35\,\mathrm{mm}^3$. Expert annotations of organs showed Left Ventricle (LV) and Right Ventricle (RV), Left Atrium and Right Atrium, Pulmonary Artery (PA), Ascending Aorta, and Myocardium (MYO) (Figure 6.3).

We subdivided each of these datasets into two equally sized subsets. Two instances of our complete segmentation method (U-Nets and PASM models) were then created. Each instance was trained on only one subset and evaluated on the held out subset, thereby realizing cross validation.

6.2. Metrics

We compare segmentation quality in terms of Dice score and Hausdorff Distance (HD). Consider two label images $Y, \hat{Y} \subset \mathbb{L}^{N \times M}, \mathbb{L} \coloneqq \{0, N_L\}$ with N_L positive labels for an individual dataset's list of risk structures. The Dice score then measures the similarity

between the two label images as

$$\text{Dice} : \mathbb{L}^{N \times M} \times \mathbb{L}^{N \times M} \to [0, 1]$$
$$\text{Dice}(X, Y) = \frac{2|X \cap Y|}{|X||Y|}.$$

This is an indicator for the average volume overlap between expert annotation and segmentation results. While it is useful for quantifying competing methods, the range for a good or satisfying value depends on the individual risk structure's size, intra- and inter-clinician variability and the application.

The Hausdorff Distance (HD) gives the maximum symmetric surface distance between the two sets by

$$\text{HD} : \mathbb{L}^{N \times M} \times \mathbb{L}^{N \times M} \to \mathbb{R}$$
$$\text{HD}(X, Y) = \max \left\{ \sup_{x \in X} \inf_{y \in Y} d(x, y), \sup_{y \in Y} \inf_{x \in X} d(x, y) \right\}.$$

In addition to Dice scores, the Hausdorff function serves as a significant indicator for capturing the boundary of an organ.

6.3. Open Source Repository

We made the C++ and python code of our preoperative surgical planning framework publicly available [1] so that the research community can benefit from these methods and reproduce our experiments. This environment supports the comparison of methods for individual sub tasks, the execution of clinical studies with the use of an interactive GUI for surgeons and finally provides transparency and reproducibility for our work.

The repository itself consists of a modular framework for 3D data processing (using ITK [276], VTK [213], ACVD [244] and tensorflow [160]), trajectory planning (using OMPL [231]) and convex optimization (under Gurobi [100]). The integrated GUI based on Qt offers visual-interactive support for the generation of image processing pipelines, the setup of problem formulations (Formulation 2, Formulation 3) and analysis of performance of motion planning algorithms from Chapter 5. Finally, it includes the code to run our experiments in [72, 73, 75, 77].

---

[1] https://github.com/MECLabTUDA/MUKNO

6.4. Planning in Real & Synthetic Anatomies

Computation of feasible trajectories and subsequent optimization, i.e. execution of the motion planning algorithms of Chapter 5, requires to define the parameter set of either of the two formulations Formulation 2 or Formulation 3. This in turn requires the placement of start and goal states for the initial and goal regions C_I, C_Q, which takes place in the 3D surface representation extracted from CT label images. For all experiments, we followed the following procedure to generate the planning setup for both real and synthetic anatomies. In the upcoming sections, we refer to these basic setups and add minor modifications if needed.

Real Anatomies   For each CT image a corresponding label image with segmentations of risk structures was available. We extracted surface meshes using Marching Cubes [150] and refined those to uniformly dense meshes using approximated centroidal voronoi diagrams [244]. These meshes were then used for interactive placement of start and goal regions in Formulation 2 and Formulation 3 as well as during the collision detection calls in Algorithm 2 and Algorithm 4. The obstacle region C_{Obs} was defined as the set of all vertices of these meshes. For each anatomy we then manually placed initial and goal states q_I, q_G in the environment:

For *Temporal Bone Surgery* we considered three different clinical scenarios: Planning of (non-)linear access canals for a cochlear implantation (Cochlea-Access, Fig. 6.4) and computing nonlinear trajectories for a drilling unit in vestibular schwannoma removal. For the latter, we considered two different approaches both ending at the internal auditory canal: one through the superior semicircular canal (SSC-Access), the other through the retrolabyrinthine region [230] (RL-Access). In each dataset and for each of the three applications (RL-, SSC-, Cochlea-Access) we placed one state within the temporal bone and one state on the skull's surface to define the regions C_I and C_G of the strict Formulation 2. Start states were positioned at the bottom of the internal auditory canal, at its top and finally at the round window for the RL-, SSC- and Cochlea-Access, respectively. This resembled a potential position of an acoustic neuroma (RL-, SSC-Access) or the entry point of the electrode in a cochlear implant (Cochlea-Access). The directions (resembling the instrument's *line of view*) at these goal states were defined as a compromise between the respective organ's normal at this position and a direction towards the skull's surface. Last, three states were placed on the skull with orientations approximately orthogonal to its surface which served as start states for the individual access paths. For the relaxed Formulation 3, we allowed deviations of the direction at the single goal state q_G via the
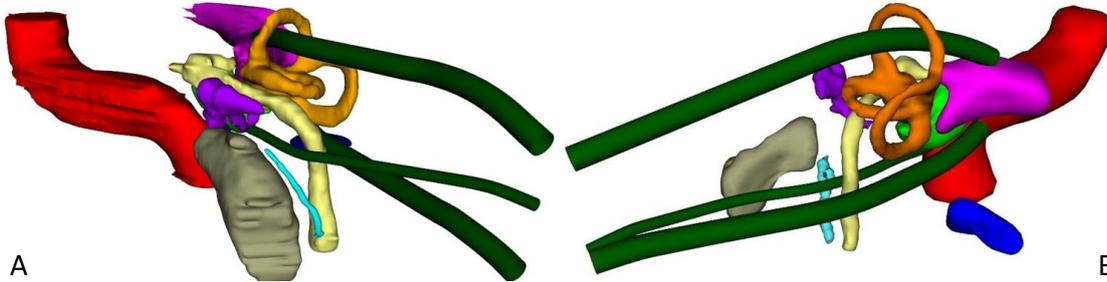
Figure 6.4.: Examples of the access paths (Cochlea-/SSC-/RL-Access) for real (**A**) and synthetic (**B**) anatomies.

parameter $\phi_G > 0$ and replaced the single state c_I with a set of states on the skull by interactively drawing a polygon on its surface and extracting the corresponding vertices inside to define M_G. The directions for each of these states were defined by placing an anchor point at the facial recess (Cochlea-Access), in between the superior semicircular canal (SSC) (SSC-Access), or within the retrolabyrinthine region anterior to the facial nerve (RL-Access).

For *Endovascular Aortic Repair* and *Pulmonary Artery Access* we created single start and goal states q_I, q_G. Planning for those scenarios was done using the strict formulation, i.e. with no deviation from the direction. For the first scenario, using the SegTHOR dataset, we placed q_I within the lower part of the descending aorta pointing upwards along the medial axis and q_G inferior to the ascending aorta (Figure 6.5) pointing to the heart. For the second scenario, we placed q_I within the right atrium close to the superior vena cava pointing towards the tricuspid valve and q_G within the visible part of the pulmonary artery pointing along its centerline away from the pulmonary valve. This resembles a typical course of a catheter in pulmonary artery catheterization within the risk structures labeled in the MMWHS dataset.

Synthetic Anatomies   For evaluation of motion planning algorithms on temporal bone surgery, we also used synthetically altered versions of real environments, including risk structures as well as start and goal regions. To this purpose, we first created linear statistical shape models [45] of the manually segmented organs. For each new synthetic anatomy, one of the real anatomies was chosen randomly to serve as an atlas, including
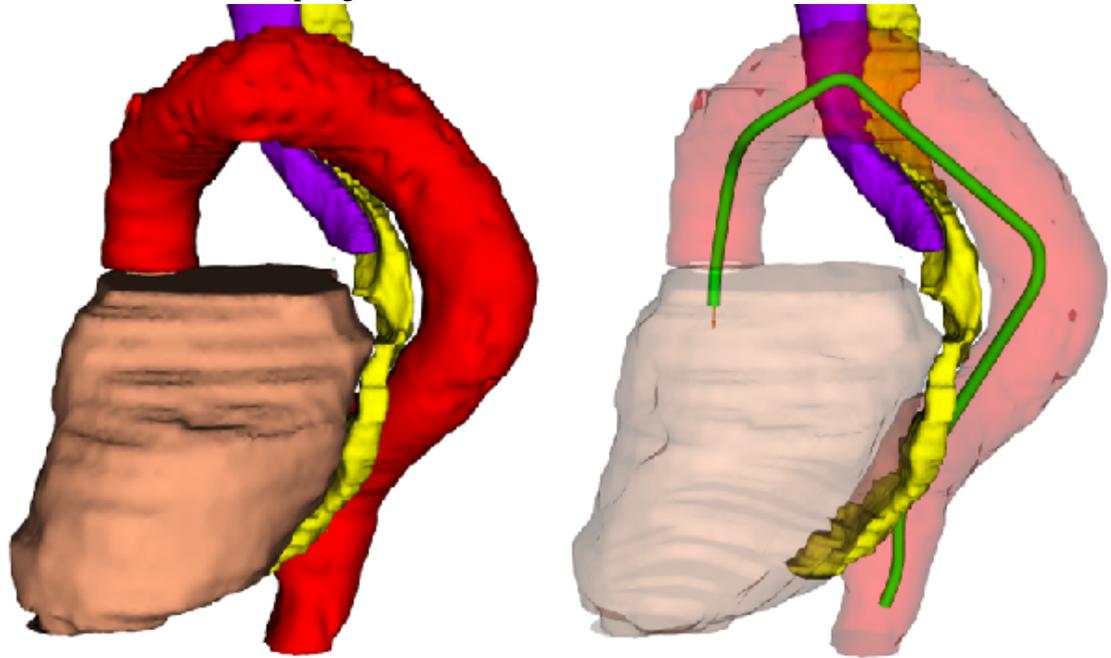
Figure 6.5.: A trajectory through the aorta to the heart for a SegThor sample with 3D surface representations of aorta, heart, esophagus and trachea.

its risk structures and its goal regions. For each new synthetic anatomy, random variations of the individual statistical shape models' modes were computed by sampling the corresponding eigenvalues between ± 1.0 times of their standard deviation. The resulting model was then rigidly registered with the reference atlas to replace the original structure with its altered variant (Figure 6.4). For the respective goal states we used the ones in the atlas. The start states required a new strategy for positioning, as their original pose in the atlas might be invalid. Thus, new start states were placed above/below the center of mass of the internal auditory canal (SSC-/RL-Access) and below the center of mass of the cochlea (Cochlea-Access). For orientation, individual reference points $P_{ref} \in \mathbb{R}^3$ were computed: For the RL-Access slightly inferior to the lower side of the bounding box of the facial nerve; for the SSC-Access above the center of mass of the semicircular canals and for the Cochlea-Access in the center of mass of the chorda tympani. The start states were then oriented so that the z-axis of the local coordinate frame points to the respective reference point.

6.5. Functional Evaluation

This section evaluates the preoperative surgical pipeline presented in Chapter 3 by applying the shape regularized U-Net for segmentation of risk structures and performing subsequent planning of trajectories using the Bi-RRT on Bézier Splines. Thus, this resembles a functional evaluation of a real clinical workflow by planning on the results of segmentation methods rather than ground truth label images.

Specifically, we evaluate the usability of segmentation algorithms for planning access canals to the cochlea and the internal auditory canal on 24 CT datasets of real patients. We show that our shape regularized U-Net approach achieves similar results to the existing semi-automatic method by Becker et al. [15] in terms of Dice but provides more accurate organ shapes for the subsequent trajectory planning step. We then generalize these results by successfully applying our method on a planning problem based on the publicly available data of the SegTHOR challenge.

6.5.1. Shape-Regularized Segmentation

For both scenarios (Temporal Bone, Endovascular Access), we split the respective datasets in two equally sized subsets (first & second half) to achieve two-fold cross validation. U-Nets and Probabilistic Active Shape Model (PASM)s were trained on one subset. Predictions and shape model iterations were performed on the other.

Experimental Setup for Temporal Bone: We first trained PASM models on the two datasets. We then manually selected, according to [15], three points on the medial axis of the nerves (at the start, end and in the middle of the object) and bounding boxes of the remaining structures within the 24 CT datasets. These were used to initialize the PASM models, resulting in 24 volume segmentations I^S based on the semi-automatic method. Next, the U-Nets of our proposed methodology were trained. We then predicted an initial segmentation I^U, which resulted in cluttered structures shown in Figure 6.6. Afterwards, we computed surface meshes from these initial U-Net results, rigidly registered the mean shape of the respective PASM models against them and performed the iterative segmentation of PASM, resulting in an automatically regularized I^A. In summary, we computed three segmentations for each risk structure and each of the 24 datasets: one from the semi-automatic method, one from Deep Learning initialization and one from our shape regularized U-Net approach. Our proposed segmentation procedure needed on

■ Jugular vein ■ Carotid artery ■ Facial nerve ■ Chorda tympani ■ External auditory canal ■ Internal auditory canal ■ Cochlea ■ Semicircular canals ■ Ossicles
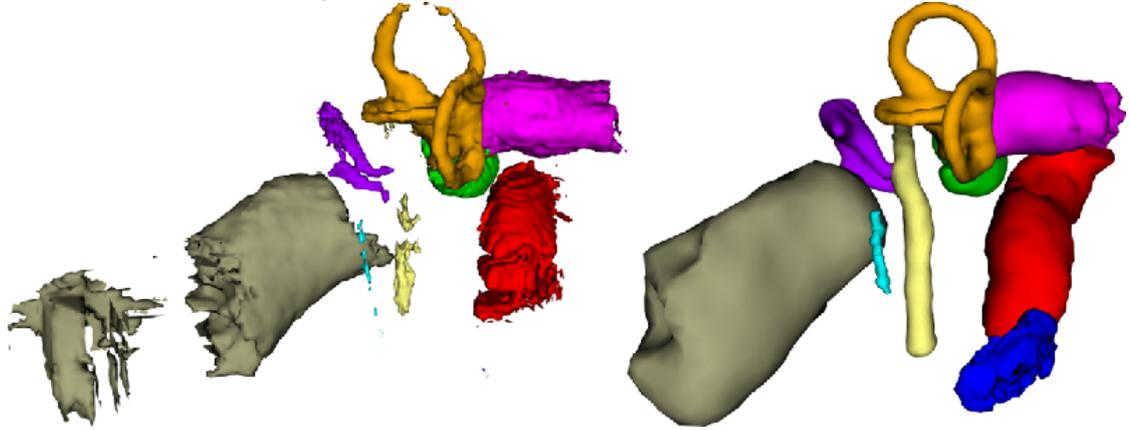
Figure 6.6.: Representative dataset with fragmented structures and regularized counterparts.

average about 4 minutes ($15.5\,\text{s}$ for each of the 6 nets + $16,5\,\text{s}$ for each of the 9 PASMs).

Results: We compared the two segmentation algorithms (manual PASM, shape regularization) as well as the results after initialization (U-Net). As quality metric we used the Dice coefficient, which measures the overlap between ground truth and segmentation algorithm output. Figure 6.7 shows a quantitative analysis of the computed Dice coefficients for each of the risk structures. Best results were achieved by all methods for the ICA, the cochlea, the ossicles and the SSC, as they are usually clearly visible in CT images. Lesser Dice scores were achieved for the jugular vein, IAC and EAC. Segmentation of the two nerves provided the least Dice scores.

However, many of the organs of the temporal bone do not end - within the CT images - at a clearly visible boundary (see Figure 3.4). For example, the IAC (pink) extends on the left to the brain, the EAC extends on the right outside of the skull and the jugular vein is centered around the bulb that is visible in the CT scan. On one of their boundaries, these structures therefore continue and have similar texture and gray values like surrounding tissue such that clinicians stopped their expert annotations quite arbitrarily. Regarding this issue, both semi-automatic and our solution actually provided good alignment to the respective structure's boundaries, as shown in Figure 3.4. A visual inspection (Figure 6.8, left) showed that similar reasons apply for both nerves. While Dice scores give a quantitative
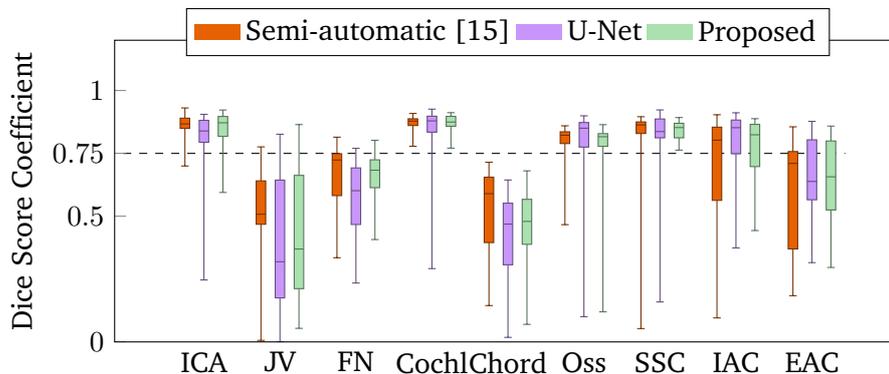
Figure 6.7.: Box-Plots of Dice coefficients from all 24 datasets for the three segmentation
techniques and all obstacles.

measurement of the global overlap, a segmentation algorithm does not necessarily provide
bad result for preoperative planning even with a low Dice score. As the right image in
Figure 6.8 shows, a more useful metric would weight regions around the planning area
higher than parts farther away. By considering the success rate of motion planning
algorithms and the computed path's closeness to planning on ground truth annotations,
the following downstream evaluation of the entire pipeline provides more meaningful
metrics.

Experimental Setup for Endovascular Access: Similarly to the Temporal Bone experiments, we trained PASM models and U-Nets on the two datasets (first and second half
of SegTHOR training data) for two-fold cross validation. We again computed an initial
segmentation $I^{\mathcal{U}}$ via a slice-by-slice U-Net approach and used the results to properly place
the mean shape of the PASM's models within the CT data. Contrary to the Temporal Bone
scenarios, this was done using nonrigid registration because the structures were large
enough and would not degenerate. An iterative step of the PASM models then produced
a final segmentation $I^{\mathcal{A}}$. For the two outputs $I^{\mathcal{U}}$ and $I^{\mathcal{A}}$, we then compared Dice scores
and Hausdorff distances.

Results: Table 6.1 shows Dice and Hausdorff distances (HD) for esophagus, heart, trachea
and aorta in the *SegTHOR* dataset. While dice is comparable, our approach achieves for
most anatomies significant improvement on Hausdorff distance. The qualitative example
in Figure 6.9 shows that a combination of fragmentation and isolated regions is often
responsible for bad quality in the U-Net approach whereas our shape regularized solution
provides realistic and accurate segmentation for planning.
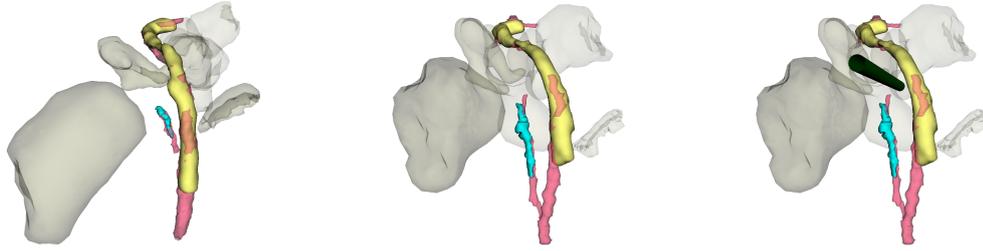
Figure 6.8.: Low Dice coefficient example of facial nerve (yellow) and chorda tympani (cyan). Ground truth annotations in light red. Left: Higher Dice sample (0.61, 0.45) where planning was infeasible. Middle: Lower Dice sample (0.55, 0.44), where planning was possible. Right: The lower dice sample with computed linear trajectory.

Table 6.1.: Results on Dice and HD with mean(SD) for SegTHOR.

	Dice		Hausdorff	
	U-Net	Ours	U-Net	Ours
Esophagus	0.46(0.18)	**0.55(0.18)**	23.91(11.08)	**21.92(8.97)**
Heart	0.90(0.03)	**0.91(0.03)**	37.05(32.82)	**16.33(5.18)**
Trachea	0.84(0.09)	**0.87(0.09)**	23.08(11.62)	**19.19(9.61)**
Aorta	0.80(0.09)	**0.86(0.08)**	26.46(9.86)	**20.86(9.68)**

6.5.2. Downstream Analysis

In the 3D environment represented by extracted surface meshes we computed trajectories for two different scenarios: Planning nonlinear trajectories for a drilling unit in vestibular schwannoma removal and for a guidewire in endovascular aortic access. According to the strong formulation for nonlinear trajectory planning in minimally-invasive surgery Formulation 2, four main items have to be defined for the underlying general motion planning formulation:

- start and goals states $q_I, q_G \in \mathbb{R}^3 \times \mathbb{S}^2$,

- a safety distance $d_{max} \in \mathbb{R}^+$ to obstacles that combines the instrument's size and potential navigation errors,

- a curvature constraint $\kappa_{max} \in \mathbb{R}^{0+}$ based on the instrument.

■ Aorta   ■ Heart   ■ Esophagus   ■ Trachea
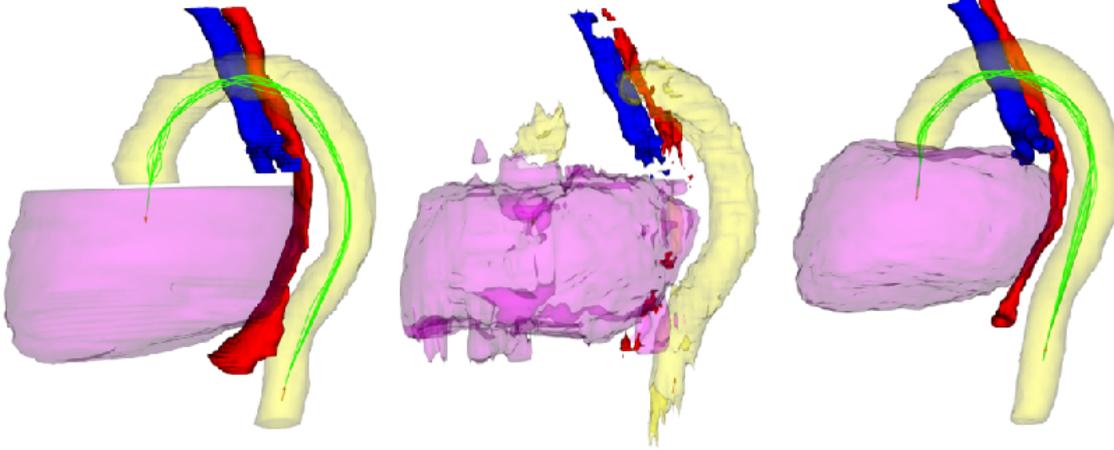
Figure 6.9.: Qualitative results on a SegThor sample (Ground Truth, U-Net & Ours). Contrary to U-Net, our shape regularized approach provided shapes for feasible planning.

Table 6.2.: Access canals' major obstacles and planning parameters.

	Obstacles	$d_{min}(mm)$	$\epsilon_I, \phi_I, \epsilon_G, \phi_G$
SSC-Acces	IAC, SSC, FN	1.5	$0.0, 0.0, 0°, 0°$
RL-Acces	IAC, SSC, FN, JV		

Experimental Setup for Temporal Bone: We try to find nonlinear trajectories to the internal auditory canal, a clinical application being vestibular schwannoma removal. We consider two alternatives with the same parameter setup (Table 6.2): an access via the superior semicircular canal (Figure 6.10, right top) and an access via the retrolabyrinthine region (Figure 6.10, right bottom). The maximum curvature constraint κ_{max} is set to our custom drilling robot's limit of $0.05 \ mm^{-1}$. We use a safety margin of 0.5 mm to the robot's radius of 1.0 mm which results in a safety distance $d_{min} = 1.5$ mm to obstacles. We then proceed to define one specific start and one specific goal state with $\epsilon_I = \phi_I = \epsilon_G = \phi_G = 0$ and utilize Bidirectional Rapidly-exploring Random Trees with cubic Bézier-Splines as steering method [74] to plan for feasible curvature constrained trajectories.

The segmentations served as obstacles during collision detection. Here, we had three different references for collision detection available: (A) ground truth annotations, (B) semi-automatic segmentation results and (C) label images from shape regularization.
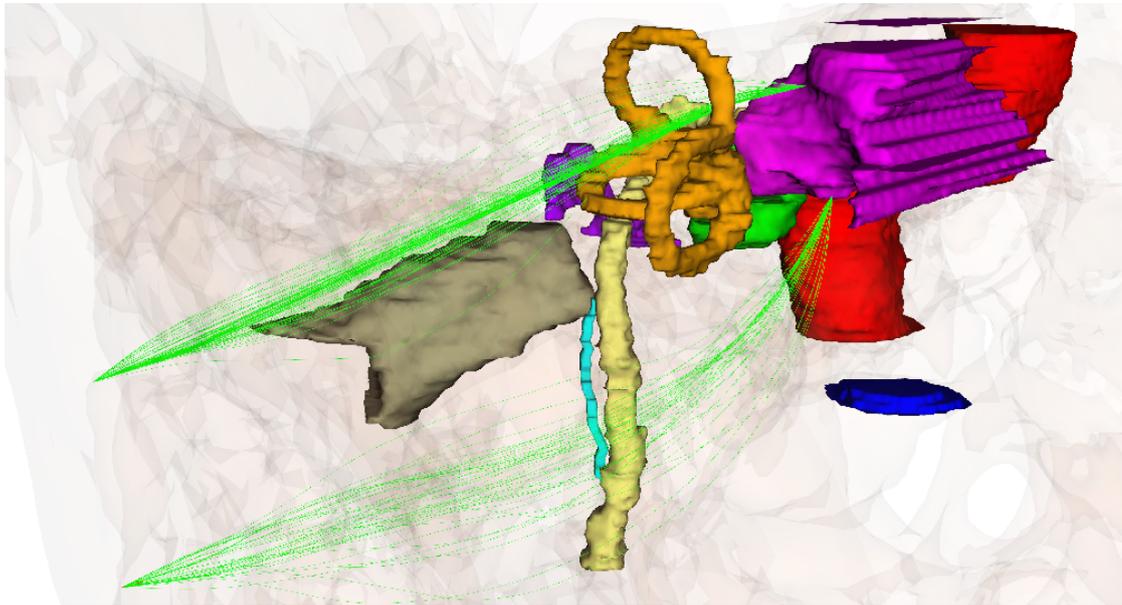
Figure 6.10.: Nonlinear trajectories to the IAC that interpolate given start and target states.

For each of these references we computed trajectories for each of the two scenarios (SSC-Access, RL-Access) along with these path's true distances to risk structures, i.e based on ground truth annotations. This procedure therefore quantified overall planning quality, clinically most relevant for CAI applications.

Results: Table 6.3 shows the results for all three scenarios. For the *SSC-Access* we see from Table 6.3, that in all cases planning with ground truth annotations and our proposed method found collision-free paths. The semi-automatic solution however provided only in 66% cases feasible trajectories. Figure 6.11 shows a representative example for the SSC-Access: Both segmentation methods provided accurate extraction of the two main risk structures (semicircular canals (orange) and facial nerve (cyan)) along the way, respecting the required safety distance of 1.5 mm. However, due to a large oversegmentation of the internal auditory canal, the proper setup of the goal state was possible only in a third of the semi-automatic cases. Figure 6.11 also shows that our proposed method undersegments the IAC towards the medial part. However, this did not negatively affect the planning pipeline.

RL-Access: Figure 6.12 shows a representative example for the RL-Access: Like in the pre-

Table 6.3.: Success rate for planning, mean minimal distance to risk structures for the three experiments (safety distance as reference) as well as failure rate.

	success rate		mean safety distance		failure rate	
	SSC	RL	SSC (1.5)	RL (1.5)	SSC	RL
ground-truth	1.0	1.0	2.19	2.35	-	-
semi-automatic	0.66	0.66	2.17	2.60	0.0	0.0
ours	1.0	1.0	2.16	2.42	0.0	0.1
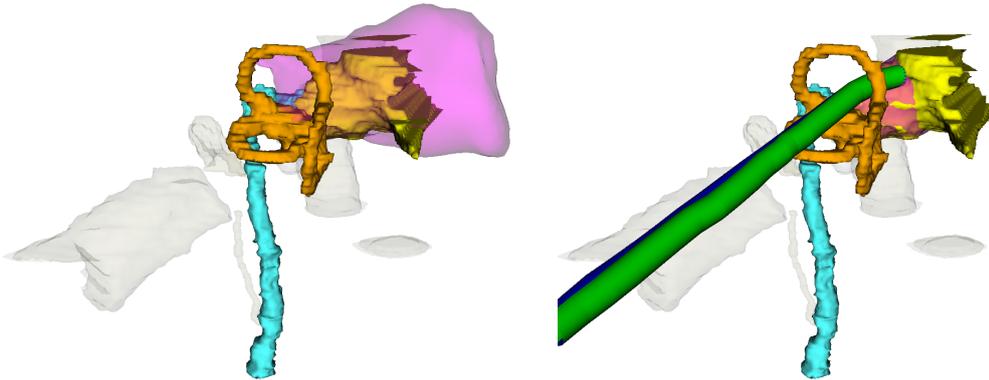
Figure 6.11.: Segmented IAC (pink) over the ground truth (yellow) for nonlinear trajectories to the IAC. Contrary to the semi-automatic solution (left), successful planning through the SSC was only feasible with our proposed approach (right).

vious case, an accurate segmentation of the IAC was necessary for a setup of proper goal states. This time, we ignored misalignment for this structure and only required precise segmentation of the two main structures along the way: facial nerve and the jugular vein. Consulting once again Table 6.3, our proposed method outperforms the semi-automatic version in terms of success rate in collision-free planning. The required safety distance was met with an average minimum distance of $2.6 \, \text{mm}$ and $2.4 \, \text{mm}$, respectively. In 10% of the cases however the automatic solution provided paths below the safety threshold due to an inaccurate segmentation of the jugular vein.

Experimental Setup for Endovascular Access: We used the three sets $M^{GT}, M^{\mathcal{U}}, M^{\mathcal{P}}$ of surfaces meshes. First, the interactive setup of the motion planning formulation in a preoperative pipeline was performed manually based on ground truth structures M^{GT}.
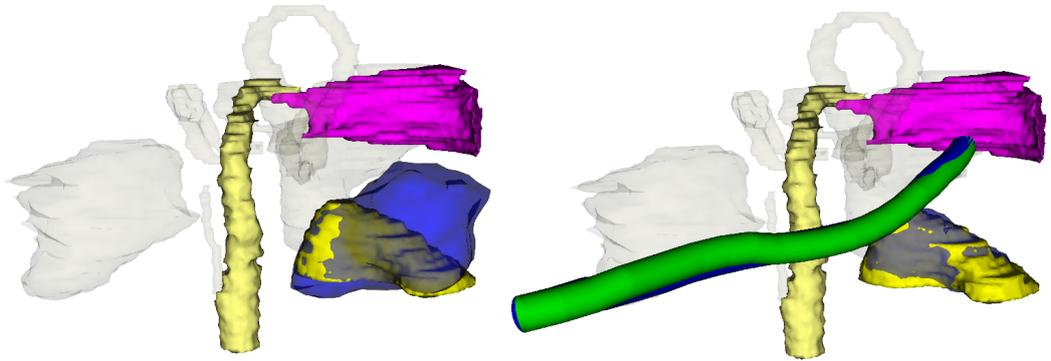
Figure 6.12.: Transparent segmented jugular vein (blue) over the ground truth (yellow) for nonlinear trajectories to the IAC. Contrary to the semi-automatic solution (left), successful planning through the retrolabyrinthine region was achieved with our proposed approach (right).

Then, we again computed access paths using the Bi-RRT on Bézier Splines three times in a row: Once using obstacles based on M^{GT}, once on $M^{\mathcal{U}}$ and once on $M^{\mathcal{P}}$, resulting in three sets of trajectories T^{GT}, $T^{\mathcal{U}}$, $T^{\mathcal{P}}$. We then measured the success rate for planning on both U-Net and PASM results, i.e. the percentage of datasets where at least one path was found for T^{GT}, $T^{\mathcal{U}}$ and $T^{\mathcal{P}}$. We then computed the distances to risk structures for T^{GT}, $T^{\mathcal{U}}$, $T^{\mathcal{P}}$ using only shapes M^{GT} as obstacles. This resulted in computing the true distance to risk structures when planning on U-Net and PASM, respectively. We then measured the mean distance of the minimum distances along each trajectory as well as the failure rate, i.e. the number of datasets were a path computed on segmentation results was actually below the critical safety distance d_{min}.

Results: A downstream analysis on trajectory planning evaluates the overall quality and usefulness of the segmentation results by adding metrics on motion planning. Table 6.4 shows the success rate of the motion planning algorithm from Section 5.3.3. The fragmented structures from U-Net do not provide suitable obstacles for planning, whereas shape regularized meshes lead to almost equal rates compared to ground truth planning. In successful cases, both U-Net and our approach achieve slightly lower but still acceptable mean minimal distances to risk structures due to the optimization step. The failure rate of 22% shows that improvement of the segmentation procedure is still necessary and is further discussed on the conclusion.

This evaluation of the entire pipeline consequently more realistically evaluated the us-

Table 6.4.: Quantitative results on planning metrics for SegThor.

	success rate (%)	mean safety distance (mm)	failure rate (%)
Ground-Truth	98	4.70	-
U-Net	43	4.44	17
Ours	90	3.59	22

ability of segmentation algorithms for preoperative planning. By considering trajectory planning with metrics such as success rate and the computed path's closeness to ground truth annotations a more meaningful interpretation of the segmentation step is possible.

6.6. Generalization

Planning trajectories in a preoperative surgical planning pipeline appears in more applications that just vestibular schwannoma removal or endovascular aortic repair. We evaluated our complete approach for several more applications to show the general applicability of the shape regularized planning approach as well as the robustness of our proposed nonlinear trajectory planning methods. This section applies the relaxed formulation of section Section 5.4 first to linear access canals for minimally-invasive cochlear implantation and then to nonlinear trajectories for endovascular pulmonary artery access. Our motion planner then samples unit vectors deviating up to five degrees from the optimal entry direction. In each case, the points of the initial point cloud are projected onto the line that starts at the goal position and points along this sampled direction. If the projected point is less than ϵ_I mm away from the original start state, the planner checks for collision with obstacles and returns a feasible linear path if no collision occurred.

6.6.1. Linear Cochlea-Access

Experimental Setup: The preoperative step for a minimally-invasive cochlear implantation requires a linear canal has to be planned from the surface of the skull to the round window at the cochlea (Figure 6.13). To ensure, the electrode can be inserted into the cochlea from a direction that optimizes its functionality, we set start and goal deviations, according to required precision [240], to $\epsilon_I = 1.0, \phi_I = \pi$, and $\epsilon_G = 0.0, \phi_G = \pi/36$ (5°).
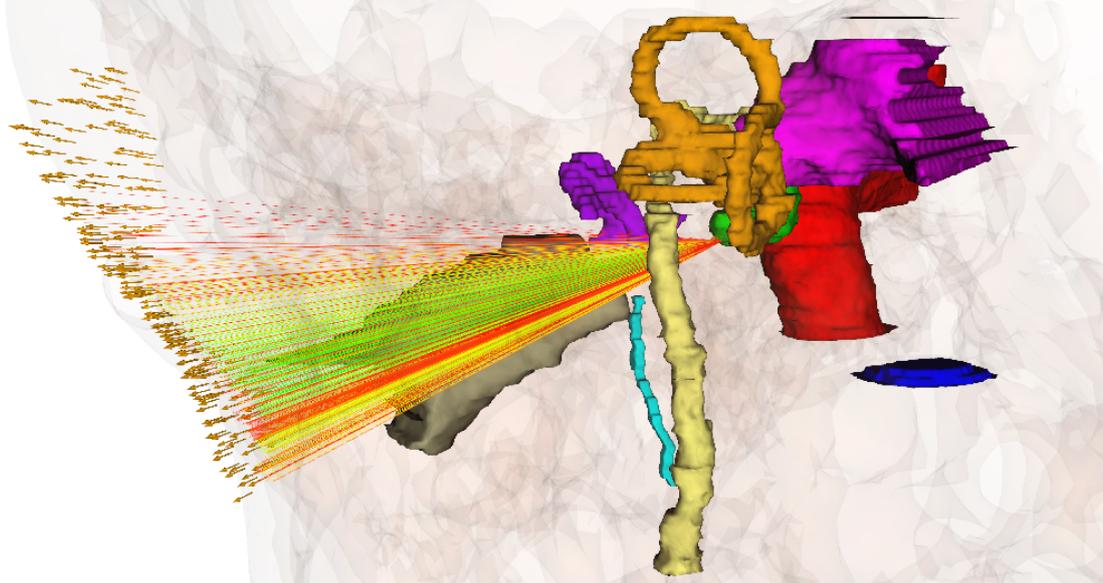
Figure 6.13.: Linear paths (colored lines) from start states (orange arrows) to the cochlea. Found solutions observe lower (red) to higher (green) distances to risk structures.

Using parameter setups of exemplary linear drilling units for cochlear implantations [253] that consider navigation errors and heat exposure, we combine drilling radius and additional safety margin to a minimum distance to obstacles of $d_{min} = 0.8\ mm$. For linear canals the maximum curvature constraint defaults to zero.

Results: In 90% of the cases, planning on ground truth annotations resulted in a collision free path with the required safety distance, i.e. a preoperative surgical planning of the minimally-invasive procedure should have been possible (Table 6.5). The remaining 10% observed not enough clearance to obstacles. With our procedure, planning of a linear canal to the cochlea was equally successful, whereas with the semi-automatic variant [15] only in 66% of the cases planning was successful. In all cases, this infeasible trajectory planning was due to an oversegmentation of the internal auditory canal. On average, the resulting paths achieved a true minimum distance to risk structures of 1.15 mm for the semi-automatic and 1.04 mm for our solution. In Figure 6.14 we see segmentations and

■ Jugular vein ■ Carotid artery ■ Facial nerve ■ Chorda tympani ■ External auditory canal ■ Internal auditory canal ■ Cochlea ■ Semicircular canals ■ Ossicles
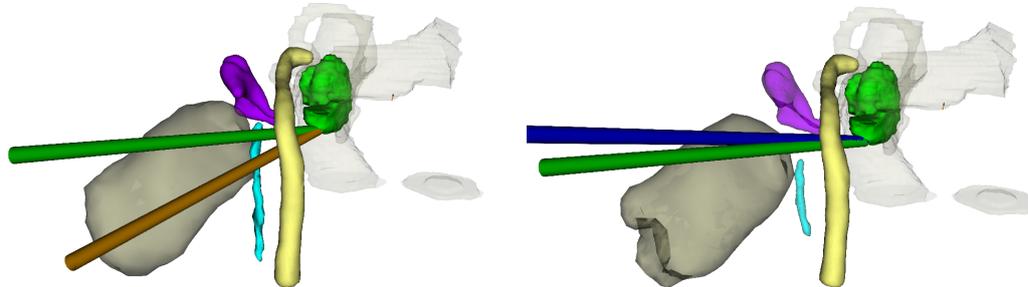
Figure 6.14.: Linear paths to the cochlea resulting from planning on ground truth (green), semi-automatic (orange, left) and our procedure (blue, right).

Table 6.5.: Success rate for planning and mean minimal distance to risk structures for the three experiments (safety distance as reference).

	success rate (%)	mean safety distance (mm)	failure rate ($d < d_{min}$, %)
ground-truth	0.9	1.39	-
semi-automatic	0.65	1.15	0.0
ours	0.9	1.04	0.18

paths for both the semi-automatic (left, orange) and shape regularized procedure (right, blue) together with the most important obstacles as a qualitative example. We note, that in 10% of the cases solutions of the automatic method fell below the safety distance when evaluated on ground truth obstacles. This was due to an inaccurate segmentation of the superior part of the chorda tympani.

6.6.2. Endovascular Access to Pulmonary Arteries

We evaluate a preoperative surgical planning workflow using the MMWHS dataset. The corresponding pipeline, automating laborious tasks while at the same time giving the surgeon control over crucial parts, is shown in (Figure 6.15).
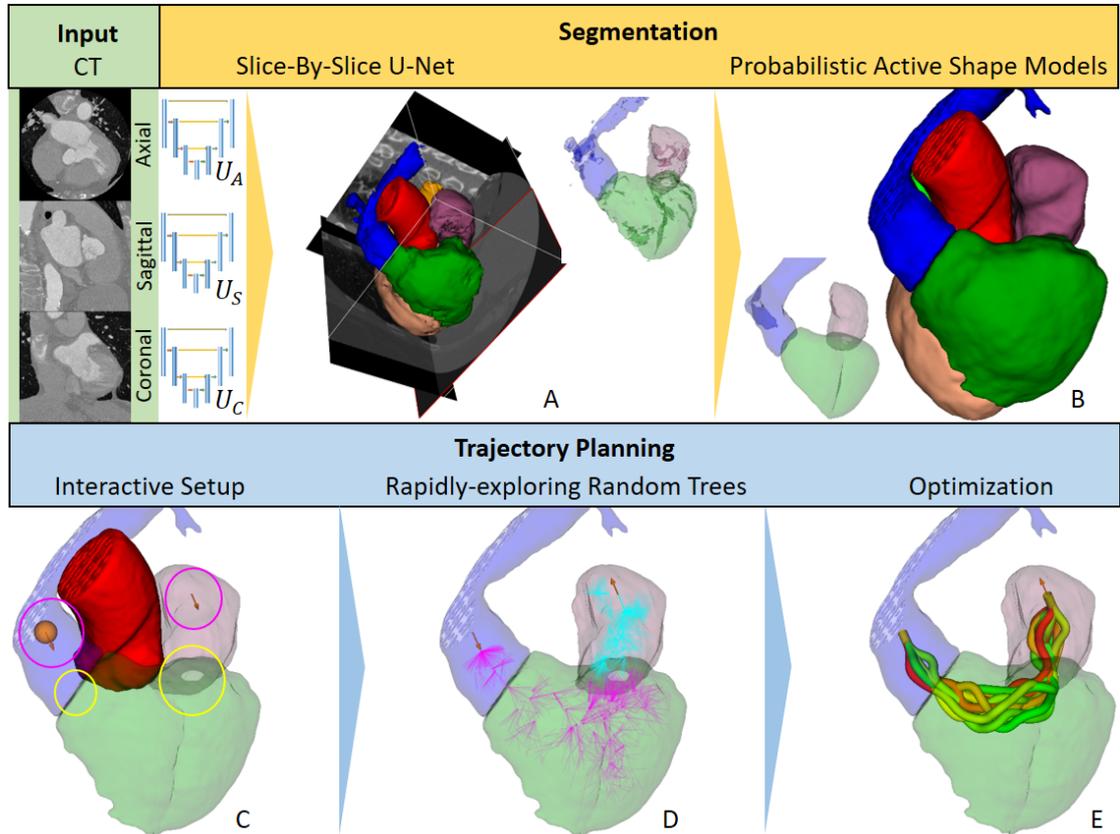
Figure 6.15.: Preoperative pipeline for pulmonary artery access: A CT scan serves as input for 2D U-Nets to predict an initial segmentation (A). Probabilistic ASMs regularize the shapes of fragmented structures (B). A surgeon then interactively defines start and goal states (pink circles) and creates openings (yellow circles) (C). Bi-RRTs find feasible trajectories (D, search graphs in pink & cyan). Computed paths can be locally optimized using SCO (E).

Experimental Setup: Based on a CT scan, our segmentation algorithm automatically extracts organs at risk while guaranteeing realistic shaped boundaries. Given the 3D environment of risk structures, a surgeon initializes the motion planning problem. We consider a parameter setup of the relaxed Formulation 3 with $q_I \in C = \mathbb{R}^3 \times \mathbb{S}^2$, $q_G \in$

Table 6.6.: Results on Dice and HD with mean(SD) for MMWHS.

| | Dice | | Hausdorff | |
	U-Net	Ours	U-Net	Ours
Left Ventricle	0.89(0.07)	0.90(0.07)	14.63(10.99)	**8.56(3.03)**
Right Ventricle	0.86(0.05)	0.86(0.08)	23.05(15.01)	**12.07(5.80)**
Left Atrium	0.91(0.05)	0.90(0.08)	17.67(14.07)	**11.55(6.26)**
Right Atrium	0.86(0.05)	**0.88(0.05)**	23.30(14.85)	**10.98(3.16)**
Left Myocardium	0.86(0.05)	**0.88(0.03)**	19.35(15.96)	**9.62(3.05)**
Ascending Aorta	0.90(0.20)	**0.92(0.16)**	17.22(12.31)	**14.82(17.51)**
Pulmonary Artery	0.83(0.09)	0.83(0.08)	32.80(15.80)	**29.42(15.52)**

$\mathbb{R}^3 \times \mathbb{S}^2$, $d_{min} = 3.5$ and $\kappa_{max} = 0.2$. This step requires interactive placement of a suitable start configuration q_S for the instrument within the right atrium as well as a specific goal state q_G within the pulmonary artery. Moreover, it includes the creation of transitions between neighboring labels: at the tricuspid valve between right atrium and ventricle, at the pulmonary valve between right ventricle and pulmonary artery. We use our Bi-directional Rapidly-exploring Random Tree with Bézier-Splines as steering functions to compute multiple feasible trajectories. The planner parameters were set to $\Delta t = 10.0$, $\rho = 0.05$, $T_{max} = 1.0$, $n_c = 10$, $r = 1.0$, $c_r = 20$, $c_h = 40.0$. An iteration of sequential convex optimization [77, 214] improves clearance to obstacles for these paths. We weighted between obstacle distance and path length setting $\alpha_O = 10$ and $\alpha_\Gamma = 0.1$.

Results: The evaluation on the MMWHS dataset shows similar results to the SegTHOR experiment of section Section 6.5.1, with comparable Dice between shape regularization and U-Net but HD scores clearly outperforming the U-Net approach (Table 6.6). Having the same success rate of 90% but an even lower failure rate of 6% we conclude that shape regularization on deep learning solutions provides a promising approach for future endovascular procedures.

A downstream analysis on trajectory planning evaluates the overall quality and usefulness of the segmentation results by adding metrics on motion planning. Table 6.7 shows the success rate of the motion planning algorithm from Section 5.3.3. The fragmented structures from U-Net do not provide suitable obstacles for planning, whereas shape regularized meshes lead to almost equal rates compared to ground truth planning. In successful cases, both U-Net and our approach achieve slightly lower but still acceptable mean minimal distances to risk structures due to the optimization step.

Table 6.7.: Quantitative results on planning metrics for MMWHS.

	success rate (%)	mean safety distance (mm)	failure rate (%)
Ground-Truth	100	4.39	-
U-Net	70	4.20	0
Ours	90	3.75	6

6.7. Curvature-Constrained Motion Planning

This section demonstrates the advantageous of planning with Bi-RRTs, their optimization using sequential convex optimization and finally the applicability of translating from Bézier Splines to Circular Arcs. First, the benefits of κ-RRT-Connect , our proposed Bi-RRT of section Section 5.3.3 on Bézier Splines and Circular Arcs, are demonstrated on real temporal bone CT data of patients. Their general performance is then shown on a large set of anatomically plausible synthetic anatomies. Finally, we show that these new algorithms outperform state of the art RRT approaches for this specific problem.

While our Bi-RRT on Bézier Splines efficiently solves the two point Boundary Value Problem (BVP) in Formulation 2, access paths computed by this method do not provide optimal distance to surrounding anatomy. We show that the sequential convex optimization approach of Section 5.6, that rearranges Bézier Splines computed by an RRT-connect, achieves locally optimal clearance. Experiments were performed for two scenarios: catheter insertion through the aorta using the SegTHOR dataset and Temporal Bone Surgery using our in-house data. We compare distances to risk structures along computed trajectories from κ-RRT-Connectwith those optimized by Sequential Convex Optimization (SCO).

Finally, translating Bézier Splines, as introduced in Section 5.3.4, is an alternative way to compute feasible trajectories along Circular Arcs for Formulation 2. Our evaluation on real patient data of both temporal bone and aorta showed that our proposed hybrid two step approach achieves on average 55% higher replanning rates and provides 31% larger clearance to risk structures than the κ-B-RRT-Connectalgorithm that solves the BVP with 3D Dubins Paths. For temporal bone surgery, we additionally evaluated our approach on synthetic anatomies using the same setup as in Section 6.7.1. Consequently, our translation approach improves trajectory quality with regard to clinical safety and provides a robust alternative to planning for circular arcs.

Table 6.8.: Parameters for the relaxed Formulation 2 of the three access paths.

	κ_{max}	ϵ_I	ϕ_I (deg)	d_{min} (mm)	T_{max} (s)
Cochlea-Access	0.05	1.0	5	0.8	20
SSC-Access	0.05	1.0	5	1.5	20
RL-Access	0.05	1.0	5	2.0	20

6.7.1. Comparison between Bi-RRT and RRT

Experimental Setup: We consider real and synthetic anatomies in temporal bone surgery and compute nonlinear trajectories for a cochlear access (Cochlea-Access) and two accesses to the internal auditory canal (IAC) (SSC-Access and RL-Access). For computation of trajectories, we use two state of the art RRT planners (Bevel-Tip-RRTfor Circular Arcs [187] and SB-RRTfor Bézier Splines [267]) and our Bi-RRT counterparts presented in section Section 5.3.3 (κ-B-RRT-Connectand κ-SB-RRT-Connect, respectively). For each scenario, we set up the relaxed Formulation 2 so RRT planners were able to find solutions, too.

In both setups we let each of the four planners (Bevel-Tip-RRT vs. κ-B-RRT-Connectand SB-RRT vs. κ-SB-RRT-Connect) calculate as many paths as possible within 20 seconds for all three applications (Cochlea-, SSC-, RL-Access). We used the number of found paths to quantify the performance of each planner. In order to compare the quality of paths computed by each planner, we measured for each trajectory both the deviation at the goal state and the minimal distance to risk structures. For goal biasing we chose a value of $\rho = 0.25$. The *attempt_connection* method of κ-RRT-Connect was most successful with parameters $c_h = 5.0$ mm and $c_r = 11, 19$ mm for height and radius of the cone. Parameters for the relaxed formulation are shown in Table 6.8.

Results: We start with analyzing the motion planners' results on real anatomies. Then, we discuss their generalization on synthetic data.

Real Anatomies First, we look at the number of paths found in a specific time to ensure a planner is fast enough for intra-operative replanning [187]. Figure Figure 6.16 and Table 6.9 show the statistical distributions: For both the Cochlea- and the SSC-Access our RRT-Connect algorithms clearly outperformed standard RRT planners. In the case of the RL-Access the Spline-Based-RRT showed similar performance but none of the three

Table 6.9.: Performance of each planner for the real anatomies (**A=Bevel-Tip RRT**, **B=Bevel-Tip Bi-RRT**, **C=Spline-Based RRT**, **D=Spline-Based Bi-RRT**). Measured in median number of paths (#), median number of paths per second (#/s) and percentage of failed scenarios (F).

	Cochlea-Access			SSC-Access			RL-Access		
	#	#/s	F(%)	#	#/s	F(%)	#	#/s	F(%)
A	0	0	80	1	0.05	50	0	0	75
B	**2635**	**131.75**	5	**760**	**38**	**0**	4	0.2	45
C	17	0.85	5	14	0.7	5	9	0.45	**25**
D	2031	101.55	**0**	442	22.1	**0**	**17**	**0.85**	40

algorithms really stands out. The number of paths found per second and the low number of failures indicate that κ-RRT-Connects work very well for the first two access canals and we can expect that successful intra-operational planning can be performed in minimal time. In contrast, the search through the retro-labyrinthine region was unsuccessful for almost half of the anatomies. This is, however, not unexpected because the risk structures vary highly between patients: in case of a narrow passage between facial nerve and chorda tympani, a small semicircular canal or a high reaching bulb of the jugular vein, the creation of a feasible access path was impossible. Indeed, a careful inspection showed that in the 6 cases algorithm C failed, a high reaching jugular vein bulb made a trajectory of the requested size completely impossible. The discrepancy between the first two problem formulations and the latter is also due the nature of relevant obstacles in the respective area. In the first two cases a bottleneck had to be passed (two nerves / the SSC), whereas for the RL-Access the facial nerve and the jugular vein had to be circumnavigated.

Now we look at the matching of the goal's pose. Naturally, RRT-Connect algorithms matched the orientation of goal states perfectly, whereas the RRTs were limited to an approximation (Figure 6.17). We also note, that in all three cases both Bevel-Tip-RRT and Spline-Based-RRT tended to accomplish the maximal allowed deviation rather than a perfect match.

Next, we focus on the minimal distance an access path had to risk structures as this is usually the most relevant metric to clinicians. To this purpose, we interpolated between the states of the search tree at a resolution of 0.1 mm. For each of those interpolated states, we then sampled points on a circle with radius r_d and orthogonal to the state's direction and computed the minimal distance to the next obstacle. Figure Figure 6.18 shows in small images the narrowest region that had to be passed together with three
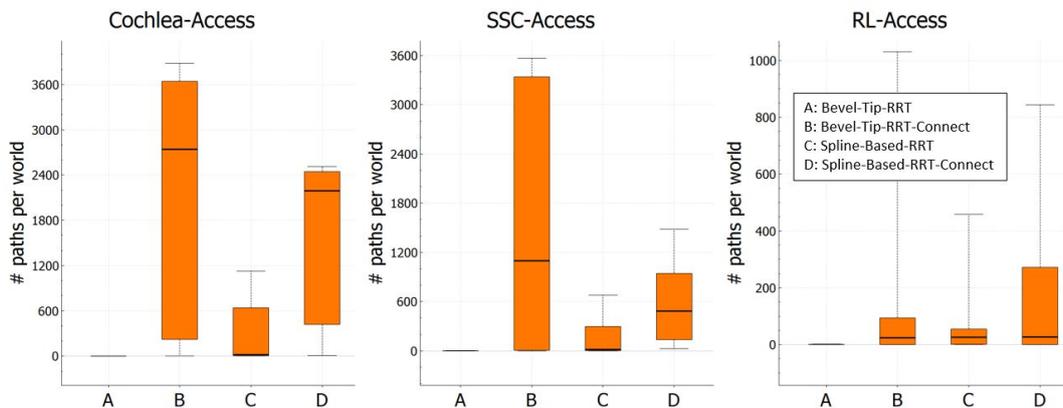
Figure 6.16.: Box-Plots for each access canal about the number of paths found by the individual planners in 22 real anatomies (higher=better).
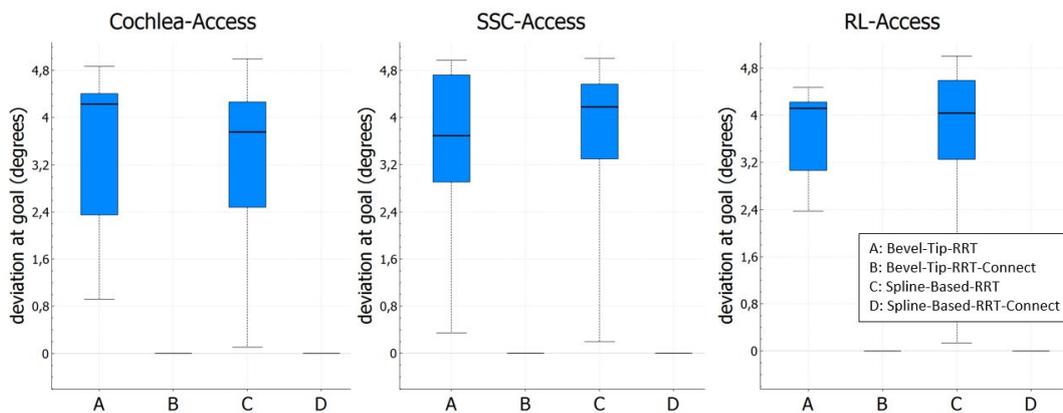
Figure 6.17.: Box-Plots about deviation at the goal for real anatomies (lower=better).

statistics for each planner across all 22 anatomies: the percentage how often it computed the best path for a specific anatomy (Best), the mean minimal distance its best path had to risk structures (Mean) and the overall best path it computed across all anatomies (Max). Clear superiority of a specific algorithm was not observable although the Spline-Based-RRT tended to find paths with the largest distance more often. Hence, our new κ-RRT-Connect did not suffer from lower quality. From the observed distances we also got an impression of the average size of the passed bottleneck. This can help in the design for the robot prototype. According to Table 6.9, for example, κ-RRT-Connect always found

A=Bevel-Tip RRT, B=Bevel-Tip Bi-RRT, C=Spline-Based RRT , D=Spline-Based Bi-RRT

	Best (%)	Mean (mm)	Max (mm)			Best (%)	Mean (mm)	Max (mm)			Best (%)	Mean (mm)	Max (mm)
A	5.3	0.48	0.64		A	5.3	0.96	1.29		A	26	1.32	2.24
B	10.5	0.65	1.12		B	15.8	1.04	1.50		B	5.3	1.46	1.94
C	**42.1**	0.67	**1.32**		C	**42.1**	1.02	**1.63**		C	**57.9**	**1.66**	**2.35**
D	**42.1**	**0.68**	1.15		D	36.8	**1.13**	1.55		D	10.5	1.56	2.13
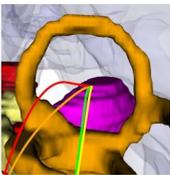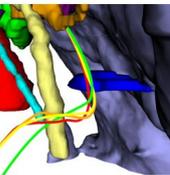
Figure 6.18.: Close-Up of the narrowest region of each access canal. The corresponding shows the mean and max distance of each planner over all real anatomies together with the percentage of how often each planner found the best path according to the maximum distance.
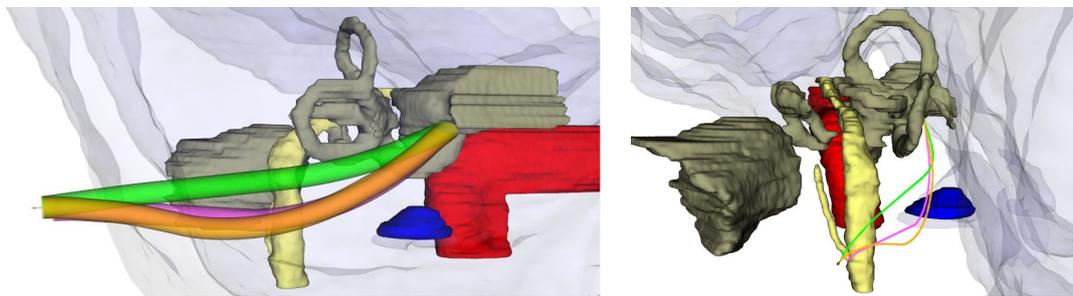
Figure 6.19.: RL-Access planned by a standard RRT (pink tube) with safety distance 1.0 mm and by a κ-RRT-Connect (green, orange) with safety distances 1.0 mm and 1.5 mm, respectively.

trajectories for an SSC-Access with the specifications in Table 6.8, having on average still a minimal distance above 1.0 mm to the nearest obstacle.

Last we address the issue that in many scenarios the Spline-Based-RRT found paths with the highest minimal distance. A closer inspection showed that the κ-RRT-Connect just quickly found a solution as soon as the relevant obstacle had been passed. When we enlarged the allowed safety distance, the κ-RRT-Connect computed paths with similar minimal distances. Figure Figure 6.19 shows an example of this behavior for the RL-Access with safety distance 1.0 mm and 1.5 mm.

Synthetic Anatomies   To study the generalization of these specific cases, we then looked at synthetic scenarios. Instead of real anatomies we now worked with variances based on atlases of real data combined with the shape space of the statistical shape models. Our

Table 6.10.: Performance of each planner for the synthetic anatomies (A=Bevel-Tip RRT, B=Bevel-Tip Bi-RRT, C=Spline-Based RRT , D=Spline-Based Bi-RRT). Measured in median number of paths (#), median number of paths per second (#/s) and percentage of failed scenarios (F).

	Cochlea-Access			SSC-Access			RL-Access		
	#	#/s	F (%)	#	#/s	F (%)	#	#/s	F (%)
A	0	0	80	0	0	57	0	0	66
B	208	10.4	**0**	398	19.9	12	27	1.35	37
C	15	0.75	7	14	0.7	7	15	0.75	**26**
D	**762**	**38.1**	**0**	**1144**	**57.2**	**0**	**273**	**13.65**	30

evaluations then included a much broader variety of anatomies. By randomly sampling the shape space we also made sure that the individual real anatomies did not provide edge cases for the algorithms, a standard approach in motion planning [87, 123].
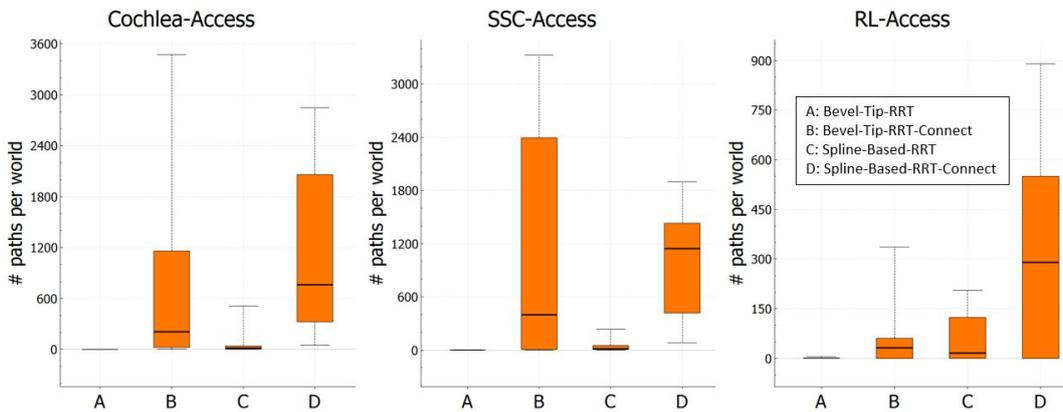
Figure 6.20.: Box-Plots about success rates of the planners in 100 synthetic anatomies (higher=better).

The results in Figure 6.20 and Table 6.10 show how the planners performed for each access canal. From the box plots we can conclude, that κ-RRT-Connect again tended to find many more paths. Their performances according to Table 6.10 supported the results of the real cases: For the given parameters of Table 6.8 access paths for the Cochlea- and SSC-Access were always possible whereas for the RL-Access a high reaching jugular vein often prevented a feasible trajectory to be found. The number of paths found per second again indicated that Bi-directional RRTs are suitable for intra-operational planning. An
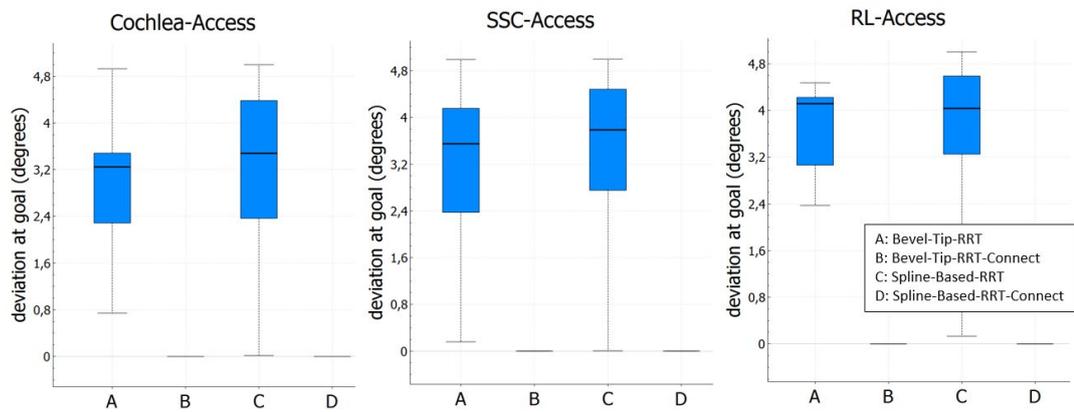
Figure 6.21.: Box-Plots about deviation at the goal for 100 random synthetic anatomies (lower=better).

analysis of the orientation at the goal showed equivalent results to the real cases: RRTs hardly realize a good match of the desired orientation (Figure 6.21). Although this was expected, it clearly supports our claim, that bidirectional planners are required, if precise replanning is necessary.
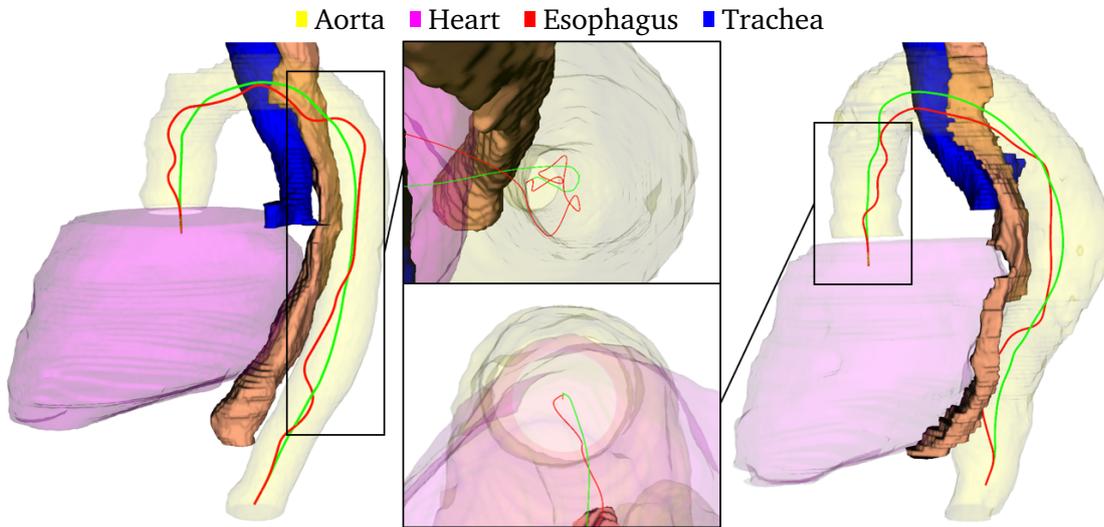
Figure 6.22.: Two examples of the Aorta-Access with initial (red) and corresponding optimized (green) trajectories. The weighted cost function on length and clearance to risk structures lead to smooth trajectories close to the aorta's centerline.

6.7.2. Optimization of Bi-RRT trajectories

Both temporal bone surgery and Endovascular Aortic Repair (EVAR) benefit from optimized clearance to risk structures, because damage of Organs at Risk (OAR) could lead to facial nerve paresis in temporal bone surgery or severe complications in EVAR due to piercing or otherwise damaging the aortic wall. As the previous experiments showed superior performance of Bézier Spline trajectories, we further improved on this scheme using sequential convex optimization.

Experimental Setup: We extracted surface meshes from expert annotations of both the 40 SegTHOR CT images as well as our temporal bone dataset. We then defined a strong formulation, planned trajectories using Bi-RRT on Bézier Splines and tried to optimize the resulting paths.

Catheter insertion: Initially, we planned trajectories for catheters through the aorta (Figure 6.22). The start state q_S was placed at the lowest part of the descending aorta, the goal state q_G at the entrance to the left ventricle. We set the curvature constraint to $\kappa_{max} = 0.1\,\text{mm}^{-1}$ and safety distance to $d_{min} = 20.0\,\text{mm}$. The RRT-connect used a

Table 6.11.: Quantitative Comparison for Aorta-Access.

| | Aorta-Access | |
	RRT [74]	Ours
success rate	-	81.0
mean distance	7.1	**11.2**
Aorta	1.9 ± 0.3	**3.0 ± 1.6**
Heart	8.4 ± 2.1	**10.3 ± 1.7**

Table 6.12.: Quantitative Comparison for RL- and SSC-Access.

| | RL-Access | | SSC-Access | |
	RRT [74]	Ours	RRT [74]	Ours
success rate	-	87.8	-	94.8
mean distance	4.9	**5.5**	5.0	**5.2**
Brain	1.8 ± 0.5	**2.0 ± 0.6**	2.0 ± 0.8	**2.1 ± 0.8**
facial nerve (FN)	1.8 ± 0.7	1.8 ± 0.9	2.8 ± 0.5	**2.9 ± 0.5**
jugular vein (JV)	3.3 ± 2.1	3.3 ± 2.1	-	-
SSC	1.5 ± 0.7	**1.6 ± 0.7**	1.0 ± 0.2	**1.1 ± 0.3**

step size of $15\,$mm, resulting on average in $N_{\mathcal{W}} = 25$ waypoints for the optimization. Figure 6.22 shows two representative examples with distance threshold $\theta = 30\,$mm and cost weights $\alpha_\Gamma = 0.1, \alpha_O = 10$.

Temporal Bone Surgery: We placed a start state q_I at the surface of the lateral skull base and a goal state q_G at the internal auditory canal for two different approaches: An access via the retrolabyrinthine region (RL-Access) and an access via the superior semicircular canal (SSC-Access). Initial parameters were set to $\kappa_{max} = 0.1\ \mathrm{mm}^{-1}$ and $d_{min} = 1.5$ mm and a step size of $6\,$mm, resulting in $N_{\mathcal{W}} \approx 8$ waypoints. Figure 5.9 shows a representative example with distance threshold $\theta = 5\,$mm and cost weights $\alpha_\Gamma = 1, \alpha_O = 10$.

Results: Running the optimization sequence for *Catheter insertion* took on average $1.1\,$s. With a success rate of 80.97% we were able to optimize the majority of trajectories, showing that the convexifications are suitable. Along the entire trajectory our clearance-optimized paths achieved a much higher mean and minimum distance to the two obstacles aorta and heart (Table 6.11, Aorta-Access). Such improved trajectories thus significantly reduce the risk of harming organ boundaries.

Temporal Bone Surgery: Table 6.11 (RL- & SSC-Access) shows a comparison between

Table 6.13.: Parameters for the Problem Formulations and Planners.

	κ_{max}	d_{min}	T_{max}	ΔT_{max}	Δ_t	(C_h, C_r)
Temporal	0.05	2.0	1.0	0.1	6	(12,6)
Aorta	0.1	2.0	5.0	1.0	15	(45, 5)

initial and optimized planning. The high success rate demonstrates that our convexified cost and constraint functions for length and curvature are suitable to optimize Bézier Spline trajectories. As a consequence of the increase in overall mean distance, minimally-invasive approaches using our method would stay farther away from risk structures until the respective bottle necks (the SSC for SSC-Access; facial nerve, jugular vein and brain for RL-Access). Due to the very narrow passages in temporal bone surgery (Figure 5.9, closeup) the differences in minimal distance at the bottlenecks were negligible.

6.7.3. Translation to Circular Arcs

The previous optimization scheme is only applicable to Bézier Spline trajectories. A translation of such paths for instruments such as Bevel-Tip needles that follow Circular Arcs would make the whole approach accessible to more clinical applications. This section investigates the potential of our translation approach for temporal bone surgery as well as percutaneous transluminal coronary angioplasty.

Experimental Setup: We compared our method with the state of the art RRT-connect solution that directly steers via circular arcs and connects its two search trees with 3D Dubins Paths [74]. Planners were given the same fixed time constraint T_{max} of the strong problem formulation to compute as many trajectories as possible. Each planner restarted the search, if they failed to connect their trees within a smaller time frame ΔT_{max}. This strategy was more successful than ongoing planning for the entire time T_{max}. After setting up the strong Formulation 2 for each individual dataset, we computed initial trajectories with both planners. From these initial trajectories, the one with largest distance to obstacles was chosen as a reference Γ_{opt} for replanning. This Γ_{opt} consisted of a sequence of states $\{q\}_i \subset \mathbb{R}^3 \times \mathbb{S}^2, 0 \leq i \leq N$. For replanning, we then repeatedly planned trajectories to the goal based on reference Γ_{opt}, replacing the initial state q_I in each step with the next $q_j \in \{q\}_i, 1 \leq j \leq N - 1$, of Γ_{opt} until no further solutions had been found. This provided a robustness quality metric, named percental replanning rate, that indicated from how many states of the original trajectory replanning was possible.

■ Jugular vein ■ Carotid artery ■ Facial nerve ■ Chorda tympani ■ External auditory canal ■ Internal auditory canal ■ Cochlea ■ Semicircular canals ■ Ossicles ■ Aorta ■ Heart ■ Esophagus ■ Trachea
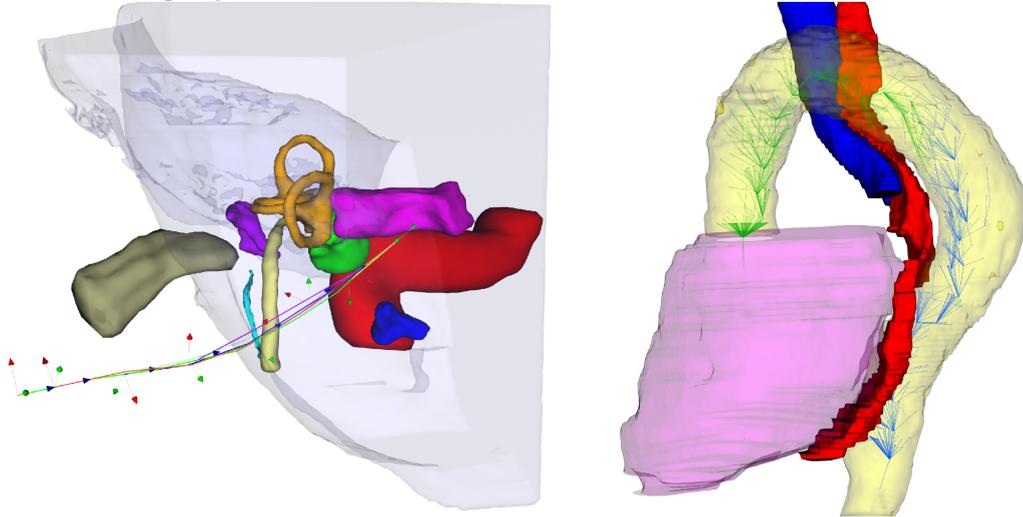
Figure 6.23.: **Left:** Motion planning in a synthetic temporal bone anatomy. Replanned trajectories (colored lines) from different states along the initial path. **Right:** Search graph of a Spline-Based RRT-connect (blue & green). Its steering function provides a more robust way to travel through narrow or cluttered environments than the use of circular arcs and 3D Dubins Paths.

For *Temporal Bone Surgery*, we targeted a miniaturized version of our prototype with a radius of 1.0 mm and added a safety distance of 1.0 mm to account for heat exposure during drilling, resulting in a safety distance d_{min} of 2.0 mm. The curvature constraint $\kappa_{max} = 0.05$ mm^{-1} reflected the maximum turning angle of the robot (Table 6.13). Although the temporal bone exhibits highly varying anatomies such hardware capabilities would allow feasibility of the approach in the majority of cases with an average length of trajectories of 4.25 mm. For both methods, we then tried to find feasible initial and replanning trajectories within $T_{max} = 1.0$ s with $\Delta T_{max} = 0.1$ s. These values were chosen as a trade off between speed and high success rate. In addition to using 20 real patient examples, we extrapolated 1000 random worlds by using synthetic anatomies [74]. A synthetic anatomy consisted of a small perturbation of the obstacles, where statistical shape models [45] of the individual risk structures were used to slightly alter their shape. This methodology led to anatomically realistic and clinically meaningful random worlds.

For *percutaneous transluminal coronary angioplasty*, we used the publicly available SegTHOR dataset [241] to evaluate the motion planners within the aorta, i.e. on the first part of the guidewire's path to the coronary arteries. The dataset consisted of 40 CT images along with segmentations of aorta, heart, esophagus and trachea Figure 6.23). For each scenario, we placed the start state q_I at the inferior part of each dataset's segmented descending aorta pointing up. The goal state q_G we placed within the left ventricle pointing down, slightly below the lowest part of the ascending aorta. This prevented planners from search within the heart for feasible trajectories. We set $r_{max} = 0.96\mu$m, comparable to existing catheters, and added an additional safety margin to keep away from the vessel's boundaries, resulting in a safety distance $d_{min} = 2.0$ mm. With our guidewire design we targeted currently existing catheters with a maximum bend between $30-70°$/mm. We set the curvature constraint to $\kappa_{max} = 0.1$ mm^{-1} which generously respected catheter designs and allowed for easier planning. Once these parameters were defined we performed the initial and replanning procedure with $T_{max} = 5.0$ s with $\Delta T_{max} = 1$ s, once again as a trade off between speed and high success rate.

Results: For *Temporal Bone Surgery*, the results of both planners on real as well as synthetic data are shown in Table 6.14. For all experiments, we first measured the success rate on initial planning, i.e., for how many datasets at least one trajectory could be found. As we manually placed the start and goal states in a favorable way for motion planning, a high success rate was expected. Overall, our proposed planner achieved only a slightly lower success rate than the original version, showing its robustness for temporal bone surgery. In the rare cases where it failed, the extremely narrow environment provided not enough free space for the translation from Bézier splines to circular arcs. Next, we measured the number of trajectories computed within T_{max} and derived the average time it would need to find a feasible solution. As is took only a few steps to plan through the retrolabyrinthine region to the internal auditory canal and only two obstacles (facial nerve and jugular vein) had to be circumnavigated, both planners required only milliseconds to find a feasible path. In terms of quality, we realized a significant increase in distance to risk structures of on average 35% with our proposed approach and thus an improved clinical quality of trajectories. This beneficial effect can be explained by the steering mechanism of Bézier splines which only approximate the waypoints drawn by the planner (Figure 5.4). Finally, the replanning rate of our approach was on average 41.8% higher compared to the existing solution, showing that the Bézier approach with translation to arcs is very robust.

We then evaluated the 1000 synthetic anatomies. Figure 6.23 shows one of the random worlds as a quality example with replanned trajectories. From Table 6.14 we observe that the results from real data were almost matched. Only the number of paths found per

Table 6.14.: Results of temporal bone planning. While Circular Arcs show slightly better scores in initial success rate, our translation scheme provides safer paths and robust replanning.

Temporal Bone (Real Data)	Arcs[74]	Proposed
success rate (%)	**100.0**	93.3
# paths	268.7 ± 229.8	216.9 ± 152.2
average time (ms)	18.61 ± 8.58	23.06 ± 11.86
min distance (mm)	2.0 ± 0.1	2.7 ± 0.4
replanning rate (%)	54.4 ± 27.2	96.2 ± 9.7

Temporal Bone (Synthetic Data)	Arcs[74]	Proposed
success rate (%)	**100.0**	86.4
# paths	62.2 ± 44.4	53.4 ± 40.4
average time (ms)	16.08 ± 6.71	18.73 ± 8.51
min distance (mm)	2.0 ± 0.1	2.8 ± 0.4
replanning rate (%)	53.8 ± 26.1	92.1 ± 17.8

planner dropped. However, this was an expected result: While start and goal states were tailored for the real scenarios, they were sub-optimal for altered synthetic anatomies.

Aorta Experiment: Planning through the aorta provided a different scenario, as motion planners had to cope with a narrow tube-like environment instead of the cluttered one described before. Figure 6.23 shows a qualitative example of the variation of curved aortas in the SegTHOR dataset together with the search tree of our proposed version. Quantitative results are shown in Table 6.15. Both in initial and in replanning success rate, our Bézier approach outperformed the existing solution by about 55% and 55.2%, respectively. Again, this can be explained by the approximated waypoints that are used in the search tree. This construction mechanism naturally allows the planning to stay slightly farther away from boundaries than the direct approach. We emphasize that quality in terms of distance to risk structures was again improved around 27%.

6.8. Summary

This chapter performed retrospective in silico evaluation of preoperative surgical planning as presented in Chapter 3 for Temporal Bone Surgery and endovascular procedures. The

Table 6.15.: Results of aorta planning.

Aorta (Real Data)	Arcs[74]	Proposed
success rate	45.0	**100.0**
# paths	0.7 ± 1.0	8.0 ± 3.2
average time (s)	7.4 ± 4.4	0.6 ± 0.1
min distance (mm)	2.9 ± 0.6	3.7 ± 0.5
replanning rate (%)	13.4 ± 13.8	68.6 ± 24.2

automatic shape regularized segmentation approach of Chapter 4 showed competitive performance on Dice scores and Hausdorff distances while providing suitable label images for further trajectory planning. The trajectory planning step was thoroughly evaluated on real and synthetic anatomies. The proposed Bi-RRTs on Bézier Splines and Circular Arcs with 3D Dubins Paths proved to be more suitable than their RRT counterparts. The sequential convex optimization scheme on Bézier Splines improved distance to risk structures while smoothing out the stochastic nature of typical RRT paths. The translation approach showed superior performance compared to planning directly with the Bi-RRT on Circular Arcs.

Preoperative surgical planning employing shape regularized U-Nets and optimized trajectory planning with cubic Bézier Splines is a robust and fast solution to finding feasible access paths for flexible nonlinear instruments. The in silico evaluation of this solution allows a thorough analysis of the preoperative step in new robot-assisted approaches.

7. Conclusion

This chapter first gives a short summary and list of contributions. It then discusses limitations of each part in the pipeline and suggests directions for future work.

7.1. Summary

Robot-assisted interventions with flexible instruments are an ongoing trend in minimally-invasive surgery that improve clinical outcome at the expense of added complexity. Before clinical translation of these new approaches, a thorough evaluation of these procedures is essential even though only limited available data is usually accessible for specific cases. This thesis covers the preoperative surgical planning step of these approaches and provides automatic solutions for the two major parts, segmentation and trajectory planning.

In particular, this thesis presents a complete preoperative surgical planning pipeline for robot-assisted minimally-invasive procedures, performing successive steps of automatic segmentation and optimized trajectory planning. Contributions lie in three fields: in silico evaluation, segmentation and motion planning (Table 7.1). For segmentation, a shape-regularized deep learning approach for plausible shape extraction in minimally-invasive temporal bone surgery as well as Endovascular Aortic Repair (EVAR) is presented [73, 75]. New methods in curvature constrained trajectory planning cover Bi-RRTs using either Bézier Splines or Circular arcs together with 3D Dubins Paths [74]. An optimization scheme on sequential convex optimization [77] together with a translation from one technique to the other [72] makes the whole concept widely adoptable to approaches with flexible needles and endoscopes, drilling units as well as guidewires.

In silico experiments are based on three different datasets: the training sets of both the MMWHS [68] and SegTHOR [241] challenge as well as an in-house dataset of the temporal bone. For Temporal Bone Surgery, experimental results on the whole pipeline prove the feasibility of our combined approach of automatic segmentation and trajectory

Table 7.1.: Contributions in this thesis for preoperative surgical planning.

Contribution	Benefits
In silico evaluation	
Synthetic Anatomies	clinical motion planning evaluation
Downstream Metrics	Functional evaluation of segmentation
Segmentation	
Shape Regularized U-Nets	Automation for Temporal Bone
	Suitable results for motion planning
Motion Planning	
Bi-RRT on Bézier Splines	robust and precise planning in $\mathbb{R}^3 \times \mathbb{S}^2$
Bi-RRT on Circular Arcs	
Bézier Spline Optimization	locally optimal solutions
Bézier Spline Translation	optimal planning on Circular Arcs

planning, making a vital step to robust and safe robot-assisted procedures in this field. For Endovascular Aortic Repair, our experiments show promising results for automatic segmentation for 3D printing as well as feasibility of an Electromagnetic Tracking (EMT) guided insertion of guidewires, the latter with the potential of minimizing radiation exposure for both patients and clinicians. In short, the proposed automatic pipeline leads to an efficient and unbiased workflow for preoperative surgical planning. Finally, an open-source framework is published that enables the proposed experimental setup of synthetic anatomies for statistically significant evaluation on scarce datasets, the interactive execution of preoperative planning as well as the functional evaluation on downstream tasks with new application driven metrics.

7.2. Discussion & Future Work

While the proposed solutions allow complete preoperative surgical planning for flexible instruments, individual steps still show limitations and can be further improved or expanded. The following three sections list in detail future work for in silico experiments, automatic shape regularized segmentation and curvature constrained trajectory planning.

7.2.1. In Silico Evaluation

The proposed pipeline, performing successive steps of segmentation, interactive problem definition and trajectory planning, can be quickly setup in our interactive framework, thoroughly evaluated using functional evaluation on planning metrics and experimentally validated by synthetic anatomies. To the best of our knowledge, existing tools such as Slicer 3D do not provide equivalent or similar opportunities in such a general way. However, due to their wide adoption and rich available features in terms of both image processing and visual interaction, a migration of our works into these framework would come with many benefits. First, such tools already provide extensive tools for image post processing, allowing for manual correction during evaluation of the pipeline in a clinical workflow. Together with existing plugins for these frameworks, individual parts of our work, such as nonlinear trajectory planning and optimization, would be easily extendable to other applications and thus more useful for the research community. Finally, the interactive tools is not yet properly evaluated by clinicians on a clinical workflow but only used for setup of our experiments. An implementation of a user interface for ergonomic execution of the pipeline in a clinical workflow by clinicians would be a valuable contribution and result in hints to further improve on the individual solutions within the whole procedure.

While our functional evaluation shows promising results for both Temporal Bone Surgery and Endovascular Aortic Repair, it is not considered a replacement of phantom experiments. Further analysis should therefore setup experiments using real prototypes of the investigated instruments. For temporal bone surgery using the proposed drilling units, a suitable next step could include trajectory planning and subsequent navigation in styrofoam blocks. However, due to the current state of the drilling robot prototype, experiments for EVAR seem more realistic. Here, 3D printing of the aorta allows for easy creation of suitable upscaled environments. Such enlarged phantoms could be used to create trajectories for the currently existing guidewires.

The evaluation on synthetic anatomies is still a novelty in the community. First, new samples are created using multiple atlases together with rigid registration. This does not cover varying poses of organs, which is naturally the case in between patients. By leveraging the statistical variety in articulated atlases [120], it might be possible to cover these variations as well and build more advanced samples for evaluation. Second, these synthetic worlds only allow the creation of new samples for trajectory planning. A system that provides new samples for segmentation would also greatly benefit the evaluation of these pipelines in data scarce environments. To this purpose, the use of Generative

Adversarial Nets [97], e.g. generating new random CT volumes of the temporal bone, would allow a simulation of the complete pipeline.

Finally, the focus of this pipeline should be extended to include intraoperative navigation. For applications such as EVAR or needle insertion, this would require to simulate or track soft tissue deformation [3]. Otherwise, navigation would be performed on preoperative data only, thereby ignoring changes induced by respiratory or heart motion as well as by deformations resulting from instrument forces. Intraoperative navigation thus requires regular replanning. For the trajectory planning step of the pipeline, this could mean to perform anytime path planning [135], where the search tree of the current solutions is kept and the RRT keeps searching for more or lower cost solutions. If misalignment of instruments increases too much, rapid replanning from the current pose of the instrument would be necessary.

7.2.2. Shape Regularized Segmentation

The experiments show that global metrics such as Dice are of limited use and that an evaluation on distances to risk structures provides a more realistic analysis in Computer-Assisted Interventions (CAI) settings. The main reason for this is the necessity to extract anatomically plausible shapes of organs, resulting in feasible collision-detection during planning. However, the proposed slice-by-slice U-Net initialization with a PASM post processing should be viewed as an early work, showing the value of shape regularization for preoperative surgical planning. A major contribution would compare existing solutions using Conditional Random Field (CRF)s, CRF-Recurrent Neural network (RNN) and other model-based approaches such as slice-by-slice Active Contour (AC) for the investigated applications. Having multiple such solutions in a publicly available framework would greatly benefit other researchers in using and setting up a thorough evaluation of Preoperative Surgical Planning (PSP).

To improve on the current metrics, hybrid loss guided networks [190] would probably boost the performance of our U-Nets. The initialization of PASMs could then better capture critical features: the inferior part of the descending aorta (Figure 6.9), the transitions of the right ventricle to both pulmonary artery and right atrium, and finally the tiny structures of the temporal bone, where currently the chorda tympani is sometimes completely missing. However, our review in section Section 2.2.5 shows that regularization is an active field with the search for including true shape spaces in deep learning architectures being a prominent topic [181, 184, 273]. An end-to-end trainable solution for anatomically plausible segmentation could exceed the existing approaches. Finally, Statistical Shape

Models are only adoptable, if the underlying organs exhibit a statistical variation. The presented pipeline should thus include solutions for more diverse structures such as the coronary arteries.

7.2.3. Trajectory Planning

Our curvature constrained planning demonstrated that preoperative surgical planning for nonlinear access paths is possible for cluttered environments such as the otobasis as well as for narrow regions such the aorta or heart chambers. The proposed tailored RRT-Connect algorithms using either Bézier Splines or Circular Arcs with 3D Dubins Paths outperform state of the art one-directional planners and provide a robust and fast method for planning access paths. With the clearance optimization scheme, resulting trajectories are also locally clinically optimal. With our solution for translating Bézier Splines to circular arcs trajectories we made this planning method available for applications using instruments such as bevel-tip needles that move along circular motions.

Currently, our planning method is a purely geometric approach and does not consider uncertainty of any kind. But during intra-operative navigation, noisy sensor measurements or soft tissue deformation might invalidate preoperatively feasible paths and thus have to be considered. In future, the pipeline should therefore address these kinds of uncertainty by modeling each of these factors. Sensor uncertainty could for example be included into the convex optimization scheme similar to the approach by Sun and Alterovitz [234] for needle insertion for liver biopsy. Soft tissue simulation on the other hand has been investigated in [3].

Deriving the optimal translation from a Bézier Spline to a Circular Arc is also an interesting topic, i.e. computing the arc closest to the original spline. For this problem, either an analytic expression or a cheap numerical solution has to be found. Likely, this would further increase the success rate of planning as well as decrease the failure rate reported in the experiment section.

As convex optimization results in locally instead of globally optimal paths, incorporation of an RRT*-like stochastic optimization scheme is a promising research direction for future work as well. In this case, a Bi-RRT could plan a first solution γ_I. The RRT*-like optimization could improve γ_I by sampling within this trajectory, resulting in a clearance optimized γ_O that still observes the typical wiggly course. The proposed SCO scheme on Bézier Splines could then remove these irregularities by smoothing γ_O due to its cost function on both clearance and length to a final path γ_f.

Finally, the guidewire approach could be extended to cases such as percutaneous transluminal coronary angioplasty due to arteriosclerosis where guidewires are used to position catheters to dilate an occlusion in coronary vessels. This would require to perform preoperative surgical planning on the whole path from incision at the surface to locations of stenosis. This could be achieved by a subdivision of the problem: planning first from the groin to the aortic arc, then to the transition from aorta to coronary arteries and in a final step to the clinical target.

A. Publications

This thesis is partially based on the following publications:

1. Johannes Fauser, Igor Stenin, Julia Kristin, Thomas Klenzner, Jörg Schipper, and Anirban Mukhopadhyay. "Optimizing Clearance of Bézier Spline Trajectories for Minimally-Invasive Surgery". In: *Medical Image Computing and Computer Assisted Intervention – MICCAI 2019*. Ed. by Dinggang Shen, Tianming Liu, Terry M. Peters, Lawrence H. Staib, Caroline Essert, Sean Zhou, Pew-Thian Yap, and Ali Khan. Cham: Springer International Publishing, 2019, pp. 20–28

2. Johannes Fauser, Moritz Fuchs, Ahmed Ghazy, Bernhard Dorweiler, and Anirban Mukhopadhyay. "Preoperative Planning for Guidewires Employing Shape-Regularized Segmentation and Optimized Trajectories". In: *OR 2.0 Context-Aware Operating Theaters and Machine Learning in Clinical Neuroimaging*. Ed. by Luping Zhou, Duygu Sarikaya, Seyed Mostafa Kia, Stefanie Speidel, Anand Malpani, Daniel Hashimoto, Mohamad Habes, Tommy Löfstedt, Kerstin Ritter, and Hongzhi Wang. Cham: Springer International Publishing, 2019, pp. 12–20

3. Johannes Fauser, Romol Chadda, Yannik Goergen, Markus Hessinger, Paul Motzki, Igor Stenin, Julie Kristin, Thomas Klenzner, Jörg Schipper, Stefan Seelecke, Roland Werthschützky, Mario Kupnik, and Anirban Mukhopadhyay. "Planning for Flexible Surgical Robots via Bézier Spline Translation". In: *IEEE Robotics and Automation Letters* 4.4 (Oct. 2019), pp. 3270–3277

4. Johannes Fauser, Igor Stenin, Markus Bauer, Wei-Hung Hsu, Julia Kristin, Thomas Klenzner, Jörg Schipper, and Anirban Mukhopadhyay. "Toward an automatic preoperative pipeline for image-guided temporal bone surgery". In: *Intern. J. of Comp. Ass. Radiology and Surgery* (Mar. 2019)

5. Johannes Fauser, Igor Stenin, Julia Kristin, Thomas Klenzner, Jörg Schipper, Dieter Fellner, and Anirban Mukhopadhyay. "Generalized Trajectory Planning for Nonlinear Interventions". In: *OR 2.0 Context-Aware Operating Theaters, Computer*

Assisted Robotic Endoscopy, Clinical Image-Based Procedures, and Skin Image Analysis.
Cham: Springer International Publishing, 2018, pp. 46–53

6. Johannes Fauser, Georgios Sakas, and Anirban Mukhopadhyay. "Planning nonlinear access paths for temporal bone surgery". In: *Intern. J. of Comp. Ass. Radiology and Surgery* 13.5 (May 2018), pp. 637–646

7. Johannes Fauser, Igor Stenin, Julia Kristin, Thomas Klenzner, Jörg Schipper, and Georgios Sakas. "A software tool for planning and evaluation of non-linear trajectories for minimally invasive lateral skull base surgery". In: *Tagungsb. der 15. Jahrestag. der Dtsch. Ges. f. Comput.- und Roboterass. Chirurgie e.V. (CURAC)*. 2016, pp. 125–126

B. Awards

My works *Toward an automatic preoperative pipeline for image-guided temporal bone surgery* [75] and *Preoperative Planning for Guidewires Employing Shape-Regularized Segmentation and Optimized Trajectories* [73] were both acknowledge with a *Best Paper Runner Up* in IPCAI 2019 and in MICCAI 2019 OR 2.0 workshop, respectively. For my work Optimizing Clearance of Bézier Spline Trajectories for Minimally-Invasive Surgery [77] in MICCAI 2019, I was awarded with a *Graduate Student Travel Award*.
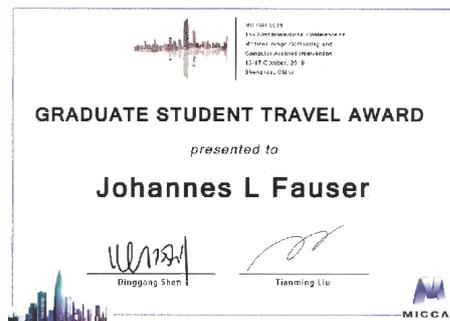
C. Teaching Assistance

2017-2019   **Deep Learning for Medical Imaging**, TU Darmstadt, Winter Term, 1 lecture each semester: *Segmentation*

2019   **Computer Graphics 2**, TU Darmstadt, Summer Term, 8 lectures:: *Bézier-Curves & -Surfaces, Mesh Compression*

2016-2019   **Image Processing**, TU Darmstadt, Summer Term, 1-2 lectures: *Color, Morphology, Image Compression*

2016-2019   **Medical Image Processing**, TU Darmstadt, Winter Term, 2-3 lectures: *Segmentation 1-3*

D. Supervising Activities

Bachelor Theses

1. Karanveer Singh Chahota. "Optimierung nichtholonomer Pfadplanung entlang mehrerer Wegpunkte". Bachelor's Thesis. Darmstadt: Technische Universität, 2018

2. Christoph Bauer. "Segmentierung des Unterkiefergelenks und der Mastoidzellen in CT-Daten des Felsenbeins". Bachelor's Thesis. Darmstadt: Technische Universität, 2017

3. Moritz Weissenberger. "Interaktive Analyse von geplanten medizinischen Bohrkanälen". Bachelor's Thesis. Darmstadt: Technische Universität, 2017

4. Wei-Hung Hsu. "Felsenbeinsegmentierung". Bachelor's Thesis. Darmstadt: Technische Universität, 2017

Master Theses

1. Felix Bernhard. "Nichtholonome Pfadplanung im Felsenbein unter Verwendung des Bevel-Tip-RRT". Master's Thesis. Darmstadt: Technische Universität, 2017

2. Evgheni Croitor. "Automatische Pfadplanung für nicht-lineare Bohrkanäle im Felsenbein". Master's Thesis. Darmstadt: Technische Universität, 2017

3. Alexander Geurts. "Identifikation und Visualisierung unzugänglicher Zugangswege in nichtholonomer Pfadplanung". Master's Thesis. Darmstadt: Technische Universität, 2017

4. Yeimy Paola Valencia Usme. "Automatische Segmentierung der Paukenhöhle und des Antrum Mastoideum". Master's Thesis. Darmstadt: Technische Universität, 2017

E. Curriculum Vitae

Personal Data	
Name	Johannes Ludwig Fauser
Date (Place) of Birth	04.02.1987 (Tübingen)
Nationality	German

Work Experience	
10/2015 - 12/2019	**Research Associate**, *Technical University Darmstadt*, Department of Computer Science, Interactive Graphics Systems Group, Darmstadt.
07/2013 - 09/2015	**Research Associate**, Fraunhofer*Institute for Factory Operation and Automation IFF*, Business Unit *Measurement and Testing Technology*, Magdeburg.

Education	
10/2006 - 08/2012	**Diploma in Mathematics**, *Karlsruhe Institute of Technology*, Karlsruhe.
	Thesis: Implementation of a Mumford-Shah Functional for Segmentation and Inversion of CT-Data using the Level-Set Method.
1997 - 2006	**High School Diploma (Abitur)**, *Gymnasium Langensteinbach*, Langensteinbach.

Glossary

A∗ (pronounced "ay star") A heuristic search algorithm for motion planning. 33, 39, 40

ACVD A VTK extension for remeshing of triangle meshes based of the works of Valette and Chassery [244] (presenting Approximated Centroidal Voronoi Diagrams) and Valette et al. [243]. Found at https://github.com/valette/ACVD. 47, 89

Bi-RRT Bi-directional Rapidly-exploring Trees grow two RRT search trees and try to connect both in between [129]. Also called RRT-connect. 9, 62, 74, 78, 82, 86, 92, 106–108, 110, 111, 113, 119–121, 125

CRISP The Continuum Reconfigurable Incisionless Surgical Parallel (CRISP) robot is a new type of continuum robot for minimally-invasive surgery [6]. 40, 41

Dice An objective measurement function for segmentation quality. 2, 7, 45, 49, 88

Gurobi The Gurobi Optimizer offers state of the art performance for a variety of (non-)convex optimization problems [100] and is freely available for academic purposes. 47, 89

ITK The Insight Segmentation and Registration Toolkit (ITK) [276] is an open-source, cross platform framework offering an exhausting number of both basic and state-of-the-art image processing algorithms written in C**++**. 47, 89

ITK-SNAP ITK-SNAP [277] is a software application dedicated to medical image segmentation that provides, among others, methods for semi-automatic segmentation using active contours and easy intuitive manual delineation. 13

MITK The Medical Imaging Interaction Toolkit (MITK) [257] is an open-source framework for interactive medical image processing extending the functionality of ITK and VTK. 12–14

MMWHS The Multi-Modality Whole Heart Segmentation challenge offers a publicy available dataset of chest CT scans with labels for the major heart chambers as well as visible parts of the pulmonary artery and the ascending aorta. 26, 88, 91, 103, 105, 121

NOMAD atlas-navigated optimal medial axis and deformable model algorithm (NOMAD), proposed in [173] for tubular structures. 22, 23

OMPL The Open Motion Planning Library (OMPL) is an open-source library offering state-of-the-art sampling-based motion planning algorithms [231] and an outstanding design for trajectory planning. 47, 89

ROS The Robot Operating System (ROS) [198] is a flexible framework for writing robot software [205]. 47

RRT* (pronounced "RRT star") A modification of the RRT that guarantees probabilistic completeness and asymptotic optimality. 37, 38, 41, 125

RRT-connect RRT-connect grows two RRT search trees and tries to connect both in between [129]. Also called Bi-RRT. 137

SegTHOR **Seg**mentation of **TH**oracic **O**rgans at **R**isk is a challenge of ISBI 2019 with thoracic CT images and labels for the heart, aorta, esophagus and trachea. 26

Slicer 3D Slicer 3D [79] is an open source software platform for medical image informatics, image processing, and three-dimensional visualization [226]. 12–14, 47, 123

SOFA The Simulation Open Framework Architecture (SOFA) [71] is an open-source framework primarily targeted at real-time simulation, with an emphasis on medical simulation [227]. 12

stent graft A stent graft or endograft is a tubular implant that is placed within the lumen of a vessel. It is used in EVAR to regulate blood flow around aneurysms. 4, 24

U-Net One of the most robust and widely used CNNs for segmentation [204]. 23, 43, 53, 93, 105, 138

V-Net An adaptation of the U-Net architecture using dense blocks [162]. 28, 30

VTK The Visualization Toolkit (VTK) is an open-source, freely available software system for 3D computer graphics, modeling, image processing, volume rendering, scientific visualization, and 2D plotting [213]. 47, 89, 137

Acronyms

AAA Abdominal Aortic Aneurysm 23–26

AC Active Contour 29–31, 53, 124

AFT Adaptive Fractal Tree 40, 41

ASM Active Shape Model 5, 9, 11, 14–16, 23, 29, 47, 53, 57

aVAE Adversarial Variational Autoencoder 29, 31, 32

BVP Boundary Value Problem 69, 106

CAI Computer-Assisted Interventions 46, 47, 49, 124

CBCT Cone Beam Computed Tomography 22, 23, 30, 31

ce-CT contrast-enhanced CT 23, 25, 29

Chorda chorda tympani 21, 23, 86

CNN Convolutional Neural Network 11, 14, 17, 18, 20, 23

Cochlea cochlea 21–23, 86

CRF Conditional Random Field 9, 11, 18, 20, 26–28, 124

CT Computed Tomography 1, 4, 14

CTA Computed Tomographic Angiography 14, 23, 25, 29

EAC external auditory canal 21–23, 86

EMT Electromagnetic Tracking 39, 122

EVAR Endovascular Aortic Repair 24, 43, 63, 112, 121, 123, 124

PCA Principal Component Analysis 15

PCW posterior canal wall 21, 23

PDE Partial Differential Equation 14

PSP Preoperative Surgical Planning 124

RL Reinforcement learning 40, 41

RNN Recurrent Neural network 20, 27, 28, 124

RRT Rapidly-exploring Random Tree 11, 33, 34, 37, 43, 61, 62, 74, 78, 86, 106, 107, 119, 124, 137

RV Right Ventricle 29, 31, 32, 88

SCC semicircular canals 21, 23, 86

SCO Sequential Convex Optimization 36, 37, 39–41, 78, 82, 106, 125

SSC superior semicircular canal 22, 91

SSM Statistical Shape Model 13, 15–17, 22, 23, 31, 32, 47, 49, 50

SVM Support Vector Machine 23, 25

UAV Unmanned Aerial Vehicle 33, 34, 37, 38

UWG Underwater Glider 33, 37, 38

Bibliography

[1] Amir Alansary, Konstantinos Kamnitsas, Alice Davidson, Rostislav Khlebnikov, Martin Rajchl, Christina Malamateniou, Mary Rutherford, Joseph V. Hajnal, Ben Glocker, Daniel Rueckert, and Bernhard Kainz. "Fast Fully Automatic Segmentation of the Human Placenta from Motion Corrupted MRI". In: *Medical Image Computing and Computer-Assisted Intervention – MICCAI 2016*. Ed. by Sebastien Ourselin, Leo Joskowicz, Mert R. Sabuncu, Gozde Unal, and William Wells. Cham: Springer International Publishing, 2016, pp. 589–597.

[2] Thomas Albrecht, Marcel Lüthi, and Thomas Vetter. "Deformable Models". In: *Encyclopedia of Biometrics*. Ed. by Stan Z. Li and Anil Jain. Boston, MA: Springer US, 2009, pp. 210–215.

[3] Ron Alterovitz and Ken Goldberg. *Motion Planning in Medicine: Optimization and Simulation Algorithms for Image-Guided Procedures*. Springer, 2008.

[4] Felix Ambellan, Alexander Tack, Moritz Ehlke, and Stefan Zachow. "Automated segmentation of knee bone and cartilage combining statistical shape knowledge and convolutional neural networks: Data from the Osteoarthritis Initiative". In: *Medical Image Analysis* 52 (2019), pp. 109–118.

[5] G. Ambrosino, M. Ariola, U. Ciniglio, F. Corraro, A. Pironti, and M. Virgilio. "Algorithms for 3D UAV Path Generation and Tracking". In: *Proceedings of the 45th IEEE Conference on Decision and Control*. Dec. 2006, pp. 5275–5280.

[6] P. L. Anderson, A. W. Mahoney, and R. J. Webster. "Continuum Reconfigurable Parallel Robots for Surgery: Shape Sensing and State Estimation With Uncertainty". In: *IEEE Robotics and Automation Letters* 2.3 (July 2017), pp. 1617–1624.

[7] A. Azizi, C. Tremblay, and S. Martel. "Trajectory planning for vascular navigation from 3D angiography images and vessel centerline data". In: *2017 Intern. Conf. on Manip., Autom. and Robot. at Small Scales (MARSS)*. July 2017, pp. 1–6.

[8]   Fabian Balsiger, Yannick Soom, Olivier Scheidegger, and Mauricio Reyes. "Learning Shape Representation on Sparse Point Clouds for Volumetric Image Segmentation". In: *Medical Image Computing and Computer Assisted Intervention – MICCAI 2019*. Ed. by Dinggang Shen, Tianming Liu, Terry M. Peters, Lawrence H. Staib, Caroline Essert, Sean Zhou, Pew-Thian Yap, and Ali Khan. Cham: Springer International Publishing, 2019, pp. 273–281.

[9]   S. Bano, S. Y. Ko, and F. Rodriguez y Baena. "Smooth path planning for a biologically-inspired neurosurgical probe". In: *2012 Annual International Conference of the IEEE Engineering in Medicine and Biology Society*. Aug. 2012, pp. 920–923.

[10] H. Banzhaf, L. Palmieri, D. Nienhüser, T. Schamm, S. Knoop, and J. M. Zöllner. "Hybrid curvature steer: A novel extend function for sampling-based nonholonomic motion planning in tight environments". In: *2017 IEEE 20th International Conference on Intelligent Transportation Systems (ITSC)*. Oct. 2017, pp. 1–8.

[11] Christoph Bauer. "Segmentierung des Unterkiefergelenks und der Mastoidzellen in CT-Daten des Felsenbeins". Bachelor's Thesis. Darmstadt: Technische Universität, 2017.

[12] Ryan A. Beasley. "Medical Robots: Current Systems and Research Directions". In: *Journal of Robotics* 2012 (2012), p. 14.

[13] Meike Becker. "Patientenspezifische Planung für die Multi-Port Otobasischirurgie". PhD thesis. Darmstadt: Technische Universität, Oct. 2014.

[14] Meike Becker, Stefan Hansen, Stefan Wesarg, and Georgios Sakas. "Path Planning for Multi-port Lateral Skull Base Surgery Based on First Clinical Experiences". In: *Clinical Image-Based Procedures. Translational Research in Medical Imaging: Second International Workshop, CLIP 2013, Held in Conjunction with MICCAI 2013, Nagoya, Japan, September 22, 2013, Revised Selected Papers*. Cham: Springer International Publishing, 2014, pp. 23–30.

[15] Meike Becker, Matthias Kirschner, and Georgios Sakas. "Segmentation of risk structures for otologic surgery using the Probabilistic Active Shape Model (PASM)". In: *Proc.SPIE* 9036 (2014), pp. 9036–7.

[16] Meike Becker, Matthias Kirschner, and Georgios Sakas. "Segmentation of risk structures for otologic surgery using the Probabilistic Active Shape Model (PASM)". In: *Medical Imaging 2014: Image-Guided Procedures, Robotic Interventions, and Modeling*. Ed. by Ziv R. Yaniv and David R. Holmes III. Vol. 9036. International Society for Optics and Photonics. SPIE, 2014, pp. 172–178.

[17] Meike Becker, Matthias Kirschner, and Stefan Wesarg. "Konsistente Parametrisierung von Flächen vom Geschlecht 1 zur Bildung eines statistischen Formmodells des Wirbels". In: *Bildverarbeitung für die Medizin 2011: Algorithmen - Systeme - Anwendungen Proceedings des Workshops vom 20. - 22. März 2011 in Lübeck*. Ed. by Heinz Handels, Jan Ehrhardt, Thomas M. Deserno, Hans-Peter Meinzer, and Thomas Tolxdorff. Berlin, Heidelberg: Springer Berlin Heidelberg, 2011, pp. 74–78.

[18] Jur van den Berg, Sachin Patil, and Ron Alterovitz. "Motion planning under uncertainty using iterative local optimization in belief space". In: *The International Journal of Robotics Research* 31.11 (2012), pp. 1263–1278.

[19] Philipp Berg, Samuel Voß, Sylvia Saalfeld, Gábor Janiga, Aslak W. Bergersen, Kristian Valen-Sendstad, Jan Bruening, Leonid Goubergrits, Andreas Spuler, Nicole M. Cancelliere, David A. Steinman, Vitor M. Pereira, Tin Lok Chiu, Anderson Chun On Tsang, Bong Jae Chung, Juan R. Cebral, Salvatore Cito, Jordi Pallarès, Gabriele Copelli, Benjamin Csippa, György Paál, Soichiro Fujimura, Hiroyuki Takao, Simona Hodis, Georg Hille, Christof Karmonik, Saba Elias, Kerstin Kellermann, Muhammad Owais Khan, Alison L. Marsden, Hernán G. Morales, Senol Piskin, Ender A. Finol, Mariya Pravdivtseva, Hamidreza Rajabzadeh-Oghaz, Nikhil Paliwal, Hui Meng, Santhosh Seshadhri, Matthew Howard, Masaaki Shojima, Shin-ichiro Sugiyama, Kuniyasu Niizuma, Sergey Sindeev, Sergey Frolov, Thomas Wagner, Alexander Brawanski, Yi Qian, Yu-An Wu, Kent D. Carlson, Dan Dragomir-Daescu, and Oliver Beuing. "Multiple Aneurysms AnaTomy CHallenge 2018 (MATCH): Phase I: Segmentation". In: *Cardiovascular Engineering and Technology* 9.4 (Dec. 2018), pp. 565–581.

[20] Felix Bernhard. "Nichtholonome Pfadplanung im Felsenbein unter Verwendung des Bevel-Tip-RRT". Master's Thesis. Darmstadt: Technische Universität, 2017.

[21] Gedas Bertasius, Jianbo Shi, and Lorenzo Torresani. "Semantic Segmentation with Boundary Neural Fields". In: *CoRR* abs/1511.02674 (2015).

[22] P. J. Besl and N. D. McKay. "A method for registration of 3-D shapes". In: *IEEE Trans. on Pattern Anal. and Machine Int.* 14.2 (Feb. 1992), pp. 239–256.

[23] Stephen Boyd and Lieven Vandenberghe. *Convex Optimization*. New York, NY, USA: Cambridge University Press, 2004.

[24] Chaim Broit. "Optimal Registration of Deformed Images". AAI8207933. PhD thesis. Philadelphia, PA, USA, 1981.

[25] Marleen de Bruijne, Bram van Ginneken, Max A Viergever, and Wiro J Niessen. "Interactive segmentation of abdominal aortic aneurysms in CTA images". In: *Medical Image Analysis* 8.2 (2004), pp. 127–138.

[26] J. Burgner-Kahrs, D. C. Rucker, and H. Choset. "Continuum Robots for Medical Applications: A Survey". In: *IEEE Transactions on Robotics* 31.6 (Dec. 2015), pp. 1261–1280.

[27] C. Caborni, S. Y. Ko, E. De Momi, G. Ferrigno, and F. R. y Baena. "Risk-based path planning for a steerable flexible probe for neurosurgical intervention". In: *2012 4th IEEE RAS EMBS International Conference on Biomedical Robotics and Biomechatronics (BioRob)*. June 2012, pp. 866–871.

[28] Jinzheng Cai, Le Lu, Zizhao Zhang, Fuyong Xing, Lin Yang, and Qian Yin. "Pancreas Segmentation in MRI Using Graph-Based Decision Fusion on Convolutional Neural Networks". In: *Medical Image Computing and Computer-Assisted Intervention – MICCAI 2016*. Ed. by Sebastien Ourselin, Leo Joskowicz, Mert R. Sabuncu, Gozde Unal, and William Wells. Cham: Springer International Publishing, 2016, pp. 442–450.

[29] J. Cao, J. Cao, Z. Zeng, and L. Lian. "Optimal path planning of underwater glider in 3D dubins motion with minimal energy consumption". In: *OCEANS 2016 - Shanghai*. Apr. 2016, pp. 1–7.

[30] Marco Caversaccio, Kate Gavaghan, Wilhelm Wimmer, Tom Williamson, Juan Ansò, Georgios Mantokoudis, Nicolas Gerber, Christoph Rathgeb, Arne Feldmann, Franca Wagner, Olivier Scheidegger, Martin Kompis, Christian Weisstanner, Masoud Zoka-Assadi, Kai Roesler, Lukas Anschuetz, Markus Huth, and Stefan Weber. "Robotic cochlear implantation: surgical procedure and first clinical experience". In: *Acta Oto-Laryngologica* 137.4 (2017), pp. 447–454.

[31] Kenny H. Cha, Lubomir Hadjiiski, Ravi K. Samala, Heang-Ping Chan, Elaine M. Caoili, and Richard H. Cohan. "Urinary bladder segmentation in CT urography using deep-learning convolutional neural network and level sets". In: *Medical Physics* 43.4 (2016), pp. 1882–1896.

[32] Karanveer Singh Chahota. "Optimierung nichtholonomer Pfadplanung entlang mehrerer Wegpunkte". Bachelor's Thesis. Darmstadt: Technische Universität, 2018.

[33] *CHASE: Child Heart and Health Study in England*. `https://blogs.kingston.ac.uk/retinal/chasedb1/`. Accessed: 14.02.2020.

[34] Xiaojun Chen, Lu Xu, Huixiang Wang, Fang Wang, Qiugen Wang, and Ron Kikinis. "Development of a surgical navigation system based on 3D Slicer for intraoperative implant placement surgery". In: *Medical engineering & physics* 41 (Mar. 2017), pp. 81–89.

[35] Y. Chen, J. M. Oliveira, and I. W. Hunter. "Two-axis bend sensor design, kinematics and control for a continuum robotic endoscope". In: *2013 IEEE International Conference on Robotics and Automation*. May 2013, pp. 704–710.

[36] Yanjie Chen, Wenjun Xu, Zheng Li, Shuang Song, Chwee Ming Lim, YaoNan Wang, and Hongliang Ren. "Safety-Enhanced Motion Planning for Flexible Surgical Manipulator Using Neural Dynamics". In: *IEEE Transactions on Control Systems Technology* 25 (2017), pp. 1711–1723.

[37] Ruida Cheng, Holger R. Roth, Le Lu, Shijun Wang, Baris Turkbey, William Gandler, Evan S. McCreedy, Harsh K. Agarwal, Peter Choyke, Ronald M. Summers, and Matthew J. McAuliffe. "Active appearance model and deep learning for more accurate prostate segmentation on MRI". In: *Medical Imaging 2016: Image Processing*. Ed. by Martin A. Styner and Elsa D. Angelini. Vol. 9784. International Society for Optics and Photonics. SPIE, 2016, pp. 678–686.

[38] W. Chi, J. Liu, M. E. M. K. Abdelaziz, G. Dagnino, C. Riga, C. Bicknell, and G. Yang. "Trajectory Optimization of Robot-Assisted Endovascular Catheterization with Reinforcement Learning". In: *2018 IEEE/RSJ International Conference on Intelligent Robots and Systems (IROS)*. Oct. 2018, pp. 3875–3881.

[39] François Chollet et al. *Keras*. `https://keras.io`. 2015.

[40] Patrick Ferdinand Christ, Mohamed Ezzeldin A. Elshaer, Florian Ettlinger, Sunil Tatavarty, Marc Bickel, Patrick Bilic, Markus Rempfler, Marco Armbruster, Felix Hofmann, Melvin D'Anastasi, Wieland H. Sommer, Seyed-Ahmad Ahmadi, and Bjoern H. Menze. "Automatic Liver and Lesion Segmentation in CT Using Cascaded Fully Convolutional Neural Networks and 3D Conditional Random Fields". In: *Medical Image Computing and Computer-Assisted Intervention – MICCAI 2016*. Ed. by Sebastien Ourselin, Leo Joskowicz, Mert R. Sabuncu, Gozde Unal, and William Wells. Cham: Springer International Publishing, 2016, pp. 415–423.

[41] Özgün Çiçek, Ahmed Abdulkadir, Soeren S. Lienkamp, Thomas Brox, and Olaf Ronneberger. "3D U-Net: Learning Dense Volumetric Segmentation from Sparse Annotation". In: *Medical Image Computing and Computer-Assisted Intervention – MICCAI 2016*. Ed. by Sebastien Ourselin, Leo Joskowicz, Mert R. Sabuncu, Gozde Unal, and William Wells. Cham: Springer International Publishing, 2016, pp. 424–432.

[42] Rachel Claridge, Sam Arnold, Neil Morrison, and André M. van Rij. "Measuring abdominal aortic diameters in routine abdominal computed tomography scans and implications for abdominal aortic aneurysm screening". In: *Journal of Vascular Surgery* 65.6 (2017), pp. 1637–1642.

[43] David B. Comber, E. Bryn Pitt, Hunter B. Gilbert, Matthew W. Powelson, Emily Matijevich, Joseph S. Neimat, Robert J. Webster III, and Eric J. Barth. "Optimization of Curvilinear Needle Trajectories for Transforamenal Hippocampotomy". In: *Operative Neurosurgery* 13.1 (2017), pp. 15–22.

[44] Benoît Combès and Sylvain Prima. "An Efficient EM-ICP Algorithm for Symmetric Consistent Non-linear Registration of Point Sets". In: *Medical Image Computing and Computer-Assisted Intervention – MICCAI 2010*. Ed. by Tianzi Jiang, Nassir Navab, Josien P. W. Pluim, and Max A. Viergever. Berlin, Heidelberg: Springer Berlin Heidelberg, 2010, pp. 594–601.

[45] T.F. Cootes, C.J. Taylor, D.H. Cooper, and J. Graham. "Active Shape Models-Their Training and Application". In: *Computer Vision and Image Understanding* 61.1 (1995), pp. 38–59.

[46] Noah J. Cowan, Ken Goldberg, Gregory S. Chirikjian, Gabor Fichtinger, Ron Alterovitz, Kyle B. Reed, Vinutha Kallem, Wooram Park, Sarthak Misra, and Allison M. Okamura. "Robotic Needle Steering: Design, Modeling, Planning, and Image Guidance". In: *Surgical Robotics: Systems App. and Vis.* Boston, MA: Springer US, 2011, pp. 557–582.

[47] Evgheni Croitor. "Automatische Pfadplanung für nicht-lineare Bohrkanäle im Felsenbein". Master's Thesis. Darmstadt: Technische Universität, 2017.

[48] Joanna Czajkowska, Christian Feinen, Marcin Grzegorzek, Matthias Raspe, and Ralph Wickenhöfer. "A New Aortic Aneurysm CT Series Registration Algorithm". In: *Information Technologies in Biomedicine, Volume 3*. Ed. by Ewa Piętka, Jacek Kawa, and Wojciech Wieclawek. Cham: Springer International Publishing, 2014, pp. 15–26.

[49] B. Dahroug, B. Tamadazte, S. Weber, L. Tavernier, and N. Andreff. "Review on Otological Robotic Systems: Toward Microrobot-Assisted Cholesteatoma Surgery". In: *IEEE Reviews in Biomedical Engineering* 11 (2018), pp. 125–142.

[50] K. Deb, A. Pratap, S. Agarwal, and T. Meyarivan. "A fast and elitist multiobjective genetic algorithm: NSGA-II". In: *IEEE Transactions on Evolutionary Computation* 6.2 (Apr. 2002), pp. 182–197.

[51] E. W. Dijkstra. "A note on two problems in connexion with graphs". In: *Numerische Mathematik* 1.1 (Dec. 1959), pp. 269–271.

[52] Ellen D. Dillavou, Satish C. Muluk, and Michel S. Makaroun. "Improving aneurysm-related outcomes: Nationwide benefits of endovascular repair". In: *Journal of Vascular Surgery* 43.3 (2006), pp. 446–452.

[53] Jing Dong, Mustafa Mukadam, Frank Dellaert, and Byron Boots. "Motion Planning as Probabilistic Inference using Gaussian Processes and Factor Graphs". In: *Robotics: Science and Systems*. 2016.

[54] Bernhard Dorweiler, Hazem El Beyrouti, Christian Friedrich Vahl, Pia-Elisabeth Baqué, and Ahmed Ghazy. "Gefäßmedizin in der Zukunft - Möglichkeiten mit 3D-Druckverfahren". In: *Zentralbl Chir* EFirst (2019).

[55] Qi Dou, Hao Chen, Yueming Jin, Lequan Yu, Jing Qin, and Pheng-Ann Heng. "3D Deeply Supervised Network for Automatic Liver Segmentation from CT Volumes". In: *Medical Image Computing and Computer-Assisted Intervention – MICCAI 2016*. Ed. by Sebastien Ourselin, Leo Joskowicz, Mert R. Sabuncu, Gozde Unal, and William Wells. Cham: Springer International Publishing, 2016, pp. 149–157.

[56] Qi Dou, Lequan Yu, Hao Chen, Yueming Jin, Xin Yang, Jing Qin, and Pheng-Ann Heng. "3D deeply supervised network for automated segmentation of volumetric medical images". In: *Medical Image Analysis* 41 (2017). Special Issue on the 2016 Conference on Medical Image Computing and Computer Assisted Intervention (Analog to MICCAI 2015), pp. 40–54.

[57] Georg Dougherty. *Medical Image Processing*. New York: Springer, 20011.

[58] *DRIVE: Digital Retinal Images for Vessel Extraction*. `http://www.isi.uu.nl/Research/Databases/DRIVE/`. Accessed: 14.02.2020.

[59] Yan Duan, Sachin Patil, John Schulman, Ken Goldberg, and P. Abbeel. "Planning locally optimal, curvature-constrained trajectories in 3D using sequential convex optimization". In: *2014 IEEE Intern. Conf. on Robot. and Autom. (ICRA)*. May 2014, pp. 5889–5895.

[60] L. E. Dubins. "On Curves of Minimal Length with a Constraint on Average Curvature, and with Prescribed Initial and Terminal Positions and Tangents". In: *American Journal of Mathematics* 79.3 (1957), pp. 497–516.

[61] Vincent Duindam, Ron Alterovitz, S. Sastry, and Ken Goldberg. "Skrew-Based Motion Planning for Bevel-Tip Flexible Needles in 3D Environments with Obstacles". In: *IEEE Int. Conf. on Rob. a. Autom.* May 2008, pp. 2483–2488.

[62] Vincent Duindam, Jijie Xu, Ron Alterovitz, Shankar Sastry, and Ken Goldberg. "3D Motion Planning Algorithms for Steerable Needles Using Inverse Kinematics". In: *Int J Rob Res* 57 (2009), pp. 535–549.

[63] H. Eilers, S. Baron, T. Ortmaier, B. Heimann, C. Baier, T. S. Rau, M. Leinung, and O. Majdani. "Navigated, robot assisted drilling of a minimally invasive cochlear access". In: *2009 IEEE International Conference on Mechatronics*. Apr. 2009, pp. 1–6.

[64] M. Elbanhawi and M. Simic. "Sampling-Based Robot Motion Planning: A Review". In: *IEEE Access* 2 (2014), pp. 56–77.

[65] J. A. Engh and at al. "Flexible Needle Steering System for Percutaneous Access to Deep Zones of the Brain". In: *Proc. of IEEE 32nd Ann. Northeast Bioeng. Conf.* Apr. 2006, pp. 103–104.

[66] Caroline Essert, Claire Haegelen, Florent Lalys, Alexandre Abadie, and Pierre Jannin. "Automatic computation of electrode trajectories for Deep Brain Stimulation: a hybrid symbolic and numerical approach". In: *International Journal of Computer Assisted Radiology and Surgery* 7.4 (July 2012), pp. 517–532.

[67] Caroline Essert, Pramod P. Rao, Afshin Gangi, and Leo Joskowicz. "3D Modelling of the Residual Freezing for Renal Cryoablation Simulation and Prediction". In: *Medical Image Computing and Computer Assisted Intervention – MICCAI 2019*. Ed. by Dinggang Shen, Tianming Liu, Terry M. Peters, Lawrence H. Staib, Caroline Essert, Sean Zhou, Pew-Thian Yap, and Ali Khan. Cham: Springer International Publishing, 2019, pp. 209–217.

[68] "Evaluation of Algorithms for Multi-Modality Whole Heart Segmentation: An Open-Access Grand Challenge". In: *CoRR* abs/1902.07880 (2019).

[69] Mitchell N. Faddis, Walter Blume, Jennifer Finney, Andrew Hall, John Rauch, Jon Sell, Kyongtae Ty Bae, Michael Talcott, and Bruce Lindsay. "Novel, Magnetically Guided Catheter for Endocardial Mapping and Radiofrequency Catheter Ablation". In: *Circulation*. Vol. 106. 23. Nov. 2002, pp. 2980–2985.

[70] Zhou Fang, Mengyun Qiao, Yi Guo, Yuanyuan Wang, Jiawei Li, Shichong Zhou, and Cai Chang. "Combining a Fully Convolutional Network and an Active Contour Model for Automatic 2D Breast Tumor Segmentation from Ultrasound Images". In: *Journal of Medical Imaging and Health Informatics* 9.7 (2019), pp. 1510–1515.

[71] François Faure, Christian Duriez, Hervé Delingette, Jérémie Allard, Benjamin Gilles, Stéphanie Marchesseau, Hugo Talbot, Hadrien Courtecuisse, Guillaume Bousquet, Igor Peterlik, and Stéphane Cotin. "SOFA: A Multi-Model Framework for Interactive Physical Simulation". In: *Soft Tissue Biomechanical Modeling for Computer Assisted Surgery*. Ed. by Yohan Payan. Vol. 11. Studies in Mechanobiology, Tissue Engineering and Biomaterials. Springer, June 2012, pp. 283–321.

[72] Johannes Fauser, Romol Chadda, Yannik Goergen, Markus Hessinger, Paul Motzki, Igor Stenin, Julie Kristin, Thomas Klenzner, Jörg Schipper, Stefan Seelecke, Roland Werthschützky, Mario Kupnik, and Anirban Mukhopadhyay. "Planning for Flexible Surgical Robots via Bézier Spline Translation". In: *IEEE Robotics and Automation Letters* 4.4 (Oct. 2019), pp. 3270–3277.

[73] Johannes Fauser, Moritz Fuchs, Ahmed Ghazy, Bernhard Dorweiler, and Anirban Mukhopadhyay. "Preoperative Planning for Guidewires Employing Shape-Regularized Segmentation and Optimized Trajectories". In: *OR 2.0 Context-Aware Operating Theaters and Machine Learning in Clinical Neuroimaging*. Ed. by Luping Zhou, Duygu Sarikaya, Seyed Mostafa Kia, Stefanie Speidel, Anand Malpani, Daniel Hashimoto, Mohamad Habes, Tommy Löfstedt, Kerstin Ritter, and Hongzhi Wang. Cham: Springer International Publishing, 2019, pp. 12–20.

[74] Johannes Fauser, Georgios Sakas, and Anirban Mukhopadhyay. "Planning nonlinear access paths for temporal bone surgery". In: *Intern. J. of Comp. Ass. Radiology and Surgery* 13.5 (May 2018), pp. 637–646.

[75] Johannes Fauser, Igor Stenin, Markus Bauer, Wei-Hung Hsu, Julia Kristin, Thomas Klenzner, Jörg Schipper, and Anirban Mukhopadhyay. "Toward an automatic preoperative pipeline for image-guided temporal bone surgery". In: *Intern. J. of Comp. Ass. Radiology and Surgery* (Mar. 2019).

[76] Johannes Fauser, Igor Stenin, Julia Kristin, Thomas Klenzner, Jörg Schipper, Dieter Fellner, and Anirban Mukhopadhyay. "Generalized Trajectory Planning for Nonlinear Interventions". In: *OR 2.0 Context-Aware Operating Theaters, Computer Assisted Robotic Endoscopy, Clinical Image-Based Procedures, and Skin Image Analysis*. Cham: Springer International Publishing, 2018, pp. 46–53.

[77] Johannes Fauser, Igor Stenin, Julia Kristin, Thomas Klenzner, Jörg Schipper, and Anirban Mukhopadhyay. "Optimizing Clearance of Bézier Spline Trajectories for Minimally-Invasive Surgery". In: *Medical Image Computing and Computer Assisted Intervention – MICCAI 2019*. Ed. by Dinggang Shen, Tianming Liu, Terry M. Peters, Lawrence H. Staib, Caroline Essert, Sean Zhou, Pew-Thian Yap, and Ali Khan. Cham: Springer International Publishing, 2019, pp. 20–28.

[78] Johannes Fauser, Igor Stenin, Julia Kristin, Thomas Klenzner, Jörg Schipper, and Georgios Sakas. "A software tool for planning and evaluation of non-linear trajectories for minimally invasive lateral skull base surgery". In: *Tagungsb. der 15. Jahrestag. der Dtsch. Ges. f. Comput.- und Roboterass. Chirurgie e.V. (CURAC)*. 2016, pp. 125–126.

[79] Andriy Fedorov, Reinhard Beichel, Jayashree Kalpathy-Cramer, Julien Finet, Jean-Christophe Fillion-Robin, Sonia Pujol, Christian Bauer, Dominique Jennings, Fiona Fennessy, Milan Sonka, John Buatti, Stephen Aylward, James V. Miller, Steve Pieper, and Ron Kikinis. "3D Slicer as an image computing platform for the Quantitative Imaging Network". In: *Magnetic resonance imaging* 30.9 (Nov. 2012). S0730-725X(12)00181-6[PII], pp. 1323–1341.

[80] A. Ferreira, J. M. R. S. Tavares, and F. Gentil. "A review of segmentation algorithms for ear image data". In: *7th Iberian Conf. on Inf. Sys. and Techn. (CISTI 2012)*. June 2012, pp. 1–6.

[81] L. Fichera, N. P. Dillon, D. Zhang, I. S. Godage, M. A. Siebold, B. I. Hartley, Jack H. Noble, P. T. Russell, Robert F. Labadie, and R. J. Webster. "Through the Eustachian Tube and Beyond: A New Miniature Robotic Endoscope to See Into the Middle Ear". In: *IEEE Rob. and Autom. Letters* 2.3 (July 2017), pp. 1488–1494.

[82] H. Fu, Y. Xu, D. W. K. Wong, and J. Liu. "Retinal vessel segmentation via deep learning network and fully-connected conditional random fields". In: *2016 IEEE 13th International Symposium on Biomedical Imaging (ISBI)*. Apr. 2016, pp. 698–701.

[83] Huazhu Fu, Yanwu Xu, Stephen Lin, Damon Wing Kee Wong, and Jiang Liu. "DeepVessel: Retinal Vessel Segmentation via☐Deep Learning and Conditional Random☐Field". In: *Medical Image Computing and Computer-Assisted Intervention – MICCAI 2016*. Ed. by Sebastien Ourselin, Leo Joskowicz, Mert R. Sabuncu, Gozde Unal, and William Wells. Cham: Springer International Publishing, 2016, pp. 132–139.

[84] M. Fu, A. Kuntz, R. J. Webster, and Ron Alterovitz. "Safe Motion Planning for Steerable Needles Using Cost Maps Automatically Extracted from Pulmonary Images". In: *2018 IEEE/RSJ International Conference on Intelligent Robots and Systems (IROS)*. Oct. 2018, pp. 4942–4949.

[85] K. H. Fuchs. "Minimally Invasive Surgery". In: *Endoscopy* 34.02 (2002). 154, pp. 154–159.

[86] Alexiades G., Dhanasingh A, and Jolly C. "Method to estimate the complete and two-turn cochlear duct length". In: *Otology & Neurotology* 36.5 (May 2015), pp. 904–7.

[87] Jonathan D. Gammell, Siddhartha S. Srinivasa, and Timothy D. Barfoot. "BIT*: Batch Informed Trees for Optimal Sampling-based Planning via Dynamic Programming on Implicit Random Geometric Graphs". In: *CoRR* abs/1405.5848 (2014).

[88] F. Ganet, M. Q. Le, J. F. Capsal, P. Lermusiaux, L. Petit, A. Millon, and P. J. Cottinet. "Development of a smart guide wire using an electrostrictive polymer: option for steerable orientation and force feedback". In: *Sci Rep* 5 (Dec. 2015), pp. 18593–18593.

[89] M. Gao, Z. Xu, L. Lu, A. Wu, I. Nogues, R. M. Summers, and D. J. Mollura. "Segmentation label propagation using deep convolutional neural networks and dense conditional random field". In: *2016 IEEE 13th International Symposium on Biomedical Imaging (ISBI)*. Apr. 2016, pp. 1265–1268.

[90] Nicolas Gerber, Brett Bell, Kate Gavaghan, Christian Weisstanner, Marco Caversaccio, and Stefan Weber. "Surgical planning tool for robotically assisted hearing aid implantation". In: *International Journal of Computer Assisted Radiology and Surgery* 9.1 (Jan. 2014), pp. 11–20.

[91] Alexander Geurts. "Identifikation und Visualisierung unzugänglicher Zugangswege in nichtholonomer Pfadplanung". Master's Thesis. Darmstadt: Technische Universität, 2017.

[92] Ahmed Ghazy, Rayan Chaban, Christian-Friedrich Vahl, and Bernhard Dorweiler. "Development and evaluation of 3-dimensional printed models of the human tracheobronchial system for training in flexible bronchoscopy". In: *Interactive CardioVascular and Thoracic Surgery* 28.1 (July 2018), pp. 137–143.

[93] Kristina A. Giles, Frank Pomposelli, Allen Hamdan, Mark Wyers, Ami Jhaveri, and Marc L. Schermerhorn. "Decrease in total aneurysm-related deaths in the era of endovascular aneurysm repair". In: *Journal of Vascular Surgery* 49.3 (2009), pp. 543–550.

[94] Rohit Girdhar, David F. Fouhey, Mikel Rodriguez, and Abhinav Gupta. "Learning a Predictable and Generative Vector Representation for Objects". In: *Computer Vision – ECCV 2016*. Ed. by Bastian Leibe, Jiri Matas, Nicu Sebe, and Max Welling. Cham: Springer International Publishing, 2016, pp. 484–499.

[95]   Ehsan Golkar, Pramod P. Rao, Leo Joskowicz, Afshin Gangi, and Caroline Essert. "GPU-based 3D iceball modeling for fast cryoablation simulation and planning". In: *International Journal of Computer Assisted Radiology and Surgery* 14.9 (Sept. 2019), pp. 1577–1588.

[96]   Rafael C. Gonzalez and Richard E. Woods. *Digital image processing*. New York, N.Y., 2018.

[97]   Ian Goodfellow, Jean Pouget-Abadie, Mehdi Mirza, Bing Xu, David Warde-Farley, Sherjil Ozair, Aaron Courville, and Yoshua Bengio. "Generative Adversarial Nets". In: *Advances in Neural Information Processing Systems 27*. Ed. by Z. Ghahramani, M. Welling, C. Cortes, N. D. Lawrence, and K. Q. Weinberger. Curran Associates, Inc., 2014, pp. 2672–2680.

[98]   Josephine Granna, Arya Nabavi, and Jessica Burgner-Kahrs. "Computer-assisted planning for a concentric tube robotic system in neurosurgery". In: *International Journal of Computer Assisted Radiology and Surgery* 14.2 (Feb. 2019), pp. 335–344.

[99]   Xiaotao Guo, Lawrence H. Schwartz, and Binsheng Zhao. "Automatic liver segmentation by integrating fully convolutional networks into active contour models". In: *Medical Physics* 46.10 (2019), pp. 4455–4469.

[100]   LLC Gurobi Optimization. *Gurobi Optimizer Reference Manual*. 2019.

[101]   N. Hamze, P. Collet, and C. Essert. "Evolutionary approaches for surgical path planning: A quantitative study on Deep Brain Stimulation". In: *2017 IEEE Congress on Evolutionary Computation (CEC)*. June 2017, pp. 1087–1094.

[102]   Noura Hamzé, Jimmy Voirin, Pierre Collet, Pierre Jannin, Claire Haegelen, and Caroline Essert. "Pareto Front vs. Weighted Sum for Automatic Trajectory Planning of Deep Brain Stimulation". In: *Medical Image Computing and Computer-Assisted Intervention – MICCAI 2016: 19th International Conference, Athens, Greece, October 17-21, 2016, Proceedings, Part I*. Ed. by Sebastien Ourselin, Leo Joskowicz, Mert R. Sabuncu, Gozde Unal, and William Wells. Cham: Springer International Publishing, 2016, pp. 534–541.

[103]   Miaofei Han, Guang Yao, Wenhai Zhang, Guangrui Mu, Yiqiang Zhan, Xiaoping Zhou, and Yaozong Gao. "Segmentation of CT Thoracic Organs by Multi-resolution VB-nets". In: *SegTHOR@ISBI*. 2019.

[104] Patrick Hangge, Yash Pershad, Avery A. Witting, Hassan Albadawi, and Rahmi Oklu. "Three-dimensional (3D) printing and its applications for aortic diseases". In: *Cardiovascular diagnosis and therapy* 8.Suppl 1 (Apr. 2018). cdt-08-S1-S19[PII], S19–S25.

[105] P. E. Hart, N. J. Nilsson, and B. Raphael. "A Formal Basis for the Heuristic Determination of Minimum Cost Paths". In: *IEEE Transactions on Systems Science and Cybernetics* 4.2 (July 1968), pp. 100–107.

[106] Ali Hatamizadeh, Assaf Hoogi, Debleena Sengupta, Wuyue Lu, Brian Wilcox, Daniel Rubin, and Demetri Terzopoulos. "Deep Active Lesion Segmentation". In: *Machine Learning in Medical Imaging*. Ed. by Heung-Il Suk, Mingxia Liu, Pingkun Yan, and Chunfeng Lian. Cham: Springer International Publishing, 2019, pp. 98–105.

[107] B. He, D. Xiao, Q. Hu, and F. Jia. "Automatic Magnetic Resonance Image Prostate Segmentation Based on Adaptive Feature Learning Probability Boosting Tree Initialization and CNN-ASM Refinement". In: *IEEE Access* 6 (2018), pp. 2005–2015.

[108] Tobias Heimann, Sascha Münzing, Hans-Peter Meinzer, and Ivo Wolf. "A Shape-Guided Deformable Model with Evolutionary Algorithm Initialization for 3D Soft Tissue Segmentation". In: *Information Processing in Medical Imaging*. Ed. by Nico Karssemeijer and Boudewijn Lelieveldt. Berlin, Heidelberg: Springer Berlin Heidelberg, 2007, pp. 1–12.

[109] "Felsenbein". In: *Der Radiologe* 54.4 (2014). Ed. by C. Herold, S. Delorme, T. Helmberger, and W. Reith. petrous portion of the temporal bone, pp. 321–355.

[110] C. Herz, K. MacNeil, P. A. Behringer, J. Tokuda, A. Mehrtash, P. Mousavi, R. Kikinis, F. M. Fennessy, C. M. Tempany, K. Tuncali, and A. Fedorov. "Open Source Platform for Transperineal In-bore MRI-guided Targeted Prostate Biopsy". In: *IEEE Transactions on Biomedical Engineering* (2019), pp. 1–12.

[111] A. Hoogi, A. Subramaniam, R. Veerapaneni, and D. L. Rubin. "Adaptive Estimation of Active Contour Parameters Using Convolutional Neural Networks and Texture Analysis". In: *IEEE Transactions on Medical Imaging* 36.3 (Mar. 2017), pp. 781–791.

[112] S. Hota and D. Ghose. "Optimal geometrical path in 3D with curvature constraint". In: *2010 IEEE/RSJ Int. Conf. on Intelligent Robots and Systems*. Oct. 2010, pp. 113–118.

[113]   S. Hota and D. Ghose. "Optimal path planning for an aerial vehicle in 3D space".
         In: *49th IEEE Conference on Decision and Control (CDC)*. Dec. 2010, pp. 4902–
         4907.

[114]   S. Hota and D. Ghose. "Optimal transition trajectory for waypoint following". In:
         2013 IEEE Int. Conf. on Control Applications (CCA). Aug. 2013, pp. 1030–1035.

[115]   Wei-Hung Hsu. "Felsenbeinsegmentierung". Bachelor's Thesis. Darmstadt: Tech-
         nische Universität, 2017.

[116]   K. Hu, Q. Gan, Y. Zhang, S. Deng, F. Xiao, W. Huang, C. Cao, and X. Gao. "Brain
         Tumor Segmentation Using Multi-Cascaded Convolutional Neural Networks and
         Conditional Random Field". In: *IEEE Access* 7 (2019), pp. 92615–92629.

[117]   Yuzhou Hu, Yi Guo, Yuanyuan Wang, Jinhua Yu, Jiawei Li, Shichong Zhou, and
         Cai Chang. "Automatic tumor segmentation in breast ultrasound images using a
         dilated fully convolutional network combined with an active contour model". In:
         Medical Physics 46.1 (2019), pp. 215–228.

[118]   Fabian Isensee, Jens Petersen, André Klein, David Zimmerer, Paul F. Jaeger, Simon
         Kohl, Jakob Wasserthal, Gregor Koehler, Tobias Norajitra, Sebastian J. Wirkert,
         and Klaus H. Maier-Hein. "nnU-Net: Self-adapting Framework for U-Net-Based
         Medical Image Segmentation". In: *CoRR* abs/1809.10486 (2018).

[119]   C. Jin, J. Feng, L. Wang, H. Yu, J. Liu, J. Lu, and J. Zhou. "Left Atrial Appendage
         Segmentation Using Fully Convolutional Neural Networks and Modified Three-
         Dimensional Conditional Random Fields". In: *IEEE Journal of Biomedical and
         Health Informatics* 22.6 (Nov. 2018), pp. 1906–1916.

[120]   Florian Jung, Sebastian Steger, Oliver Knapp, Matthias Noll, and Stefan Wesarg.
         "COSMO - Coupled Shape Model for Radiation Therapy Planning of Head and Neck
         Cancer". In: *Clinical Image-Based Procedures. Translational Research in Medical
         Imaging: Third International Workshop, CLIP 2014, Held in Conjunction with
         MICCAI 2014, Boston, MA, USA, September 14, 2014, Revised Selected Papers*.
         Ed. by Marius George Linguraru, Cristina Oyarzun Laura, Raj Shekhar, Stefan
         Wesarg, Miguel Ángel González Ballester, Klaus Drechsler, Yoshinobu Sato, and
         Marius Erdt. Cham: Springer International Publishing, 2014, pp. 25–32.

[121]   M. Kalakrishnan, S. Chitta, E. Theodorou, P. Pastor, and S. Schaal. "STOMP:
         Stochastic trajectory optimization for motion planning". In: *2011 IEEE Interna-
         tional Conference on Robotics and Automation*. May 2011, pp. 4569–4574.

[122] Konstantinos Kamnitsas, Christian Ledig, Virginia F.J. Newcombe, Joanna P. Simpson, Andrew D. Kane, David K. Menon, Daniel Rueckert, and Ben Glocker. "Efficient multi-scale 3D CNN with fully connected CRF for accurate brain lesion segmentation". In: *Medical Image Analysis* 36 (2017), pp. 61–78.

[123] Sertac Karaman and Emilio Frazzoli. "Sampling-based algorithms for optimal motion planning". In: *The International Journal of Robotics Research* 30.7 (2011), pp. 846–894.

[124] Matthias Kirschner. "The Probabilistic Active Shape Model: From Model Construction to Flexible Medical Image Segmentation". PhD thesis. TU Darmstadt, 2013.

[125] H. Martin Kjer, Jens Fagertun, Sergio Vera, Debora Gil, Miguel Ángel González Ballester, and Rasmus R. Paulsen. "Free-form image registration of human cochlear mu CT data using skeleton similarity as anatomical prior". In: *Pattern Recognition Letters* 76 (2016). Special Issue on Skeletonization and its Application, pp. 76–82.

[126] Thomas Klenzner, Chiu Chun Ngan, Felix Bernhard Knapp, Hayo Knoop, Jan Kromeier, Antje Aschendorff, Evangelos Papastathopoulos, Joerg Raczkowsky, Heinz Wörn, and Joerg Schipper. "New strategies for high precision surgery of the temporal bone using a robotic approach for cochlear implantation". In: *European Archives of Oto-Rhino-Laryngology* 266.7 (Oct. 2008), p. 955.

[127] Philipp Krähenbühl and Vladlen Koltun. "Efficient Inference in Fully Connected CRFs with Gaussian Edge Potentials". In: *Advances in Neural Information Processing Systems 24*. Ed. by J. Shawe-Taylor, R. S. Zemel, P. L. Bartlett, F. Pereira, and K. Q. Weinberger. Curran Associates, Inc., 2011, pp. 109–117.

[128] In: *Radiologie up2date* 19.1 (2019). Ed. by K.-F. Kreitner, J. Barkhausen, E. Hattingen, D. Maintz, and C. Stroszczynski. Bildgebende Diagnostik des Innenohrs vor Cochleaimplantation, pp. 79–89.

[129] James J. Kuffner Jr. and Steve M. LaValle. "RRT-connect: An efficient approach to single-query path planning". In: *Proceedings 2000 ICRA. Millennium Conference. IEEE Int. Conf. on Rob. and Autom. Symposia Proc. (Cat. No.00CH37065)*. Vol. 2. 2000, 995–1001 vol.2.

[130] A. Kuntz, A. W. Mahoney, N. E. Peckman, P. L. Anderson, F. Maldonado, R. J. Webster, and Ron Alterovitz. "Motion planning for continuum reconfigurable incisionless surgical parallel robots". In: *2017 IEEE/RSJ International Conference on Intelligent Robots and Systems (IROS)*. Sept. 2017, pp. 6463–6469.

[131] A. Kuntz, L. G. Torres, R. H. Feins, R. J. Webster, and Ron Alterovitz. "Motion planning for a three-stage multilumen transoral lung access system". In: *2015 IEEE/RSJ International Conference on Intelligent Robots and Systems (IROS)*. Sept. 2015, pp. 3255–3261.

[132] John D. Lafferty, Andrew McCallum, and Fernando C. N. Pereira. "Conditional Random Fields: Probabilistic Models for Segmenting and Labeling Sequence Data". In: *Proceedings of the Eighteenth International Conference on Machine Learning*. ICML '01. San Francisco, CA, USA: Morgan Kaufmann Publishers Inc., 2001, pp. 282–289.

[133] Florent Lalys, Vincent Yan, Adrien Kaladji, Antoine Lucas, and Simon Esneault. "Generic thrombus segmentation from pre- and post-operative CTA". In: *International Journal of Computer Assisted Radiology and Surgery* 12.9 (Sept. 2017), pp. 1501–1510.

[134] Fabien Lareyre, Cédric Adam, Marion Carrier, Carine Dommerc, Claude Mialhe, and Juliette Raffort. "A fully automated pipeline for mining abdominal aortic aneurysm using image segmentation". In: *Scientific Reports* 9.1 (2019), p. 13750.

[135] Steve M. LaValle. *Planning Algorithms*. Cambridge University Press, 2006.

[136] Steve M. LaValle. *Rapidly-exploring random trees: A new tool for path planning*. Technical Report 98-11. Dept. of Computer Science, Iowa State University, US, 1998.

[137] T.C. Lee, R.L. Kashyap, and C.N. Chu. "Building Skeleton Models via 3-D Medial Surface Axis Thinning Algorithms". In: *CVGIP: Graphical Models and Image Processing* 56.6 (1994), pp. 462–478.

[138] Y. Li, C. P. Ho, M. Toulemonde, N. Chahal, R. Senior, and M. Tang. "Fully Automatic Myocardial Segmentation of Contrast Echocardiography Sequence Using Random Forests Guided by Shape Model". In: *IEEE Transactions on Medical Imaging* 37.5 (May 2018), pp. 1081–1091.

[139] Yangyan Li, Rui Bu, Mingchao Sun, and Baoquan Chen. "PointCNN: Convolution On X-Transformed Points". In: *CoRR* abs/1801.07791 (2018).

[140] Z. Li, A. Lin, X. Yang, and J. Wu. "Left ventricle segmentation by combining convolution neural network with active contour model and tensor voting in short-axis MRI". In: *2017 IEEE International Conference on Bioinformatics and Biomedicine (BIBM)*. Nov. 2017, pp. 736–739.

[141] Zeju Li, Yuanyuan Wang, Jinhua Yu, Zhifeng Shi, Yi Guo, Liang Chen, and Ying Mao. "Low-Grade Glioma Segmentation Based on CNN with Fully Connected CRF". In: *Journal of Healthcare Engineering* 2017 (2017), p. 12.

[142] Libin Liang, Derek Cool, Nirmal Kakani, Guangzhi Wang, Hui Ding, and Aaron Fenster. "Development of a Multi-objective Optimized Planning Method for Microwave Liver Tumor Ablation". In: *Medical Image Computing and Computer Assisted Intervention – MICCAI 2019*. Ed. by Dinggang Shen, Tianming Liu, Terry M. Peters, Lawrence H. Staib, Caroline Essert, Sean Zhou, Pew-Thian Yap, and Ali Khan. Cham: Springer International Publishing, 2019, pp. 110–118.

[143] Y. Lin and S. Saripalli. "Path planning using 3D Dubins Curve for Unmanned Aerial Vehicles". In: *2014 International Conference on Unmanned Aircraft Systems (ICUAS)*. May 2014, pp. 296–304.

[144] Geert Litjens, Thijs Kooi, Babak Ehteshami Bejnordi, Arnaud Arindra Adiyoso Setio, Francesco Ciompi, Mohsen Ghafoorian, Jeroen A.W.M. van der Laak, Bram van Ginneken, and Clara I. Sánchez. "A survey on deep learning in medical image analysis". In: *Medical Image Analysis* 42.Supplement C (2017), pp. 60–88.

[145] F. Liu, A. Garriga-Casanovas, R. Secoli, and F. Rodriguez y Baena. "Fast and Adaptive Fractal Tree-Based Path Planning for Programmable Bevel Tip Steerable Needles". In: *IEEE Robotics and Automation Letters* 1.2 (July 2016), pp. 601–608.

[146] Ping Liu, Jing Qin, Bin Duan, Qiong Wang, Xiaoyu Tan, Baoliang Zhao, Peneyra Libao Jonnathan, Chee-Kong Chui, and Pheng-Ann Heng. "Overlapping radiofrequency ablation planning and robot-assisted needle insertion for large liver tumors". In: *The International Journal of Medical Robotics and Computer Assisted Surgery* 15.1 (2019). e1952 RCS-18-0049.R3, e1952.

[147] Wen P. Liu, Mahdi Azizian, Jonathan Sorger, Russell H. Taylor, Brian K. Reilly, Kevin Cleary, and Diego Preciado. "Cadaveric Feasibility Study of da Vinci Si–Assisted Cochlear Implant With Augmented Visual Navigation for Otologic Surgery". In: *JAMA Otolaryngology–Head & Neck Surgery* 140.3 (Mar. 2014), pp. 208–214.

[148] J. Long, E. Shelhamer, and T. Darrell. "Fully convolutional networks for semantic segmentation". In: *2015 IEEE Conference on Computer Vision and Pattern Recognition (CVPR)*. June 2015, pp. 3431–3440.

[149] Karen López-Linares, Nerea Aranjuelo, Luis Kabongo, Gregory Maclair, Nerea Lete, Mario Ceresa, Ainhoa García-Familiar, Iván Macía, and Miguel A. González Ballester. "Fully automatic detection and segmentation of abdominal aortic throm-

bus in post-operative CTA images using Deep Convolutional Neural Networks". In: *Medical Image Analysis* 46 (2018), pp. 202–214.

[150] William E. Lorensen and Harvey E. Cline. "Marching Cubes: A High Resolution 3D Surface Construction Algorithm". In: *Proceedings of the 14th Annual Conference on Computer Graphics and Interactive Techniques*. SIGGRAPH '87. New York, NY, USA: ACM, 1987, pp. 163–169.

[151] Jen-Tang Lu, Rupert Brooks, Stefan Hahn, Jin Chen, Varun Buch, Gopal Kotecha, Katherine P. Andriole, Brian Ghoshhajra, Joel Pinto, Paul Vozila, Mark Michalski, and Neil A. Tenenholtz. "DeepAAA: Clinically Applicable and Generalizable Detection of Abdominal Aortic Aneurysm Using Deep Learning". In: *Medical Image Computing and Computer Assisted Intervention – MICCAI 2019*. Ed. by Dinggang Shen, Tianming Liu, Terry M. Peters, Lawrence H. Staib, Caroline Essert, Sean Zhou, Pew-Thian Yap, and Ali Khan. Cham: Springer International Publishing, 2019, pp. 723–731.

[152] P. Lu, L. Barazzetti, V. Chandran, K. Gavaghan, S. Weber, N. Gerber, and M. Reyes. "Highly Accurate Facial Nerve Segmentation Refinement From CBCT/CT Imaging Using a Super-Resolution Classification Approach". In: *IEEE Transactions on Biomedical Engineering* 65.1 (Jan. 2018), pp. 178–188.

[153] Jingting Ma, Feng Lin, Stefan Wesarg, and Marius Erdt. "A Novel Bayesian Model Incorporating Deep Neural Network and Statistical Shape Model for Pancreas Segmentation". In: *Medical Image Computing and Computer Assisted Intervention – MICCAI 2018*. Ed. by Alejandro F. Frangi, Julia A. Schnabel, Christos Davatzikos, Carlos Alberola-López, and Gabor Fichtinger. Cham: Springer International Publishing, 2018, pp. 480–487.

[154] Jingting Ma, Anqi Wang, Feng Lin, Stefan Wesarg, and Marius Erdt. "A novel robust kernel principal component analysis for nonlinear statistical shape modeling from erroneous data". In: *Computerized Medical Imaging and Graphics* 77 (2019), p. 101638.

[155] Jun Ma and Xiaoping Yang. "Automatic dental root CBCT image segmentation based on CNN and level set method". In: *Medical Imaging 2019: Image Processing*. Ed. by Elsa D. Angelini and Bennett A. Landman. Vol. 10949. International Society for Optics and Photonics. SPIE, 2019, pp. 668–674.

[156] Iván Macía, Jon Haitz Legarreta, Céline Paloc, Manuel Graña, Josu Maiora, Guillermo García, and Mariano de Blas. "Segmentation of Abdominal Aortic Aneurysms in CT Images Using a Radial Model Approach". In: *Intelligent Data*

Engineering and Automated Learning - IDEAL 2009. Ed. by Emilio Corchado and Hujun Yin. Berlin, Heidelberg: Springer Berlin Heidelberg, 2009, pp. 664–671.

[157] Josu Maiora, Borja Ayerdi, and Manuel Graña. "Random forest active learning for AAA thrombus segmentation in computed tomography angiography images". In: *Neurocomputing* 126 (2014). Recent trends in Intelligent Data Analysis Online Data Processing, pp. 71–77.

[158] Nerea Mangado, Mario Ceresa, Nicolas Duchateau, Hans Martin Kjer, Sergio Vera, Hector Dejea Velardo, Pavel Mistrik, Rasmus R. Paulsen, Jens Fagertun, Jérôme Noailly, Gemma Piella, and Miguel Ángel González Ballester. "Automatic Model Generation Framework for Computational Simulation of Cochlear Implantation". In: *Annals of Biomedical Engineering* 44.8 (Aug. 2016), pp. 2453–2463.

[159] Juan Antonio Martínez-Mera, Pablo G. Tahoces, José M. Carreira, Jorge Juan Suárez-Cuenca, and Miguel Souto. "A hybrid method based on level set and 3D region growing for segmentation of the thoracic aorta". In: *Computer Aided Surgery* 18.5-6 (Sept. 2013), pp. 109–117.

[160] Martín Abadi, Ashish Agarwal, Paul Barham, Eugene Brevdo, Zhifeng Chen, Craig Citro, Greg S. Corrado, Andy Davis, Jeffrey Dean, Matthieu Devin, Sanjay Ghemawat, Ian Goodfellow, Andrew Harp, Geoffrey Irving, Michael Isard, Yangqing Jia, Rafal Jozefowicz, Lukasz Kaiser, Manjunath Kudlur, Josh Levenberg, Dandelion Mané, Rajat Monga, Sherry Moore, Derek Murray, Chris Olah, Mike Schuster, Jonathon Shlens, Benoit Steiner, Ilya Sutskever, Kunal Talwar, Paul Tucker, Vincent Vanhoucke, Vijay Vasudevan, Fernanda Viégas, Oriol Vinyals, Pete Warden, Martin Wattenberg, Martin Wicke, Yuan Yu, and Xiaoqiang Zheng. *TensorFlow: Large-Scale Machine Learning on Heterogeneous Systems*. Software available from tensorflow.org. 2015.

[161] Alireza Mehrtash, Mehran Pesteie, Jorden Hetherington, Peter A. Behringer, Tina Kapur, William M. 3rd Wells, Robert Rohling, Andriy Fedorov, and Purang Abolmaesumi. "DeepInfer: Open-Source Deep Learning Deployment Toolkit for Image-Guided Therapy". In: *Proceedings of SPIE–the International Society for Optical Engineering* 10135 (Feb. 2017). 101351K[PII], 101351K.

[162] F. Milletari, N. Navab, and S. Ahmadi. "V-Net: Fully Convolutional Neural Networks for Volumetric Medical Image Segmentation". In: *2016 Fourth International Conference on 3D Vision (3DV)*. Oct. 2016, pp. 565–571.

[163] D. S. Minhas, J. A. Engh, M. M. Fenske, and C. N. Riviere. "Modeling of Needle Steering via Duty-Cycled Spinning". In: *2007 29th Annual International Conference of the IEEE Engineering in Medicine and Biology Society*. Aug. 2007, pp. 2756–2759.

[164] B. Moghaddam and A. Pentland. "Probabilistic visual learning for object representation". In: *IEEE Transactions on Pattern Analysis and Machine Intelligence* 19.7 (July 1997), pp. 696–710.

[165] Miguel Monteiro, Mário A. T. Figueiredo, and Arlindo L. Oliveira. "Conditional Random Fields as Recurrent Neural Networks for 3D Medical Imaging Segmentation". In: *CoRR* abs/1807.07464 (2018).

[166] Brent C. Munsell, Andrew Temlyakov, Martin Styner, and Song Wang. "Pre-organizing Shape Instances for Landmark-Based Shape Correspondence". In: *International Journal of Computer Vision* 97.2 (Apr. 2012), pp. 210–228.

[167] Richard M. Murray, Zexiang Li, and S. Shankar Sastry. *A Mathematical Introduction to Robotic Manipulation*. CRC Press LLC, 1994.

[168] Vinod Nair and Geoffrey E. Hinton. "Rectified Linear Units Improve Restricted Boltzmann Machines". In: *Proceedings of the 27th International Conference on International Conference on Machine Learning*. ICML'10. Haifa, Israel: Omnipress, 2010, pp. 807–814.

[169] Fernando Navarro, Suprosanna Shit, Ivan Ezhov, Johannes Paetzold, Andrei Gafita, Jan C. Peeken, Stephanie E. Combs, and Bjoern H. Menze. "Shape-Aware Complementary-Task Learning for Multi-organ Segmentation". In: *Machine Learning in Medical Imaging*. Ed. by Heung-Il Suk, Mingxia Liu, Pingkun Yan, and Chunfeng Lian. Cham: Springer International Publishing, 2019, pp. 620–627.

[170] J. A. Nelder and R. Mead. "A Simplex Method for Function Minimization". In: *The Computer Journal* 7.4 (Jan. 1965), pp. 308–313.

[171] M. H. Nguyen, E. Abdelmaguid, J. Huang, S. Kenchareddy, D. Singla, L. Wilke, M. Bobar, E. D. Carruth, D. Uys, I. Altintas, E. D. Muse, G. Quer, and S. Steinhubl. "Analytics pipeline for left ventricle segmentation and volume estimation on cardiac MRI using deep learning". In: *2018 IEEE 14th International Conference on e-Science (e-Science)*. Oct. 2018, pp. 305–306.

[172] K. Nikolajevic and N. Belanger. "A new method based on motion primitives to compute 3D path planning close to helicopters' flight dynamics limits". In: *2016 7th International Conference on Mechanical and Aerospace Engineering (ICMAE)*. July 2016, pp. 411–415.

[173] Jack H. Noble and Benoit M. Dawant. "An atlas-navigated optimal medial axis and deformable model algorithm (NOMAD) for the segmentation of the optic nerves and chiasm in MR and CT images". In: *Med Image Anal* 15.6 (Dec. 2011), pp. 877–884.

[174] Jack H. Noble, Benoit M. Dawant, Frank M. Warren, and Robert F. Labadie. "Automatic Identification and 3-D Rendering of Temporal Bone Anatomy". In: *Otol Neurotol* 30.4 (June 2009), pp. 436–442.

[175] Jack H. Noble, Robert F. Labadie, O. Majdani, and Benoit M. Dawant. "Automatic Segmentation of Intracochlear Anatomy in Conventional CT". In: *IEEE Trans. Biomed. Eng.* 58.9 (Sept. 2011), pp. 2625–2632.

[176] Jack H. Noble, Frank M. Warren M.D., Robert F. Labadie M.D., and Benoit M. Dawant. "Automatic segmentation of the facial nerve and chorda tympani using image registration and statistical priors". In: *Medical Imaging 2008: Image Processing*. Ed. by Joseph M. Reinhardt and Josien P. W. Pluim. Vol. 6914. International Society for Optics and Photonics. SPIE, 2008, pp. 226–235.

[177] Jack H. Noble, Omid Majdani, Robert F. Labadie, Benoit M. Dawant, and J. Michael Fitzpatrick. "Automatic Determination of Optimal Linear Drilling Trajectories for Cochlear Access Accounting for Drill Positioning Error". In: *Int J Med Robot* 6.3 (Sept. 2010), pp. 281–290.

[178] Jack H. Noble, Frank M. Warren, Robert F. Labadie, and Benoit M. Dawant. "Automatic segmentation of the facial nerve and chorda tympani in CT images using spatially dependent feature values". In: *Medical physics* 35.12 (Dec. 2008). PMC2673604[pmcid], pp. 5375–5384.

[179] Jack H. Noble, Frank M. Warren, Robert F. Labadie, Benoit M., and J. Michael Fitzpatrick. "Determination of drill paths for percutaneous cochlear access accounting for target positioning error". In: vol. 6509. 2007, pp. 6509 - 6509 –10.

[180] Isabella Nogues, Le Lu, Xiaosong Wang, Holger Roth, Gedas Bertasius, Nathan Lay, Jianbo Shi, Yohannes Tsehay, and Ronald M. Summers. "Automatic Lymph Node Cluster Segmentation Using Holistically-Nested Neural Networks and Structured Optimization in CT Images". In: *Medical Image Computing and Computer-Assisted Intervention – MICCAI 2016*. Ed. by Sebastien Ourselin, Leo Joskowicz, Mert R. Sabuncu, Gozde Unal, and William Wells. Cham: Springer International Publishing, 2016, pp. 388–397.

[181] O. Oktay, E. Ferrante, K. Kamnitsas, M. Heinrich, W. Bai, J. Caballero, S. A. Cook, A. de Marvao, T. Dawes, D. P. O'Regan, B. Kainz, B. Glocker, and D. Rueckert. "Anatomically Constrained Neural Networks (ACNNs): Application to Cardiac Image Enhancement and Segmentation". In: *IEEE Transactions on Medical Imaging* 37.2 (Feb. 2018), pp. 384–395.

[182]   Francisco P M Oliveira, Diogo Borges Faria, and João Manuel R S Tavares. "Automated segmentation of the incus and malleus ossicles in conventional tridimensional computed tomography images." In: *Proceedings of the Institution of Mechanical Engineers. Part H, Journal of engineering in medicine* 228 8 (2014), pp. 810–8.

[183]   Mark Owen, Randal W. Beard, and Timothy W. McLain. "Implementing Dubins Airplane Paths on Fixed-Wing UAVs*". In: *Handbook of Unmanned Aerial Vehicles*. Ed. by Kimon P. Valavanis and George J. Vachtsevanos. Dordrecht: Springer Netherlands, 2015, pp. 1677–1701.

[184]   Nathan Painchaud, Youssef Skandarani, Thierry Judge, Olivier Bernard, Alain Lalande, and Pierre-Marc Jodoin. "Cardiac MRI Segmentation with Strong Anatomical Guarantees". In: *Medical Image Computing and Computer Assisted Intervention – MICCAI 2019*. Ed. by Dinggang Shen, Tianming Liu, Terry M. Peters, Lawrence H. Staib, Caroline Essert, Sean Zhou, Pew-Thian Yap, and Ali Khan. Cham: Springer International Publishing, 2019, pp. 632–640.

[185]   Chonhyon Park, Jia Pan, and Dinesh Manocha. "ITOMP: Incremental trajectory optimization for real-time replanning in dynamic environments". English (US). In: *ICAPS 2012 - Proceedings of the 22nd International Conference on Automated Planning and Scheduling*. 2012, pp. 207–215.

[186]   Sachin Patil and Ron Alterovitz. "Interactive motion planning for steerable needles in 3D environments with obstacles". In: *2010 3rd IEEE RAS EMBS International Conference on Biomedical Robotics and Biomechatronics*. Sept. 2010, pp. 893–899.

[187]   Sachin Patil, J. Burgner, R. J. Webster, and Ron Alterovitz. "Needle Steering in 3-D Via Rapid Replanning". In: *IEEE Transactions on Robotics* 30.4 (Aug. 2014), pp. 853–864.

[188]   Sachin Patil, J. Pan, P. Abbeel, and Ken Goldberg. "Planning Curvature and Torsion Constrained Ribbons in 3D With Application to Intracavitary Brachytherapy". In: *IEEE Transactions on Automation Science and Engineering* 12.4 (Oct. 2015), pp. 1332–1345.

[189]   S. A. Pedram, P. Ferguson, J. Ma, E. Dutson, and J. Rosen. "Autonomous suturing via surgical robot: An algorithm for optimal selection of needle diameter, shape, and path". In: *2017 IEEE International Conference on Robotics and Automation (ICRA)*. May 2017, pp. 2391–2398.

[190]   Caroline Petitjean. "Segmentation of THoracic Organs at Risk in CT Images". In: *Proceedings of the 2019 Challenge on Segmentation of THoracic Organs at Risk in CT Images (SegTHOR2019)* 2348 (2019).

[191]   Pawit Pharpatara, Bruno Hérissé, and Yasmina Bestaoui. "3-D Trajectory Planning of Aerial Vehicles Using RRT*". In: *IEEE Transactions on Control Systems Technology* 25.3 (May 2017), pp. 1116–1123.

[192]   Pawit Pharpatara, Bruno Hérissé, and Yasmina Bestaoui. "3D-shortest paths for a hypersonic glider in a heterogeneous environment". In: *IFAC-PapersOnLine* 48.9 (2015). 1st IFAC Workshop on Advanced Control and Navigation for Autonomous Aerospace Vehicles ACNAAV'15, pp. 186–191.

[193]   Pawit Pharpatara, Bruno Hérissé, R. Pepy, and Yasmina Bestaoui. "Shortest path for aerial vehicles in heterogeneous environment using RRT*". In: *2015 IEEE International Conference on Robotics and Automation (ICRA)*. May 2015, pp. 6388–6393.

[194]   Marlene Pinzi, Stefano Galvan, and Ferdinando Rodriguez y Baena. "The Adaptive Hermite Fractal Tree (AHFT): a novel surgical 3D path planning approach with curvature and heading constraints". In: *International Journal of Computer Assisted Radiology and Surgery* (Feb. 2019).

[195]   Kimerly A. Powell, Tanisha Kashikar, Brad Hittle, Don Stredney, Thomas Kerwin, and Gregory J. Wiet. "Atlas-based segmentation of temporal bone surface structures". In: *International Journal of Computer Assisted Radiology and Surgery* 14.8 (Aug. 2019), pp. 1267–1273.

[196]   Kimerly A. Powell, Tong Liang, Brad Hittle, Don Stredney, Thomas Kerwin, and Gregory J. Wiet. "Atlas-Based Segmentation of Temporal Bone Anatomy". In: *International Journal of Computer Assisted Radiology and Surgery* 12.11 (Nov. 2017), pp. 1937–1944.

[197]   Yulei Qin, Mingjian Chen, Hao Zheng, Yun Gu, Mali Shen, Jie Yang, Xiaolin Huang, Yue-Min Zhu, and Guang-Zhong Yang. "AirwayNet: A Voxel-Connectivity Aware Approach for Accurate Airway Segmentation Using Convolutional Neural Networks". In: *Medical Image Computing and Computer Assisted Intervention – MICCAI 2019*. Ed. by Dinggang Shen, Tianming Liu, Terry M. Peters, Lawrence H. Staib, Caroline Essert, Sean Zhou, Pew-Thian Yap, and Ali Khan. Cham: Springer International Publishing, 2019, pp. 212–220.

[198] Morgan Quigley, Brian Gerkey, Ken Conley, Josh Faust, Tully Foote, Jeremy Leibs, Eric Berger, Rob Wheeler, and Andrew Ng. "ROS: an open-source Robot Operating System". In: *Proc. of the IEEE Intl. Conf. on Robotics and Automation (ICRA) Workshop on Open Source Robotics*. Kobe, Japan, May 2009.

[199] M. Rajchl, M. C. H. Lee, O. Oktay, K. Kamnitsas, J. Passerat-Palmbach, W. Bai, M. Damodaram, M. A. Rutherford, J. V. Hajnal, B. Kainz, and D. Rueckert. "DeepCut: Object Segmentation From Bounding Box Annotations Using Convolutional Neural Networks". In: *IEEE Transactions on Medical Imaging* 36.2 (Feb. 2017), pp. 674–683.

[200] N. Ratliff, M. Zucker, J. A. Bagnell, and S. Srinivasa. "CHOMP: Gradient optimization techniques for efficient motion planning". In: *2009 IEEE International Conference on Robotics and Automation*. May 2009, pp. 489–494.

[201] Kyle B. Reed, Ann Majewicz, Vinutha Kallem, Ron Alterovitz, Ken Goldberg, Noah J. Cowan, and Allison M. Okamura. "Robot-Assisted Needle Steering". In: *IEEE robotics & automation magazine* 18.4 (Dec. 2011), pp. 35–46.

[202] H. Ren, E. Campos-Nanez, Z. Yaniv, F. Banovac, H. Abeledo, N. Hata, and K. Cleary. "Treatment Planning and Image Guidance for Radiofrequency Ablation of Large Tumors". In: *IEEE Journal of Biomedical and Health Informatics* 18.3 (May 2014), pp. 920–928.

[203] III Robert J. Webster and Bryan A. Jones. "Design and Kinematic Modeling of Constant Curvature Continuum Robots: A Review". In: *The International Journal of Robotics Research* 29.13 (2010), pp. 1661–1683.

[204] Olaf Ronneberger, Philipp Fischer, and Thomas Brox. "U-Net: Convolutional Networks for Biomedical Image Segmentation". In: *Medical Image Computing and Computer-Assisted Intervention – MICCAI 2015: 18th International Conference, Munich, Germany, October 5-9, 2015, Proceedings, Part III*. Cham: Springer Intern. Publishing, 2015, pp. 234–241.

[205] *ROS website*. https://www.ros.org/about-ros/. Accessed: 10.12.2019.

[206] Esmeralda Ruiz Pujadas, Gemma Piella, Hans Martin Kjer, and Miguel Angel González Ballester. "Random walks with statistical shape prior for cochlea and inner ear segmentation in micro-CT images". In: *Machine Vision and Applications* 29.3 (Apr. 2018), pp. 405–414.

[207] Christian Rupprecht, Elizabeth Huaroc, Maximilian Baust, and Nassir Navab. "Deep Active Contours". In: *CoRR* abs/1607.05074 (2016).

[208] Zein Salah, F. Damman, Erwin Schwaderer, M. Maassen, Dirk Bartz, and Wolfgang Straßer. "Preoperative Planning of a Complete Mastoidectomy: Semiautomatic Segmentation and Evaluation". In: *International Journal of Computer Assisted Radiology and Surgery* 1.4 (2006), pp. 213–222.

[209] Ahad Salimi, Mohammad Ali Pourmina, and Mohammad-Shahram Moin. "Fully automatic prostate segmentation in MR images using a new hybrid active contour-based approach". In: *Signal, Image and Video Processing* 12.8 (Nov. 2018), pp. 1629–1637.

[210] S. Sanan, Y. Chen, C. A. Lehocky, C. Gong, C. N. Riviere, and H. Choset. "3D Motion Planning for Steerable Needles using Path Sets". In: 2014.

[211] Jörg Schipper, Antje Aschendorff, Iakovos Arapakis, Thomas Klenzner, Christian Barna Teszler, Gerd Jürgen Ridder, and Roland Laszig. "Navigation as a quality management tool in cochlear implant surgery". In: *The Journal of Laryngology & Otology* 118.10 (2004), pp. 764–770.

[212] Philipp Schleer, Sergey Drobinsky, Matias de la Fuente, and Klaus Radermacher. "Toward versatile cooperative surgical robotics: a review and future challenges". In: *International Journal of Computer Assisted Radiology and Surgery* 14.10 (Oct. 2019), pp. 1673–1686.

[213] Will Schroeder, Ken Martin, and Bill Lorensen. *The Visualization Toolkit (4th ed.)* 4th ed. Kitware, 2006.

[214] John Schulman, Yan Duan, Jonathan Ho, Alex Lee, Ibrahim Awwal, Henry Bradlow, Jia Pan, Sachin Patil, Ken Goldberg, and Pieter Abbeel. "Motion planning with sequential convex optimization and convex collision checking". In: *The Int. J. of Rob. Res.* 33.9 (2014), pp. 1251–1270.

[215] John Schulman, Jonathan Ho, Alex X. Lee, Ibrahim Awwal, Henry Bradlow, and Pieter Abbeel. "Finding Locally Optimal, Collision-Free Trajectories with Sequential Convex Optimization". In: *Robotics: Science and Systems*. 2013.

[216] Alexander Seitel, Markus Engel, Christof M. Sommer, Boris A. Radeleff, Caroline Essert-Villard, Claire Baegert, Markus Fangerau, Klaus H. Fritzsche, Kwong Yung, Hans-Peter Meinzer, and Lena Maier-Hein. "Computer-assisted trajectory planning for percutaneous needle insertions". In: *Medical Physics* 38.6Part1 (2011), pp. 3246–3259.

[217]   S. Sen, A. Garg, D. V. Gealy, S. McKinley, Y. Jen, and Ken Goldberg. "Automating multi-throw multilateral surgical suturing with a mechanical needle guide and sequential convex optimization". In: *2016 IEEE International Conference on Robotics and Automation (ICRA)*. May 2016, pp. 4178–4185.

[218]   Levent Sennaroglu and Münir Demir Bajin. "Classification and Current Management of Inner Ear Malformations". In: *Balkan medical journal* 34.5 (Sept. 2017). PMC5635626[pmcid], pp. 397–411.

[219]   Daniel M. Shabanzadeh and Lars T. Sørensen. "Laparoscopic Surgery Compared With Open Surgery Decreases Surgical Site Infection in Obese Patients: A Systematic Review and Meta-Analysis". In: *Annals of Surgery* 256.6 (Dec. 2012), pp. 934–945.

[220]   M. Shakeri, S. Tsogkas, E. Ferrante, S. Lippe, S. Kadoury, N. Paragios, and I. Kokkinos. "Sub-cortical brain structure segmentation using F-CNN'S". In: *2016 IEEE 13th International Symposium on Biomedical Imaging (ISBI)*. Apr. 2016, pp. 269–272.

[221]   Madhavan Shanmugavel, Antonios Tsourdos, Rafal Zbikowski, and Brian White. In: Guidance, Navigation, and Control and Co-located Conferences. 0. American Institute of Aeronautics and Astronautics, Aug. 2007. Chap. 3D Path Planning for Multiple UAVs Using Pythagorean Hodograph Curves.

[222]   Dinggang Shen, Guorong Wu, and Heung-Il Suk. "Deep Learning in Medical Image Analysis". In: *Annu Rev Biomed Eng* 19 (June 2017), pp. 221–248.

[223]   H. Shen and J. Zhang. "Fully connected CRF with data-driven prior for multi-class brain tumor segmentation". In: *2017 IEEE International Conference on Image Processing (ICIP)*. Sept. 2017, pp. 1727–1731.

[224]   A. Shkolnik, M. Walter, and R. Tedrake. "Reachability-guided sampling for planning under differential constraints". In: *2009 IEEE Int. Conf. on Rob. a. Autom.* May 2009, pp. 2859–2865.

[225]   Thanongchai Siriapisith, Worapan Kusakunniran, and Peter Haddawy. "Outer Wall Segmentation of Abdominal Aortic Aneurysm by Variable Neighborhood Search Through Intensity and Gradient Spaces". In: *Journal of Digital Imaging* 31.4 (Aug. 2018), pp. 490–504.

[226]   *Slicer 3D website*. `https://www.slicer.org/`. Accessed: 10.12.2019.

[227]   *SOFA website*. `https://www.sofa-framework.org/about/features/`. Accessed: 10.12.2019.

[228] B. S. Spottiswoode, D. J. van den Heever, Y. Chang, S. Engelhardt, S. Du Plessis, F. Nicolls, H. B. Hartzenberg, and A. Gretschel. "Preoperative Three-Dimensional Model Creation of Magnetic Resonance Brain Images as a Tool to Assist Neurosurgical Planning". In: *Stereotactic and Functional Neurosurgery* 91.3 (2013), pp. 162–169.

[229] *STARE: STructured Analysis of the Retina.* `https://cecas.clemson.edu/~ahoover/stare/`. Accessed: 14.02.2020.

[230] I. Stenin, Stefan Hansen, Meike Becker, Georgios Sakas, Dieter Fellner, Thomas Klenzner, and Jörg Schipper. "Minimally Invasive Multi-Port Surgery of the Lateral Skull Base". In: *BioMed Research International*. Vol. 2014. 2014, p. 7.

[231] Ioan A. Şucan, Mark Moll, and Lydia E. Kavraki. "The Open Motion Planning Library". In: *IEEE Robotics & Automation Magazine* 19.4 (Dec. 2012). `http://ompl.kavrakilab.org`, pp. 72–82.

[232] P. Sudhakara, V. Ganapathy, and K. Sundaran. "Optimal trajectory planning based on bidirectional spline-RRT* for wheeled mobile robot". In: *2017 Third International Conference on Sensing, Signal Processing and Security (ICSSS)*. May 2017, pp. 65–68.

[233] W. Sun, J. van den Berg, and Ron Alterovitz. "Stochastic Extended LQR for Optimization-Based Motion Planning Under Uncertainty". In: *IEEE Transactions on Automation Science and Engineering* 13.2 (Apr. 2016), pp. 437–447.

[234] Wen Sun and Ron Alterovitz. "Motion planning under uncertainty for medical needle steering using optimization in belief space". In: *2014 IEEE/RSJ International Conference on Intelligent Robots and Systems*. Sept. 2014, pp. 1775–1781.

[235] H. J. Sussmann. "Shortest 3-dimensional paths with a prescribed curvature bound". In: *Proceedings of 1995 34th IEEE Conference on Decision and Control*. Vol. 4. Dec. 1995, 3306–3312 vol.4.

[236] Philip J. Swaney, Arthur W. Mahoney, Andria A. Remirez, Erik Lamers, Bryan I. Hartley, R ichard H. Feins, Ron Alterovitz, and Robert J. 3rd Webster. "Tendons, Concentric Tubes, and a Bevel Tip: Three Steerable Robots in One Transoral Lung Access System". In: *IEEE Int Conf Robot Autom* 2015 (May 2015), pp. 5378–5383.

[237] A. Tack, A. Mukhopadhyay, and S. Zachow. "Knee menisci segmentation using convolutional neural networks: data from the Osteoarthritis Initiative". In: *Osteoarthritis and Cartilage* 26.5 (May 2018), pp. 680–688.

[238]   Pablo G. Tahoces, Luis Alvarez, Esther González, Carmelo Cuenca, Agustín Trujillo, Daniel Santana-Cedrés, Julio Esclarín, Luis Gomez, Luis Mazorra, Miguel Alemán-Flores, and José M. Carreira. "Automatic estimation of the aortic lumen geometry by ellipse tracking". In: *International Journal of Computer Assisted Radiology and Surgery* 14.2 (Feb. 2019), pp. 345–355.

[239]   Min Tang, Sepehr Valipour, Zichen Zhang, Dana Cobzas, and Martin Jagersand. "A Deep Level Set Method for Image Segmentation". In: *Deep Learning in Medical Image Analysis and Multimodal Learning for Clinical Decision Support*. Ed. by M. Jorge Cardoso, Tal Arbel, Gustavo Carneiro, Tanveer Syeda-Mahmood, João Manuel R.S. Tavares, Mehdi Moradi, Andrew Bradley, Hayit Greenspan, João Paulo Papa, Anant Madabhushi, Jacinto C. Nascimento, Jaime S. Cardoso, Vasileios Belagiannis, and Zhi Lu. Cham: Springer International Publishing, 2017, pp. 126–134.

[240]   Renato Torres, Guillaume Kazmitcheff, Daniele De Seta, Evelyne Ferrary, Olivier Sterkers, and Yann Nguyen. "Improvement of the insertion axis for cochlear implantation with a robot-based system". In: *European Archives of Oto-Rhino-Laryngology* 274.2 (Feb. 2017), pp. 715–721.

[241]   R. Trullo, C. Petitjean, S. Ruan, B. Dubray, D. Nie, and D. Shen. "Segmentation of organs at risk in thoracic CT images using a sharpmask architecture and conditional random fields". In: *14th IEEE Intern. Symp. on Biom. Imag.* 2017, pp. 1003–1006.

[242]   Yeimy Paola Valencia Usme. "Automatische Segmentierung der Paukenhöhle und des Antrum Mastoideum". Master's Thesis. Darmstadt: Technische Universität, 2017.

[243]   Sebastien Valette, Jean-Marc Chassery, and Remy Prost. "Generic Remeshing of 3D Triangular Meshes with Metric-Dependent Discrete Voronoi Diagrams". In: 14 (Mar. 2008), pp. 369–381.

[244]   Sébastien Valette and Jean-Marc Chassery. "Approximated Centroidal Voronoi Diagrams for Uniform Polygonal Mesh Coarsening". In: *Comput. Graph. Forum* 23 (2004), pp. 381–390.

[245]   B. van Ginneken, A. F. Frangi, J. J. Staal, B. M. ter Haar Romeny, and M. A. Viergever. "Active shape model segmentation with optimal features". In: *IEEE Transactions on Medical Imaging* 21.8 (Aug. 2002), pp. 924–933.

[246] EHJ Voormolen, Stralen van M., P. A. Woerdeman, JPW Josien Pluim, HJ No-
       ordman, MA Max Viergever, L. Regli, and JW Berkelbach van der Sprenkel.
       "Determination of a facial nerve safety zone for navigated temporal bone surgery".
       In: *Neurosurgery* 70.1 (2012), pp. 50–.

[247] Christian Wachinger, Martin Reuter, and Tassilo Klein. "DeepNAT: Deep con-
       volutional neural network for segmenting neuroanatomy". In: *NeuroImage* 170
       (2018). Segmenting the Brain, pp. 434–445.

[248] D. J. Walton, D. S. Meek, and J. M. Ali. "Planar G2 transition curves composed of
       cubic Bézier spiral segments". In: *Journal of Computational and Applied Mathe-
       matics* 157.2 (2003), pp. 453–476.

[249] Guotai Wang, Jonathan Shapey, Wenqi Li, Reuben Dorent, Alex Demitriadis,
       Sotirios Bisdas, Ian Paddick, Robert Bradford, Shaoting Zhang, Sébastien Ourselin,
       and Tom Vercauteren. "Automatic Segmentation of Vestibular Schwannoma from
       T2-Weighted MRI by Deep Spatial Attention with Hardness-Weighted Loss". In:
       Medical Image Computing and Computer Assisted Intervention – MICCAI 2019. Ed.
       by Dinggang Shen, Tianming Liu, Terry M. Peters, Lawrence H. Staib, Caroline
       Essert, Sean Zhou, Pew-Thian Yap, and Ali Khan. Cham: Springer International
       Publishing, 2019, pp. 264–272.

[250] Nanyang Wang, Yinda Zhang, Zhuwen Li, Yanwei Fu, Wei Liu, and Yu-Gang Jiang.
       "Pixel2Mesh: Generating 3D Mesh Models from Single RGB Images". In: *Computer
       Vision – ECCV 2018*. Ed. by Vittorio Ferrari, Martial Hebert, Cristian Sminchisescu,
       and Yair Weiss. Cham: Springer International Publishing, 2018, pp. 55–71.

[251] Yan Wang, Florent Seguro, Evan Kao, Yue Zhang, Farshid Faraji, Chengcheng Zhu,
       Henrik Haraldsson, Michael Hope, David Saloner, and Jing Liu. "Segmentation
       of lumen and outer wall of abdominal aortic aneurysms from 3D black-blood
       MRI with a registration based geodesic active contour model". In: *Medical Image
       Analysis* 40 (2017), pp. 1–10.

[252] S. K. Warfield, K. H. Zou, and W. M. Wells. "Simultaneous truth and performance
       level estimation (STAPLE): an algorithm for the validation of image segmentation".
       In: *IEEE Transactions on Medical Imaging* 23.7 (July 2004), pp. 903–921.

[253] S. Weber, N. Gerber, K. A. Gavaghan, T. Williamson, W. Wimmer, J. Anso, L.
       Brogna-Salas, D. Chen, C. Weisstanner, M. Caversaccio, and B. Bell. "Image guided
       and robotic assisted minimally invasive cochlear implantation". In: *The Hamlyn
       Symposium on Medical Robotics*. 2013, pp. 17–18.

[254] Robert J. Webster III, Jin Seob Kim, Noah J. Cowan, Gregory S. Chirikjian, and Allison M. Okamura. "Nonholonomic Modeling of Needle Steering". In: *The International Journal of Robotics Research* 25.5-6 (2006), pp. 509–525.

[255] Bilal Wehbe, Elie Shammas, and Daniel Asmar. "A novel method to generate three-dimensional paths for vehicles with bounded pitch and yaw". In: *2015 IEEE International Conference on Advanced Intelligent Mechatronics (AIM)*. July 2015, pp. 1701–1706.

[256] Moritz Weissenberger. "Interaktive Analyse von geplanten medizinischen Bohrkanälen". Bachelor's Thesis. Darmstadt: Technische Universität, 2017.

[257] Ivo Wolf, Marcus Vetter, Ingmar Wegner, Marco Nolden, Thomas Bottger, Mark Hastenteufel, Max Schobinger, Tobias Kunert, and Hans-Peter Meinzer. "The medical imaging interaction toolkit (MITK): a toolkit facilitating the creation of interactive software by extending VTK and ITK". In: *Medical Imaging 2004: Visualization, Image-Guided Procedures, and Display*. Ed. by Robert L. Galloway Jr. Vol. 5367. International Society for Optics and Photonics. SPIE, 2004, pp. 16–27.

[258] Kai-jian Xia, Hong-sheng Yin, and Yu-dong Zhang. "Deep Semantic Segmentation of Kidney and Space-Occupying Lesion Area Based on SCNN and ResNet Models Combined with SIFT-Flow Algorithm". In: *Journal of Medical Systems* 43.1 (Nov. 2018), p. 2.

[259] Diao Xianfen, Chen Siping, Liang Changhong, and Wang Yuanmei. "3D Semi-automatic Segmentation of the Cochlea and Inner Ear". In: *2005 IEEE Engineering in Medicine and Biology 27th Annual Conference*. Jan. 2005, pp. 6285–6288.

[260] S. Xie and Z. Tu. "Holistically-Nested Edge Detection". In: *2015 IEEE International Conference on Computer Vision (ICCV)*. Dec. 2015, pp. 1395–1403.

[261] F. Xing, Y. Xie, and L. Yang. "An Automatic Learning-Based Framework for Robust Nucleus Segmentation". In: *IEEE Transactions on Medical Imaging* 35.2 (Feb. 2016), pp. 550–566.

[262] Jijie Xu, Vincent Duindam, Ron Alterovitz, and Ken Goldberg. "Motion planning for steerable needles in 3D environments with obstacles using rapidly-exploring Random Trees and backchaining". In: *2008 IEEE International Conference on Automation Science and Engineering*. Aug. 2008, pp. 41–46.

[263] Jun Xu, Lei Gong, Guanhao Wang, Cheng Lu, Hannah Gilmore, Shaoting Zhang, and Anant Madabhushi. "Convolutional neural network initialized active contour model with adaptive ellipse fitting for nuclear segmentation on breast histopathological images". In: *Journal of Medical Imaging* 6.1 (2019), pp. 1–16.

[264] Xuanang Xu, Fugen Zhou, and Bo Liu. "Automatic bladder segmentation from CT images using deep CNN and 3D fully connected CRF-RNN". In: *International Journal of Computer Assisted Radiology and Surgery* 13.7 (July 2018), pp. 967–975.

[265] Atsushi Yaguchi, Kota Aoyagi, Akiyuki Tanizawa, and Yoshiharu Ohno. "3D fully convolutional network-based segmentation of lung nodules in CT images with a clinically inspired data synthesis method". In: *Medical Imaging 2019: Computer-Aided Diagnosis*. Ed. by Kensaku Mori and Horst K. Hahn. Vol. 10950. International Society for Optics and Photonics. SPIE, 2019, pp. 862–868.

[266] Kwangjin Yang, S. K. Gan, J. Huh, and S. Joo. "Optimal spline-based RRT path planning using probabilistic map". In: *2014 14th Int. Conf. on Control, Autom. and Systems (ICCAS 2014)*. Oct. 2014, pp. 643–646.

[267] Kwangjin Yang, Sangwoo Moon, Seunghoon Yoo, Jaehyeon Kang, Nakju Lett Doh, Hong Bong Kim, and Sanghyun Joo. "Spline-Based RRT Path Planner for Non-Holonomic Robots". In: *Journal of Intelligent & Robotic Systems* 73.1 (2014), pp. 763–782.

[268] Kwangjin Yang and S. Sukkarieh. "3D smooth path planning for a UAV in cluttered natural environments". In: *2008 IEEE/RSJ International Conference on Intelligent Robots and Systems*. Sept. 2008, pp. 794–800.

[269] Kwangjin Yang and S. Sukkarieh. "An Analytical Continuous-Curvature Path-Smoothing Algorithm". In: *IEEE Transactions on Robotics* 26.3 (June 2010), pp. 561–568.

[270] L. Yang, J. Qi, Z. Jiang, D. Song, J. Han, and J. Xiao. "Guiding attraction based random tree path planning under uncertainty: Dedicate for UAV". In: *2014 IEEE Int. Conf. on Mech. a. Autom.* Aug. 2014, pp. 1182–1187.

[271] S. X. Yang and M. Meng. "Neural network approaches to dynamic collision-free trajectory generation". In: *IEEE Transactions on Systems, Man, and Cybernetics, Part B (Cybernetics)* 31.3 (June 2001), pp. 302–318.

[272] S. X. Yang and M. Q. -. Meng. "Real-time collision-free motion planning of a mobile robot using a Neural Dynamics-based approach". In: *IEEE Transactions on Neural Networks* 14.6 (Nov. 2003), pp. 1541–1552.

[273] Jiawen Yao, Jinzheng Cai, Dong Yang, Daguang Xu, and Junzhou Huang. "Integrating 3D Geometry of Organ for Improving Medical Image Segmentation". In: *Medical Image Computing and Computer Assisted Intervention – MICCAI 2019*. Ed. by Dinggang Shen, Tianming Liu, Terry M. Peters, Lawrence H. Staib, Caroline Essert, Sean Zhou, Pew-Thian Yap, and Ali Khan. Cham: Springer International Publishing, 2019, pp. 318–326.

[274] Xiaojiang Yi, Sile Chen, Wei Wang, Liaonan Zou, Dechang Diao, Yansheng Zheng, Yaobin He, Hongming Li, Lijie Luo, Wenjun Xiong, and Jin Wan. "A Systematic Review and Meta-Analysis of Laparoscopic and Open Distal Pancreatectomy of Nonductal Adenocarcinomatous Pancreatic Tumor (NDACPT) in the Pancreatic Body and Tail". In: *Surgical Laparoscopy Endoscopy & Percutaneous Techniques* 27.4 (Aug. 2017), pp. 206–219.

[275] Jun-Hai Yong and Fuhua (Frank) Cheng. "Geometric Hermite curves with minimum strain energy". In: *Computer Aided Geometric Design* 21.3 (2004), pp. 281–301.

[276] T.S. Yoo, M. J. Ackerman, W. E. Lorensen, W. Schroeder, V. Chalana, S. Aylward, D. Metaxas, and R. Whitaker. "Engineering and Algorithm Design for an Image Processing API: A Technical Report on ITK - The Insight Toolkit". In: Amsterdam: IOS Press Amsterdam, 2002, pp. 586–592.

[277] Paul A. Yushkevich, Joseph Piven, Heather Cody Hazlett, Rachel Gimpel Smith, Sean Ho, James C. Gee, and Guido Gerig. "User-Guided 3D Active Contour Segmentation of Anatomical Structures: Significantly Improved Efficiency and Reliability". In: *Neuroimage* 31.3 (2006), pp. 1116–1128.

[278] Qi Zeng, Davood Karimi, Emily H. T. Pang, Shahed Mohammed, Caitlin Schneider, Mohammad Honarvar, and Septimiu E. Salcudean. "Liver Segmentation in Magnetic Resonance Imaging via Mean Shape Fitting with Fully Convolutional Neural Networks". In: *Medical Image Computing and Computer Assisted Intervention – MICCAI 2019*. Ed. by Dinggang Shen, Tianming Liu, Terry M. Peters, Lawrence H. Staib, Caroline Essert, Sean Zhou, Pew-Thian Yap, and Ali Khan. Cham: Springer International Publishing, 2019, pp. 246–254.

[279] Jiemin Zhai and Huiqi Li. "An Improved Full Convolutional Network Combined with Conditional Random Fields for Brain MR Image Segmentation Algorithm and its 3D Visualization Analysis". In: *Journal of Medical Systems* 43.9 (July 2019), p. 292.

[280]   Dongqing Zhang, Jianing Wang, Jack H. Noble, and Benoit M. Dawant. "Accurate Detection of Inner Ears in Head CTs Using a Deep Volume-to-Volume Regression Network with False Positive Suppression and a Shape-Based Constraint". In: *Medical Image Computing and Computer Assisted Intervention – MICCAI 2018*. Ed. by Alejandro F. Frangi, Julia A. Schnabel, Christos Davatzikos, Carlos Alberola-López, and Gabor Fichtinger. Cham: Springer International Publishing, 2018, pp. 703–711.

[281]   Lei Zhao, Tao Wan, Hongxiang Feng, and Zengchang Qin. "Improved Nuclear Segmentation on Histopathology Images Using a Combination of Deep Learning and Active Contour Model". In: *Neural Information Processing*. Ed. by Long Cheng, Andrew Chi Sing Leung, and Seiichi Ozawa. Cham: Springer International Publishing, 2018, pp. 307–317.

[282]   Xiaomei Zhao, Yihong Wu, Guidong Song, Zhenye Li, Yong Fan, and Yazhuo Zhang. "Brain Tumor Segmentation Using a Fully Convolutional Neural Network with Conditional Random Fields". In: *Brainlesion: Glioma, Multiple Sclerosis, Stroke and Traumatic Brain Injuries*. Ed. by Alessandro Crimi, Bjoern Menze, Oskar Maier, Mauricio Reyes, Stefan Winzeck, and Heinz Handels. Cham: Springer International Publishing, 2016, pp. 75–87.

[283]   Xiaomei Zhao, Yihong Wu, Guidong Song, Zhenye Li, Yazhuo Zhang, and Yong Fan. "A deep learning model integrating FCNNs and CRFs for brain tumor segmentation". In: *Medical Image Analysis* 43 (2018), pp. 98–111.

[284]   S. Zhu, W. Gao, Y. Zhang, J. Zheng, Z. Liu, and G. Yuan. "3D automatic MRI level set segmentation of inner ear based on statistical shape models prior". In: *2017 10th International Congress on Image and Signal Processing, BioMedical Engineering and Informatics (CISP-BMEI)*. Oct. 2017, pp. 1–6.

[285]   Feng Zhuge, Geoffrey D. Rubin, Shaohua Sun, and Sandy Napel. "An abdominal aortic aneurysm segmentation method: Level set with region and statistical information". In: *Medical Physics* 33.5 (2006), pp. 1440–1453.

[286]   Christos Zohios, Georgios Kossioris, and Yannis Papaharilaou. "Geometrical methods for level set based abdominal aortic aneurysm thrombus and outer wall 2D image segmentation". In: *Computer Methods and Programs in Biomedicine* 107.2 (2012), pp. 202–217.

[287]   Matt Zucker, Nathan Ratliff, Anca D. Dragan, Mihail Pivtoraiko, Matthew Klingensmith, Christopher M. Dellin, J. Andrew Bagnell, and Siddhartha S. Srinivasa. "CHOMP: Covariant Hamiltonian optimization for motion planning". In: *The International Journal of Robotics Research* 32.9-10 (2013), pp. 1164–1193.